UNIVERSIDAD DE GRANADA

TESIS DOCTORAL
PROGRAMA DE DOCTORADO EN FÍSICA Y CIENCIAS DEL ESPACIO

Ferrogeles con control remoto de la microestructura mediante campos magnéticos

Autor
Alberto León Cecilla

Directores
Modesto Torcuato López López
Departamento de Física Aplicada, Universidad de Granada
Luis Álvarez de Cienfuegos Rodríguez
Departamento de Química Orgánica, Universidad de Granada

Grupo de Física de Interfases y Sistemas Coloidales
Departamento de Física Aplicada
Granada, 2024

Editor: Universidad de Granada. Tesis Doctorales
Autor: Alberto León Cecilia
ISBN: 978-84-1195-611-6
URI: https://hdl.handle.net/10481/97718

¡Qué descansada vida
la del que huye del mundanal ruido,
y sigue la escondida
senda por donde han ido
los pocos sabios que en el mundo han sido!

Oda I-Vida retirada. Fray Luis de León

Agradecimientos

A mi familia, por apoyarme, acompañarme y ayudarme durante todos estos años. Estos tres últimos años no han sido fáciles pero nos han servido para reencontrarnos y a hacer más llevaderos los momentos difíciles.
A mis directores de tesis, Modesto y Luis, por su guía, apoyo y comprensión durante estos cinco años. Me siento afortunado de en 2019 haber empezado a trabajar con vosotros y haber llegado hasta aquí.
A mis excompañeros de despacho. A Cristina, por su inestimable ayuda desde que empecé en la investigación y por enseñarme casi todo lo que he necesitado estos años (no solo a hacer carteles). A Alfrediño por los buenos momentos de estupideces y tonterías. A Ana Belén por escucharme y ayudarme con la Química.
A Fran, con el que he trabajado codo con codo. Gracias por toda la ayuda en el laboratorio, en especial en los momentos que más la necesitaba.
Al resto del grupo I6, un buen ambiente hace maravillas.
A Laura Quesada de la Torre por la maravillosa imagen de la Figura 5.6, que reflejó perfectamente lo que tenía en mente.

Financiación

La investigación que ha dado fruto a esta tesis doctoral ha sido posible gracias al proyecto de I+D+i PID2020-118498GB-I00 financiado por MCIN/AEI/10.13039/501100011033. Los experimentos mostrados en el Capítulo 3 se realizaron en la línea MIRAS del sincrotrón ALBA con la colaboración del personal de ALBA.

La realización de esta tesis ha sido posible gracias a la ayuda FPU19/01801 financiada por MCIN/AEI/10.13039/501100011033 y FSE "El FSE invierte en tu futuro", y por la Universidad de Granada.

La estancia de investigación realizada en *Max Planck Institute for Intelligent Systems* ha sido financiada por el Ministerio de Ciencia, Innovación y Universidades, en el programa de ayudas complementarias a la movilidad destinadas a beneficiarios del programa de Formación del Profesorado Universitario, convocatoria de 2023 (EST23/00363).

Abstract

In the last decade, there has been an increasing interest in developing materials that can respond to diverse stimuli. The functionality of these materials is understood as their capacity to alter their physical properties or shape in response to external stimuli. Among these materials, magnetic hydrogels stand out due to their softness, high water content, light weight, mechanical properties, miniaturization potential, controllability without contact, and safe interaction with living tissues and organisms. They are defined as three-dimensional cross-linked polymer networks swollen by water, in which magnetic particles (MPs) are inserted. The polymers and MPs give these materials the ability to respond to different stimuli, such as temperature, pH, chemical compounds, and magnetic fields. These characteristics make them ideal materials for applications related to tissue engineering, bioelectronics, drug delivery, wound dressing, cancer treatment, environmental remediation, soft robots, and soft actuators.

The starting hypothesis of this thesis is the possibility of exerting precise control over the microstructure and spatial distribution of MPs in hydrogels by applying mechanical stresses or magnetic fields with adequate spatial modulation. The validity of this hypothesis is based on the results of previous works [Mredha et al., 2018, Lopez-Lopez et al., 2015, Scionti et al., 2013], where the possibility of modifying the hydrogel microstructure by applying external mechanical and magnetic stimuli was shown.

In this thesis, hydrogels and ferrogels with precise control of their microstructure and magnetic behavior were prepared. These materials were characterized from a macroscopical point of view via their mechanical properties and magnetic behavior, and from a microscopical point of view using different techniques such as scanning electron microscopy (SEM) and Fourier-Transform Infrared (FT-IR) spectroscopy. In addition, different types of applications in the field of soft actuators and sensors were designed for these ferrogels based on their properties.

To summarize, we studied alginate hydrogels with an anisotropic internal structure controlled by a mechanical stress or the alignment of functionalized MPs. Regarding these materials, we demonstrated that the anisotropy was reflected macroscopically, in their mechanical properties, and microscopically, in the arrangement of the polymeric

fibers. Subsequently, the analysis focused on semi-interpenetrating polymer network (SIPN) ferrogels based on acrylamide and biopolymers, which showed promising properties for soft robots, actuators, and sensors. These applications demonstrated the potential and versatility of SIPN ferrogels, which can be prepared under different experimental conditions, such as shape, MPs, and polymerization processes, and can sense and actuate under different environmental conditions.

Contents

Chapter 1. Introduction *

1.1 Introduction

In the last decade, a wide range of functional materials that can respond to diverse stimuli, such as light, humidity, heat, pH, electric field, magnetic field, solvents, etc., have been developed [Arif et al., 2024, Liu et al., 2022]. The functionality of these stimuli-responsive materials (SRMs) is understood as their capacity to change their physical properties or shape under the application of an external physical stimulus [Lucarini et al., 2022]. Among these SRMs, polymeric ones stand out due to their wide range of mechanical properties, tunability, and affordable synthesis procedures. Examples of polymeric materials include thermosetting and thermoplastic elastomers, shape memory polymers, liquid crystal elastomers, photopolymers, and hydrogels, which are our main focus here.

In general, hydrogels have the ability to naturally respond to certain stimuli, such as temperature, pH, different chemical compounds, and so on, due to the nature of the polymeric fibers that form the material network. Nevertheless, they are unable to naturally respond to magnetic fields; thus, particles with magnetic properties are embedded in the material structure through different methods, such as blending, in situ precipitation, and grafting-onto [Chung et al., 2021]. These magnetic hydrogels or ferrogels are smart materials that change their physical properties or shape under an external magnetic field. Modulating the magnitude, direction, and distribution of the latter, ferrogels can be easily manipulated or even heated, dramatically enhancing their potential applications [Wu et al., 2020]. They are characterized by their softness, light weight, large deformations, tunable mechanical properties, fast and accurate response to external stimuli, complete non-contact interactions, miniaturization potential,

*Part of the content of this chapter has been extracted and adapted from Leon-Cecilla, A., Vazquez-Perez, F. J., Lopez-Lopez, M. T. (2024). *Soft magnetoresponsive actuators - Engineering and Biomedical Applications*, Magneto Responsive Soft Nanosystems. Royal Society of Chemistry (under review).

heating capacity, and safe interaction with living tissues and organisms. Additionally, magnetic fields can penetrate air, water, or even living tissues, making these materials prominent for applications in different technological and biomedical fields [Li et al., 2024, He et al., 2023, Taghizadeh et al., 2023, Wang et al., 2022a, Liu et al., 2020b].

1.2 Synthesis of Magnetic Hydrogels or Ferrogels

As previously mentioned, ferrogels have two main components: the polymeric matrix and the magnetic particles (MPs). In the subsections below, we describe the main properties of these two fundamental components of ferrogels because the final properties of these materials strongly depend on the physicochemical properties of these two building blocks and the coupling between them.

1.2.1 Magnetic Particles

The nature of MPs is very diverse: nano- or micro-sized, ferri-/ferromagnetic (soft and hard) or superparamagnetic, mono- or multidomain, isotropic or anisotropic, etc. In Table 1.1 there is a compilation of the most commonly used MPs in hydrogels and their characteristics, which can be found in the scientific literature. Normally, the maximum volume fraction of MPs that the material matrix can allocate is around 0.4 [Dargahi et al., 2019]. Furthermore, MPs can be arranged inside a material matrix in two distinct configurations: 1) directionally oriented, which gives rise to magnetic and mechanical anisotropic properties [Zhai et al., 2023, Shi et al., 2020]; 2) randomly distributed, which results in an isotropic material [Mañas-Torres et al., 2021b]. To align the particles, it is only necessary to apply a magnetic field during the fabrication process. Additionally, MPs can be magnetized by an external field, which can disappear shortly after removing the magnetic field in soft- and superparamagnetic MPs or remain after removing it in hard-MPs [Moreno-Mateos et al., 2022]. Soft-MPs are characterized by high permeability, low coercivity and remanence, and reversible magnetization, whereas hard MPs have lower permeability, high coercivity and remanence, and irreversible magnetization behavior. In general, soft MPs can only be used to achieve simple and limited actuation [Goudu et al., 2020], while hard-MPs, after magnetization, can align themselves in the field direction, introducing internal torques that give rise to complex functionalities [Tang et al., 2021a].

The particle size is an important parameter in magnetic properties. When particles are sufficiently small, superparamagnetism appears, which manifests as particles with no remanence and coercivity while still possessing high permeability, in general, due to their monodomain nature [Xuan et al., 2009]. Some advantages of superparamagnetic MPs include the possibility of inductive heating under alternating magnetic fields [Chen et al., 2023b, Ganguly and Margel, 2022], their homogeneous distribution within the material without settling due to their size, and

their biocompatibility [Campos et al., 2021]. However, the magnetic programmability required in soft robots and actuators is very limited with these MPs, and they are usually relegated to biomedical applications such as hyperthermia therapy and drug delivery [Tay et al., 2018b].

Table 1.1: Types of MPs and their main characteristics (magnetic behavior and morphology) that can be found in the literature regarding magnetic hydrogels or ferrogels.

Material	Magnetic behaviour	Morphology	References
Iron Oxides (magnetite, maghemite)	Soft ferromagnetic Superparamagnetic	Spheric, flower, rod (10 nm - 30 µm)	[Wang et al., 2022b] [Goudu et al., 2020] [Gao et al., 2019]
Carbonyl iron	Soft ferromagnetic	Spheric (1 - 40 µm)	[Lawrence and Rao, 2023] [Selzer and Odenbach, 2020]
Ferrites	Hard ferromagnetic	Spheric (40 nm - 400 nm)	[Rincón-Iglesias et al., 2020] [Naderi and Azizian, 2018]
Neodymium (NdFeB)	Hard ferromagnetic	Spheric (5 -25 µm)	[Liu et al., 2021] [Kuang et al., 2021]
Nickel	Soft ferromagnetic	Spheric, rod (nanometric)	[Awasthi et al., 2020] [Safronov et al., 2019]

On the one hand, the application of a uniform magnetic field to isotropic ferrogels with soft-MPs induces dipole-dipole interactions between neighboring particles that are magnetized by the field. The magnetized particles tend to align with the field and arrange within the material matrix, which leads to changes in the mechanical properties of the material. This response is reflected at a macroscale level, causing an elongation or contraction of the material under a magnetic field, which is often referred to as magnetostriction [Vazquez-Perez et al., 2021]. On the other hand, when an external magnetic field is applied to an anisotropic ferrogel with soft-MPs, magnetic forces arise from the dipole-dipole interaction between the magnetized particles. Depending on the field orientation, it can either help maintain the chain orientation, opposing mechanical deformations, or produce a torque within the material. The first effect significantly increases the apparent stiffness of the material, which is often referred to as magnetorheological effect, while the second effect translates into the alignment of the material with the external field. In the case of hard-MPs, torques can be readily exploited from individual magnetic dipole moments because of the intrinsic remanence of this type of particles [Kim and Zhao, 2022].

In some cases, to increase the coupling between the MPs and the matrix of the material, the particles surface are chemically treated and coated with different compounds that change its chemical nature. This opens the possibility of chemical or physical bonding between the particles and the polymeric chains, which enhances the structural and chemical stability of magnetic composite materials (grafting-onto) [Daya et al., 2022, Barczak et al., 2020]. On top of that, it also avoids

particle aggregation due to Van der Waals forces and particle settling, leading to a homogeneous distribution across the material matrix.

1.2.2 Polymeric Matrix

Hydrogels are defined as three-dimensional (3D) cross-linked hydrophilic polymer networks swollen by a water-based solvent. The degree of swelling of these materials depends on temperature and humidity, as well as the solvation energy, entropy of the polymer chains, and presence of ionic and nonionic solutes in the solvent in which the hydrogel is immersed. They are characterized by their soft consistency, high water content, mechanical tunability, biocompatibility, natural response to certain stimuli, and resemblance to living tissues. To obtain a hydrogel, the starting point is a mixture of an aqueous solvent and polymers, which has to reach the gelling point through a physical or chemical process. This point is a phase transition from a solution to a gel state, where the percolation of the polymer network through the aqueous phase is observed. In the 3D polymeric structure that results from this process, scale invariance laws are satisfied, *i.e.* the structure is self-similar and can be described using the mathematical formalism developed for fractal geometry [Larson, 1999].

Regarding the nature of the interactions that keep the polymeric chains joined, hydrogels can be classified into three groups [Estevam et al., 2023, Pal and Banerjee, 2018]:

- Physical hydrogels. These hydrogels are cross-linked by ionic or intermolecular interactions such as Van der Waals, electrostatic, dipole-dipole, dipole-induced, hydrophobic, or hydrogen bonding. These interactions can occur between polymers or between the polymer and other components, such as functionalized MPs. Linkages in physical gels can break and reform in a dynamic equilibrium that leads to self-healing capabilities [Qiu and Zhang, 2023].
- Chemical hydrogels. In this case, the polymer network is formed by the covalent bonding of the components through a chemical reaction such as free radical reactions. These hydrogels are irreversible and more stable.
- Entangled hydrogels. These gels are formed by topological interactions of polymer chains without any chemical interactions, such as those described above.

Another classification can be performed by considering the chemical structure of the polymeric network [Estevam et al., 2023, Pal and Banerjee, 2018]:

- Homopolymerics. The hydrogel is formed by a particular monomer, which is the basic structural component of the entire network.

- Copolymerics. In this case, the hydrogel presents different kinds of monomers, with at least one of them hydrophilic, being all these monomers part of the polymer chains that constitute the hydrogel.
- Interpenetrating polymer networks (IPNs). They are multipolymeric structures formed by the combination of two or more independent cross-linked networks. They are usually prepared in a sequential process in which one polymeric network is cross-linked at each step. Depending on the method employed, multiple networks can be generated simultaneously.

From the previous classifications, hydrogel INPs have gained increasing interest owing to their mechanical properties and applicability. The prominent characteristic that makes them appealing to different research fields is their enhanced toughness, while maintaining the properties of every constituent polymeric matrix even in the presence of MPs [Zhang et al., 2023, Lee et al., 2019]. A particular type of IPNs are semi-IPNs, which are simple networks or IPNs with at least one linear or branched polymer entangled in the 3D structure of the hydrogels. In general, hydrogels are mechanically weak and brittle because of their high-water content [Kuang et al., 2023], being mainly used for biomedical, tissue engineering, and drug delivery applications [Kim and Zhao, 2022, Mañas-Torres et al., 2021a]. However, hydrogels intended for soft actuators and robots are expected to possess considerable toughness, tear resistance, and notch insensitivity [Liu et al., 2020b], characteristics that are met by IPNs.

1.2.3 Magnetic Hydrogels or Ferrogels

As previously mentioned, magnetic hydrogels or ferrogels are obtained by the addition of MPs to a hydrogel matrix. There are three methods to include them in the hydrogel matrix: blending, in situ precipitation, and grafting-onto [Lavrador et al., 2021]. In the blending method, MPs, which do not form chemical bonds with polymeric fibers, are entrapped within the polymeric network without control over their dispersion and agglomeration. In the in situ precipitation method, the precursor solutions for the synthesis of MPs are infused in the hydrogel network, followed by triggering the chemical reaction that precipitates MPs in the hydrogel, allowing uniform dispersion and the incorporation of larger amounts of particles. However, this method is suitable only for hydrogels that can endure alkaline conditions [Tang et al., 2019]. Finally, the grafting-onto method is similar to the blending method. In this case, the particle surface has attached or adsorbed certain functional groups that chemically interacts with the polymer chains serving as anchoring points. In addition, this functionalized surface enhances the structural and chemical stability of the final composite material. Another aspect that must be considered is the possible corrosion of MPs in the aqueous environment of hydrogels, which can be accelerated in the presence of other chemical compounds used during the synthesis of the material. Therefore, iron oxide

MPs and functionalized or coated MPs are used to address this issue [Małecki et al., 2016]. When particles are added, it is important to consider the possible interactions that can arise between them and the polymer chains that can actuate, in some cases, as anchoring points if the have an adequate functionalization [Ahmadian et al., 2023].

Regarding the nature of the polymeric fibers, there are two groups of hydrogels based on natural or synthetic polymers. Naturally derived polymers have been widely used owing to their physicochemical properties, compatibility with biological tissues, and natural degradability. Among them, carbohydrate polymers such as alginate [Ganguly et al., 2022, Yu et al., 2020, Rutkowski et al., 2019, Emi et al., 2018], chitosan [Gang et al., 2019, Gao et al., 2019, Wang et al., 2018, Naderi and Azizian, 2018], cellulose [Chen et al., 2022a, Yan et al., 2022, Gan et al., 2021], and animal-derived products such as fibrin [Bonhome-Espinosa et al., 2017, Omidinia-Anarkoli et al., 2017], hyaluronic acid [Shi et al., 2019, Tay et al., 2018a], collagen [Wright et al., 2022, Betsch et al., 2018], gelatin [Edward and Golecki, 2023, Yang et al., 2022], are used. Apart from these natural polymers, synthetic polymers, such as gelatin methacryloyl [Dong et al., 2020, Goudu et al., 2020], poly(N-isopropylacrylamide) [Selzer and Odenbach, 2020, Huang et al., 2019, Wang et al., 2019], acrylamide [Gong et al., 2022, Zhang et al., 2020a, Hu et al., 2019], poly(acrylic acid) [Bardajee et al., 2020, Lima-Tenório et al., 2015], poly(vinyl alcohol) [Lawrence and Rao, 2023, Liu et al., 2021], poly(ethylene glycol) [Kuang et al., 2021, Filippi et al., 2019, Chin et al., 2018], are also used among others. It is important to note that in magnetic hydrogels, the magnetic phase is generally composed of iron oxides because of their intrinsic biocompatibility and high resistance to corrosion in aqueous media. However, in some cases, other types of MPs are used depending on the intended application, as reflected in Table 1.1.

1.2.4 Fabrication Methods

Among the most common fabrication methods are mold casting and additive manufacturing. In order to choose the best approach to produce the hydrogel, the nature of the polymers involved and their gelling process, the shape and functionality of the final product, and the intended microstructure and distribution of MPs must be considered.

Mold Casting

Mold casting is a conventional and straightforward strategy in which liquid materials are poured or injected into molds to fabricate the final material with the desired shape. The advantages of this method include its simplicity, easy design, which is limited only by the mold, and low manufacturing cost. This method generally comprises four steps: preparing the raw materials, pouring or injecting the mixture

into the mold, curing and demolding [An et al., 2023]. Before curing, the mixture should be degassed in a vacuum chamber or a similar device to extract the bubbles that can remain trapped in the mixture and become defects in the final polymeric matrix. During the gelling process, it is possible to apply a magnetic field to create chain-like anisotropic structures when soft-MPs and superparamagnetic particles are used. Nevertheless, the magnetic programmability is really limited, requiring the use of complex, nonhomogeneous, and high intensity magnetic fields to obtain well-designed materials [Park et al., 2023, Lucarini et al., 2022].

Additive Manufacturing

Additive manufacturing (AM) or 3D printing is a technique for fabricating soft polymeric composites, which stands out due to its high accuracy, versatility, and scalability to an industrial level [Khalid et al., 2024]. Nevertheless, this technique also has its drawbacks, such as high cost, limitations in printing materials, and the need for post processing. As an improvement of 3D printing, four-dimensional (4D) printing has emerged, allowing more accurate control of the shape and functionality of printed materials using SRMs [Megdich et al., 2023, Merazzo et al., 2021]. Different approaches have been used to obtain the materials, such as direct ink writing (DIW) [Saadi et al., 2022] and photo-polymerization (VP) [Xiong et al., 2018].

1.3 Properties and Characterization of Ferrogels

1.3.1 General Properties

In the field of polymeric materials, the mechanical properties of the material matrix are crucial to their final performance. In addition, the inclusion of particles, such as MPs, must be considered because their presence affects the final physical properties of the composite [Song et al., 2020]. In the case of magnetic polymeric materials, in particular ferrogels, different multiphysical couplings occur within the material when an external magnetic field is applied, creating internal forces in the composite matrix and altering the magnetic field [Garcia-Gonzalez et al., 2021, Moreno et al., 2021]. The biocompatibility, stiffness, toughness, and other characteristics of the ferrogels have to be analyzed in order to select the best performing material for the intended application. Regarding the mechanical properties, the primary studied magnitudes are the mechanical moduli under dynamic or quasi-static shear, compressive, and tensile stresses, being the viscoelastic moduli (storage modulus G' and loss modulus G'') and the elastic moduli the most relevant. The values of these moduli vary from tens to thousands of Pascals (Pa). In the case of biomedical applications, moduli values should be close to those of biological tissue (*i.e.*, of the order of 100 - 1000 Pa) [Zhalmuratova and Chung, 2020, Scionti et al., 2013]. In addition, toughness and tear

resistance are also crucial in determining the suitability of a ferrogel in many fields.

Bringing the focus to the magnetic properties of ferrogels, they inherit the magnetic behavior of the MPs included in the polymeric matrix, behaving as continuous soft or hard magnetic matter with an effective magnetization that is always lower than that of isolated particles. Another interesting feature of ferrogels for soft robots and actuators is their fatigue life under purely mechanical loads and under magneto-mechanical types of loading under temperature-controlled conditions, which they might often experience in their functional lifetime as actuators [Bastola and Hossain, 2020].

In some cases, the materials are mechanically reinforced with anisotropic fillers to meet the required properties. Normally, these types of modified ferrogels are designed to mimic soft biological tissues, which are natural fibre-reinforced and mechanically complex soft materials [Zhai et al., 2023].

1.3.2 Characterization Techniques

From a mechanical point of view, the common devices used for characterizing the mechanical and magnetorheological properties of ferrogel are rheometers and universal testing machines. The former allows to perform quasi-static and dynamic stress-strain tests under shear for relatively soft samples, while the latter is also used for dynamic and quasi-static characterization of stiffer samples under tensile or compressive stresses [Mondal et al., 2023, Moreno et al., 2021]. In both cases, a magnetic field can be applied to the sample while measuring, using commercial accessories, handmade coils, or permanent magnet systems. The application of a magnetic field during the measurement process allows observation of the magnetorheological effect, which depends on numerous factors such as the type of polymeric matrix, concentration, type and distribution of MPs, use of additives, and the magnetic field strength [Bastola and Hossain, 2020]. The sample can be subjected to compressive, tensile or shear stresses in either the dynamic or quasi-static regime, and relaxation experiments [Moreno et al., 2021]. Under dynamic conditions, the stress is applied following an oscillatory function that can grow in amplitude at a fixed frequency (stress or strain amplitude sweeps) or in frequency with a fixed amplitude (frequency sweeps), and in response the viscoelastic moduli are measured. Under quasi-static conditions, the strain is constantly increased, and the stress is measured, obtaining the elastic moduli. The magnetorheological effect is measured by applying a homogeneous magnetic field to the sample during the measurement, which changes the stiffness of the material due to the magnetic interactions among the MPs that drag the polymeric chains with them in their migration. This effect is much more pronounced at small strains [Yarali et al., 2022, Zhang et al., 2020c]. Confined magnetic-field-induced stress studies can also be performed. These studies involve applying an external magnetic field to measure the mechanical response of the

materials. The magnetically induced actuation leads to particle-particle interactions within the sample that cause a macroscopic expansion, confined in the instrument geometry. The instrument measures the axial force due to magnetically induced deformation [Moreno-Mateos et al., 2022, Moreno et al., 2021]. Sometimes, the rheological behavior of the pre-cured polymeric solution is monitored to characterize the cross-linking kinetics [Lee et al., 2020] or the viscosity and yielding of pre-gel mixtures in the case of additive manufacturing [Chen et al., 2019].

Regarding the magnetic properties, the magnetization curves are measured using vibrating-sample magnetometers (VSM) or superconducting quantum interference devices (SQUID). On the one hand, in VSM, the magnetic properties are measured based on Faraday's Law of Induction. The sample is placed in a uniform magnetic field that generates a net magnetic moment in the sample, which changes as a function of time as the sample oscillates up and down. This induces a current in the pickup coils of the VSM, which is proportional to the magnetization of the sample. This allows to measure at different angles with respect to the magnetization of the sample. However, it is not well suited for determining the magnetization loop due to demagnetizing effects, and corrections must be taken into consideration [Martin et al., 2000]. On the other hand, SQUID is sufficiently sensitive for measuring fields around 10^{-14} T, thus it is not commonly used to characterize these materials, being more suitable for the characterization of MPs [Calascione et al., 2021, Barrera et al., 2019, Evans et al., 2012].

The composition and, in some cases, the structure of ferrogels can be observed using Fourier Transform Infrared (FT-IR) spectroscopy. FT-IR is a technique used to obtain an spectrum of absorption or transmission in the infrared spectral range [Qi et al., 2019]. Another commonly used technique to study the structure and composition of these materials is X-ray diffraction (XRD), which is a versatile nondestructive analytical technique used to determine the phase composition, crystal structure, and orientation of the composites or MPs [Yao et al., 2018]. Finally, the microstructure is commonly observed by direct methods such as scanning electron microscopy (SEM) [Zhou et al., 2020]. This technique allows us to observe the distribution of MPs, analyze the chemical composition of the samples using an energy dispersive X-ray spectrometer (EDX), or obtain information about the polymeric network. Nevertheless, despite the fact of being one of the most common methods used to observe the microstructure of polymeric materials, it lacks reliability due to the alteration of the sample during the required preparation procedures for this technique [Zhou et al., 2020].

1.3.3 Applications of Ferrogels

In this chapter, the applications of ferrogels have been briefly mentioned several times. As a summary, they are used in: tissue engineering [Almeida et al., 2023, Taghizadeh

et al., 2023,Hao and Mao, 2023,Zhang et al., 2020b,Koons et al., 2020], bioelectronics [Li et al., 2024, Li et al., 2021, Guo and Ma, 2018], drug delivery [Xia et al., 2023,Ganguly and Margel, 2021], wound dressing [Nam and Mooney, 2021,Qu et al., 2018, Dimatteo et al., 2018], cancer treatment [Andrade et al., 2021], environmental remediation [Gang et al., 2021, Weerasundara et al., 2020], soft robots [Zhao et al., 2022, Goudu et al., 2020, Liu et al., 2020b], and actuators [He et al., 2023, Vazquez-Perez et al., 2021]. Their interest resides in their softness, high water content, porosity, wide range of mechanical properties, degradability, biocompatibility, low cost, and responsiveness to magnetic fields, which gives them the ability to be heated, transported, and deformed without direct contact. To this extensive list of interesting properties, additional properties can be added, but drawbacks such as their general brittleness, notch sensitivity, and short lifespan in aqueous environments should not be overlooked. These characteristics make them of utmost interest and are the focus of numerous studies.

1.4 Hypothesis and Aims

The starting hypothesis of this doctoral thesis is the possibility of exerting precise control over the microstructure and spatial distribution of MPs in hydrogels by applying mechanical stresses or magnetic fields with adequate spatial modulation. The validity of this hypothesis is based on the results of previous works [Mredha et al., 2018, Lopez-Lopez et al., 2015, Scionti et al., 2013], where the possibility of modifying the hydrogel microstructure by applying external mechanical and magnetic stimuli is shown.

In this thesis, the aim was to prepare hydrogels and ferrogels, with precise control of their microstructure and magnetic behavior. These materials were characterized from a macroscopical point of view through their mechanical properties under different stresses and their bulk magnetic behavior, and from a microscopical point of view using different techniques such as scanning electron microscopy (SEM) and Fourier-Transform Infrared (FT-IR) spectroscopy. In addition, different types of applications were designed based on the properties of the studied hydrogels.

To achieve that, different types of polymers, such as sodium alginate, cellulose, and polyacrylamide were used. These polymers have the ability to form hydrogels via supramolecular and covalent polymerization, allowing the trapping of different types of MPs within their polymeric structure. Several hydrogels and ferrogels were synthesized with suitable internal order owing to the nature of the polymers, their interaction with the MPs, and their spatial arrangement, which were controlled by magnetic fields. As a result, the ferrogels exhibited tunable mechanical properties through the concentration, nature, size, and spatial arrangement of the MPs, as well as their polymeric structure. These ferrogels were designed with the aim of possessing the properties required for their intended use in soft actuators and robots, as well as in

other fields of current interest such as extracellular matrix scaffolds. To achieve these general objectives, the following specific objectives were set:

- **Functionalization of the MPs surface:** (i) use of MPs of different sizes and shapes; (ii) functionalization of the MP surface by the adsorption of appropriate molecules to provide them with biocompatibility and enable physical or chemical interaction with the polymeric fibers of the hydrogel network.
- **Synthesis of ferrogels:** fabrication of hydrogels and/or ferrogels with a controlled microstructure via mechanical stresses or the alignment of MPs under different magnetic field distributions. As the magnetic phase, functionalized commercial MPs were used, whereas natural or synthetic polymers were used as the polymeric matrix.
- **Characterization of the macroscopic physical properties of ferrogels:** (i) magnetic behavior and response to magnetic fields; (ii) mechanical properties under different stresses in various directions; (iii) macroscopic integrity and swelling capacity.
- **Characterization of microscopic properties:** (i) nature of the fibers, internal patterning, and degree of cross-linking. (ii) distribution of MPs within the hydrogel network, using spectroscopic techniques and electron microscopy, such as FT-IR, SEM, and EDX.
- **Theoretical modeling and simulation:** theoretical modeling of the ferrogels to understand their macroscopic behavior from the perspective of the physical mechanisms governing it, considering their microstructure. In addition, computational simulations were performed for different magnetic field distributions.
- **Applications of ferrogels:** design of applications of the hydrogels in the fields of actuators, sensors, and soft robots, which are currently of growing interest.

1.5 Structure of the Thesis

This thesis is structured in three thematic parts:

Part I. This part focuses on the development and characterization of anisotropic alginate-based hydrogels. The anisotropy was reached through two different methods: applying a mechanical stress to nonmagnetic hydrogels in Chapter 2, or applying a uniform magnetic field during the gelling process of ferrogels in Chapter 3. This was done with the aim of arranging the polymeric network to study its effects on the macromechanical properties and microstructure of the hydrogels.

Part II. This part focuses on a particular semi-IPN ferrogel based on polyacrylamide and various biopolymers. On the one hand, in Chapter 4 the material is fully designed and characterized, and some applications, such as a magnetic valve and gas sensor, are presented. On the other hand, in Chapter 5 the previous material was employed as a torsional actuator and multi-stimuli responsive programable actuator.

Part III. Finally, Chapters 6 and 7 present, respectively, the main conclusions of this thesis and a summary of the most relevant results in Spanish.

Part I

Chapter 2. Mechanically Structured Sodium Alginate Hydrogels [†]

2.1 Introduction

An outstanding characteristic of hydrogels is their swelling capacity, which is related to their high water content. However, the dehydration of a hydrogel leads to a decrease in its swelling degree, resulting in an increase in the polymer concentration. This fact, along with the resulting polymer–polymer interactions, can have a drastic impact on the mechanical properties of these soft materials. As the porosity and microstructure of hydrogels are crucial characteristics for their application as extracellular matrices [Chaudhuri et al., 2020], the effects of dehydration processes have been studied from the perspective of the changes in their macroscopic and microscopic properties [Mredha et al., 2018, Scionti et al., 2013]. For example, most synthesized hydrogels generally have an isotropic internal structure, whereas natural tissues, such as cartilage [Fox et al., 2009, Poole et al., 2001], muscle [Huxley, 1988, Weber and Murray, 1973], and skin [Proksch et al., 2008, Madison, 2003], show anisotropic and well-defined hierarchical structures. Indeed, anisotropy often plays an essential role in many natural processes and mechanisms, including mass transport, surface lubrication, and force generation. As nature is a source of inspiration for many advanced materials and applications, it is not surprising that anisotropic hydrogels are receiving increasing attention in the field of biomimetics [Mredha and Jeon, 2022]. In line with these research interests, different strategies for the preparation of anisotropic hydrogels have emerged in recent years. The most common procedures for obtaining hydrogels with an internal anisotropic structure involve the application of directional stimuli, such as

[†]The content of this chapter is an adaptation of Leon-Cecilla, A., Vazquez-Perez, F. J., Gila-Vilchez, C., Álvarez de Cienfuegos, L., Lopez-Lopez, M. T. (2023). Alginate Hydrogels Reinforced by Dehydration under Stress-Application to a Soft Magnetic Actuator. *Gels*, 9:39. [Leon-Cecilla et al., 2023].

gradients of temperature or ionic concentration [Sano et al., 2018]. Furthermore, the inclusion of MPs into the hydrogel formulation opens the possibility of obtaining an anisotropic internal structure through the application of external electric or magnetic fields [Mañas-Torres et al., 2021b, Zhu et al., 2020, Gila-Vilchez et al., 2019b, Lopez-Lopez et al., 2015]. Nevertheless, these strategies involve technical difficulties in terms of biocompatibility and suitability. Therefore, the use of dehydration processes combined with mechanical deformations has been widely proposed as a simple and versatile way to obtain anisotropic hydrogels [Liu et al., 2020a, Qin et al., 2019, Mredha et al., 2018, Sano et al., 2018, Kong et al., 2018, Contreras-Montoya et al., 2018, Scionti et al., 2013]. In a previous work [Mredha et al., 2018], the authors used a method based on dehydration under tensile stress to fabricate anisotropic hydrogels with aligned fibrous structures, which resulted in enhanced Young's modulus values. Similarly, in another study [Scionti et al., 2013], the authors used compression as a method to induce the alignment of polymeric fibers in parallel layers, reporting an improvement in the mechanical properties with respect to noncompressed samples. However, one question arises whether this improvement was only due to the water loss caused by the compression. Although several studies have investigated the effects of dehydration on the microstructure of hydrogels, their consequences on the mechanical properties of hydrogels are usually undervalued and misunderstood. As a result, the lack of complete rheological studies is obvious when focusing on the role of dehydration in the mechanical properties of hydrogels and their connection to changes at the microscopic level. Furthermore, the potential effects of hydrogel dehydration on hydrogel-based actuators and robots for medical applications are unknown.

In connection with what has been discussed, the aim of this chapter was to comprehensively analyze the effects of partial dehydration under a mechanical stress on the mechanical properties of alginate hydrogels. Apart from that, it was analyzed whether these changes substantially improve the response of soft magnetic actuators based on polymeric hydrogels. As previously mentioned, alginate was selected as the polymer for the hydrogels preparation. This polymer, a polysaccharide extracted from brown algae, is characterized by its biocompatibility, nontoxicity, abundance in source, and low cost [Ahmed, 2015]. Furthermore, alginate hydrogels can be easily synthesized by adding a source of divalent cations to a sodium alginate solution and they allow the inclusion of large amounts of MPs with negligible phase disruption, as demonstrated in previous works [Barczak et al., 2020, Gila-Vilchez et al., 2018]. In this chapter, we study alginate hydrogels based on two sodium alginates with different molecular weights that were dehydrated using two different methods (dehydration under tensile stress and dehydration under compressive stress). We analyze the influence of dehydration on the properties of these hydrogels in terms of water loss, molecular weight of the alginates, mechanical properties, and microscopic structure. These materials could have interesting applications in tissue engineering because of their improved overall performance after dehydration. Additionally, we study the

effect that dehydration under compression had on the actuation of an alginate-based magnetic hydrogel gripper that was able to bend under a magnetic field. These results demonstrated that dehydration under a controlled stress positively affects the robustness of alginate hydrogels and enhances the response of the ferrogel gripper to a magnetic field. Apparently, new bonds between polymer fibers were created during the stress-controlled dehydration processes (SCDPs) in addition to the increase in polymer concentration. These two changes appear to be responsible for the enhancement of the properties and actuation of the alginate hydrogels.

The results presented in this chapter not only provide a complete picture of the effect of dehydration under controlled stresses on the final mechanical properties of alginate hydrogels but also analyze the consequences of these changes on the responsiveness of a soft magnetic actuator.

2.2 Materials and Methodology

2.2.1 Materials

Low-viscosity sodium alginate (LVSA) of molecular weight 120000-160000 g/mol, calcium carbonate ($CaCO_3$), D-glucono-δ-lactone (GDL), calcium chloride ($CaCl_2$), sodium hydroxide (NaOH) from Sigma Aldrich (USA). Medium-viscosity sodium alginate (MVSA) of molecular weight 10000-600000 g/mol from PanReac AppliChem ITW Reagents (Spain). Silica-coated iron powder (Fe-CC) from BASF (Germany). The Fe-CC powder consisted of spherical micronsized particles of diameter 1.4 $\pm$ 0.6 µm, volumetric mass density of 7.71 $\pm$ 0.19 g/cm^3, and a typical soft ferromagnetic behavior with a maximum magnetization M_S = 1587 $\pm$ 2 kA/m. The solutions were prepared in milli-Q water.

2.2.2 Synthesis of Nonmagnetic and Magnetic Hydrogels

As previously mentioned, two different sodium alginates were used to prepare the hydrogels. Differences in molecular weight are reflected in the viscosity of 1 % w/w solution of each alginate, ranging from 15 - 25 mPas for the sodium alginate from Sigma-Aldrich and 350 - 550 mPas for the one from PanReac AppliChem, according to the respective manufacturers. In addition, the molecular weight distributions are also different, being broader the distribution of the MVSA.

In order to prepare isotropic nonmagnetic and magnetic hydrogels, a two-step protocol reported in a previous work [Gila-Vilchez et al., 2018] was used with minor modifications. Briefly, to synthesize the nonmagnetic hydrogels, we prepared 12 mL of sodium alginate solutions in water at concentrations of 4.0, 4.5, 5.0, and 5.5 % w/w, to which 36 mg of $CaCO_3$ were added and homogenized using a vortex mixer.

Afterwards, we added 128.2 mg of GDL and homogenized the resulting mixture. Then, we poured this mixture into a square container (80.85 mm $\times$ 80.85 mm $\times$ 2 mm) and left the pre-gel solution undisturbed at room temperature for 2 hours. After this time, we added to the gel 12 mL of a 0.5 M $CaCl_2$ solution, and the sample was left gelling overnight at room temperature. We prepared two types of these hydrogels, one containing only LVSA (AH100-0) and the other one containing a 50-50 % mixture of LVSA and MVSA (AH50-50) (see Table 2.1).

Table 2.1: Concentrations of LVSA, MVSA, and Fe-CC in the synthesized hydrogels. CXAH100-0 and CXAH50-50 are the control samples, where X is the total alginate concentration. MYAH is the hydrogel for the actuator, where Y is the concentration of MPs.

Sample	% w/w LVSA	% w/w MVSA	% v/v Fe-CC
C4.0AH100-0	4.00	0	0
C4.0AH50-50	2.00	2.00	0
C4.5AH100-0	4.50	0	0
C4.5AH50-50	2.25	2.25	0
C5.0AH100-0	5.00	0	0
C5.0AH50-50	2.50	2.50	0
C5.5AH100-0	5.50	0	0
C5.5AH50-50	2.75	2.75	0
M0AH	0	1.00	0
M5AH	0	1.00	5.0
M7.5AH	0	1.00	7.5
M10AH	0	1.00	10.0
M20AH	0	1.00	20.0

In the case of the hydrogels used for the actuator, two different parts were prepared: a magneto-active part that responded to the applied magnetic field and a nonmagnetic passive part that remained unaltered. For the magnetic part, the previous protocol was slightly modified to incorporate magnetic microparticles into the actuator. To 10 mL of an MVSA solution at a concentration of 1 % w/w, 15 mg of $CaCO_3$ were added, followed by homogenization. Subsequently, 53.4 mg of GDL were added and homogenized. Silica-coated iron powder was then added (see Table 2.1) and homogenized by vortex mixing followed by 10 min in an ultrasonic bath. The mixture was then poured into a cross-shaped mold and left gelling for two hours at room temperature. Afterwards, 10 mL of a 45 mM aqueous solution of $CaCl_2$ were added, and the sample was left gelling overnight at room temperature. The nonmagnetic part of the magnetic actuators was prepared in the same way but without introducing MPs into the formulation. Note that in this case, we only used MVSA at a concentration of 1 % w/w to obtain the appropriate stiffness of the polymer matrix to maximize the magnetic response of the hydrogels. With this alginate and concentration, we obtained a flexible actuator that maintained adequate consistency for manipulation and actuation.

2.2.3 Stress-Controlled Dehydration Processes (SCDPs)

Two different stress-controlled dehydration processes based on the methods described in previous works [Mredha et al., 2018, Scionti et al., 2013] were used. These SCDPs were differentiated by the type of stress applied: tensile or compressive stress (Figure 2.1 A). The hydrogels used in these processes were C4.0AH100-0 and C4.0AH50-50, where the total alginate concentration before the application of the SCDP was 4 % w/w. To dehydrate these hydrogels under tensile stress, a homemade device was used, which fixed the ends of the sample and stretched it (Figure 2.1 B and C). First, the hydrogels were cut into a rectangular shape (25 mm $\times$ 50 mm $\times$ 2 mm). Then, two of these gels were simultaneously fixed and slightly stretched in the device (Figure 2.1 C). The system was then placed in a desiccator at room temperature, and a partial vacuum was created. The samples were left drying for 8, 14, and 24 h to obtain different water losses. During the process, the relative humidity inside the desiccator was controlled using a 25 % w/w NaOH solution, which maintained a relative humidity of 60 % at 25 °C [Madge, 1961]. Note that due to long dehydration times, controlling the temperature and relative humidity was crucial for obtaining reproducible degrees of the water loss. During the process, the hydrogels shrank because of water loss, generating a rising tensile stress in the longitudinal direction of the sample because the two edges of the hydrogel remained fixed. The increasing tensile stress during dehydration was the reason behind the changes studied here, and not the initial negligible stress applied to the hydrogels by the homemade device.

For the dehydration of the nonmagnetic hydrogels under compressive stress, square-shaped (28 mm $\times$ 28 mm $\times$ 2 mm) samples were placed between two glass plates surrounded by blotting paper. A weight of 6.5 kg was placed on the top of the upper plate (Figure 2.1 D) to apply the compressive force. We left the samples dry under these conditions for 10, 20, and 30 minutes, obtaining different reproducible degrees of dehydration. In the case of the hydrogels for the magnetic actuator, because of their softer consistency, the hydrogels were placed between two pieces of blotting paper, compressed with a much smaller weight (96 g), and for a shorter time (90 s). The process was repeated up to two times for some samples. In compressive SCDPs, it was not necessary to control the temperature and relative humidity because of the experimental setup and speed of the process. In addition, because our focus was on the final concentration of polymer fibers after dehydration, rather dissimilar dehydration times were used in each case due to the different kinetics of each SCDP.

2.2.4 Mechanical Characterization

To characterize their mechanical properties, the hydrogels were separately subjected to uniaxial tensile and oscillatory stresses. The tensile tests were carried out using a hybrid rheometer (Discovery HR-1, TA Instruments, USA) at room temperature. For this purpose, the samples were cut into the shape of a dog bone and fixed between

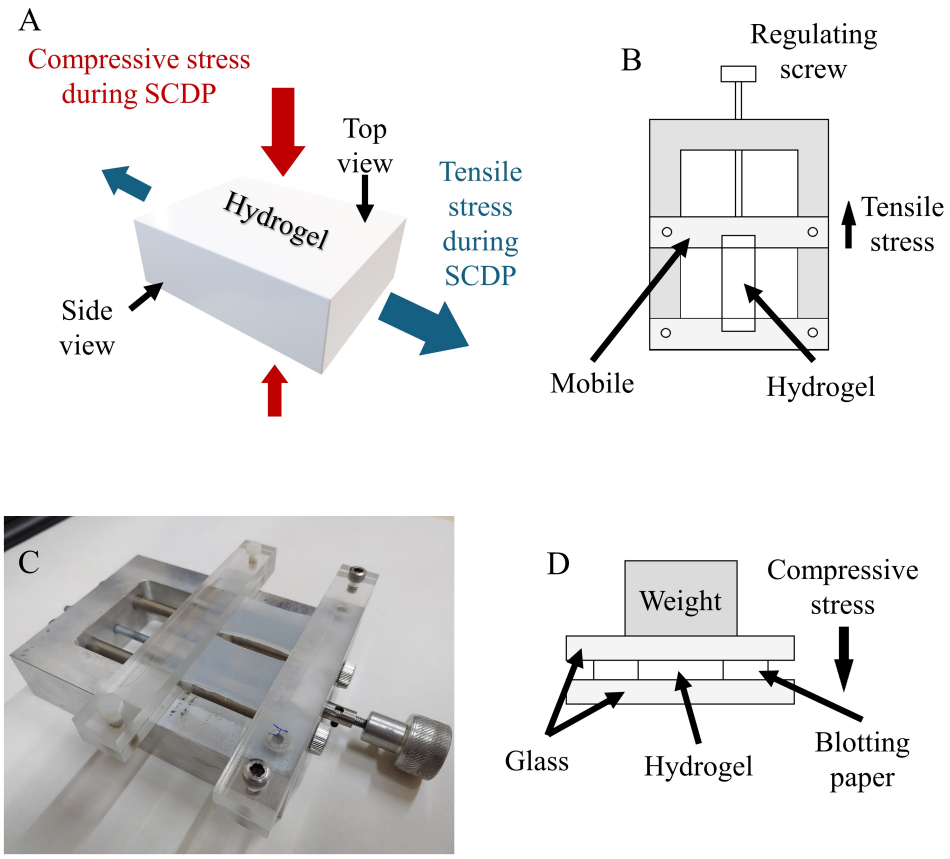

Figure 2.1: A) Sketch showing the directions of the stresses applied to the alginate hydrogels during the SCDPs. B) and C) sketch and image, respectively, of the device used in the dehydration process under tensile stress. D) Sketch of the dehydration process under compressive stress.

the two clamps of the tensile geometry. These clamps had a grooved surface that prevented the sample from slipping. During the measurement, the lower clamp remained static while the upper clamp moved away. In all cases, we applied a stretching preload of 0.3 N normal axial force to establish a reproducible starting condition. The hydrogels were then stretched at a constant rate of 50.0 µm/s until breakage. Then, from the obtained engineering stress vs. strain curves, the Young's modulus (E), the strain at break (ϵ_b), and the stress at the break (σ_b) were calculated. Young's modulus was calculated as the slope of the linear regression of tensile stress (σ) versus strain (ϵ) [Draghi, 2017]:

$$E = \frac{F/S}{(l - l_0)/l_0} = \frac{\sigma}{\epsilon} \tag{2.1}$$

, where l is the length of the sample during the test, l_0 the initial length of the sample, F is the applied force, and S is the cross-sectional area of the sample. Finally, the strain and stress at break were obtained from the last point of the curves before breakage.

The characterization of the viscoelastic behavior of the alginate hydrogels under oscillatory shear was carried out using a rotational rheometer (Physica MCR 300, Anton Paar, Austria) with a plate–plate geometry of 20 mm of diameter at a constant temperature of 25.0 $\pm$ 0.1 °C. For this purpose, the hydrogels were placed on the lower plate of the measuring system, and the upper plate descended until it came into contact with the top surface of the sample. To ensure reproducibility, the hydrogels were subjected to a constant normal force of 0.1 N for 100 s before the rheological measurement. This normal force was also maintained during the entire measurement to ensure proper contact between the hydrogel and the geometry. The rheological behaviors of the samples were analyzed using amplitude and frequency sweeps. In the amplitude sweeps, we subjected the samples to oscillatory shear strain with increasing strain amplitude (logarithmic ramp from γ_i = 0.01 % to γ_f = 10 %) and constant frequency ν_0 = 1 Hz. From these measurements, we obtained the values of the storage modulus G' and loss modulus G'' as functions of the shear strain γ. In frequency sweeps, we subjected the samples to oscillatory shear with constant strain amplitude (γ_0 = 0.1 %) and increasing frequency (logarithmic ramp from ν_i = 0.1 Hz to ν_f = 20 Hz). From these measurements, we obtained G' and G'' as functions of frequency. Each sweep contained 23 points during which the same shear amplitude and frequency were maintained for 10 s.

2.2.5 Scanning Electron Microscopy (SEM)

The microscopic structure of the alginate hydrogels was characterized by scanning electron microscopy (SEM) using a HITACHI S-510 microscope.

2.2.6 Analysis of the Actuation Behavior of a Hydrogel-Based Magnetic Actuator

To analyze the actuation behavior of the ferrogels, a planar cross-shaped actuator consisting of two magnetic hydrogel beams (active parts) connected to a central nonmagnetic hydrogel beam (passive part) was designed. To do so, a cross-shaped mold was used, where the pre-gel mixtures of the nonmagnetic hydrogel and the magnetic hydrogel were poured into different zones separated by a ring (Figure 2.2 A). The ring was then removed to cross-link the hydrogels in the same way as described above in subsection 2.2.2. After the gelling process was completed, the actuator was placed on an aluminum support at medium height inside an electric coil connected to a DC power supply, which was used for the application of the magnetic field.

The study of the bending of the ferrogel beams was performed by increasing the applied magnetic field step-wisely up to a maximum field strength of 60 kA/m. After that, the field was decreased to zero to investigate the potential hysteresis of the actuation. For each field value, we waited for 30 s before measuring the bending angle with respect to the off-state position. Note that because of the lack of continuity of the adhesion forces between the actuator and the support, and the interest in the balance between magnetic, elastic, and gravitational forces. Initially, the ferrogel beams were manually detached from the support surface. If equilibrium was reached at a zero angle, the field was increased and proceeded in the same manner. Once the equilibrium was reached at an angle greater than zero, we increased the field step-wisely, and no manual detachment was required. The bending angles were calculated from the values of the height of the free end of the magnetic beams with respect to the off-state position, which were directly measured (Figure 2.2 B).

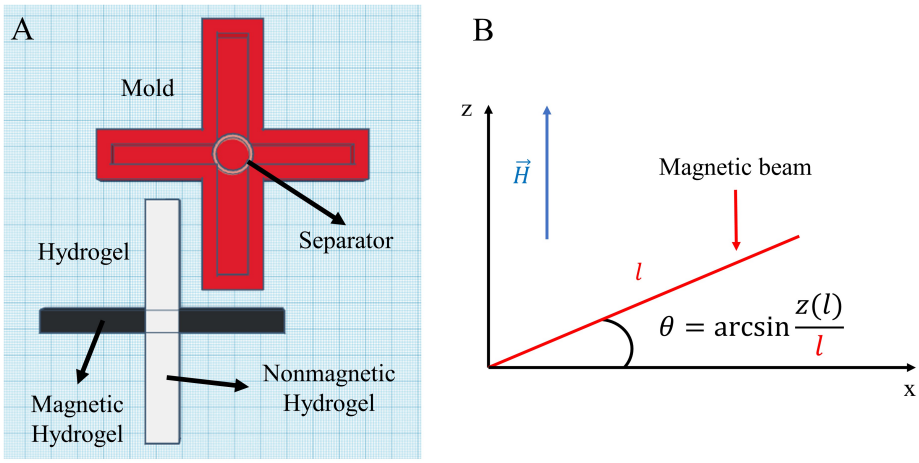

Figure 2.2: A) Sketch of the mold and the actuator. B) Approximation used for calculating the angle of the magnetic beam of the actuator.

2.2.7 Statistical Analysis

For each set of experimental conditions, at least three different samples were measured, and the corresponding mean values and standard deviations are provided in this chapter. When differences between values corresponding to different samples and/or experimental conditions were not clear, we performed t-tests with a significance level of 0.05 to determine the statistical significance of the differences. For more details on these tests, see Tables A.1, A.2, and A.3.

2.3 Results and Discussion

2.3.1 Macroscopic Appearance and Swelling Behavior

The nondehydrated alginate hydrogels retained the shape of the molds used for their preparation and exhibited a homogeneous macroscopic appearance. The materials also exhibited similar macroscopic appearance and homogeneity after the SCDPs. In all cases, hydrogels were translucent because of the high polymer concentration. Furthermore, the hydrogel volume decreased due to the partial loss of bulk water during the SCDPs. The relatively high alginate concentration in conjunction with the high cross-linking density resulted in robust alginate hydrogels that could be easily manipulated before and after dehydration. However, there were differences in consistency between the AH100-0 and AH50-50 samples, which were reflected in their mechanical properties.

Table 2.2: Hydrogels mean alginate concentration (c) and water loss (wl) after the two SCDP were performed at different times. The alginate concentration before the SCDP was 4 % w/w (C4.0AH100-0 and C4.0AH50-50) in all cases. The data for AH100-0 samples were previously reported in [Gila Vilchez, 2022].

Stress Applied	Time	AH100-0		AH50-50	
		c (% w/w)	wl (% w/w)	c (% w/w)	wl (% w/w)
Compressive	10 min	4.72 ± 0.21	16 ± 4	4.41 ± 0.04	9.8 ± 0.9
	20 min	5.00 ± 0.16	21 ± 3	4.61 ± 0.07	13.8 ± 1.4
	30 min	5.3 ± 0.3	26 ± 5	4.79 ± 0.07	17.1 ± 1.3
Tensile	8 h	4.67 ± 0.07	15.0 ± 1.4	4.87 ± 0.11	19 ± 2
	14 h	4.86 ± 0.12	18 ± 2	5.34 ± 0.10	26.1 ± 1.6
	24 h	5.48 ± 0.21	28 ± 3	6.2 ± 0.3	37 ± 3

As previously mentioned, the degree of dehydration was quantified using the alginate concentration and water loss after the SCDPs. To do so, the masses of the freshly prepared hydrogels and their final masses, after the SCDPs, were measured to calculate the final polymer concentration and water loss. Table 2.2 shows the mean final alginate concentration of the hydrogels and the water loss after dehydration at three different times for each SCDP method. As can be observed, we obtained similar alginate final concentrations by controlling and repeating the dehydration conditions in each process. While the alginate concentration of the freshly prepared hydrogels was 4 % w/w, once dehydrated, we obtained a range of alginate concentrations between 4.41 $\pm$ 0.04 % w/w (wl = 9.8 $\pm$ 0.9 % w/w) and 6.2 $\pm$ 0.3 % w/w (wl = 37 $\pm$ 3 % w/w).

The freshly prepared hydrogels were also dehydrated without applying any stress for 24 h at room temperature in contact with blotting paper. Alginate concentrations of 7.7 $\pm$ 0.3 % w/w (wl = 49.9 $\pm$ 2.2 % w/w) for the AH100-0 samples and 8.5 $\pm$ 0.9

% w/w (wl = 55 $\pm$ 6 % w/w) for the AH50-50 samples were obtained. The hydrogels were then rehydrated by immersing them in milli-Q water for an additional 24 h to partially recover the lost water. This resulted in alginate concentrations of 5.23 $\pm$ 0.17 % w/w (wl = 24.4 $\pm$ 0.3 % w/w) for the AH100-0 samples and 7.4 $\pm$ 0.7 % w/w (wl = 48 $\pm$ 6 % w/w) for the AH50-50 samples. Nevertheless, the initial state of hydration was not recovered in any case, indicating the formation of new stable bonds among polymer chains during dehydration, most likely hydrogen bonds formed between the -OH groups of alginate, as reported in a previous study on alginate hydrogels [Mredha et al., 2018].

2.3.2 Mechanical Characterization of Alginate Hydrogels

Mechanical Characterization under Tensile Stress

In the uniaxial tensile characterization carried out for control samples (Figure 2.3 A and B), it is clear that for a given value of the tensile strain amplitude, the corresponding tensile stress increased with the concentration of alginate for AH100-0 (Figure 2.3 A) and AH50-50 (Figure 2.3 B). Consequently, the Young's modulus, defined as the slope of these curves, increased with alginate concentration in the control samples. This behavior is expected from the classical theory of the mechanical properties of networks and gels, which predicts an increase in robustness with the increase in volume concentration of polymer strands [Rubinstein and Colby, 2014, Grosberg and Chochlov, 1994]. However, it is likely that other factors played a role, for example, the maximum stress and deformation at break were much larger for AH50-50 than for AH100-0 samples (compare Figure 2.3 A and B). As previously mentioned, the aim of this chapter is to elucidate whether dehydration processes under a controlled stress affect the mechanical properties of hydrogels beyond the increase in polymer concentration observed in Figure 2.3 A and B. The answer is clear in Figure 2.3 C and D, where it is observed that the SCDP under compression result in considerably higher values of the tensile stress for a given value of the tensile strain amplitude for both AH100-0 and AH50-50 samples, in comparison with the control samples –remark the similar ranges of alginate concentrations for control samples and samples subjected to a SCDP (*cf.* Table 2.1 and 2.2). In the case of the SCDP under tensile stress, there was a clear enhancement of tensile stress with respect to control samples at a given strain amplitude for AH50-50 samples, whereas no appreciable effect was observed for AH100-0 samples (Figure 2.3 C and D). Correspondingly, the resulting Young's modulus (Figure 2.3 E and F) was generally more enhanced in samples subjected to a SCDP than in control samples, confirming the positive effect of dehydration and the consequent formation of new bonds between alginate fibers during the SCDPs. This effect was stronger in AH50-50 samples, where a larger increase in Young's modulus was observed regardless of the type of stress applied during the SCDPs.

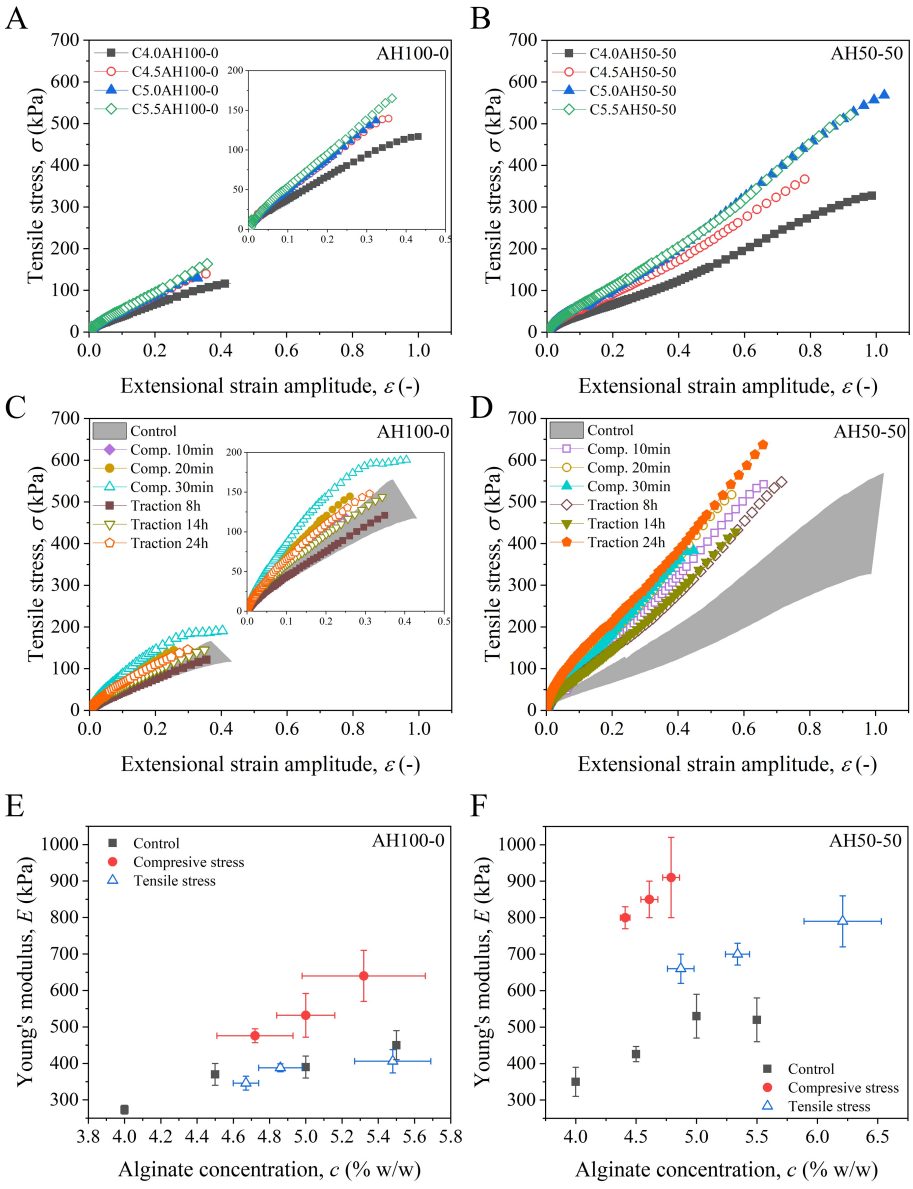

Figure 2.3: Results from uniaxial tensile characterization. From A) to D) strains vs. stress example curves for the different samples studied. A) and B) control samples of the two types of alginate hydrogels. The insets show the same data on different scales. C) and E) strain vs. stress curves for each SCDP. The shaded bands represent the range of values for control samples. In E) and F), the values of Young's modulus for each SCDPs and alginate concentrations obtained after dehydration are shown, along with the values for control samples. Note that the same scales are used on both axes.

From the curves of Figure 2.3, the stress and maximum deformation at break were obtained. For these two magnitudes (Figure A.1), statistically significant differences were observed between the two types of alginate hydrogels, with much higher values

for AH50-50 than for AH100-0 samples. Regarding the role of the SDCP, a slight decrease in deformation at the fracture occurs, whereas the stress at break increased slightly for the AH100-0 samples and more strongly for the AH50-50 samples subjected to a SCDP with respect to the control samples.

Mechanical Characterization under Oscillatory Shear Stress

The rheological characterization of the samples under oscillatory shear stress revealed a solid-like viscoelastic behavior typical of these materials (Figures 2.4 and A.2). The curves corresponding to the amplitude sweeps (Figure 2.4 rows (i,ii)) show that both moduli present an initial plateau zone that define the linear viscoelastic region (LVR). After this plateau zone, the storage modulus exhibits a sharp decrease, whereas the loss modulus shows a small peak followed by a sharp decrease for larger deformations. The region where the viscoelastic moduli do not remain constant is known as the nonlinear viscoelastic region. Within this zone, the inner structure of the hydrogel breaks, resulting in lower elasticity of the material, as evidenced by a lower value of G'. The shear strain amplitude (γ_0) at which a maximum in G'' is observed, is known as the yielding point, at which the dissipation of energy is maximum and it marks the onset of the destruction of the polymeric network [Moghimi et al., 2017]. Similarly to Young's modulus, it is expected that both G' and G'' increase with polymer content in cross-linked samples, and this is indeed what is observed in general terms for control samples (Figure 2.4 column A), although differences are almost negligible and tendencies are not always clear, very likely due to small differences in alginate content. The effect of compression during the SCDP on the G' and G'' values of the final hydrogels was clear (Figure 2.4 column B). As observed for both AH100-0 and AH50-50 samples, compression during the SCDP resulted in considerably larger values of G' and G'' compared with the control samples with a similar alginate content. A similar enhancement with respect to the control samples was obtained for the AH100-0 samples subjected to tensile stress during SCDP, whereas no significant differences were observed for the AH50-50 samples dehydrated under similar conditions (Figure 2.4 column C).

Finally, the results of frequency sweeps (Figure A.3) demonstrated a slight increase in both G' and G'' with frequency, although the lost tangent ($\tan\delta = G''/G'$) was maintained higher than 0.1 for the entire range of frequencies under study, which means that no relative changes in the ratio between viscous and elastic character was observed. Furthermore, no significant differences in the shape of the curves of G' and G'' vs. frequency were caused by the SCDP, indicating that the rearrangement of the fibers did not change the nature of the main interaction between the polymer chains (electrostatic bonds), which is primarily responsible for the mechanical spectra of the material.

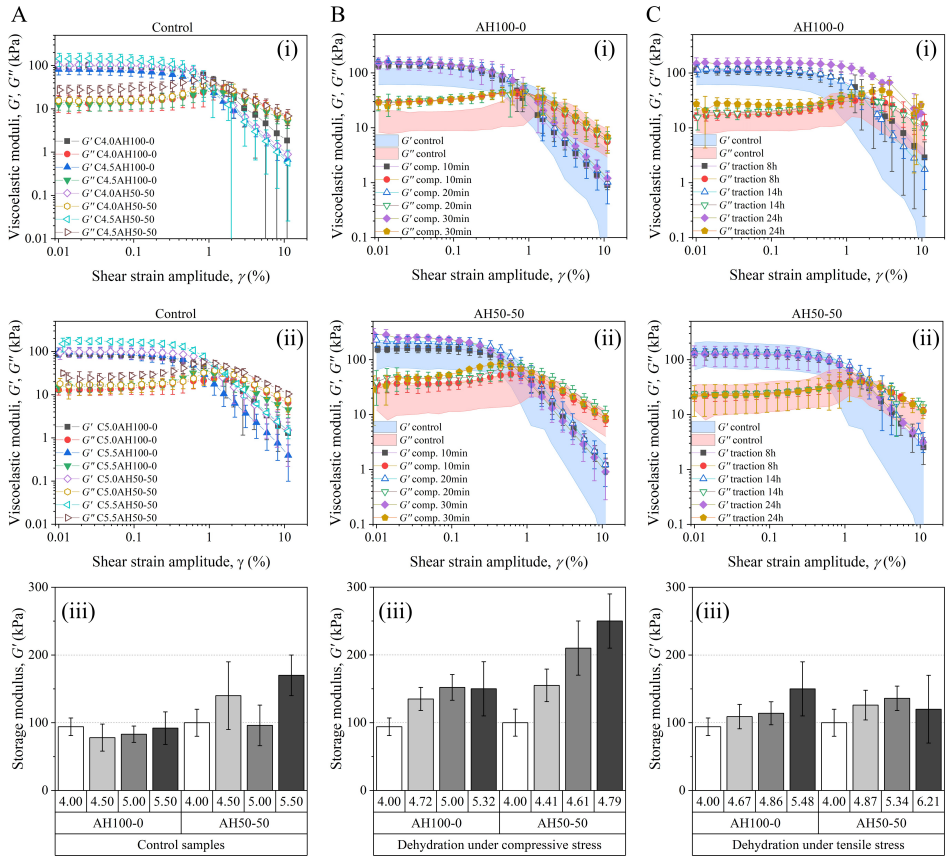

Figure 2.4: Results of rheological characterization under oscillatory shear. The data in each column are related to the stress applied during dehydration: A) control samples, B) samples dehydrated under compressive stress, and C) samples dehydrated under tensile stress (the data for AH100-0 samples were previously reported in [Gila Vilchez, 2022]). The data in the first two rows are presented as a comparison between the curves obtained for (i) AH100-0 and (ii) AH50-50, and in the third row (iii), the values of the storage modulus (G') within the LVR are shown. The areas in (B, (i)), (B, (ii)), (C, (i)), and (C, (ii)) represent the ranges of values for the control samples. Note that the same scales are used in both axes.

2.3.3 Analysis of the Anisotropy in the Hydrogels

From the results of previous sections, it is clear that changes in the mechanical properties of samples subjected to a SCDP were not just a consequence of the increase in polymer concentration. The creation of new bonds between polymer fibers (very likely hydrogen bonds between the -OH groups of alginate) also played a key role in the final properties of the dehydrated hydrogels. To further investigate the effects of the SCDPs on hydrogels, their mechanical anisotropy was studied.

From the mechanical point of view, due to the planar geometry of our samples, only the hydrogels dehydrated under tensile stress could be characterized in two relevant perpendicular directions, parallel and perpendicular to the direction of the

stress applied during the SCDP. From the results obtained under uniaxial tensile tests (Figure 2.5), the existence of anisotropic mechanical behavior is clear. As observed for both types of samples (AH100-0 and AH50-50), the Young's modulus in the direction parallel to the SCDP stress is higher than in the perpendicular direction. In comparison with the values of Young's modulus (Figure 2.5 A) for the control samples (C4.0AH100-0 and C4.0AH50-50), a statistically significant increase was only obtained for measurements in the parallel direction to the stress during the SCDP. The stress at break (Figure 2.5 B) also demonstrated larger values (although only statistically significant for AH50-50 samples) in the parallel direction with respect to the perpendicular direction. For this quantity, the values of the AH50-50 samples were considerably larger than those of the nondehydrated sample, regardless of the direction. Regarding the maximum deformation at break (Figure 2.5 C), an inverse tendency occurred, with lower values in the parallel direction, although the differences observed in this case are only statistically significant for the AH50-50 samples. It should be noted that, in general, the effects and differences observed for the AH50-50 samples are much stronger than those for the AH100-0 samples, demonstrating a relevant role of the length of the polymer fibers on the changes caused by the SCDP.

These results of mechanical characterization indicate the appearance of new bonds between the polymer chains of samples subjected to a SCDP, as well as the potential changes of polymer fibers arrangement at the microscopic level. To elucidate this point, we investigated the microscopic structure of the samples using SEM images (Figure 2.5 D-F). As observed for the control samples not subjected to a SCDP, homogeneous and isotropic porous structures without any fiber arrangement were obtained (Figure 2.5 D). For the samples subjected to SCDP under tensile stress, similar isotropic structures to control samples were observed in the case of AH100-0 samples (Figure 2.5 E), whereas a clearer anisotropic structure consisting of parallel bands was observed for AH50-50 samples (Figure 2.5 F). These observations agree with the mechanical anisotropy discussed above, which is much more evident in the AH50-50 samples than in the AH100-0 samples (Figure 2.5 A-C). Furthermore, note that similar results in terms of the existence of anisotropy were obtained for samples subjected to SCDP under compressive stress (Figure A.4).

As a general conclusion, dehydration under a stress generated anisotropic and tougher hydrogels with respect to nondehydrated hydrogels containing similar concentrations of polymers. It is likely that the asymmetry induced by the SCDP resulted in hydrogen bonds formed between the -OH groups of the alginate fibers aligned in a privileged direction, which can be responsible for this reinforcement at the macroscopic level, as well as for the permanent changes in the hydrogel shape and the mechanical and microstructural anisotropy.

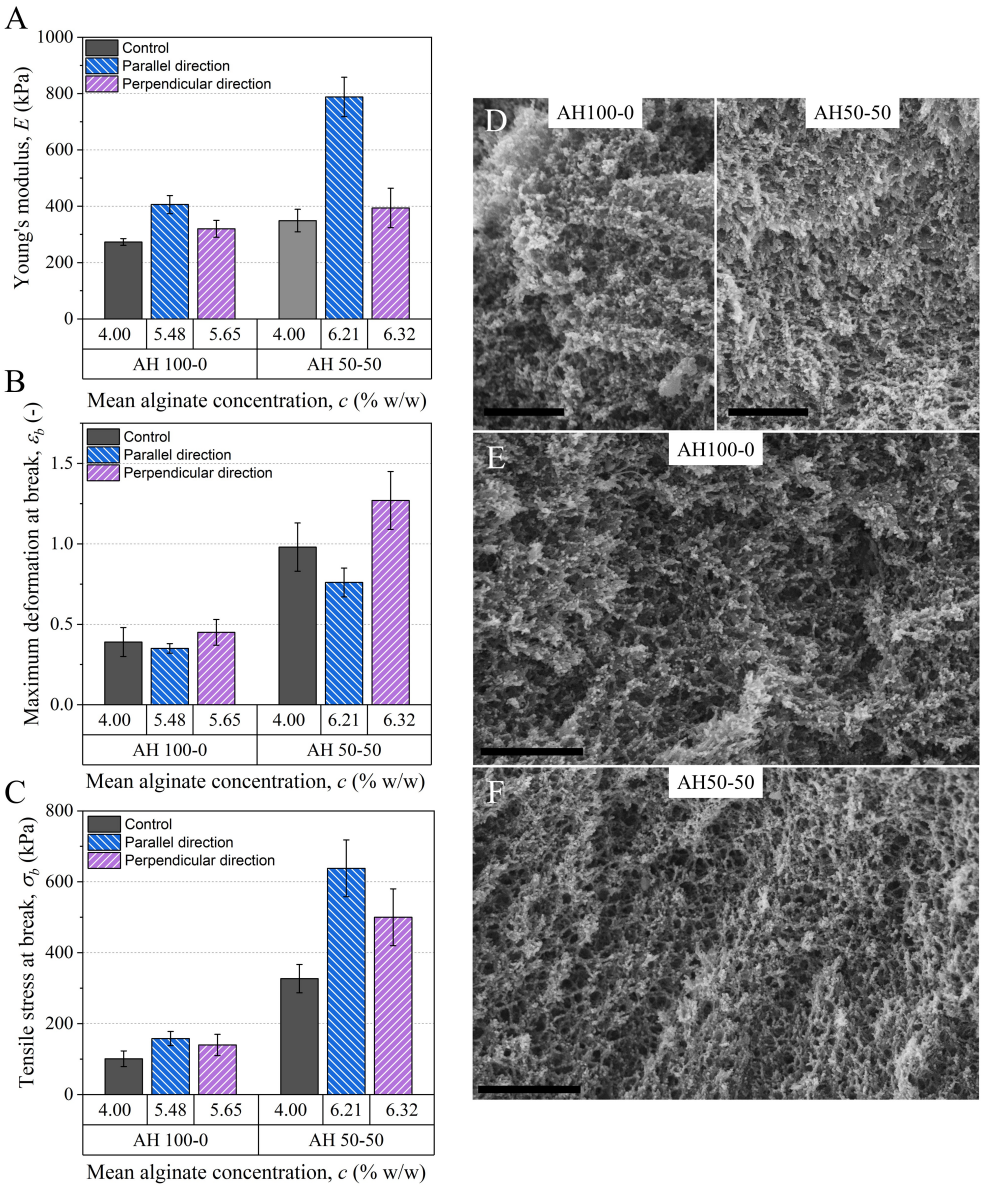

Figure 2.5: Young's modulus E, stress at break σ_b, deformation at break ϵ_b, and microscopic structure of dehydrated alginate hydrogels under tensile stress. Data for control samples are included for comparison. In each graph (A–C), from left to right, the value for control samples (C4.0AH100-0 and C4.0AH50-50), the value for samples measured under uniaxial tensile stress parallel to the direction of the SCDP stress, and the value for the samples measured under uniaxial tensile stress perpendicular to the direction of the SCDP stress are shown. D) SEM images of the polymeric networks of AH100-0 and AH50-50 samples after their preparation (top view). E) and F) SEM images of the polymeric networks of AH100-0 and AH50-50 (top view), respectively, after a SCDP under tensile stress of 24 h. Scale bars represent 1 µm.

2.3.4 Role of a SCDP in the Response of a Hydrogel-Based Magnetic Actuator

In this section, we investigate whether a SCDP can also positively affect the magnetic actuation of hydrogels. According to previous results, dehydration under compressive stress resulted in a stronger enhancement of the mechanical properties than under tensile stress (*cf.*, Figures 2.3 and 2.4). For this reason, we are going to only focus on dehydration under compressive stress.

Table 2.3: MPs concentration (Fe-CC) and alginate concentration (c) of the different hydrogels after the first and second dehydration (F.D. and S.D., respectively).

	Fe-CC (% v/v)		*c (% w/w)*	
	F.D.	S.D.	F.D.	S.D.
M5AH	7.3 ± 1.4	8.0 ± 1.2	1.5 ± 0.3	1.7 ± 0.3
M7.5AH	9.7 ± 1.6	12.2 ± 2.5	1.33 ± 0.23	1.7 ± 0.4
M10AH	14.7 ± 1.2	18.4 ± 1.8	1.56 ± 0.15	2.03 ± 0.23
M20AH	26 ± 5	36 ± 6	1.4 ± 0.4	1.9 ± 0.6

In Table 2.3, the concentrations of MPs and alginate polymer after dehydration under compressive stress in the magnetic hydrogels are shown. Similarly to previous results, dehydration under compressive stress caused an overall increase in Young's modulus (Figure 2.6 A). Under a sufficiently intense magnetic field applied perpendicular to the actuator plane, the magnetic hydrogel beams bent because of the magnetic torque. The misalignment between the magnetic beams and the direction of the applied magnetic field resulted in a gripping movement (Figure 2.6 B). The response to magnetic stimuli can be quantified by the equilibrium angle of the magnetic beams of the actuator (Figure 2.2 B). This equilibrium was reached as a balance between the magnetic, gravitational, and elastic torques. The rigorous analysis of the problem is complicated; however, a rough idea can be obtained using some simple approximations. First, in the dipolar approximation, the magnetic torque, $\vec{T}_m$, acting on a body of magnetic moment, $\vec{m}$, in a magnetic field of strength $\vec{H}$ is given by the following equation:

$$\vec{T}_m = \mu_c \vec{m} \times \vec{H} \tag{2.2}$$

, μ_c being the magnetic permeability of the carrier medium. Note that $\vec{m}$ is an extensive quantity, thus it is the summation of the magnetic moments of individual particles within the magnetic hydrogel. Regarding the hydrogel elasticity, according to Euler-Bernoulli beam theory, the bending moment, T_b, is given by the following equation:

$$T_b = EI \frac{d^2 u(x)}{dx^2} \tag{2.3}$$

, E being the Young's modulus, I the second moment of area of the beam, and $(d^2u(x))/(dx^2)$ the curvature of the beam. Finally, the gravitational torque, T_g is roughly given by the following equation:

$$T_g = \frac{1}{2} W l cos(\theta) \tag{2.4}$$

, where W is the weight of the beam, l its length, and θ the angle of inclination of the beam with respect to the horizontal (off-state) position. Note that in the expression of the gravitational torque, the beam is approximated to a straight line (Figure 2.2 B), whereas in the real case, a curvature exists and the angle $\theta = arcsin(du(x)/dx)$ is not uniform (Figure 2.6 B). Qualitatively, the magnetic torque increases with the concentration of MPs in the magnetic hydrogel beam and the strength of the applied magnetic field, whereas the bending moment increases with the Young's modulus and the curvature of the beam. Regarding the gravitational torque is maximum in the off-state position and decreases as the angle of inclination increases.

The experiments demonstrated that there was a threshold value of the magnetic field strength required to obtain a response from the magnetic beams (*i.e.*, to obtain a nonzero equilibrium angle with respect to the off-state position) (Figures 2.6 C and A.5). The existence of this threshold field strength agrees with the observation that the gravitational torque was nonzero (indeed, it was maximum) in the off-state position. In equilibrium, the gravitational torque must be completely balanced by the magnetic torque as soon as the magnetic hydrogel beam is detached from the horizontal surface used as support –note that the normal force exerted by the horizontal surface on the actuator that balances the gravitational force in the absence of an applied magnetic field disappears as soon as the actuator is detached from the surface. When the magnetic field strength exceeded the threshold value, there was a progressive increase in the actuation angle with a tendency to saturation for the highest values of the field (Figures 2.6 C and A.5). Subsequently, the actuation angle was progressively decreased until zero as the applied magnetic field decreased to zero from its maximum value. In all cases, the angle obtained by increasing the magnetic field was smaller than that obtained by decreasing the magnetic field, indicating the existence of hysteresis. Furthermore, the threshold value of the magnetic field strength was lower when the field strength was decreased than when it was increased (Figures 2.6 C and A.5).

In order to analyze the role of the concentration of MPs and the SCDP in the actuation behavior of the cross-shaped actuators, it is important to focus on two magnitudes: the equilibrium angle at the maximum applied field (57 kA/m) and the threshold value of the magnetic field strength. In our case, the angle at the maximum applied field increased with the increasing particle content for both nondehydrated (pristine) and dehydrated hydrogels (Figure 2.6 D). This result is consistent with the expression of the magnetic torque, which is proportional to the magnetic moment

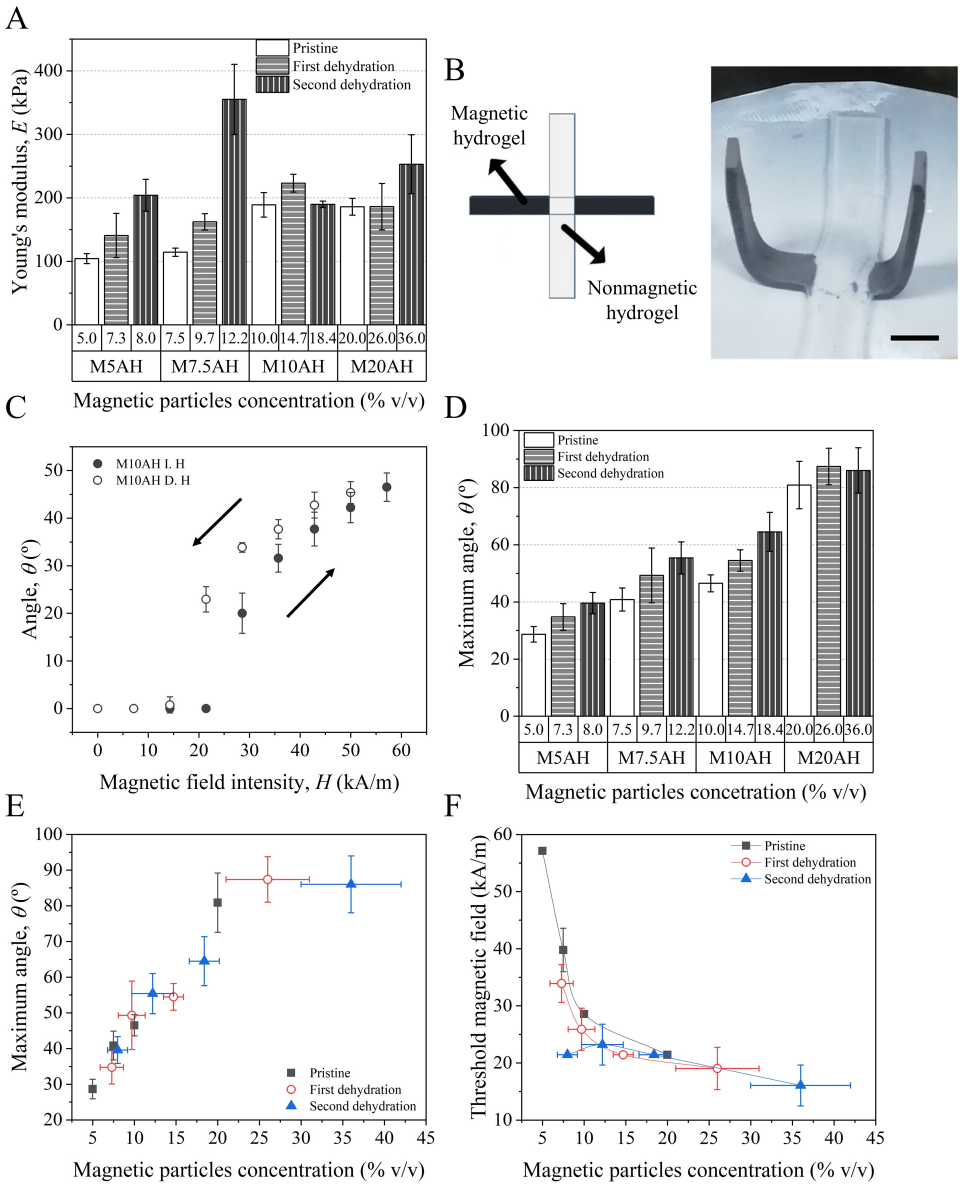

Figure 2.6: Mechanical response and actuation of the magnetic actuator. A) Young's modulus, (E) of the active part of the actuator before and after two dehydration steps under compressive stress. B) Sketch and image of the actuator (on-state). The scale bar is 10 mm. C) Angle as a function of the magnetic field intensity for a pristine actuator with a particle concentration of 10% v/v. I.: Increasing; D.: Decreasing. D) Maximum angle reached by the actuator at a magnetic field intensity of 57 kA/m. E) Maximum angle reached by the actuator at a field of 57 kA/m as a function of the concentration of MPs. F) Threshold magnetic field as a function of the concentration od MPs of the actuator.

of the ferrogel. In addition, no effect due to dehydration was observed, except for the effect caused by an increase in particle concentration. All experimental data for

the pristine and dehydrated samples fitted on a single master curve (Figure 2.6 E). Regarding the threshold magnetic field strength, it decreases with the concentration of MPs, as expected from the proportionality of the magnetic torque with the magnetic moment of the hydrogel beam (Figure 2.6 F). Furthermore, the data of this quantity for the different samples (pristine, 1st dehydration, and 2nd dehydration) did not fit in a single master curve, showing a tendency of the threshold magnetic field to decrease in dehydrated samples relative to pristine samples. This result indicates that the SCDP had a positive influence on the actuation behavior of the cross-shaped actuators. It seems that the potential changes in the microstructure of the magnetic hydrogels originated by the SCDP facilitated their bending response under a magnetic field.

2.4 Conclusions

In this chapter, we have studied the influence of SCDPs on the mechanical properties of alginate hydrogels. From the mechanical characterization, we found that dehydration results in an increase in the robustness of the hydrogel, which can be connected to an increase in the concentration of polymer fibers, as predicted by classical theories of the mechanical properties of networks and gels. However, this increase in robustness was significantly higher for hydrogels subjected to compressive or tensile stress during dehydration than for nondehydrated hydrogels containing similar polymer concentrations. This can only be due to the arrangement of polymer fibers, caused by these dehydration processes. Indeed, we corroborated that reversible rehydration of alginate hydrogels was impossible, which may be due to the appearance of hydrogen bonds between the -OH groups of the alginate fibers during dehydration. Microscopic analysis of the fiber network by SEM images and an anisotropic mechanical characterization provided some evidence for the existence of structural anisotropy, which was characterized by the appearance of polymer bands in some samples. In addition, we reported the results of the SCDPs on the response of a cross-shaped magnetic actuator under a magnetic field. The actuator consisted of a central nonmagnetic hydrogel beam connected to two lateral magnetic hydrogel beams that bent in response to the applied fields. For all the samples, we observed a threshold value of the magnetic field, which was required to obtain a significant bending of the magnetic hydrogel beams. Interestingly, this threshold value tended to decrease for samples subjected to dehydration under compression compared to nondehydrated samples containing similar MPs concentrations. This result indicated that the changes caused by the dehydration under compression positively influence the actuation of magnetic hydrogels.

Chapter 3.
Magnetically Structured Sodium Alginate Hydrogels

3.1 Introduction

Most hydrogels are synthesized through polymerization or self-assembly of uniformly dissolved/dispersed molecular components in aqueous media, resulting in generally isotropic polymeric networks. However, there is an increasing interest in creating materials with anisotropic structures and hierarchical internal order at different scales. This interest is primarily due to the fact that many biological systems have a well-defined anisotropic hierarchical structure that gives them, to some extent, their characteristic mechanical properties, such as muscles, cartilage, and skin. In these biological tissues, anisotropy plays a fundamental role in processes such as nutrient transport, surface lubrication, force transmission, and adaptive response to external stresses [Huxley, 1974]. Similarly, the presence of anisotropic structures in culture media have shown a strong influence in cell proliferation, migration, and differentiation [Marelli et al., 2015, McClendon and Stupp, 2012], therefore, anisotropic hydrogels have the potential to replicate natural extracellular matrices for tissue regeneration. However, obtaining such anisotropy is not trivial and requires the material biocompatibility. There are several procedures to obtain anisotropic hydrogels in which a stimulus is applied in a certain direction, such as an external mechanical stress (Chapter 2), an electric field, a magnetic field, or an ionic concentration gradient [Sano et al., 2018, Mredha et al., 2018, Scionti et al., 2013]. In general, when the anisotropy is achieved by applying an external field, particles that can align when subjected to such fields must be used. Nevertheless, these particles weakly interact with the polymeric chains that form the hydrogel, resulting in anisotropic structures generated by the particles themselves. However, it is possible to go one step further and coat the surface of particles with chemical or polymeric compounds. These coatings allow the particles to strongly interact with the polymeric

chains of the gel, increasing their biocompatibility and protecting them from corrosion [Pourmadadi et al., 2023, Zeng et al., 2022, Barczak et al., 2020].

Our research interest lies in the use of magnetic fields to produce anisotropic hydrogels by aligning MPs embedded in the polymeric matrix. Magnetic fields can be remotely and noninvasively applied (without direct contact with the sample) and can penetrate uniformly throughout the sample volume. Therefore, magnetic alignment is easily applicable to the synthesis of anisotropic hydrogels, which have been previously used in different works [Gila-Vilchez et al., 2019b]. However, this strategy does not necessarily result in an anisotropic arrangement of the polymeric fibers, although some studies have shown that the microstructure of magnetic hydrogels can be modified by applying magnetic fields in such a way that anisotropy occurs even at the level of the polymeric fibers [Lopez-Lopez et al., 2015]. The hypothesis behind this behavior is that MPs, in their migration in response to the application of a uniform magnetic field, drag the polymer fibers attached to them, resulting in the alignment of the fibers in the direction of the field.

To characterize the structural anisotropy of these materials, mainly two methods are used: i) measurements of the mechanical properties in different directions, parallel and perpendicular to the anisotropy direction; ii) imaging methods such as scanning electron microscopy (SEM). Normally, despite the fact that from a mechanical point of view the anisotropy is clear, other techniques such as SEM, which allow the observation of the microscopic structure, do not yield clear evidence of this macroscopically observed arrangement. An alternative to this technique is the use of FT-IR, which measures the infrared absorption or transmission spectrum of the material. This technique is normally used to establish the hydrogel composition because part of the energy radiated on the sample is absorbed by the different molecules and their vibration modes. However, Kreuzer et al. [Kreuzer et al., 2022] demonstrated by means of FT-IR polarized microspectroscopy using light from a synchrotron that when a tensile stress is applied to polyurethane thin films, it is possible to detect the anisotropic alignment of the polymer fibers induced by the applied stress. To do so, they analyzed different vibration bands in the spectrum parallel and orthogonal to the stretching direction.

The starting hypothesis of this work is the possibility of generating anisotropic hydrogels by applying a uniform magnetic field, which can be microscopically analyzed using FT-IR microspectroscopy. The validity of this hypothesis is based on the results of the previously mentioned works [Kreuzer et al., 2022, Lopez-Lopez et al., 2015]. For this reason, sodium alginate ferrogels were prepared including MPs coated with amine groups that have previously demonstrated electrostatic interaction with alginate polymers [Barczak et al., 2020]. The hydrogels were placed under uniform magnetic fields during the initial gelling stages to align the MPs and the polymer fibers. After their preparation, the anisotropic hydrogels were analyzed using polarized synchrotron radiation-based FT-IR microspectroscopy at the facilities of

ALBA synchrotron. In the spectra, peaks associated with the vibration modes of chemical groups present in alginate macromolecules were analyzed by considering the polarization of the infrared light and the type of coating in the MPs. The results shed light on the microscopic arrangement of alginate fibers, which exhibit a certain degree of arrangement in the magnetic field direction.

3.2 Materials and Methods

3.2.1 Materials

Medium-viscosity sodium alginate (MVSA) from PanReac AppliChem ITW Reagents (Spain). Calcium carbonate, ($CaCO_3$), D-glucono-δ-lactone (GDL), calcium chloride ($CaCl_2$) from Sigma Aldrich (USA). Silica-coated iron microparticles (Fe-CC) from BASF (Germany). Barium fluoride (BaF_2) windows with a diameter of 13 mm and height of 0.5 mm from Crystran Limited (UK).

3.2.2 Functionalization of Magnetic Particles

The functionalized Fe-CC microparticles were provided by PhD Mariusz Barczak, who followed the protocol in [Barczak et al., 2020]. Briefly, a certain amount of Fe-CC particles in acidified absolute ethanol were mixed with two organofunctional alkoxysilane: aminopropyltriethoxysilane (APTES) and (3-trimethoxysilylpropyl)diethylenetriamine (TMPMT) (see Table 3.1). This mixture was sonicated and stirred multiple times, after which the dispersion was washed and dried to obtain the functionalized MPs. A thorough characterization of these particles and alginate ferrogels made with them can be found in the previous work [Barczak et al., 2020].

Table 3.1: Organofunctional alkoxysilanes used for the functionalization of Fe-CC microparticles.

No.	Functional group	Monomer
B0	-	-
B1	APTES	I° amine
B2	TMPMT	I° and II° amine

3.2.3 Synthesis of Alginate Ferrogels

To synthesize the alginate ferrogels, a 1 % w/w solution of alginate was used. A mixture of 99.32 w/w % of the alginate solution, 0.15 w/w % of $CaCO_3$, and 0.53 w/w % of GDL was prepared. Firstly, the $CaCO_3$ was dispersed in the alginate solution. Then, the GDL was dissolved in the previous mixture using a vortex mixer and a

sonicator. Finally, 0.4 v/v % of functionalized Fe-CC particles were added to the pre-gel mixture, which was thoroughly mixed and sonicated to reduce aggregation and sedimentation of the MPs.

To perform the FT-IR polarized microspectroscopy measurements, it is necessary to prepare thin samples with a thickness under 100 µm. To do so, the experimental setup showed in Figure 3.1 A was used. It consisted of a rheometer with a plate-plate geometry to control the thickness of the samples and a Helmholtz coil to apply a uniform magnetic field to the sample during the gelling process. First, a droplet of the previously prepared pre-gel mixture was placed in the lower plate of the rheometer. Then, the upper plate was pulled down pressing the droplet until reaching a set gap of 90 µm (Figure 3.1 B). After placing the mixture, the field was turned on for 15 min, and the hydrogels continued gelling for additional 45 min without field. After this time, a $CaCl_2$ 45 mM solution was placed around the upper plate to start increasing the hydrogel cross-linking density, and after a couple of minutes it was slowly lifted. Finally, more $CaCl_2$ was added, and the hydrogel was left to gel with the $CaCl_2$ for other 10 min. In Table 3.2 are shown all the the samples prepared and the experimental conditions.

Table 3.2: Alginate ferrogels prepared and the experimental conditions used: functional group of the MPs, applied magnetic field, and concentration of MPs.

Sample name	Functionalization of MPs	Concentration of MPs (v/v %)	Magnetic field strength (kA/m)
Ctrl-MF0	-	0	0
MB0-MF16	B0-control	0.4	16
MB1-MF0	B1-APTES	0.4	0
MB1-MF8	B1-APTES	0.4	8
MB1-MF16	B1-APTES	0.4	16
MB2-MF16	B2-TMPET	0.4	16

The Helmholtz coil system consisted of two coils with an internal diameter of 24 cm and 2000 turns of 1.8 mm of diameter copper wire. The internal surfaces of the coils were 22 cm apart. This distance does not correspond with the Helmholtz's length, thus the applied field as a function of the current intensity was measured using a teslameter (Figure 3.1 C). To theoretically know if the magnetic field was uniformly distributed within the sample region, a COMSOL simulation was carried out (Figure 3.1 D and E). As can be observed in Figure 3.1 D, within the sample space (black circle) the magnetic field generated was uniformly distributed.

3.2.4 Synchrotron Radiation-Based FT-IR Microspectroscopy

FT-IR microspectroscopy measurements were carried out at MIRAS beamline at ALBA synchrotron (Barcelona, Spain). The beamline was equipped with a Hyperion

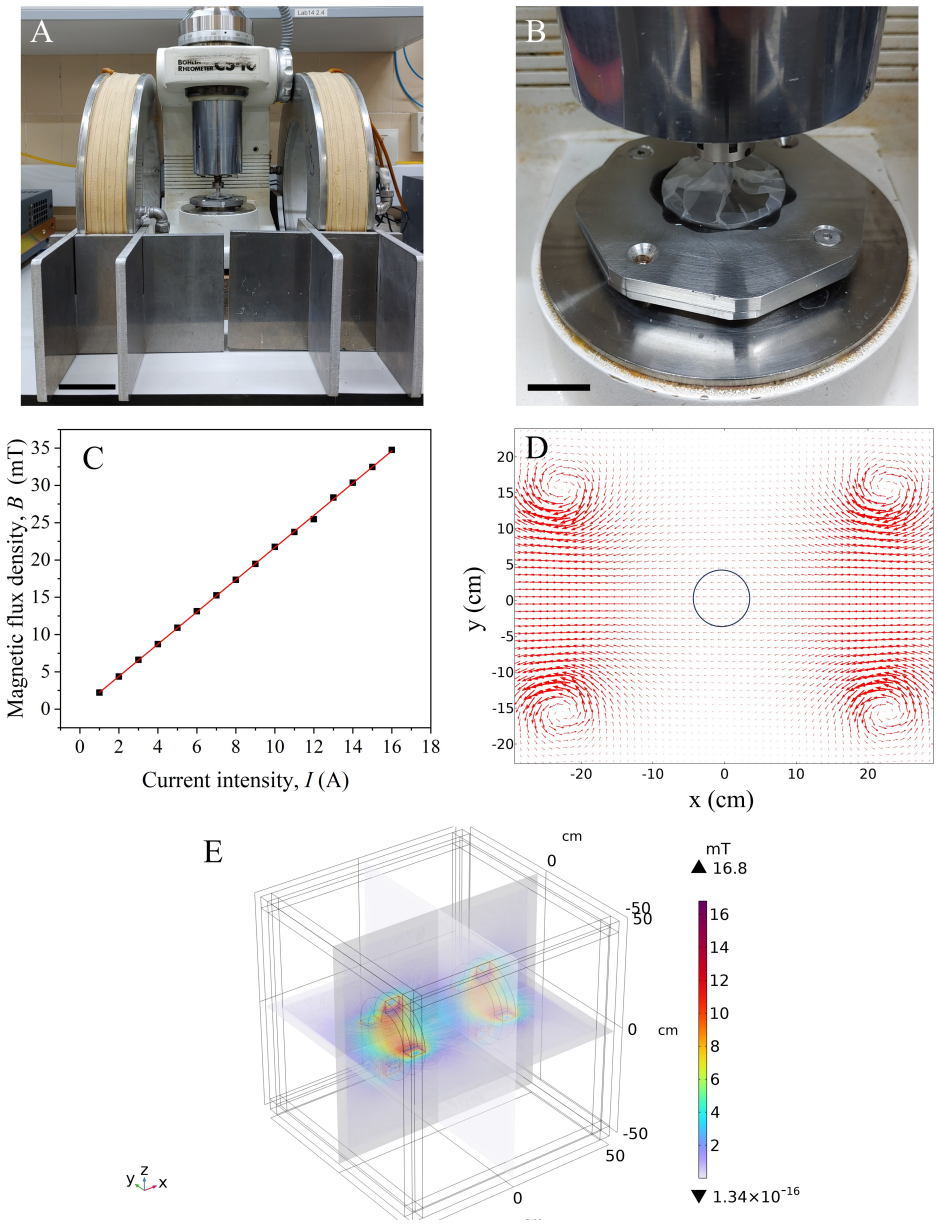

Figure 3.1: Experimental setup for the synthesis of anisotropic alginate ferrogels. A) Rheometer and Helmholtz coil. The scale bar is 10 cm. B) Zoom of the plate-plate filled with a pre-gel mixture. The scale bar is 20 mm. C) Experimental measurement of the relation between the current intensity (I) and the magnetic flux density (B) produced by the two coils in the middle of the working space. D) COMSOL simulation of the magnetic flux density of the field produced by the coils system. The black circle delimit the work space where the ferrogels were prepared. The size of the red arrows is proportional to the magnitude of the field. E) Geometry and magnetic flux density in the simulation.

3000 microscope coupled to a Vertex 70 spectrometer (Bruker, Germany), where the infrared light from the synchrotron was focused on the sample using a 36× Schwarzschild objective and matching condenser. Spectra was recorded with a liquid nitrogen cooled MCT detector.

Certain areas of the samples were measured using two different polarizations: parallel to the particle alignment (0°) and perpendicular to particle alignment (90°). Each sample was dried before the measurements to avoid water absorption bands. To place the samples in the microscope, two different methods were used : 1) between two BaF_2 windows; 2) inside a temperature and environmental control chamber (Linkam, UK). In addition, different apertures (A), number of scans, and number of mapped points were used (Table 3.3). These magnitudes affect the spectra in different ways: the aperture is related to the average spectrum over an area of the material, the lower the aperture, the narrower the area under analysis; the number of scans is related to the average spectrum over time of an area, when this parameter is increased, the noise of the signal is reduced; the number of mapped points depends on the region of interest, as will be explained later and is closely related to the aperture. The reason behind the differences in the parameters used in each case lies in the fact that the areas of interest changed from one sample to another.

Table 3.3: Experimental conditions during the synchrotron radiation-based FT-IR microspectroscopy at ALBA synchrotron. A is the aperture and Pol. the polarization.

Sample name	Method	A (μm^2)	Pol. (°)	Scans	Points
Ctrl-MF0	Linkam	20 × 20	0	256	4
	Linkam	20 × 20	90		
MB0-MF16	Linkam	20 × 20	0	256	6
	Linkam	20 × 20	90		
MB1-MF0	BaF_2	8 × 8	0	128	25
	BaF_2	8 × 8	90		
MB1-MF8	BaF_2	8 × 8	0	128	96
	BaF_2	8 × 8	90		
MB1-MF16	Linkam	20 × 20	0	512	256
	Linkam	20 × 20	90		
MB2-MF16	BaF_2	10 × 10	0	128	400
	BaF_2	10 × 10	90		

3.2.5 Analysis of the Spectra

Preprocessing and analysis of the spectra obtained at ALBA synchrotron were performed using Quasar software. The spectra was linear baseline corrected and unit vector normalized in the wavenumber region of interest between 900 cm^{-1} and 1800 cm^{-1}.

3.3 Results and Discussion

To observe changes in the arrangement of alginate chains, the vibration bands of a chemical group of the macromolecules was analyzed. In our case, the spectrum of dry alginate hydrogels without particles is shown in Figure 3.2 A, in which two peaks are marked: (a) around 1600 cm^{-1}, and (b) around 1423 cm^{-1}. These two peaks correspond to the asymmetric and symmetric stretching modes of the carboxyl group (COO^{-}) present in alginate (Figure 3.2 B). The reason for choosing this chemical group is because of the interaction between the functionalized MPs and the alginate fibers is of an electrostatic nature; the positive charge on the surface of the particles interacts with the negative charge in the carboxyl groups of the polymers, attracting each other. As a result, the arrangement of the particles is reflected in the orientation of this group and hence of the alginate fibers. To analyze these results, the ratios of the areas under each peak of both polarizations were calculated ($Area_0/Area_{90}$). These ratios indicate whether there is a change in the orientation of the chemical group because they will be higher or lower than one.

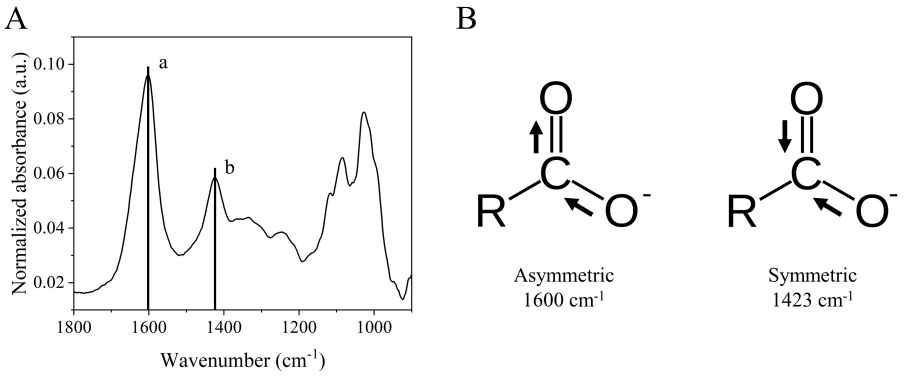

Figure 3.2: A) Average FT-IR spectrum of dry nonmagnetic alginate hydrogels, in which two peaks of interest are marked: (a) around 1600 cm^{-1}, and (b) around 1423 cm^{-1}. These peaks are related, respectively, to the asymmetric and symmetric stretching modes of carboxyl groups (COO^{-}) present in alginate macromolecules B). Depending on the sample, these peaks can be slightly shifted.

Among the samples shown in Table 3.3, three different comparisons were done: i) between an isotropic nonmagnetic hydrogel and an isotropic ferrogel with functionalized MPs (Figure 3.3); ii) between anisotropic ferrogels with B1 MPs aligned under different magnetic field strengths (Figure 3.4); iii) between anisotropic ferrogels with no functionalized B0 MPs and with B2 MPs (Figure 3.5).

Firstly, the analysis of the results is focused on the effect of the presence of functionalized MPs in the spectra. To do so, a comparison between a nonmagnetic hydrogel (Ctrl-MF0) and one with B1 MPs (MB1-MF0) is done (Figure 3.3). In Figure 3.3 A and B, it seems that the ratios of the area of the 1600 cm^{-1} and

1423 cm^{-1} peaks is near one and the value is quite homogeneous over the area of analysis. This means that there are no significant differences in the spectra under both polarization, as it is expected in this case. However, when B1 MPs are included in the hydrogels, the homogeneity of the values of the ratios drastically changed on the order of 10 %. In this case, these differences reflect that the carboxyl groups are not randomly distributed as in Ctrl-MF0, instead, they are attached to the particles and, in some cases, oriented in the direction of polarization to some degree.

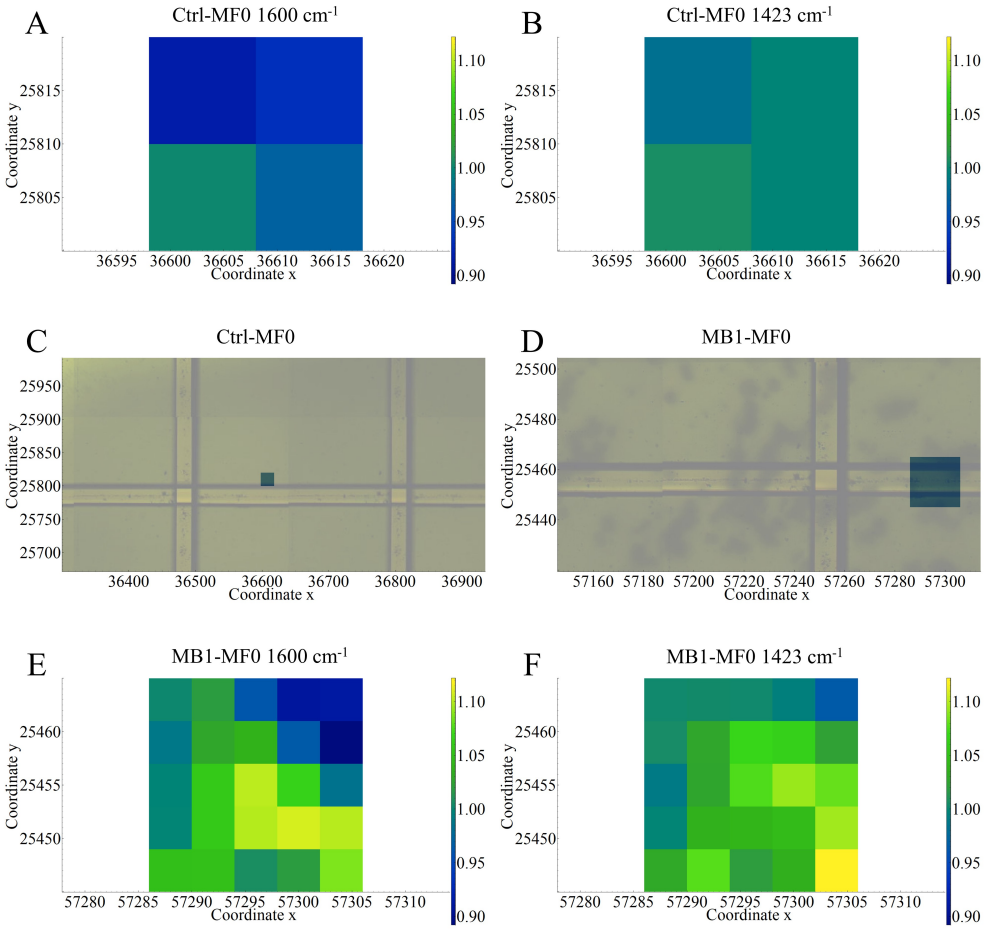

Figure 3.3: A) and B) are the 1600 cm^{-1} and 1423 cm^{-1} peaks ratios of a nonmagnetic alginate hydrogel. C) Visible image of the region analyzed in the nonmagnetic alginate hydrogel. D) Visible image of the region analyzed in an isotropic alginate ferrogel with B1 MPs. E) and F) are the 1600 cm^{-1} and 1423 cm^{-1} peaks ratios of the isotropic alginate ferrogel with B1 MPs. The coordinates are given in µm. In the visible images, the blue rectangle delimits the measured area, the yellow color is due to the polarizer, and the horizontal and vertical strips are the aperture of the microscope, which were not removed when the pictures were taken.

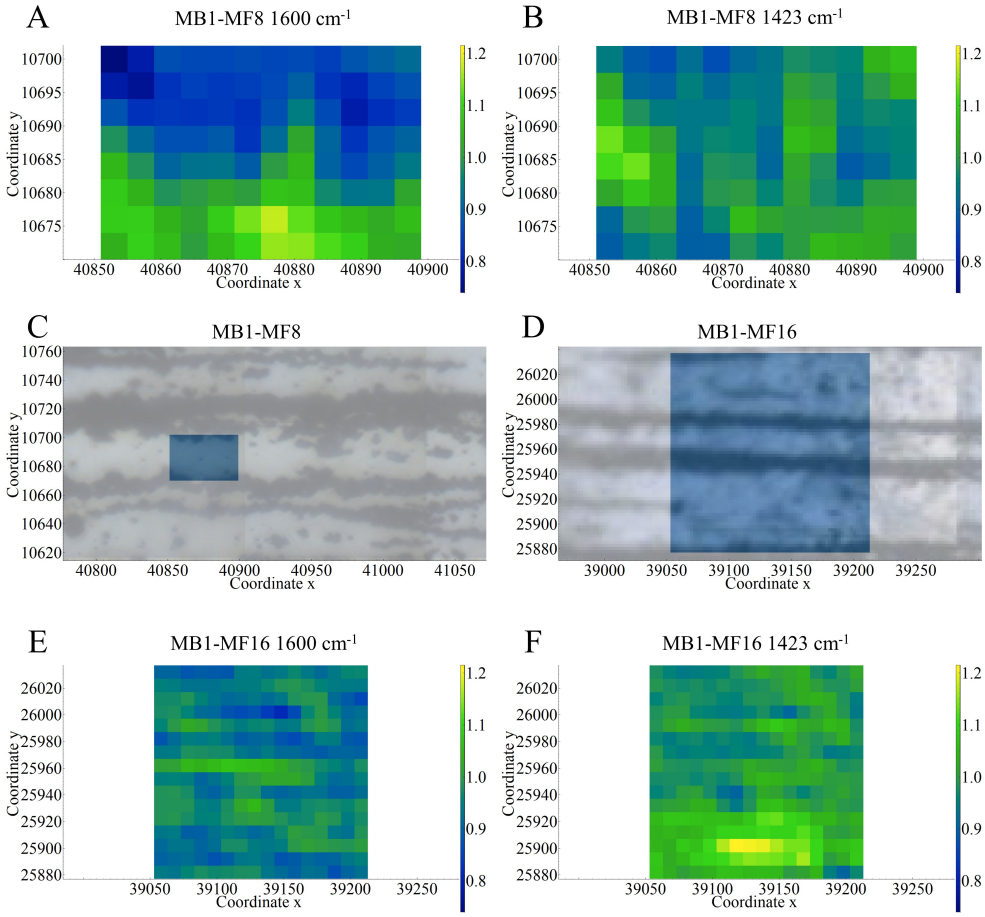

Figure 3.4: A) and B) are the 1600 cm^{-1} and 1423 cm^{-1} peaks ratios of an anisotropic ferrogel with B1 MPs aligned under an 8 kA/m magnetic field. C) Visible image of the region analyzed in the ferrogel with B1 MPs aligned under an 8 kA/m. D) Visible image of the region analyzed in an anisotropic alginate ferrogel with B1 MPs aligned under a 16 kA/m magnetic field. E) and F) are the 1600 cm^{-1} and 1423 cm^{-1} peaks ratios of the isotropic alginate ferrogel with B1 MPs aligned under a 16 kA/m. The coordinates are given in μm. In the visible images, the blue rectangle delimits the measured area.

After discussing the effect of the presence of functionalized MPs, the focus of the analysis is on the effect of the magnetic field strength. In Figure 3.4 the ratios of different areas of anisotropic ferrogels with B1 MPs aligned under 8 kA/m and 16 kA/m are shown. In the visible images of the measured areas (Figure 3.4 C and D), chain-like structures of MPs are present, but there are not appreciable differences between the two samples in this regard. However, the regions between chains in MB1-MF16 are highly populated with isolated clusters of MPs. In the case of the MB1-MF8 sample, an interesting behavior is observed for the 1600 cm^{-1} peak. The measured region is located between two particles chains, if an orientation of COO^{-} is expected due to the arrangement of the particles, an anisotropic change in the peak

ratio should be observed. In this case, this fact is evident because a decrease in the ratio is observed in the top half, whereas an increase occurs in the bottom half. Nevertheless, someone would expect a symmetric change in the ratios near the particle chains, but it does not seem to be the case, probably due to the two-dimensional nature of the analysis performed, despite the tridimensionality of the sample. Apart from that, in the mapping of the 1423 cm^{-1} peak, there are no significant changes, which are not associated with the particle chains orientation.

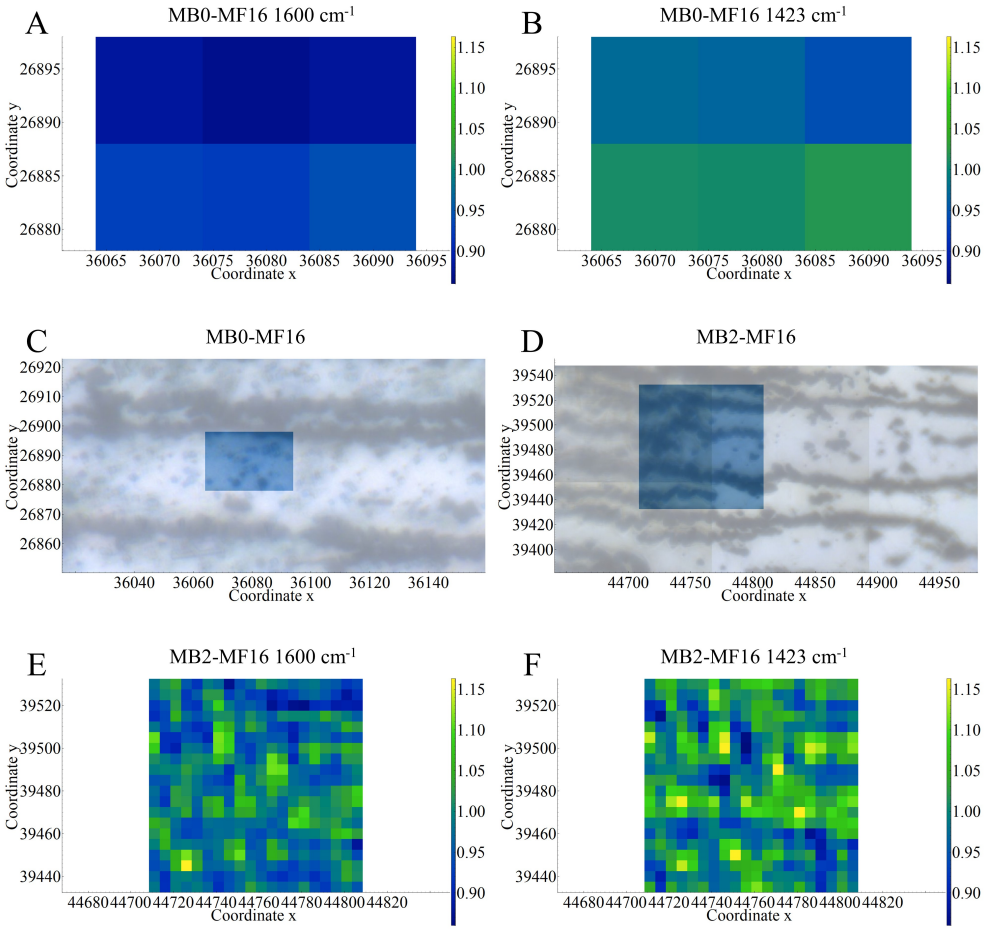

Figure 3.5: A) and B) are the 1600 cm^{-1} and 1423 cm^{-1} peaks ratios of an anisotropic ferrogel with B0 MPs aligned under a 16 kA/m magnetic field. (C) Visible image of the region analyzed in the ferrogel with B0 MPs. (D) Visible image of the region analyzed in an anisotropic alginate ferrogel with B2 MPs aligned under a 16 kA/m magnetic field. E) and F) are the 1600 cm^{-1} and 1423 cm^{-1} peak ratios of the isotropic alginate ferrogel with B2 MPs. Coordinates are given in µm. In the visible images, the blue rectangle delimits the measured area.

When the field is increased from 8 kA/m to 16 kA/m in the measured area, the changes are not as noticeable as in the 1600 cm^{-1} peak. However, near the chains at

1600 cm^{-1}, a decrease in the ratio is generally observed, but this is not clear enough due to the large area measured. The lack of clarity in these results can be attributed to two facts. First, the area under analysis is sufficiently large to lose the details observed for MB1-MF8. In addition, the aperture is more than double, thus the spectra are averaged over a larger area. Second, the presence of isolated MPs clusters all over the sample may hide the orientation of the carboxyl group due to the large averaged area.

Finally, to analyze the effect of the functionalization, two anisotropic ferrogels with nonfunctionalized (B0) and functionalized (B2) MPs are compared. Both samples were prepared under a magnetic field of 16 kA/m. In the MB0-MF16 sample (Figure 3.5 A, B, and C), similar results to those of Ctrl-MF0 (Figure 3.3 A, B, and C) are observed. The ratios of both peaks were homogeneous over the analyzed area, and their values are near unity. The particles without functionalization did not interact with the alginate fibers, therefore, no orientation of the COO^- group is observed. In the case of MB2-MF16 (Figure 3.5 D, E, and F), there are similar problems that were found in MB1-MF16 (3.5 D, E, and F), the measured area is large and filled with clusters and chains of particles that are not perfectly aligned in the horizontal direction. As a result, changes in the ratios of the peaks are observed, but there is no clear tendency in the changes that could be related to the arrangement of alginate fibers. In addition, B2 particles interact in a weaker way with alginate fibers because of their lower superficial charge [Barczak et al., 2020].

3.4 Conclusions

In this study, we analyzed the microscopic arrangement of alginate fibers in anisotropic ferrogels. These ferrogels were prepared using functionalized MPs with amine groups, which electrostatically interact with alginate polymers through their carboxyl groups. The hypothesis is that the MPs, which were arranged in chains during the gelling process, dragged the alginate fibers, generating microscopic anisotropy in the polymeric network. This fact was reflected mainly in the 1600 cm^{-1} peak ratios in the FT-IR microspectra of the samples. On the one hand, the hydrogels without particles and with nonfunctionalized particle (B0 MPs) showed homogeneous values near one over the analyzed area because no arrangement was expected in these cases. On the other hand, the ferrogels with functionalized MPs showed changes in the ratios of their FT-IR peaks, which were related to the arrangement of the alginate fibers due to the orientation of the COO^- group. Nevertheless, the only sample that showed a clear arrangement associated with the MPs alignment was MB1-MF8, where a pattern was observed.

These results provide new insights into the microscopic structure of anisotropic alginate ferrogels. However, a more detailed analysis should be conducted to undeniably confirm the presence of polymer arrangement due to particle alignment. In a future work, the analysis should be focused on smaller areas of the samples using

lower values of the aperture to not miss the details that can hide behind the averages of the spectra. In addition, other peaks should be analyzed to increase the possibilities of seeing the arrangement more clearly.

Part II

Chapter 4.
Semi-Interpenetrating Polymer Networks Based on Acrylamide and Biopolymers *

4.1 Introduction

Smart materials capable of exhibiting changes in their mechanical and optical properties in response to external stimuli have received considerable attention due to their great potential in the development of smart devices with remote actuation, such as guided catheters, artificial muscles, magnetic microvalves, multifunctional sensors, and biosensors, among others [Shi et al., 2021, Ryabchun and Bobrovsky, 2018, López-Valdeolivas et al., 2017, Zhang et al., 2015, Medina-Castillo et al., 2011]. Magnetic hydrogels based on natural biopolymers are one of the most promising types of smart materials owing to their unique combination of biocompatibility, flexibility, and responsiveness to magnetic fields [Tang et al., 2021b, Li and Su, 2018], providing unique features such as precise remote actuation [Chen et al., 2023a, Wu et al., 2022, Vazquez-Perez et al., 2021, Goudu et al., 2020]. However, achieving strong responsiveness to magnetic fields requires moderately high concentrations of MPs in the hydrogel, which usually results in loss of integrity of the polymer network or, at best, in substantial weakening of the mechanical properties and stability of the resulting magnetic hydrogel [Chen et al., 2023a, Mei et al., 2023, Vazquez-Perez et al., 2021, Mañas-Torres et al., 2021b, Gila-Vilchez et al., 2019a, Contreras-Montoya et al., 2018]. This mechanical weakness in magnetic hydrogels confines

*The content of this chapter is an adaptation of Leon-Cecilla, A., Gila-Vilchez, C., Vazquez-Perez, F. J., Capitan-Vallvey, L. F., Martos, V., Fernandez-Ramos, M. D., Álvarez de Cienfuegos, L., Medina-Castillo, A. L., Lopez-Lopez, M. T. (2024). Highly deformable and strongly magnetic semi-interpenetrating hydrogels based on alginate or cellulose. *International Journal of Biological Macromolecules*, 260:129368. [Leon-Cecilla et al., 2024].

their applicability mainly to areas that require limited low-level loading [Singh and Datta, 2023, Chen et al., 2022b], whereas works that report the use of magnetic hydrogels based on biopolymers for applications that require superior mechanical properties, such as soft actuators or artificial muscles, are scarce [He et al., 2023, Li et al., 2015]. Strategies to overcome this limitation include proper functionalization of the particle surface so that the particles participate in the polymer network by covalent or ionic bonding [Barczak et al., 2020, Bonhome-Espinosa et al., 2017] or to increase the concentration of polymer to strengthen the resulting network [Leon-Cecilla et al., 2023]. Unfortunately, the former usually requires complex and highly time-consuming protocols to functionalize the surface of the particles, which limits their practical application, and the latter results in decreased porosity, which could have a negative impact in different applications, especially in the biomedical field.

Another promising approach to prepare magnetic hydrogels that combines strong responsiveness to applied magnetic fields and mechanical stability is based on the use of interpenetrating polymeric networks (IPNs) or semi-interpenetrating polymeric networks (SIPNs) [Huang et al., 2023a, Li et al., 2022, He et al., 2021]. IPNs are systems comprising two or more three-dimensional polymeric networks that are partially intertwined at the molecular scale but have no covalent bonding with each other, whereas in SIPNs, the distinguishing feature is that molecular-scale penetration occurs between a three-dimensional polymeric network and a noncross-linked linear or branched polymer [Gold, 2019]. Both IPNs and SIPNs combine the different properties of distinct constituent materials and are considered straightforward strategies for combining and tuning the functional properties of polymeric materials. Furthermore, double network hydrogels, a special type of IPN hydrogels, are characterized by combining high water content with high mechanical compliance and toughness [Chen et al., 2023c, Li et al., 2023, Liu et al., 2023, Matsuda et al., 2019]. Due to their superior mechanical properties, these IPNs and SIPNs could withstand high concentrations of particles without substantial deterioration in their mechanical properties.

In this chapter, SIPNs consisting of a cross-linked network made of acrylamide and N,N'-methylenebisacrylamide and a biopolymer consisting of any of five different natural biopolymers (sodium alginate; 2-hydroxyethyl cellulose of two different molecular weights; carboxymethylcellulose sodium salts of two different molecular weights) were used to prepare magnetic SIPNs (Mag-SIPNs) hydrogels with excellent stretchability (strains at break up to 220 % under tensile stress), high water content (up to 87.89 % w/w) [Huang et al., 2023b], and strong responsiveness to applied magnetic fields (Figure 4.1). This last characteristic was achieved by embedding Fe-CC microparticles at moderately high concentrations (up to 26.2 % w/w) in the polymer network without substantial deterioration of the excellent mechanical properties of the SIPNs, but with a reduction in the water concentration. The use of magnetic microparticles in this work is a differential feature with respect to most works in the field of magnetic IPNs or SIPN hydrogels based mainly on magnetite nanoparticles

[Wan et al., 2023, Zhang et al., 2022, Zhang et al., 2021], with only a few examples based on magnetic microparticles [Roy et al., 2023, Mandal et al., 2021, Spangenberg et al., 2021]. The use of strongly magnetic (*e.g.*, iron) microparticles is also required to enhance the responsiveness to magnetic fields. Furthermore, the performance, reliability, and stability of the Mag-SIPN hydrogels were evaluated in a proof-of-concept application requiring strong responsiveness to magnetic fields, specifically a hydrogel luminescent oxygen sensor controlled by a magnetic field. For this, we designed a disk-like hydrogel consisting of an inner nonmagnetic circle containing O_2-sensitive luminescent nanoparticles and an outer magnetic ring. It was thanks to the strong magnetic responsiveness of the Mag-SIPNs that the luminescent oxygen sensor could be firmly fixed inside the measurement cell from the outside using a system of coaxial magnets placed around the optical fiber, allowing easy and reliable reading of the luminescent signal. This sensor solves one of the most limiting problems in the optical measure of O_2 in liquid systems, namely, the lack of fixation of the sensor in the measurement cell, which prevents a reliable reading of the optical signal from the outside.

4.2 Materials and Methods

4.2.1 Materials

Acrylamide (AAm), N,N'-methylenebisacrylamide (Bis-AAm), 2-hydroxyethyl cellulose $M_v \sim 720000$ (HC720) (2 % w/w, 25°C, water: 4500 - 6500 mPas), 2-hydroxyethyl cellulose $M_v \sim 1300000$ (HC1300) (1 % w/w, 25°C, water: 3400 - 5000 mPas), high viscosity carboxymethylcellulose sodium salts (CChigh) (1 % w/w, 25°C, water: 1500 - 3000 mPas), medium viscosity carboxymethylcellulose sodium salts (CCmedium,) (2 % w/w, 25°C, water: 400 - 1000 mPas), potassium peroxodisulfate (KPS), N,N,N',N'',N''-pentamethyldiethylenetriamine (PMDTA), and platinum octaethylporphyrin (PtOEP; luminescent O_2 probe; λ_{exc} = 380 nm, λ_{em} = 650 nm) from Sigma Aldrich (USA). Medium viscosity sodium alginate (MVSA) (1 % w/w, 20°C, water: 350 - 550 mPa) from PanReac AppliChem ITW Reagents (Spain). The relative content of mannuronic to guluronic acid in the alginates was experimentally estimated using protocols based on ellipsometry [Donati et al., 2003, Morris et al., 1980](Figure B.1). Both ellipsometric methods showed that the composition of this alginate was: Method of Donati et al. [Donati et al., 2003]: 18.7 % guluronic acid, 28.9 % mannuronic acid, and 52.4 % mixed sequences; Method of Morris et al. [Morris et al., 1980]: 17.1 % guluronic acid, 34.3 % mannuronic acid, and 48.7 % mixed sequences, which are in good agreement with the results of the method of Ref. [Donati et al., 2003]. Sodium lauryl sulfate (SDS) 95 % extra pure, chloroform ($CHCl_3$) stabilized with ethanol, and sodium hydroxide (NaOH) from Scharlau (Spain). Poly(styrene-co-maleic anhydride; 7 % maleic anhydride,

M_w=80000 Da) from ARKEMA Sartomer (France). Silica-coated iron powder (Fe-CC) from BASF (Germany). The reagents were used as received and the solutions were prepared using milli-Q water.

4.2.2 Synthesis of Mag-SIPN Hydrogels

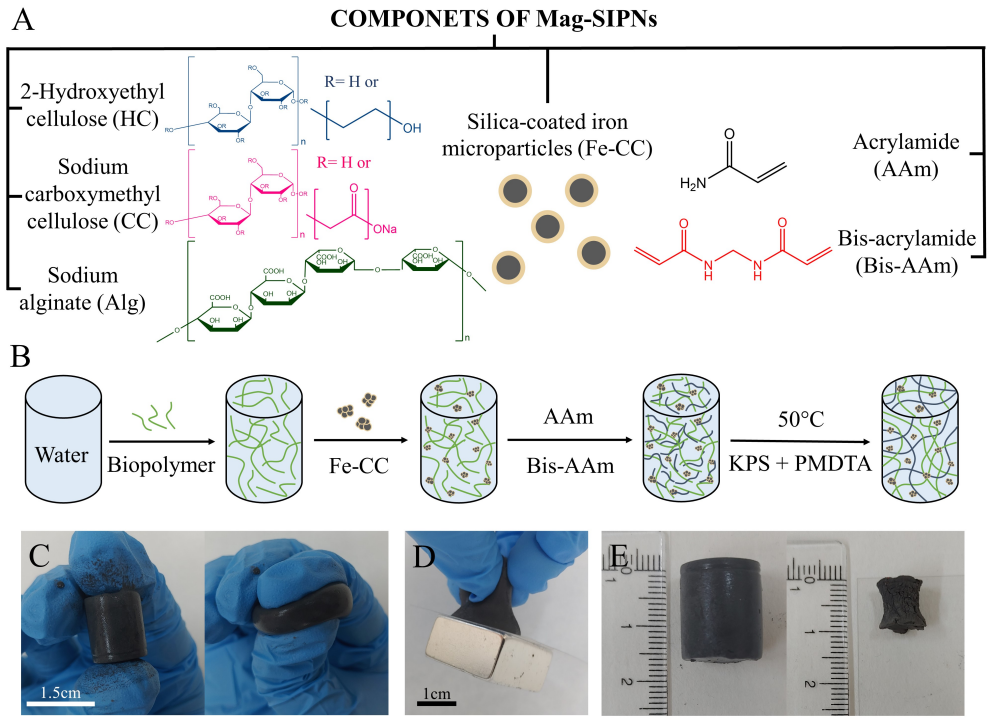

Figure 4.1: A) Chemical composition of the Mag-SIPN hydrogels. B) Preparation protocol of the Mag-SIPN hydrogels. C) High deformability of the Mag-SIPN hydrogels. D) Strong magnetic response of the Mag-SIPN hydrogels, which were able to hold a 25 × 25 × 13 mm NdFeB permanent magnet (∼ 60 g). E) Swollen (left) and dehydrated (right) Mag-SIPN hydrogel with 6.4 % w/w of Fe-CC -note that the initial content of water was 64.86 % w/w.

In Figure 4.1 B, a diagram of the preparation protocol of the Mag-SIPNs is shown. First, 1.67 % w/w water solutions of sodium alginate (Alg), 2-hydroxyethyl cellulose (HC720 and HC1300), or carboxymethylcellulose sodium salts (CChigh and CCmedium) were prepared separately. Subsequently, Fe-CC microparticles were added to the polymeric solutions. The resulting mixtures were sonicated for 15 minutes, followed by shaking (orbital rotator) until homogeneous suspensions were obtained (1 h). Afterwards, Bis-AAm and AAm were dissolved in water. The monomer (Bis-AAm/AAm) solution was then mixed with the Fe-CC microparticle suspensions for 1 h under vigorous stirring. Finally, an aqueous solution of the thermal initiator KPS (10 mg/mL) and the accelerant (PMDTA) were added to the Bis-

AAm/Aam/Fe-CC/biopolymer mixtures, and then, these mixtures were cured at 50 °C overnight. The concentrations of the compounds used were as follows: 87.89 % w/w of milli-Q water, 0.89 % w/w of biopolymer, 0.13 % w/w of Bis-AAm, 11.02 % w/w of AAm, 0.07 % w/w of KPS, and 0.11 μmol/g of PMDTA (all these concentrations are given with respect to the total mixture without particles). The Fe-CC particle concentrations were 6.4, 12.0, 17.2, 21.9, and 26.2 % w/w (with respect to the total mass of hydrogel). The final water content of the hydrogels was calculated based on these data. As an example, for a hydrogel containing 12.0 % w/w Fe-CC, the final water concentration was (100-12)×87.89/100 = 77.3432 % w/w.

4.2.3 Characterization Protocols

Characterization of Gelling Kinetics

The gelling kinetics of the Mag-SIPN hydrogels were studied by subjecting the samples to oscillatory shear stress at a constant temperature (50 ± 1 °C). A rotational rheometer (Bohlin CS-10), provided with a concentric cylindrical geometry was used. For this aim, the polymerization mixtures Fe-CC/biopolymer/AAm/Bis-AAm/KPS/PMDTA were poured into the cylinder geometry of the rheometer, and the evolution of the viscoelastic moduli were measured for an imposed oscillatory shear of constant frequency (1 Hz) and strain amplitude (0.3 %), within the linear viscoelastic region (LVR).

Characterization of Mechanical Properties

The rheological properties under oscillatory shear of the hydrogels were determined at constant temperature (25 ± 1 °C) using an MCR300 Physica Anton-Paar rheometer equipped with a plate-plate geometry of 20 mm in diameter. The LVR was determined by subjecting the hydrogels to strain amplitude sweeps at a constant frequency of 1 Hz and stepwise increasing shear strain amplitude (γ), obtaining the values of the storage (G') and loss (G'') moduli versus γ. From these curves, the characteristic values of G' and G'' corresponding to the LVR were calculated by averaging the total extension of the LVR. Afterward, the trends of G' and G'' versus frequency were obtained by performing frequency sweeps at a constant shear strain amplitude (γ_0 = 0.3 %) within the LVR and increasing the frequency from 0.1 to 10 Hz. The mechanical behavior of the hydrogels under tensile and compressive stress was determined at room temperature (25 °C) using a hybrid rheometer (Discovery HR-1, TA Instruments) and a universal testing machine (Instron 3345, Instron), respectively. For the characterization under tensile stress, samples were prepared in dog-bone-shaped molds. Before placing the samples in the instrument, their cross-sectional area was measured. Then, the samples were clamped in the geometry of the rheometer, which had a grooved surface to prevent them from slipping. Once the hydrogels

were firmly fixed in the clamps of the rheometer, a slight normal tensile axial force was applied (0.01 N) to reach a uniform starting condition for all samples and to ensure homogeneous force transmission at the beginning. During the measurements, the hydrogels were deformed at a constant rate of 50.0 μm/s until breakage. Then, from the engineering stress vs. strain curves, the tensile modulus and the tensile strain at break were obtained. The tensile modulus was calculated as the slope of the linear regression of strain versus tensile stress from a strain of 10 % to its breakage. The strain at break was obtained from the last point of the curves before the sample breakage. For measurements under compression, the materials were characterized using a plate-plate geometry with a rough surface to avoid slipping of the samples. In this case, the hydrogels were prepared with a cylindrical shape, and before measurement, the diameters of their cross-sectional areas were determined. The measurement process was carried out under the same conditions as the tensile characterization but with different directions of the force. The analysis of the results was similar to that of the tensile case, with the only difference being that the compressive modulus was determined only for strains below 20 %.

Scanning Electron Microscopy (SEM)

Samples were prepared by critical point drying and coated with a fine carbon layer. For SEM images and Energy-Dispersive X-ray spectroscopy (EDX) a Zeiss, AURIGA (FIB-FESEM) equipment was used.

Characterization of Swelling Behavior

The SIPN hydrogels were immersed in milli-Q water, and the evolution of their mass was recorded over time by extracting them from the water and determining their weight using a microbalance.

Characterization of Magnetic Behavior

Magnetization curves were measured using a magnetometer SQUID QUAMTUM DESIGN MPMS XL.

Magnetic Field-Induced Contraction of Mag-SIPN Hydrogels

Mag-SIPN hydrogels of 5 $\times$ 5 $\times$ 20 mm in size were cured as described above in adequate rectangular molds. Afterwards, the hydrogels were placed inside a reservoir of the same dimensions, and a magnetic field was applied with a 25 $\times$ 25 $\times$ 13 mm NdFeB (N40) permanent magnet. This magnet produced a field gradient of 25.8 $\pm$ 0.4 mT/mm at 0 - 8 mm from its surface and of 8.0 $\pm$ 0.3 mT/mm at 12 - 20 mm

from its surface. The contraction of each sample was video-recorded, and the linear contraction, defined as the percentage of length change ($\Delta L/L_0$) was analyzed using the open-source Tracker software.

Application as Magnetic Luminescent O_2 Sensor (ML-OSen)

The hydrogels that composed the oxygen sensor were prepared following the steps described above, using HC720 as biopolymer due to its appropriate mechanical properties and lower swelling capacity (see sections 4.3.1 and 4.3.2). One change in the protocol was required to avoid excessive swelling of the hydrogel: specifically increasing the concentration of the cross-linker agent (Bis-AAm) by a factor of four for the nonmagnetic hydrogel and by a factor of eight for the magnetic hydrogel. The sensor was composed of two different parts: a magnetic part and a nonmagnetic sensing part. First, the magnetic hydrogel with cylindrical shape was prepared with Fe-CC particles at a concentration of 26.2 % w/w . Then, a concentric cylindrical hole with a diameter of 8 mm was punctured in the ferrogel. Afterwards, a pre-gel mixture was prepared by substituting MPs by O_2-sensitive luminescent nanoparticles (Lu-NPs) at a concentration of 2.0 % w/w with respect to the total polymer mass. This mixture was poured into the hole previously punctured in the ferrogel, and the system was cured at 50 °C overnight. After gelling, the cylindrical sample was cut into disks with a thickness of 2 mm to ensure a smooth surface and good coupling with the optical fiber.

The aforementioned Lu-NPs (99 $\pm$ 7 nm of diameter) were prepared by encapsulating PtOEP into poly(styrene-co-maleic anhydride; 7 % maleic anhydride) via mini-emulsion solvent evaporation [Mistlberger et al., 2010]. First, a solution of SDS in water (0.3 mg/mL) and another one of poly(styrene-co-maleic anhydride; 7 % maleic anhydride) (105 mg/mL) and PtOEP (1.05 mg/mL) in chloroform were prepared. Both solutions were mixed at a ratio of 40:3, respectively. The biphasic mixture was cooled in an ice bath and sonicated with a high-energy probe sonicator (Branson S-450 Digital) at 50 % amplitude for 5 minutes to form a mini-emulsion. Then, the chloroform was evaporated within a few minutes under a nitrogen flow, and the maleic anhydride groups (7 %) of the Lu-NPs were hydrolyzed by adding 2 mL of NaOH 0.5 M (Lu-Nps were kept under stirring in this basic media for at least 15 minutes). Finally, the Lu-NPs were centrifuged, washed with milli-Q water, and dispersed in water at a concentration of 45 mg/mL.

Statistical Analysis

For each set of experimental conditions, at least three different samples were measured. The mean value and standard error of each quantity are provided. One-way and two-way Anova and Tukey's post-hoc (α = 0.05 in all cases) were

used to statistically compare the mean values of the magnitude under different experimental conditions, such as the natural biopolymer used and the magnetic particle concentrations. Detailed statistical comparisons are presented in Tables B.1 and B.2.

4.3 Results and Discussion

4.3.1 Mechanical Properties of Mag-SIPN Hydrogels

The nonmagnetic and magnetic SIPN hydrogels presented in this chapter were synthesized using acrylamide and N,N'-methylenebisacrylamide to form a cross-linked covalent network, along with five natural biopolymers (Table 4.1). The chemical composition of Mag-SIPNs is illustrated in Figure 4.1 A.

Table 4.1: Natural biopolymers used to synthesize the different Mag-SIPNs with the name used in the chapter and the different magnetic particles concentrations studied in each case.

Natural Biopolymer	Mag-SIPN Name	Magnetic Particles Concentration (% w/w)
Alginate (medium viscosity)	Alginate	6.4, 12.0, 17.2, 21.9, 26.2
Carboxymethylcellulose sodium salt (medium viscosity)	CCmedium	6.4
Carboxymethylcellulose sodium salt (high viscosity)	CChigh	6.4
2-Hydroxyethyl cellulose ($M_v \sim 720000$)	HC720	6.4
2-Hydroxyethyl cellulose ($M_v \sim 1300000$)	HC1300	6.4

Gelling Kinetics of Alginate Mag-SIPN Hydrogels

Firstly, the gelling kinetics of the SIPN hydrogels were studied. The presence of MPs was expected to significantly alter the kinetics. Furthermore, a long gelling time can result in the sedimentation of the microparticles before reaching the gel point, leading to the formation of nonuniform magnetic hydrogels. Therefore, achieving a high gelling rate is critical for obtaining homogeneous and reproducible Mag-SIPNs. The gelling kinetics were investigated using a Bohlin CS-10 rotational rheometer with concentric cylindrical geometry at a constant temperature of 50 $\pm$ 1 °C. The pre-gel mixtures were poured into the cylinder geometry and were subjected to oscillatory shear of constant low amplitude and frequency, monitoring the time evolution

of the storage (G') and loss (G'') moduli. The gelling kinetics of the Alginate Mag-SIPN hydrogels were investigated in relation to the concentration of both iron microparticles and N,N,N',N",N"-Pentamethyldiethylenetriamine (PMDTA; polymerization accelerant) [Haider et al., 2015]. Typical curves demonstrate the initial liquid state of the mixtures ($G' < G''$), followed by a sharp increase of both viscoelastic moduli and, finally, a plateau region with $G' > G''$, corresponding to well-formed hydrogels (Figure 4.2 A).

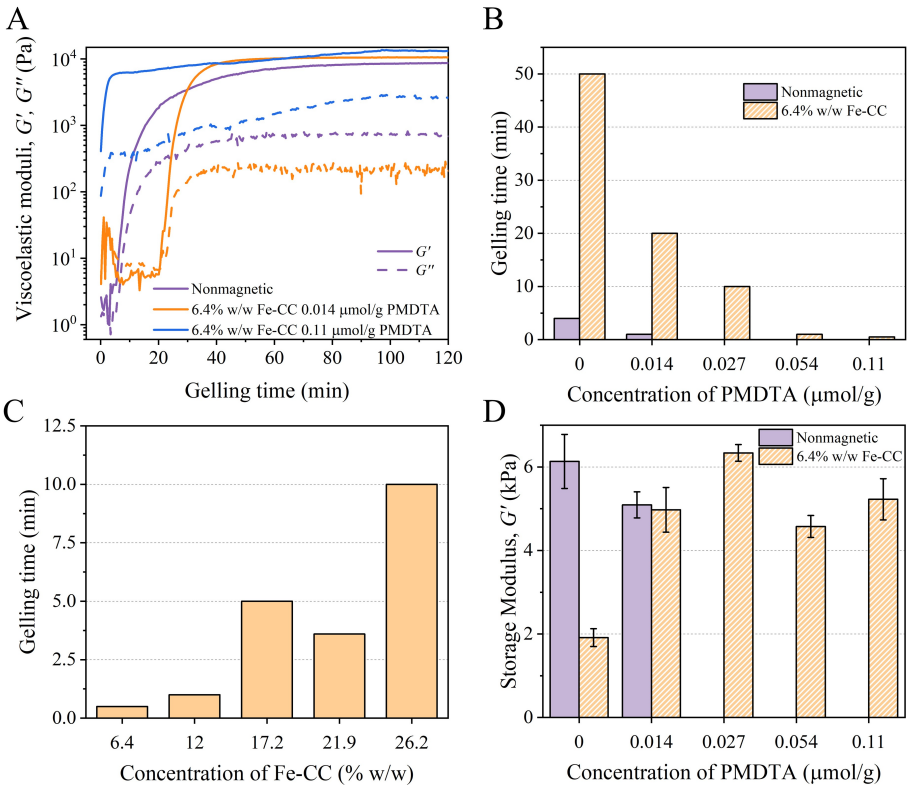

Figure 4.2: Gelling kinetics A) and gelling time B) of Alginate Mag-SIPN hydrogels at various concentrations of iron microparticles (Fe-CC) and accelerant (PMDTA). C) gelling time of Alginate Mag-SIPN hydrogels as a function of the concentration of iron microparticles (with a fixed concentration of PMDTA: 0.11 µmol/g). D) Steady-state values of the storage modulus within the linear viscoelastic region for several Alginate SIPN hydrogels at different PMDTA concentrations. Note that A, B, and C only show one representative measurement for each experimental condition.

The gel point is usually determined as the point at which G' consistently becomes higher than G'', although a more general method to detect the gel point is the Winter-Chambon criterion [Winter, 1987, Chambon and Winter, 1987]. In this study, we identified the gel point as the point at which a sharp increase in the viscoelastic moduli occurred because the crossover of G' and G'' was not observed in some cases, and this criterion yielded values similar to the crossover when applicable. We noticed a trend of the gelling time decreasing with an increase in the amount of the

accelerant (PMDTA), while the addition of MPs significantly increased the gelling time (Figure 4.2 B and C). Therefore, to maintain a fast-gelling process and prevent undesired particle settling, a larger amount of PMDTA was required as the particle content increased. However, depending on the molecular weight of the biopolymer, a slight gradient in concentration of iron particles along with the hydrogel height was unavoidable (refer to section 4.3.2).

The accelerant did not appear to have a significant effect on the final mechanical properties of nonmagnetic Alginate SIPN hydrogels, as quantified by the values of G' (Figure 4.2 D). However, in the case of Mag-SIPNs, PMDTA had a notable impact on the final mechanical properties, and a minimum concentration of PMDTA was required to achieve a storage modulus comparable to that of nonmagnetic SIPN hydrogels. It should be noted that the value of G' decreased by a factor of 3 for hydrogels containing 6.4 % w/w of iron microparticles, with respect to nonmagnetic hydrogels (Figure 4.2 D). One hypothesis for this behavior is that the gravitational settling of iron microparticles disrupted the polymerization process, requiring rapid gelling to prevent this undesirable effect and to obtain well-formed magnetic hydrogels with optimal mechanical properties. Following this result, a PMDTA concentration of 0.11 µmol/g was generally used.

Mechanical Characterization of Alginate Mag-SIPNs

A comprehensive characterization of the mechanical properties of fully gelled Alginate Mag-SIPN hydrogels under different stresses (oscillatory shear, compressive, and tensile stresses) was conducted. Strain amplitude sweeps (Figure B.2 A) demonstrated the typical behavior of a gel-like viscoelastic material, with a plateau region observed for small shear strain amplitudes where $G' > G''$. This plateau-like region defines the linear viscoelastic region (LVR). At higher strain amplitudes, the storage modulus decreased while the loss modulus initially sharply increased, followed by a subsequent decrease within a region for which $G' < G''$, corresponding to the nonlinear viscoelastic region. This indicates a breakage of the internal structure of the material. Furthermore, the viscoelastic moduli were analyzed as a function of frequency for shear strain amplitude values within the LVR (Figure B.2 B). Once again, a typical gel-like behavior was observed, characterized by values of the viscoelastic moduli that are independent of frequency, with $G' > G''$.

The effect of incorporating MPs into Alginate SIPN hydrogels was also investigated. Figure 4.3 A and B present the average values of the viscoelastic moduli within the LVR for varying concentrations of iron microparticles ranging from 6.4 to 26.2 % w/w with a fixed amount of accelerant. Consistent with the results shown in Figure 4.2 D, a decrease in the viscoelastic moduli was observed as the MPs content increased. Although the decrease in G' was not statistically significant when adding up to 6.4 % w/w of MPs compared with their nonmagnetic counterpart, a statistically

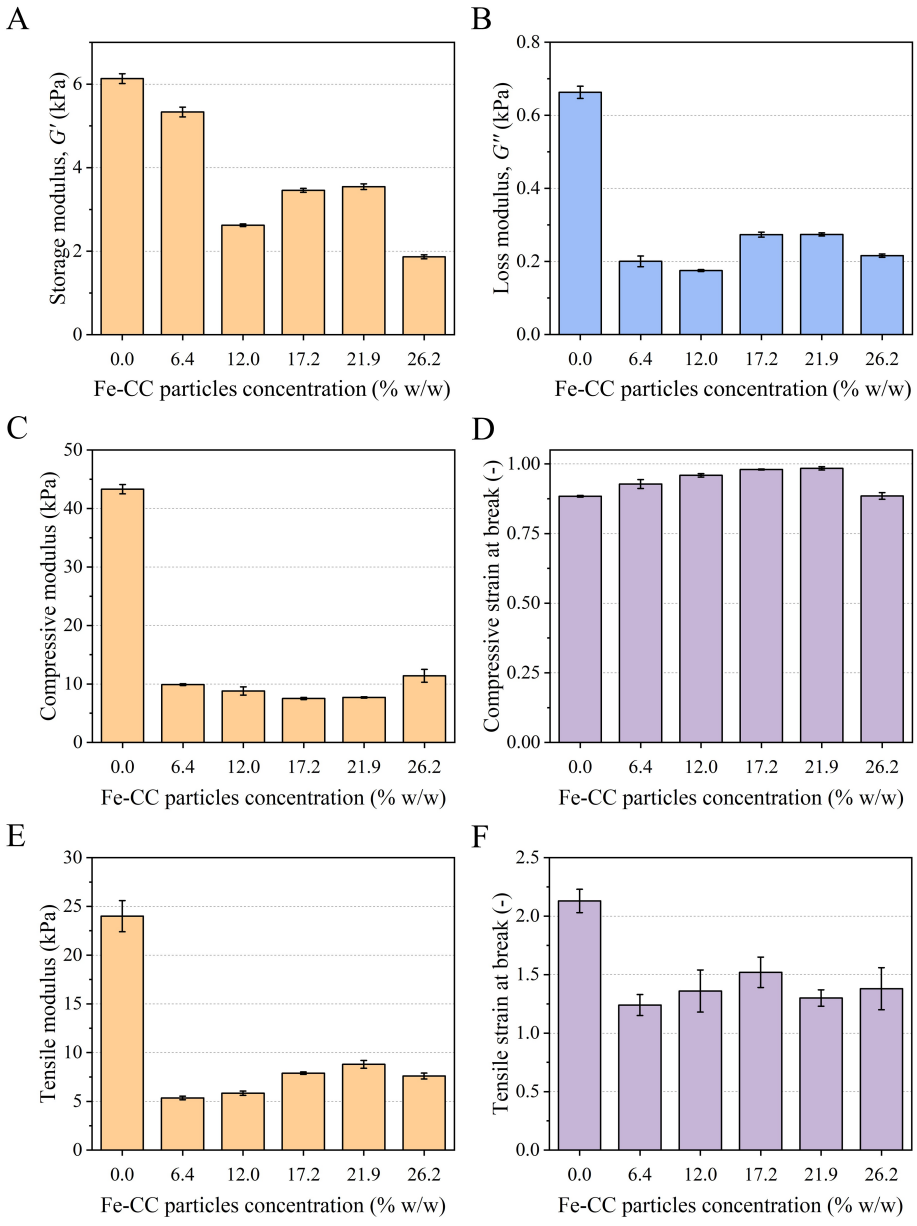

Figure 4.3: Mechanical properties of Alginate Mag-SIPN hydrogels with a fixed amount of accelerant PDMTA (0.11 µmol/g) and iron microparticle (Fe-CC) concentrations in the range 0 % to 26.2 % w/w. Storage modulus A) and loss modulus B) corresponding to the LVR for oscillatory shear measurements. Elastic modulus C) and strain at break D) obtained under compressive stress. Elastic modulus E) and strain at break F) obtained under tensile stress.

significant decrease in G' was observed for hydrogels containing 12.0 to 26.2 % w/w of MPs. This indicates that the presence of MPs disrupted the polymerization process, thereby affecting the final mechanical properties of the hydrogels.

Alginate Mag-SIPN hydrogels were also characterized under compressive and tensile stress (*cf.* Figure B.3). As observed, when iron microparticles were added to the hydrogel, a considerable decrease in the elastic moduli occurred under both compressive and tensile stress (Figure 4.3 C and E), indicating a decrease in the stiffness of the materials. Furthermore, two distinct behaviors were observed depending on the applied stress. For the compressive modulus, for particle concentrations of 17.2 and 21.9 % w/w, there was a statistically significant minimum (8.42 $\pm$ 0.19 kPa and 8.79 $\pm$ 0.25 kPa, respectively). The observed increase in compressive modulus upon further increasing the particle concentration to 26.2 % is likely due to the crowding of particles. This crowding effect should generate robust compression resistance, providing a plausible explanation for the observed increase. On the contrary, for measurements under tensile stress, the opposite situation was observed, with the tensile modulus exhibiting a statistically significant maximum (8.8 $\pm$ 0.4 kPa) at 21.9 % w/w particle concentration. Remark also that compressive modulus values were always higher than under tensile stress.

Another relevant mechanical parameter is the maximum strain that the hydrogels can withstand before breakage, which is known as the strain at break. For Alginate Mag-SIPN hydrogels (Figure 4.3 D and F), two different behaviors were observed depending on the type of applied stress. For measurements under compressive stress (Figure 4.3 D), there was mainly a slight increase in strain at break with iron microparticle content, with a statistically significant maximum for 17.2 and 21.9 % w/w –remark the enormous compressibility of the Mag-SIPN hydrogels that can be compressed until a maximum of approx. 98 % of their initial height before breakage. For measurements under tensile stress, the reverse behavior was observed, with a substantial decrease in strain at break (approximately from 210 % to 140 %) when particles were included in the formulation, although there were not statistically significant differences between samples containing MPs. This difference in behavior when samples were subjected to tensile or compressive stress was likely related to the disruption of the polymer network by the embedded particles, which were expected to create ”holes” in the polymer network (refer to section 4.3.2). Measurements under tensile stress are more sensitive to these defects in the polymer network, whereas slight enhancements under compressive stress may be due to the presence of iron microparticles opposing compression. In the case of hybrid fibrin-agarose hydrogels, similar discrepancies were observed, with the tensile modulus and stress at break under tensile stress decreasing with increasing agarose content, whereas the compressive modulus increased with agarose content [Scionti et al., 2013]. This result was related to the high water-holding capacity of agarose.

Mechanical Properties of Biopolymers Mag-SIPNs

To further modulate the mechanical properties of Mag-SIPN hydrogels, alginate was replaced by other biopolymers with different physicochemical properties.

Considering the results obtained for Alginate Mag-SIPN hydrogels (Figure 4.2 and 4.3), Mag-SIPN hydrogels based on other biopolymers were initially synthesized with concentrations of iron microparticles and PMDTA of 6.4 % w/w and 0.11 μmol/g, respectively. In the case of nonmagnetic hydrogels, an increase in the storage modulus with the molecular weight of the polymer was observed for systems based on hydroxyl cellulose (HC720 or HC1300), although no statistically significant differences with respect to alginate-based hydrogels were obtained (Figure 4.4 A and B). For hydrogels based on cellulose charged with carboxyl groups (CCmedium or CChigh), a remarkable decrease in the storage modulus (weakening) was observed with respect to the other nonmagnetic hydrogels. In all cases, the storage modulus decreased with the addition of MPs, with the highest value (statistically significant) obtained for Alginate Mag-SIPN hydrogels, whereas no statistically significant differences were obtained for the different cellulose-based Mag-SIPN hydrogels.

Hydrogels based on celluloses were also characterized under compressive and tensile stresses (see Figure 4.4 C to E). For nonmagnetic hydrogels, the highest value of the compressive modulus was obtained for the systems based on the polymer HC1300 or alginate, whereas a substantial decrease was observed for the systems based on the other biopolymers (Figure 4.4 C). A different situation was observed for the measurements under tensile stress, with the hydrogels based on alginate, CCmedium, and CChigh exhibiting the highest tensile modulus (Figure 4.4 E). Furthermore, the introduction of MPs resulted in substantial reductions of the elastic moduli in all cases (Figure 4.4 C and E). For the strain at break, interestingly, no statistically significant differences were observed for the different nonmagnetic hydrogels, although slightly higher values were obtained for hydrogels based on cellulose than for hydrogels based on alginate under tensile stress (Figure 4.4 D and F). The addition of MPs caused no substantial changes in this quantity under compressive stress (Figure 4.4 D), whereas it resulted in a decrease in measurements under tensile stress (Figure 4.4 F).

To summarize, the mechanical performance of the SIPN hydrogels (magnetic and nonmagnetic) depends not only on the type of biopolymer but also on their mean molecular weight. Furthermore, some general trends were demonstrated regarding the inclusion of MPs in the formulation, which made it possible to conclude that Mag-SIPN hydrogels showed smaller values of storage and elastic moduli while maintaining a considerable high stretchability and compressibility, as compared with non-magnetic SIPN hydrogels. This combination of lower elastic moduli with high stretchability and compressibility is ideal for applications that requires the maximization of the deformation under external stimuli, such as soft robots and actuators with remote control [Liu et al., 2020b].

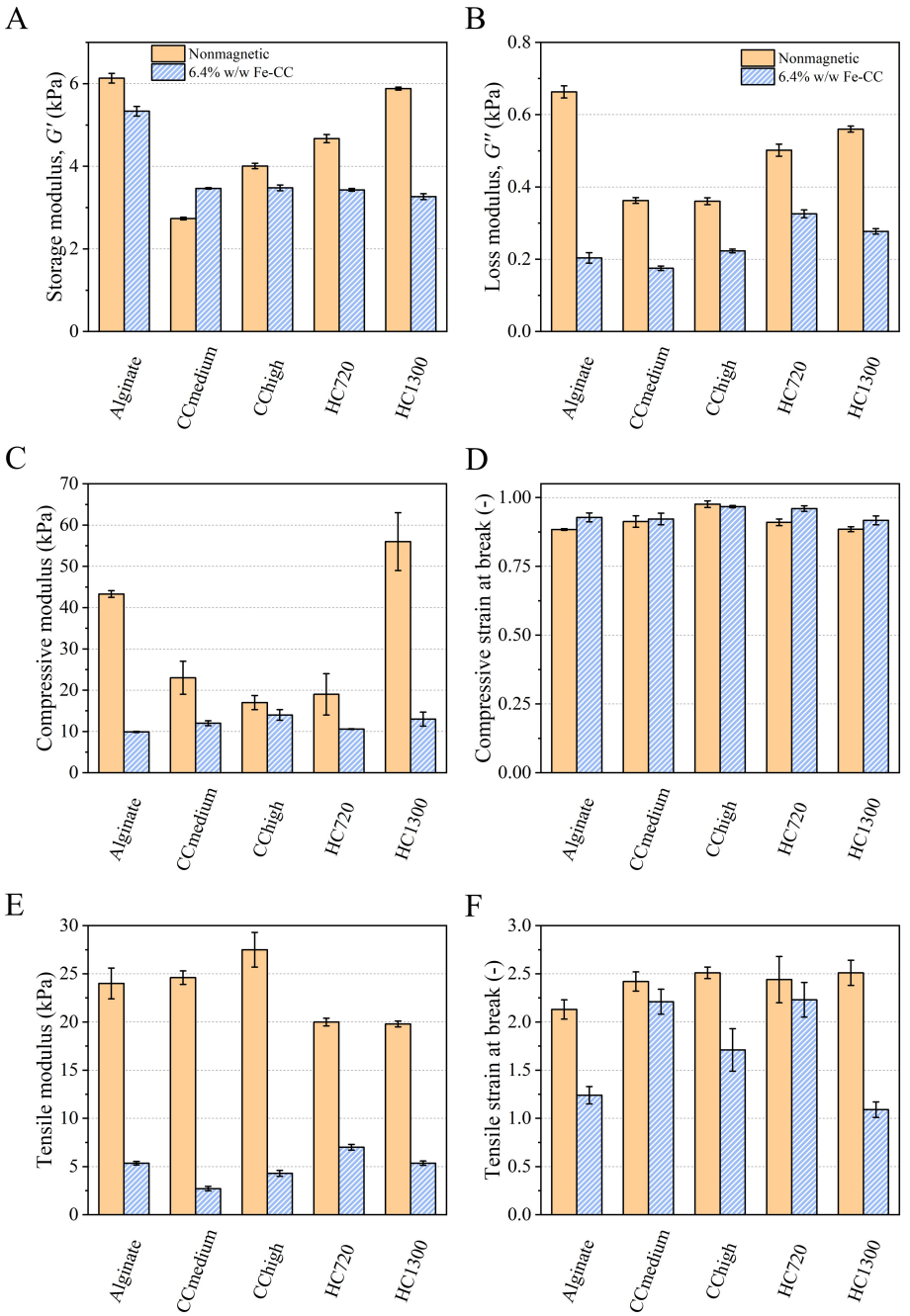

Figure 4.4: Mechanical properties of SIPN hydrogels (nonmagnetic and magnetic) based on different linear biopolymers with a fixed amount of accelerant PDMTA (0.11 µmol/g). Storage modulus A) and loss modulus(B) corresponding to the LVR for oscillatory shear measurements. Elastic modulus C) and strain at break D) obtained under compressive stress. Elastic modulus E) and strain at break F) obtained under tensile stress.

4.3.2 Morphological and Magnetic Characterization of Mag-SIPN Hydrogels

Mag-SIPN hydrogels were macroscopically homogeneous, had a soft consistency, and were easily manipulated without fracture (Figure 4.1 B). From the viewpoint of MP distribution, a macroscopic gradient in particle concentration was unavoidable for some of the Mag-SIPN hydrogels (Figure 4.5 A. It is interesting to note that Mag-SIPN hydrogels based on cellulose with high molecular weight (CChigh and HC1300) did not show any appreciable gradient in particle concentration, whereas those based on polymers of low molecular weight (HC720 or alginate) showed a visible gradient in particle concentration. Remarkably, nevertheless, not only the molecular weight was important since Mag-SIPNs based on CCmedium (medium molecular weight) showed the highest gradient in magnetic particle concentration.

Scanning electron microscopy (SEM) of Mag-SIPN hydrogels (Figure 4.5 B and B.4) showed the presence of clusters of MPs surrounded by polymeric materials (see for example the area highlighted by a red circle in Figure 4.5 B). The inclusion of these particles in the hydrogel matrix produced a slight increase in the porosity of the network (Figure B.5), possibly due to the interference of these particles with the polymerization process and because part of the polymeric material was used to coat the particles and not to form the three-dimensional network. This effect was not observed in hydrogels that did not contain MPs (Figure 4.5 C) in which a more homogeneous network and small filaments were observed.

The swelling behavior of nonmagnetic and magnetic SIPN hydrogels was studied by measuring their mass ($M_H(t)$)) over time after immersion in milli-Q water (Figure 4.5). The swelling degree was quantified using the following equation:

$$Q(t) = \frac{M_H(t) - M_H(t=0)}{M_H(t=0)} \tag{4.1}$$

Differences in swelling degree were observed when using different biopolymers; hydrogels based on alginate or carboxyl cellulose showed higher water absorption than hydrogels based on hydroxyl cellulose, independently of the molecular weight, which did not appear to play any significant role. This should be due to the presence of charges in hydrogels based on alginate or carboxyl cellulose due to the carboxyl groups, whereas hydrogels based on hydroxyl celluloses are neutral, which make its degree of swelling smaller. Note also that water absorption was clearly reflected in the volume of the hydrogels, which notably increased with increasing mass in these experiments (Figure B.6). The most relevant result of the swelling experiments was the much greater swelling demonstrated by magnetic hydrogels (Q values up to approx. 28) as compared with not magnetic hydrogels (Q values up to approx. 2) (compare Figure 4.5 D and E). Furthermore, while the water absorption of the nonmagnetic hydrogels mainly saturated within the first 24 h, the magnetic hydrogels

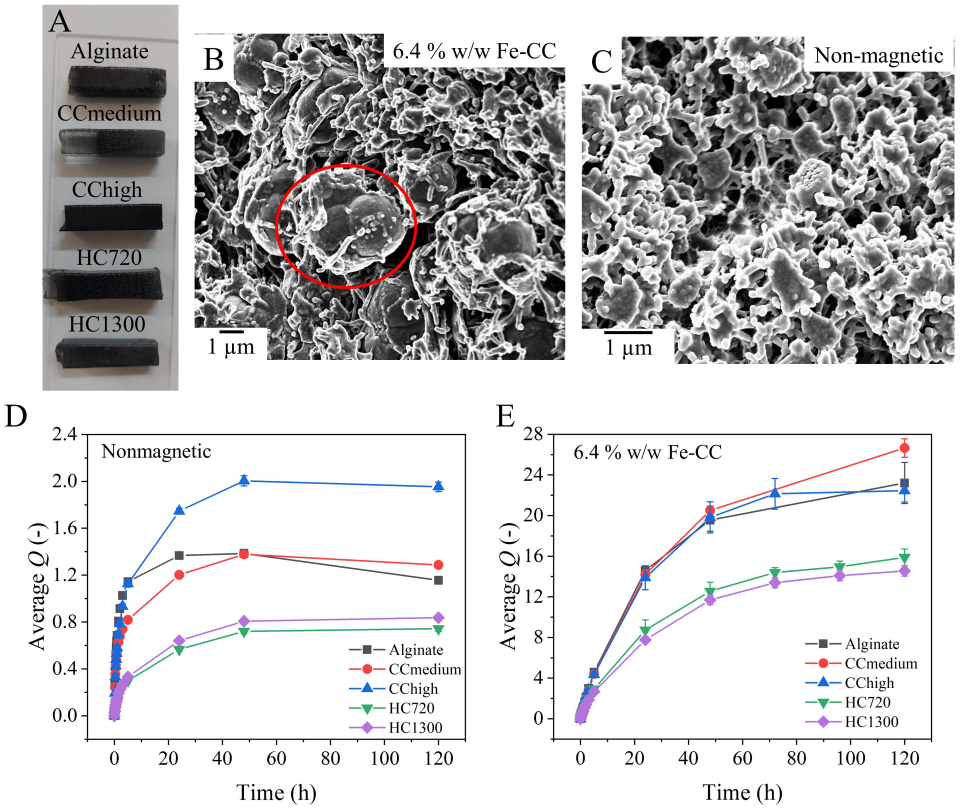

Figure 4.5: A) Mag-SIPN hydrogels containing 26.4 % w/w of MPs. A particle gradient can be observed in some cases, being more noticeable in CCmedium. B) and C) SEM images of the internal structure of HC720, with a concentration of MPs of 6.4 % w/w and without MPs, respectively. Note that in B) MPs are marked with a red circle. D) and E) Swelling behavior as a function of time of immersion in milli-Q water, D) for non-magnetic SIPN hydrogels and E) for Mag-SIPN hydrogels containing 6.4 % w/w concentration of MPs.

maintained their ability to absorb water for 48 - 72 h. An increase in swelling of polymeric hydrogels when particles were included in the network was previously reported by other authors. For example, Bonhome-Espinosa et al. [Bonhome-Espinosa et al., 2017] connected the enhancement of the swelling degree of fibrin-based magnetic hydrogels with the formation of particle clusters that served as knots in the polymeric network, resulting in a more opened structure.

The magnetization curves of the Mag-SIPN hydrogels demonstrated typical soft ferromagnetic behavior with negligible remanence and coercivity, similar to that of the powder of iron microparticles, although with much smaller maximum magnetization (Figure 4.6 A), as expected due to the extensive property of magnetization. When normalized by the maximum magnetization to account for differences in particle concentrations (Figure 4.6 B), no significant differences were observed between the samples or with respect to MPs.

4.3.3 Magnetic Field-Induced Contraction of Mag-SIPN Hydrogels

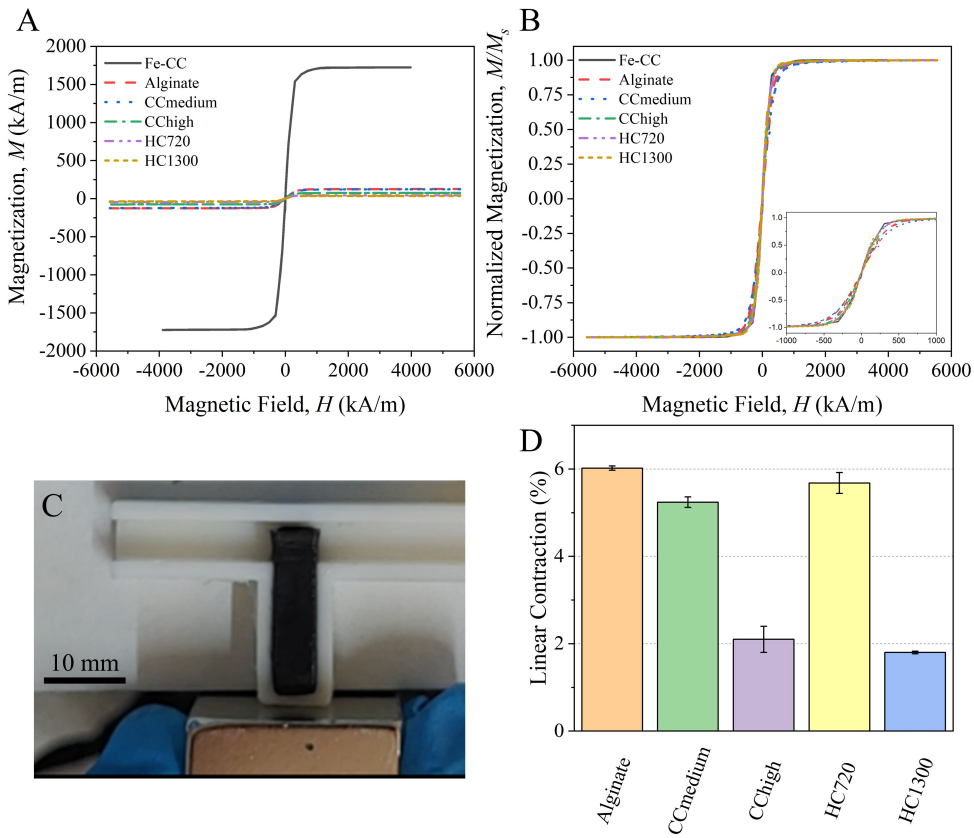

Figure 4.6: A) Magnetization curves of the iron microparticles (Fe-CC) and the different Mag-SIPN hydrogels. B) Normalized magnetization curves for comparison purposes. C) Experimental setup used to measure de deformability of the Mag-SIPNs placed in a reservoir. D) Linear contraction of the Mag-SIPN hydrogels under the magnetic field gradient generated by a permanent magnet.

As previously mentioned, one of the main areas of interest in magnetic hydrogels is their application in soft robots and actuators. For these applications, a strong, reversible, and reliable response to a magnetic field is required. In this study, the magnetic responsiveness of ferrogels was evaluated by compressing them under the action of a magnetic field gradient generated by a permanent magnet. In these experiments, the different magnetic hydrogels were placed in a reservoir connected laterally to a main canal that was blocked by the hydrogels in the absence of an applied magnetic field. To measure the compression of the hydrogels, a magnet was placed close to the hydrogels, which were contracted due to their strong magnetic character and high compressibility (*cf.* Figure 4.6 C and D). When the magnet was removed, the magnetic hydrogels tended to return to their natural, more elongated state. For more details about the experimental setup, see the work by Vazquez-Perez et al. [Vazquez-

Perez et al., 2021]. In contrast to this previous work, we used a larger NdFeB magnet, which generated a magnetic field that decayed more slowly with the distance from the magnet surface (Figure B.7) and that, consequently, resulted in a larger contraction of the magnetic hydrogels. To maximize the contraction under the action of the applied magnetic field, the hydrogels were placed with their ends with a lower concentration of particles (when there was appreciable gradient in particle concentration) close to the magnet [Zhao et al., 2011]. We evaluated in this experiment Mag-SIPN hydrogels with a concentration of MPs of 26.2 % w/w. For comparison, we also evaluated single-network magnetic alginate hydrogels containing the same concentration of MPs as described in Ref. [Vazquez-Perez et al., 2021]. It should be noticed that the Mag-SIPN hydrogels of the present work showed better magneto-mechanical response than the single-network alginate hydrogels, which for the strong magnetic field gradient of the present work showed no contraction reversibility after only one cycle of application/removal of the magnetic field (Figure B.8) –remark the stronger magnetic field gradient of the present work at the end of the magnetic hydrogels opposite to the magnet surface, as compared with the one used in Ref. [Vazquez-Perez et al., 2021] (Figure B.7). Results demonstrated large linear contraction values of the Mag-SIPN hydrogels under an applied magnetic field gradient (Figure 4.6 D). Furthermore, the Mag-SIPN hydrogels based on biopolymers of lower molecular weight contracted more in response to the applied magnetic field than the hydrogels based on biopolymers of higher molecular weight. This result is consistent with the compressibility characterization (Figure 4.4). Finally, it is remarkable that Mag-SIPN hydrogels demonstrated complete reversibility in their magnetomechanical response even after 50 cycles of application/removal of the magnetic field.

4.3.4 Evaluation of a Cellulose Mag-SIPN as a Magnetic Luminescent O_2 Sensor (ML-OSen)

Optical sensors are interesting alternatives to electrochemical sensors for monitoring biological parameters such as O_2, among others [Narayanaswamy and Wolfbeis, 2004]. In contrast to the most common electrochemical sensors, optical sensors are cost-effective and can be read without physical contact [McDonagh et al., 2008, Orellana and Moreno-Bondi, 2005, Wolfbeis, 1991]. However, most luminescence oxygen-responsive probes are highly hydrophobic; thus, over the last few decades, they have been widely encapsulated in synthetic hydrophobic polymers [Choi et al., 2016, Mistlberger et al., 2009, Medina-Castillo et al., 2009]. One main problem with these sensors, when they are intended to work in liquid environments, is fixing them to be able to read luminescent signals from the outside of the liquid container. This problem can be minimized by incorporating MPs into the sensing material [Mistlberger et al., 2009,Medina-Castillo et al., 2009,Mistlberger et al., 2008, Chojnacki et al., 2007]. Within this context, in this section we report a novel hydrogel luminescent oxygen sensor (based on phosphorescence quenching) fabricated with a

natural biopolymer that can be fixed thanks to its strong magnetic response. Because embedded MPs can dramatically affect the optical properties of the hydrogel due to their dark color (filter effect and self-absorption of luminescence emission) [Medina-Castillo et al., 2009], we designed and fabricated a disk-like Mag-SIPN hydrogel in which the inner circular region (sensing zone) was free of MPs and sensitive to O_2 by quenching of luminescence, and the outer hydrogel ring contained iron microparticles (magnetic responsive zone) (Figure 4.7 A). To introduce O_2-sensig properties in the inner SIPN hydrogel (sensing zone), O_2-sensitive luminescent nanoparticles (Lu-NPs) were previously prepared by encapsulating platinum octaethylporphyrin (PtOEP; luminescent O_2 probe; λ_{exc} = 380 nm, λ_{em} = 650 nm) into poly(styrene-co-maleic anhydride; 7 % maleic anhydride, M_w = 80000 Da) by mini-emulsion solvent evaporation [Mistlberger et al., 2010]. Then, the Lu-NPs were dispersed into the prepolymerization mixture of the inner SIPN hydrogel (sensing zone).

The hydrophobic nature of Poly(styrene-co-maleic anhydride) nanoparticles (Lu-NPs) prevents them from leaking into aqueous environments. Therefore, the anhydride groups of Lu-NPs (7 %) were previously hydrolyzed in basic media to introduce a negative charge (COO-) on their surface (Z-potential of hydrolyzed Lu-NPs was 60.0 $\pm$ 0.6 mV). After hydrolysis, the Lu-NPs were easily dispersed into the aqueous pre-gel. To manufacture the ML-OSen, the neutral biopolymer HC720 was selected to avoid aggregation due to the repulsion between negatively charged Lu-NPs and negatively charged alginate and carboxymethylcellulose, in addition to its mechanical properties and low swelling degree. Furthermore, for the fabrication of the ML-Osen, a higher cross-linker concentration was used for both the nonmagnetic SIPN hydrogel circle and the Mag-SIPN hydrogel ring, to avoid an excessive swelling, which could be detrimental to the magnetic and O_2-sensing responses (refer to section 4.2.3).

To measure the oxygen concentration in an aqueous solution from the outside of the liquid container, the fabricated ML-OSen was fixed by a magnetic field generated by an array of six block magnets (magnetic collector) placed around the optical fiber probe with a diameter of 0.5 mm, which was used for the calibration of the O_2 sensor (Figure 4.7 B and C). To determine the sensitivity and reversibility to oxygen in ML-OSen, the variation in the luminescence intensity of the inner SIPN hydrogel (sensing zone; see Figure 4.7) vs. the oxygen concentration was measured [Medina-Castillo et al., 2011]. The optical fiber probe was coupled to the homemade magnetic collector and connected to a high-resolution multi-led spectrometer. To perform measurements with this setup (see Figure B.9), the ML-OSen was introduced into a quartz cuvette (1.5 cm thick, 12 cm wide and 10 cm high) containing 100 mL of water. Then, the ML-OSen was attracted and fixed on the wall of the cuvette by the magnetic field generated by the array of magnets, and the luminescence intensity for each O_2 concentration was recorded. The different O_2 concentrations were established by bubbling into the solution a gas flow with four different percentages of O_2 balanced in N_2. Results of measurements demonstrated an almost linear correlation between

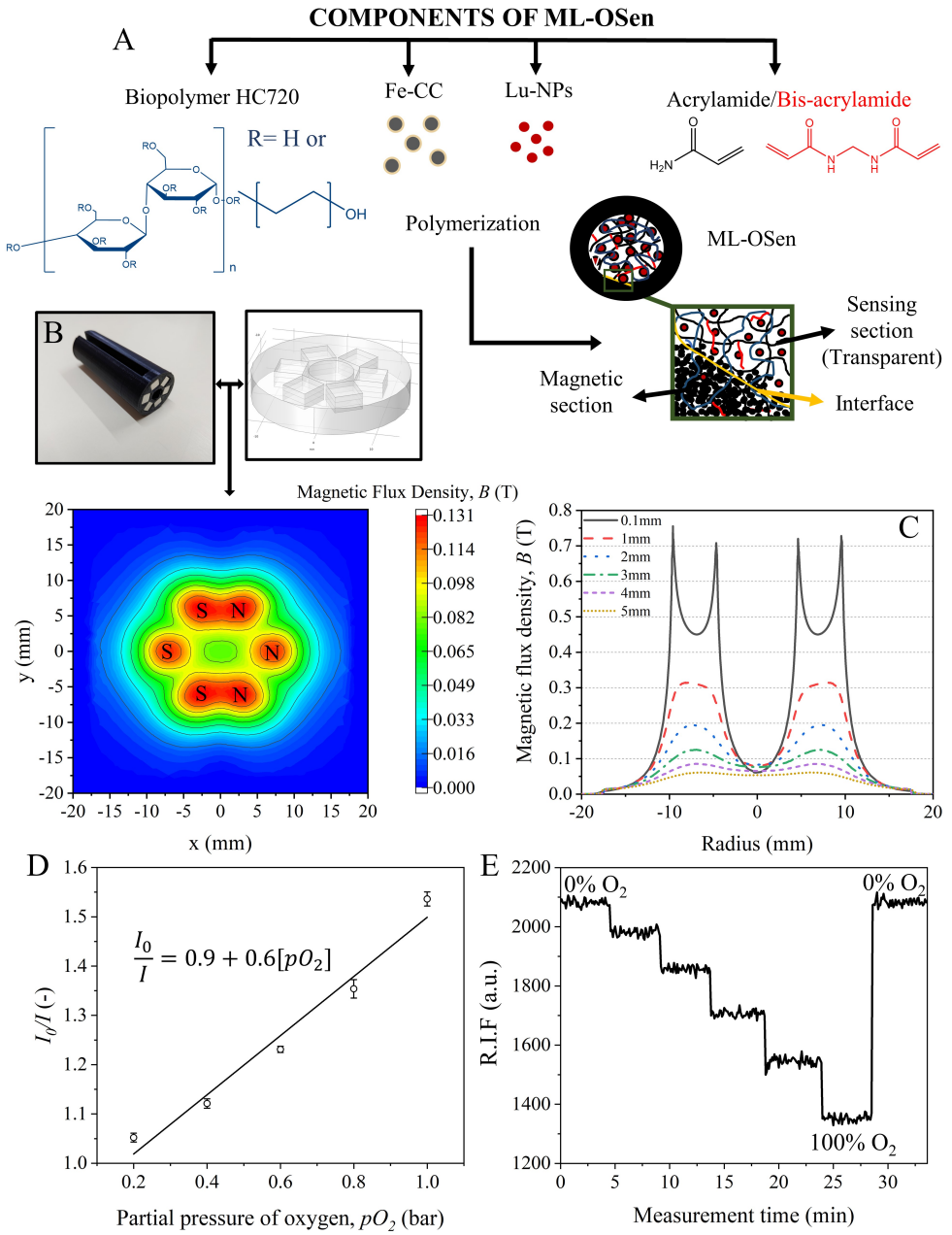

Figure 4.7: A) Composition and structure of the magnetic luminescent O_2 Sensor (ML-Osen). B) Structure of the magnetic collector and COMSOL simulation of the resulting magnetic field on a plane 3 mm above the surface of the collector. C) COMSOL simulation of the resulting magnetic field along a line at different heights above the surface of the collector. D) Stern-Volmer calibration and E) relative intensity of fluorescence (R.I.F.) vs. time.

the luminescence intensity expressed as the ratio between the intensities (I_0/I, being I_0 the intensity in absence of O_2 and I the intensity in the presence of O_2) as a function of the partial pressure of oxygen (pO_2) (Figure 4.7 D). The reversibility (Figure 4.7 E), linear correlation between I_0/I and pO_2, and stability make this proof-of-concept sensor suitable for reliable measurements of the O_2 concentration.

4.4 Conclusions

In conclusion, we have reported novel magnetic hydrogels consisting of iron microparticles dispersed in semi-interpenetrating polymer networks (SIPNs) based on a cross-linked network and five different natural biopolymers. We found that the high mechanical compliance and toughness of the SIPNs made it possible to accommodate a high load of MPs without a substantial weakening of the mechanical properties of the resulting magnetic SIPN hydrogels (Mag-SIPNs), although a minimum amount of accelerant was needed to minimize particle settling during gelling. The resulting Mag-SIPN hydrogels demonstrated ideal mechanical properties for smart actuators and sensors with remote control by magnetic field. Specifically, their rather low elastic moduli (both under tensile and compressive stresses) and viscoelastic moduli, together with extremely large compressibility and stretchability values, are optimum for maximizing the magneto-mechanical response of Mag-SIPN hydrogels under an applied magnetic field. Furthermore, the presence of MPs surprisingly enhanced the swelling capacity of the Mag-SIPN hydrogels. We also reported the compression of the Mag-SIPN hydrogels under a magnetic field gradient generated by a permanent magnet and observed considerably large compression values, as well as perfect reversibility during many cycles of application/removal of the magnetic field. The excellent performance and reversibility of the Mag-SIPN hydrogels paves the way for promising practical applications of these magnetic hydrogels as active parts with remote magnetic control in valve applications for microfluidic or gas devices, or even electromagnetic devices [Wang et al., 2020, Lin et al., 2020, Haefner et al., 2018, Mazaheri et al., 2018], given the critical relevance of valving and the attractive ability to precisely control valves for disposable biochip applications [Mohan et al., 2011, Oh and Ahn, 2006, Lu et al., 2006, Kovacs, 1998]. Finally, we reported the design and evaluation of a magnetic luminescent oxygen sensor based on the Mag-SPNs hydrogels. Owing to the strong magnetic character of these hydrogels, this sensor solves the problem of the lack of fixation in the measurement cell, which usually prevents reliable reading of optical signals. Considering that oxygen plays a vital role in cellular and enzymatic processes, real-time monitoring of the O_2 concentration in the internal microenvironment of natural hydrogels could be crucial [Bigdeli et al., 2017, Borisov and Wolfbeis, 2008, Koo et al., 2004, Xu et al., 2001].

Chapter 5.
Evaluation of Magnetic Semi-Interpenetrating Polymer Networks as Soft Actuators

5.1 Introduction

As mentioned in previous chapters, interesting and cutting-edge applications of ferrogels are related to the field of soft robots and actuators [He et al., 2023, Vazquez-Perez et al., 2021, Goudu et al., 2020, Liu et al., 2020b]. The advantages of these materials over conventional materials include their softness, manipulation without direct contact, lack of wires and electric circuits, general biocompatibility, and versatility. Nevertheless, they have some major drawbacks that are currently under intense research, such as their programmability, although this does not diminish their potential. The aim of this chapter is to evaluate ferrogels as two separate soft actuators, both based on the SIPN hydrogels composed of acrylamide and biopolymers, which were studied in Chapter 4. In this case, different types of particles, such as Fe-CC microparticles, micrometric flakes of an alloy, and neodymium-iron-bore (NdFeB) microparticles were used as magnetic phase.

The first part of this chapter focuses on the evaluation as a torsional actuator previously applied to alginate ferrogels [Vázquez Pérez, 2024]. In this case, Fe-CC particles and permalloy flakes were used to prepare cylindrical ferrogels. During the gelling process, a uniform field was applied in order to align the particles into chain-like structures contained in parallel planes perpendicular to the axis of the cylinder. This system was compared with the results from a theoretical model [Vázquez Pérez, 2024] that predicts the actuation of a magnetically anisotropic ferrogel under a uniform magnetic field when one end of the cylinder is fixed while the other is free to rotate. By fixing one end at different angles and changing the magnetic field strength, the torsion of the actuator was controlled.

In the second part of this chapter, the SIPN ferrogel containing NdFeB particles is designed as a multi-stimuli programmable actuator. In this case, two stimuli are exploited: the magnetic response due to the MPs and the swelling capacity of the acrylamide network. First, these ferrogels were prepared by partially cross-linking the alginate network via the diffusion of Ca^{2+} ions. This resulted in an cross-linking gradient, which translated into the folding of the material when swollen. This folding of the polymeric matrix can be recorded via the magnetization of the NdFeB particles. After reducing the swelling of the ferrogel, which recovers its unfolded state, the folded state can be obtained by applying a uniform magnetic field to the material, which produces internal torques in the polymeric matrix due to the tendency of the magnetic moments of the magnetized NdFeB particles to align in the field direction.

5.2 Torsional Actuator

5.2.1 Theoretical Model

Consider a ferrogel in the form of a high aspect ratio cylinder whose MPs have been structured by a uniaxial field applied perpendicular to its cylindrical axis during gelling. If a uniaxial field is applied to this composite perpendicularly to its cylindrical axis, the particle chains formed during the gelling process tend to align with the applied field so that the composite will rotate to do so. If one end of the ferrogel is fixed, the whole material is unable to rotate; therefore, the field will induce a significant torsional deformation on the free end of the cylinder, whose extent will depend on the angle θ that the chains at the fixed end make relative to the applied field Figure 5.1.

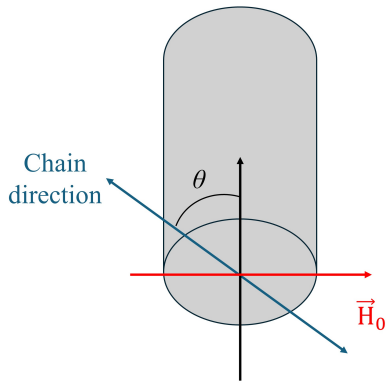

Figure 5.1: The angle θ and the direction of the field that causes actuation are shown for the ferrogel cylinder that was structured by a uniaxial field during the gelling process.

A theoretical model for this actuator was reported in a previous work [Vázquez Pérez, 2024]. This model, based on the balance between elastic and magnetic energies, analyzes the torque per unit length, $T(z)$, along the length of a cylinder, L, with anisotropic magnetic properties in planes perpendicular to its axis. Based on these assumptions, the torsional deformation of the ferrogel cylinder is given by:

$$\frac{d\theta(z)}{dz} = \frac{2}{R^2 G}\mu_0 H_0^2 (A_\parallel - A_\perp) \int_z^L sin(2\theta(z'))dz' \tag{5.1}$$

, where G is the shear modulus of the ferrogel, μ_0 is the vacuum magnetic permeability, H_0 is the strength of the applied magnetic field, and $A_\parallel$ and $A_\perp$ are effective parallel and perpendicular susceptibilities given by $\chi_\parallel/(1+n\chi_\parallel)$ and $\chi_\perp/(1+n\chi_\perp)$, respectively, where n is the demagnetization factor (around 0.5 for cylindrical samples).

This integro-differential equation is nontrivial to solve; thus, a computer program was written to obtain predictions for the torsional actuation. In this program, values of θ_j from $j=0$ to $N-1$ are defined for discrete values of z_j separated by a constant interval $\Delta z = L/(N-1)$. The angular strain at any given point k is given by the following sum:

$$\theta_{k+1} - \theta_k = \frac{2\mu_0 H_0^2}{G}(A_\parallel - A_\perp)\left(\frac{L}{R}\right)^2 \left\{ \frac{1}{(N-1)^2} \sum_{k+1}^{N} \sin(2\theta_j) \right\}, k = 0, ..., N-2 \tag{5.2}$$

The equation 5.2 for the strains is solved iteratively by first stipulating the angle θ of the chains at the fixed end of the cylinder and specifying the value of the factor $c = \left(\frac{L}{R}\right)^2 \frac{2\mu_0 H_0^2}{G}(A_\parallel - A_\perp)$. For the numerical stability of the solution, the value of c was increased step-wisely from $c/10$ to the required value in steps of $c/10$. For the initialization of the angles, the one at the fixed end was used, and at each iteration, the new angle was updated using a linear combination of the solution of the two previous iterations.

5.2.2 Materials and Methods

Materials

Acrylamide (AAm), N,N'-methylenebisacrylamide (Bis-AAm), 2-hydroxyethyl cellulose $M_v \sim 720000$ (HC720), potassium peroxodisulfate (KPS), and N,N,N',N",N"-pentamethyldiethylenetriamine (PMDTA) from Sigma Aldrich (USA). Silica-coated iron powder (Fe-CC powder) from BASF (Germany). Silicone

elastomer Eco-Flex 00-30 (Smooth-On, USA). Permalloy flakes of iron (Fe), nickel (Ni), and molybdenum (Mo) from Novamet Specialty Products Corporation (USA).

Synthesis of the Torsional Actuator

The protocol used for the synthesis of the magnetic acrylamide and cellulose SIPN hydrogel was the one previously described in Chapter 4. In this case, only 2-hydroxyethyl cellulose of $M_v \sim 720000$ was used, and the particle concentrations were 2 and 15 % v/v for the Fe-CC microparticles, and 2 % v/v for permalloy flakes, which are a new type of soft-MPs used in this application. To prepare the samples with the shape and internal organization required for the application, the mixture of pre-gel solution and MPs was poured into a transparent cylindrical mold. The mold was then placed for 40 min in a 16.5 mT uniform field generated by a Helmholtz coil in order to align the particles in chain-like structures. During this time, the hydrogel was exposed to ultraviolet (UV) light (λ = 370 nm) to initiate gelling. After that, the hydrogel was placed in an oven at 50 °C to finish the gelling of the material.

Mechanical Characterization

The mechanical characterization of the hydrogels was performed using a Discovery HR-1 rheometer (TA Instruments, USA) equipped with a 40 mm diameter parallel disk geometry. Quasi-static shear measurements were performed at constant temperature of 25 °C, where the shear stress was measured as a function of the shear strain at a constant shear rate of 10^{-4} s^{-1}. To ensure contact between the sample and geometry during the measurement, a normal force of 0.1 N was applied. From these measurements, the shear modulus, G, was obtained as:

$$\sigma = \frac{F}{S} = G\gamma \tag{5.3}$$

, where σ is the shear stress, F is the shear force applied by the upper disk, S is the sample surface in contact with the disk, and γ is the angular deformation. The modulus values obtained for the linear region of the previous curves are shown in Figure 5.2 A.

Characterization of the Susceptibility of Permalloy Flakes

To calculate the susceptibility of 2 % v/v flakes composites needed in the theoretical model, the methodology described in [Martin et al., 2000] was followed due to the necessity of applying demagnetizing field corrections to the measured magnetization (M) vs. magnetic field strength (H) curves. Cubes of 1 cm^3 were prepared using flakes at a concentration of 2 % v/v using Eco-Flex 00-30. Some of these cubes

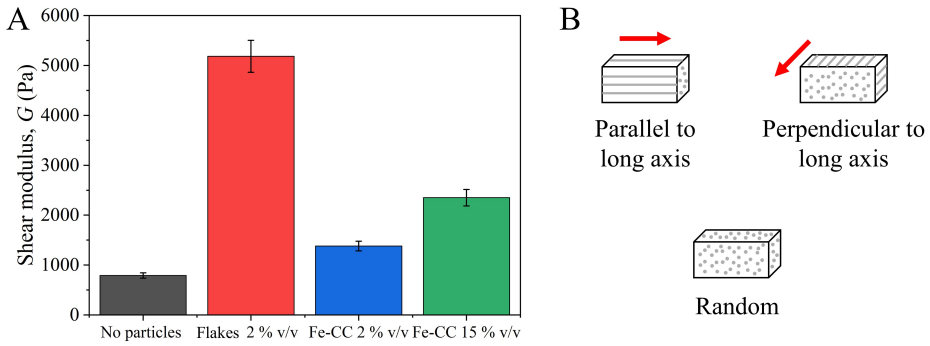

Figure 5.2: A) Shear modulus values measured for the different samples. B) Sketch of the three samples prepared to characterize the two components of the magnetic susceptibility of 2 % v/v permalloy flakes composites.

were placed in a 0.5 T uniform magnetic field generated by two electromagnetic coils to align the flakes in one preferred direction for a couple of minutes. Then, the cubes were laser-cut into solid parallelepipeds measuring approximately 3 $\times$ 3 $\times$ 5 mm^3. After all this process, three different types of samples were obtained: i) flakes aligned in the direction of the long axis of the parallelepiped; ii) flakes oriented perpendicularly to the long axis; iii) randomly distributed (cf. Figure 5.2 B).

The M vs. H curves were measured using a MicroSense EZ7 Vibrating Sample Magnetometer (VSM), aligning the long axis of the rectangle with the external field direction Figure 5.2 B. From these curves, the measured susceptibility χ_m was obtained by fitting the linear region between $\pm$ 5 kA/m. These data were corrected iteratively by searching for the zeros of the function:

$$f(\chi) = \chi - \frac{\chi_m}{1 - n(\chi)\chi_m} \tag{5.4}$$

, where χ is the corrected susceptibility and $n(\chi)$ the demagnetization factor. For more details, please see [Martin et al., 2000]. In Table 5.1, the aspect ratio, the measured susceptibility, and the corrected susceptibility are presented for each sample. The anisotropic magnetic susceptibilities of the spherical Fe-CC particle were obtained from the same work [Martin et al., 2000].

Analysis of the Actuation

The actuation of the magnetically structured cylinders was characterized by two independent experiments, following the protocol previously reported for alginate-based ferrogels [Vázquez Pérez, 2024]:

Table 5.1: Measured (χ_m) and corrected (χ) susceptibilities for 2 % v/v permalloy flakes composites.

Flake alignment	Aspect ratio	χ_m (-)	χ (-)	Mean χ (-)
Random	1.55	0.6826	0.8097	0.89 ± 0.05
	1.55	0.723	0.8667	
	1.45	0.8027	0.9939	
Parallel to long axis	1.6	1.2567	1.7244	1.74 ± 0.04
	1.6	1.3053	1.8153	
	1.6	1.2321	1.6794	
Perpendicular to long axis	1.6	0.6955	0.8237	0.94 ± 0.06
	1.5	0.7988	0.9823	
	1.55	0.8223	1.0118	

- Base fixed: in this experiment, the base of the actuator was fixed at a certain angle θ during the experiment, so that the particle chains in the base made a certain angle with the direction perpendicular to the applied field (30°, 45°, and 60°). The magnetic field strength was increased in steps of 6.51 kA/m, and the angle θ' of the particle chains at the free end was measured (Figure 5.3 A).
- Rotation of the base: while applying a constant magnetic field strength of 32.7 kA/m, the base of the actuator was rotated in 10° steps clockwise. The experiment was conducted from 90° to -90° (at the beginning and the end of the experiment the chains of particles were aligned with the magnetic field) (Figure 5.3 B).

Statistical Analysis

For each set of experimental conditions, at least three different samples were measured. The mean value and standard error of each magnitude are provided.

5.2.3 Experimental Analysis and Validation of the Theoretical Model

The response of the torsional actuator was studied by considering the type and concentration of MPs. In Figure 5.4 the results for the three ferrogels are shown. In this case, the experiment with the base fixed was performed for θ = 30°, 45°, and 60° under a magnetic field strength ranging from 0 kA/m to 52.08 kA/m. The other independent experiment was performed by rotating the base from θ = 90° to θ = -90° under a constant field strength of 32.7 kA/m.

Firstly, it is important to note that regardless of the ferrogel, the response of the actuator in equation 5.1 is reflected in parameter c, which gathers all the physical information of the material. Therefore, the differences that may arise in the results

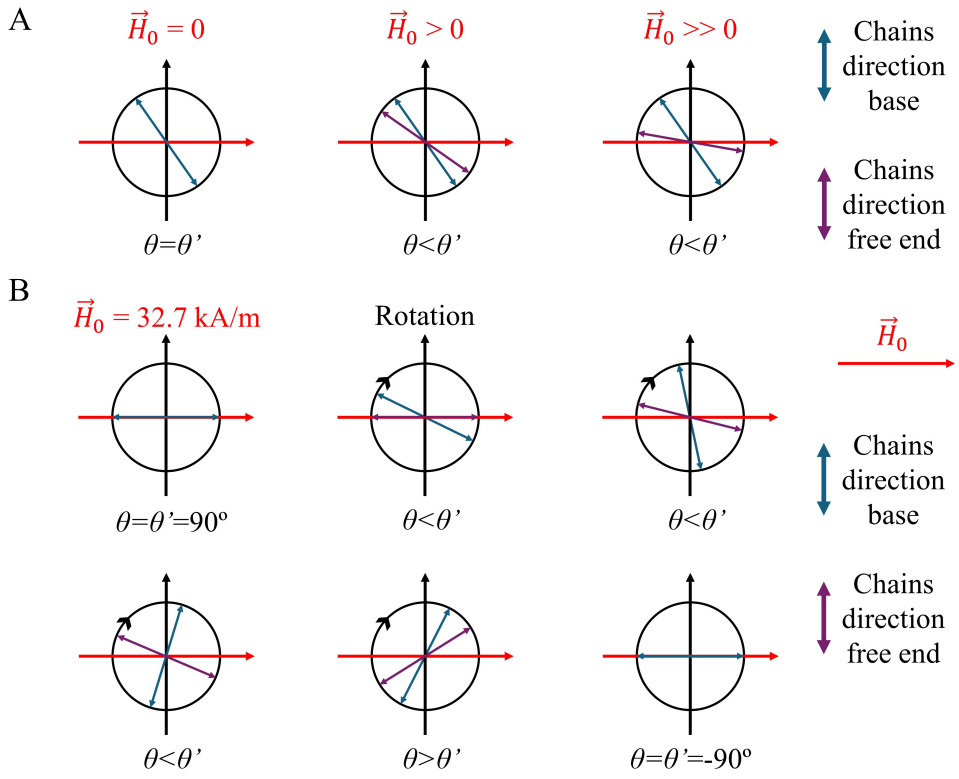

Figure 5.3: Sketch of the top view of the cylinder during the experiments. A) Experiment with the base fixed. Note that when a magnetic field is applied, the chains at the free end of the cylinder tend to align with the field. B) Experiment rotating the base. First, the chains are aligned with the applied field in the initial direction. At a certain angle in the base $\theta < 0$, the chains at the free end abruptly rotate to reduce the angle with the magnetic field.

should be, in principle, due to differences in this parameter. The values of the physical quantities involved in parameter c are reflected in Table 5.2, from which values of $4.3{\cdot}10^{-9}$ m^2/A^2 for 2 % v/v Fe-CC, $8.2{\cdot}10^{-9}$ m^2/A^2 for 15 % v/v Fe-CC, and $2.2{\cdot}10^{-9}$ m^2/A^2 for 2 % v/v permalloy flakes for the factor c/H_0^2 were obtained.

Table 5.2: Physical quantities involved in the calculus of the parameter c for each ferrogel.

Concentration	*L/R* (-)	G (Pa)	$A_{\parallel}$ (-)	$A_{\perp}$ (-)	$A_{\parallel} - A_{\perp}$ (-)	c/H_0^2 (m^2/A^2)
Fe-CC 2 % v/v	4	1400	0.26	0.11	0.15	$4.3{\cdot}10^{-9}$
Fe-CC 15 % v/v	4.5	2400	1.03	0.63	0.39	$8.2{\cdot}10^{-9}$
Flakes 2 % v/v	4	5200	0.93	0.64	0.29	$2.2{\cdot}10^{-9}$

Looking at the experimental results in Figure 5.4, it can be seen that the behavior of the three ferrogels was similar when the base of the cylinder was fixed. At 0 kA/m, θ' was equal to θ as expected, and their value was the established value in the experiment. When the field strength was increased, θ' slightly increased with a linear tendency after a small transition from the initial state to higher magnetic field values. At a magnetic field of approximately 45 kA/m, the slope of the curve decreased, indicating that the material was reaching the limit regarding the angle that the free end could reach (aligned with the applied field). This maximum angle should theoretically be 90°, but farther values of the magnetic field must be applied to reach that point. The differences when the angle of the base was changed affect the maximum angle θ' that the material reached because the equilibrium point between the elastic and magnetic energies changed with the value of θ. It also affected the form of the curve, which became somewhat a straight line for θ = 60° (Figure 5.4 C) where it was not observed the initial and final plateaus that appeared for θ = 30° (Figure 5.4 A) and θ = 45° (Figure 5.4 B). Focusing on the values of c, differences between the three samples should be observed, with the ferrogels with 15 % v/v of Fe-CC particles having a higher response. Surprisingly, 2 % v/v and 15 % v/v of Fe-CC exhibited a rather similar response despite having a c/H_0^2 of $4.3{\cdot}10^{-9}$ m^2/A^2 and $8.2{\cdot}10^{-9}$ m^2/A^2, respectively, while 2 % v/v permalloy flakes showed the highest response. The reasons behind this behavior will be discussed later.

For the experiment rotating the base in a constant field (Figure 5.4 D), the free end of the cylinder tended to align with the magnetic field as a consequence of the equilibrium between elastic and magnetic energies, whereas the angle of the base was changed. At some point, the angle of the base reached negative values, and the free end was still oriented in the initial direction with a positive angle lower than 90°. However, when the base was rotated to -10°, the free end abruptly rotated and switched to the other side, aligning with the field in the other direction. Further reduction of the angle of the base reduced the angle of the free end until it reached -90°.

Finally, it is important to compare these experimental results with the theoretical model under the same physical conditions. To do so, the quantities in Table 5.2 were used to calculate the angular displacement using equation 5.2. The experimental and theoretical results are plotted in Figure 5.5. The first thing that stands out is the disagreement between the experimental results and the theory. For 2 % v/v and 15 % v/v Fe-CC particles (*cf.* Figure 5.5 A and C), in the first experiment, the theory predicts a major torsion of the cylinder for lower magnetic field strength, and the free end is able to perfectly align with the field within the applied range. However, the experimental results show smooth torsion, and the maximum angle of the free end was around 70° for 52.08 kA/m. In the case of rotating the base, the theoretical transition of the free end occurs at a lower angle and is sharper than the experimental transition, which exhibits smooth twisting at angles over -20°. In addition, theoretically, the free end tends to be almost aligned ($\theta' \sim 90°$) with the field, whereas, experimentally,

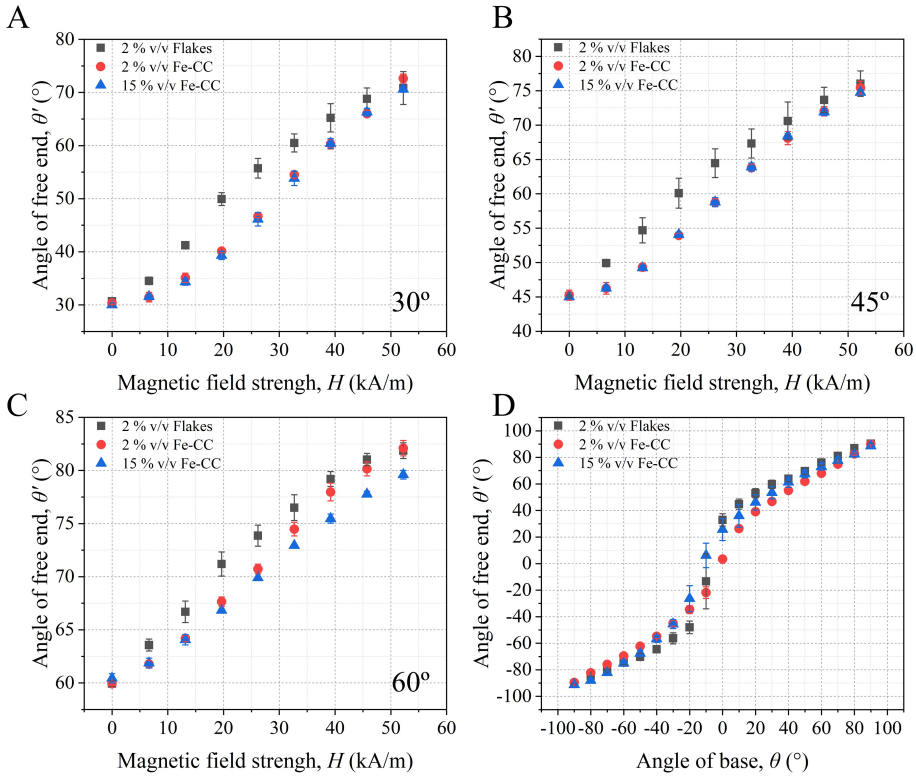

Figure 5.4: Experimental results for the response of the torsional actuator for type of ferrogel. A), B), and C) Experiments were performed with the base of the cylinder fixed at a certain angle $\theta = 30°$, $45°$, and $60°$, respectively. D) Experiments were performed by rotating the base of the cylinder from $\theta = 90°$ to $\theta = -90°$ under a constant field strength of 32.7 kA/m.

the angle of the free ends slowly reduces with the change in the angle of the base. Nevertheless, for 2 % v/v permalloy flakes, there is a better agreement between theory and experiments.

The experimental results reported by Váquez Pérez [Vázquez Pérez, 2024] for alginate-based ferrogels were in good agreement with the theoretical model. Therefore, the disagreement in this case can be attributed to the particularities of the studied materials. As previously discussed, the physical properties of the samples are gathered in the parameter c, which is connected to the shear modulus and the magnetic anisotropy of the ferrogel. These two properties explain the discrepancies between the theoretical and experimental results. In the Fe-CC case, where the differences are more noticeable, to obtain a better fit to the experimental data, the parameter c should be lower than the calculated value. Considering the two above-mentioned quantities, a hypothesis is that, experimentally, the material is stiffer and the particles are not perfectly aligned in a privileged direction. These two assumptions are possible because of the experimental difficulties associated with the free radical reaction

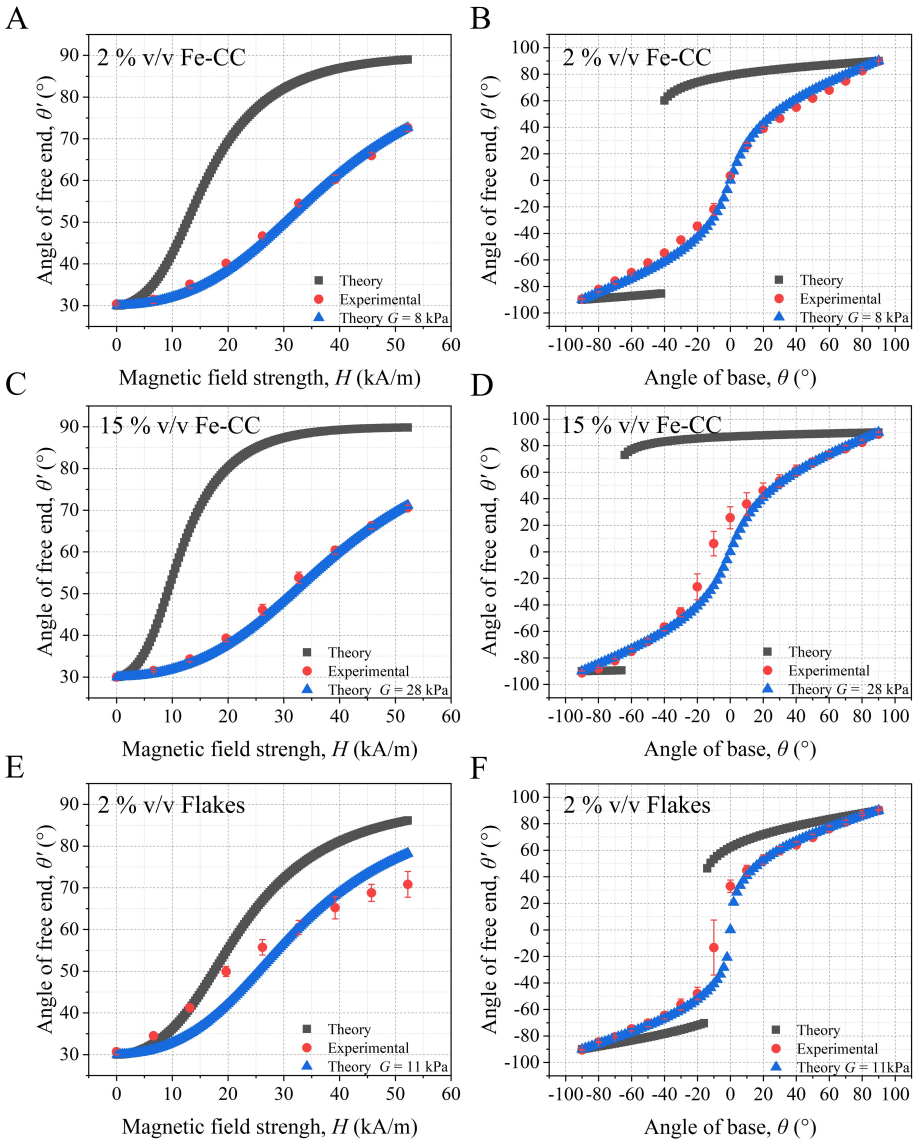

Figure 5.5: Comparison between experimental and theoretical results. On the left, experiment with the base fixed at 30°. On the right, experiment rotating the base. A) and B) results for hydrogels with 2 % v/v of Fe-CC particles. C) and D) results for hydrogels with 15 % v/v of Fe-CC particles. E) and F) results for hydrogels with 2 % v/v of permalloy flakes. Note that the theoretical data where G is specified (in blue) are the values that approximately adjust the experimental data.

involved in the polymerization of acrylamide. This reaction occurs at temperatures over 50 °C or under UV light exposure. The experimental setup did not allow us to initiate the reaction using temperature; thus, UV light was used. After 40 min of UV light exposure in a uniform magnetic field, the cylindrical ferrogels were placed

in an oven at 50 °C to finalize gelling. On the one hand, the shear modulus of the cylindrical sample can differ from that measured for disk-like samples completely gelled in the oven. On the other hand, the MPs can be misaligned due to precipitation and the two-step preparation protocol. From what was explained, it is possible that the cylindrical sample had a different shear modulus and magnetic anisotropy than the measured quantities following the protocols described in subsection 5.2.2.

To illustrate how the stiffness of the material affects the ferrogels response, in Figure 5.5, additionally to the experimental and theoretical data for our samples, the theoretical model for the shear modulus values that better fitted the curves is plotted. As can be seen, increasing the material stiffness improved the theoretical model's ability to reproduce the experimental data. As previously discussed, one hypothesis that could explain the disagreement between theory and experiment was the real stiffness of the material, and this hypothesis has been proved to be plausible. Nevertheless, the magnetic anisotropy, which is not considered in this correction, could also affect the results. To summarize, the real values of the implied quantities must differ from the estimated ones, possibly because the shear modulus is higher and the difference between the orthogonal effective susceptibilities lower. Nevertheless, slight differences between the theoretical and experimental results were observed even after correcting the data, indicating the equal relevance of the magnetic anisotropy.

5.3 Programmable Multi-Responsive Actuator

5.3.1 Hypothesis and Objective

The second actuator presented in this chapter is a programmable multi-responsive actuator. Multi-stimuli materials have gained interest in recent years for the development of soft robots because they can incorporate multi-responsive, shape memory, and self-healing capabilities into a single material [Chen et al., 2021]. In particular, ferrogels are a straightforward approach to this design principle; they can respond to magnetic fields and certain stimuli to which the polymeric network is sensitive, such as temperature [Gambin et al., 2024] or pH [Arvand et al., 2024].

From the materials studied in this thesis, the acrylamide and biopolymer SIPN ferrogels have an intrinsic multi-responsiveness. Until now, only the magnetic response have been exploited, while the swelling capacity have been overlooked despite its importance. For this reason, in this section, both stimuli are exploited to design a reconfigurable magnetic pump. However, the bare ferrogel is not sufficient to obtain an easily programmable multi-responsive material because the swelling of the polymeric network involves only a change in volume, not in shape, and the soft ferromagnetic nature of the Fe-CC particles makes the programming process more complex. Therefore, to address these issues, a cross-linking gradient was introduced into the entangled polymer of the SPIN ferrogels, and the magnetic phase of the

material was replaced by NdFeB particles with hard ferromagnetic behavior.

The concept behind the programming process is illustrated in Figure 5.6. Briefly, the acrylamide and biopolymer ferrogel is synthesized with a cross-linking gradient along its thickness. When the ferrogel is placed in a water-based solution at a certain pH, the ferrogel swells inhomogeneously. In fact, the ferrogel bends because of the differential swelling of the double network. If a high-intensity magnetic field is applied at this moment, the hard NdFeB particles will be magnetized in the field direction. After that, we can remove the field and reduce the swelling of the gel by changing the pH of the medium, obtaining a ferrogel with similar characteristics than the one synthesized. Finally, if we apply a low-intensity magnetic field to the previous ferrogel, the MPs will generate internal torques within the polymeric network to align their magnetic moment ($\vec{m}$) with the external field. This will cause the bending of the material, which will recover the shape of its swollen state. Once the filed is removed, the ferrogel will recover its no swollen form. This facile process can be exploited to design complex actuators. In our case, we designed a magnetic pump that can be programmed and actuate without contact.

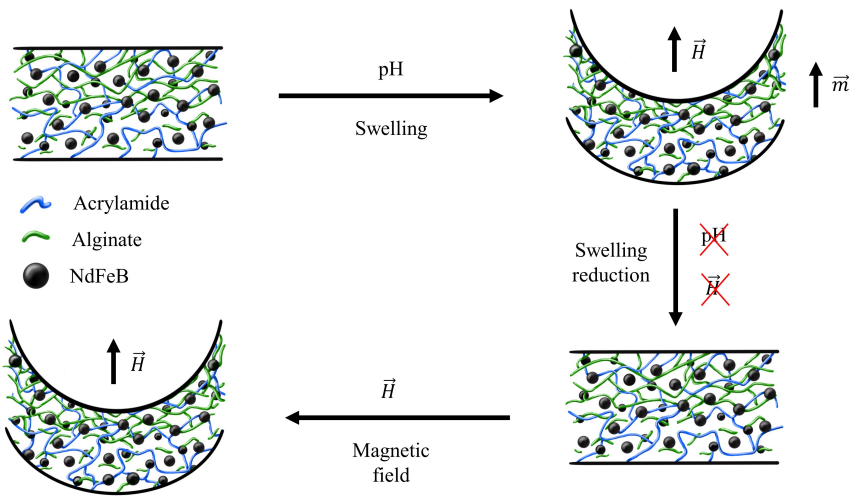

Figure 5.6: Programming and actuation process of a SIPN ferrogel with a cross-linking gradient along its thickness and hard ferromagnetic particles.

5.3.2 Materials and Methods

Materials

Acrylamide (AAm), N,N'-methylenebisacrylamide (Bis-AAm), LVSA sodium alginate, calcium sulfate ($CaSO_4$), lithium phenyl-2 4 6-trimethylbenzoylphosphinate

(TPO-Li), sodium hydroxide (NaOH) from Sigma-Aldrich (USA). Neodymium-iron-boron (NdFeB) particles with a diameter of 5 μm and density of $\rho = 7.61$ g/cm^3 from Magnequench (Germany). The solutions were prepared in milli-Q water.

Synthesis of Ferrogel Thin Films

The protocol is based on the one described in Chapter 4. First, 4.8 % w/w water solution of LVSA was prepared. Subsequently, NdFeB microparticles were added to the polymeric solution, which were stirred and sonicated for 10 min until a homogeneous suspension was obtained. Afterwards, Bis-AAm and AAm were dissolved in water and thoroughly mixed with the polymer/NdFeB suspension. Finally, an aqueous solution of the photoinitiator TPO-Li (10 mg/mL) was added to the Bis-AAm/Aam/NdFeB/alginate mixture. The pre-gel solution was injected between two glasses at a set distance of 500 μm. This setup was placed under ultraviolet light (λ = 365 nm) for 15 min. The concentrations of the compounds used were as follows: 83.93 % v/v of milli-Q water, 1.82 % v/v of LVSA, 0.1 % v/v of Bis-AAm, 9.05 % v/v of AAm, 0.1 % v/v of TPO-Li, and 5.0 % v/v of NdFeB particles.

Programming the Multi-Stimuli Hydrogel

The programming of the reconfigurable magnetic pump consisted of two phases: i) shaping of the material using its swelling capacity and cross-liking gradient; and ii) magnetization of the NdFeB particles, which magnetically recorded the shape of the material in its swollen state. To do so, the synthesized thin film following the previous protocol was dried at room temperature, and to create a cross-linking gradient along the film thickness, one of the surfaces of the hydrogel was put in contact with a solution of $CaSO_4$ 19 mM for 10 s. The ferrogel thin film (Figure 5.7 A) was then cut into the desired shape (Figure 5.7 B) using a laser. After that, the ferrogel was placed in milli-Q water until complete swelling (Figure 5.7 C). The swollen-shaped ferrogel was then placed between two VSM coils that generated a 1.8 T magnetic field that magnetized the NdFeB microparticles. Finally, the ferrogel was placed in a basic medium to reduce the swelling to recover the original planar shape of the thin film (Figure 5.7 D).

5.3.3 Actuation of the Multi-Stimuli Hydrogel

To study the actuation of the designed pump, the ferrogel was fixed in a 3D-printed frame inside a water-based solution, where it maintained its nonswollen state (Figure 5.8). This setup was placed in a triaxial coil system that generated low-intensity sinusoidal magnetic fields of 10 mT and frequencies of 1, 5, 10, and 15 Hz. To

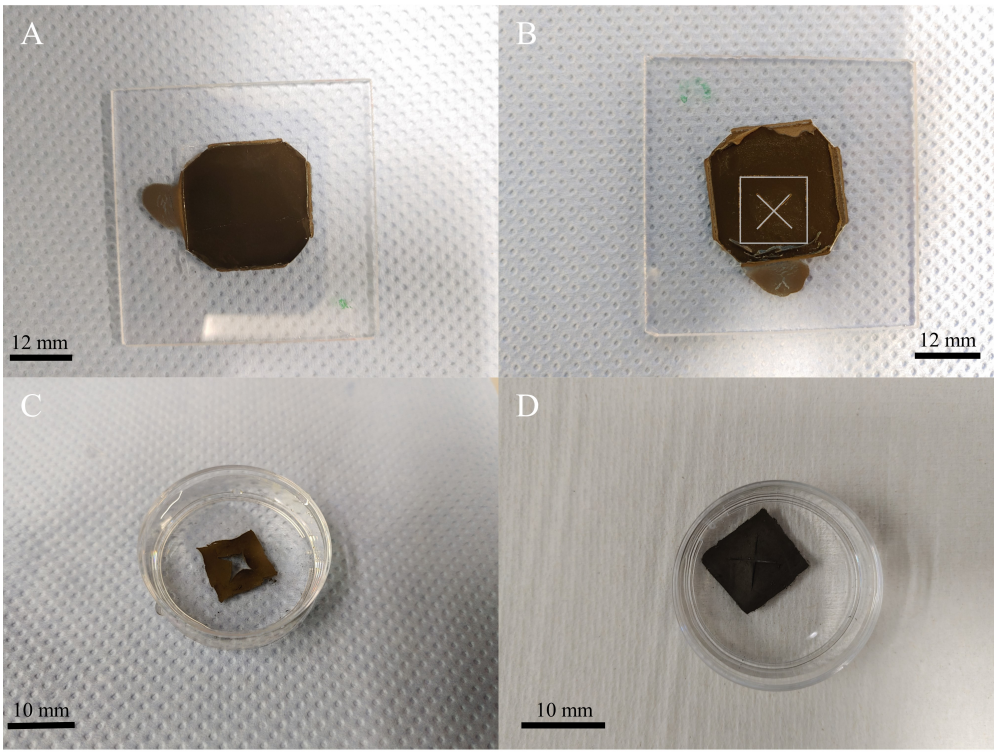

Figure 5.7: Programming process of the pump. The different stages related to swelling are shown: A) dried ferrogel thin film; B) cross-shaped pump cut on the ferrogel; C) swollen pump state. Note that the cross is open; D) no swollen state. Note that the cross is closed.

observe fluid dynamics during the pump actuation, a magenta dye was placed in the liquid.

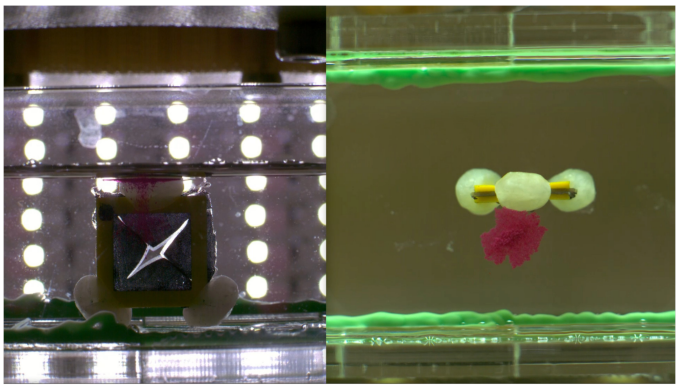

Figure 5.8: Off-state of the magnetic pump. Note that the cross is slightly open due to gravity. Side view of the system (left) and top view (right). Magenta powder is a dye used to visualize water flow due to the ferrogel pumping.

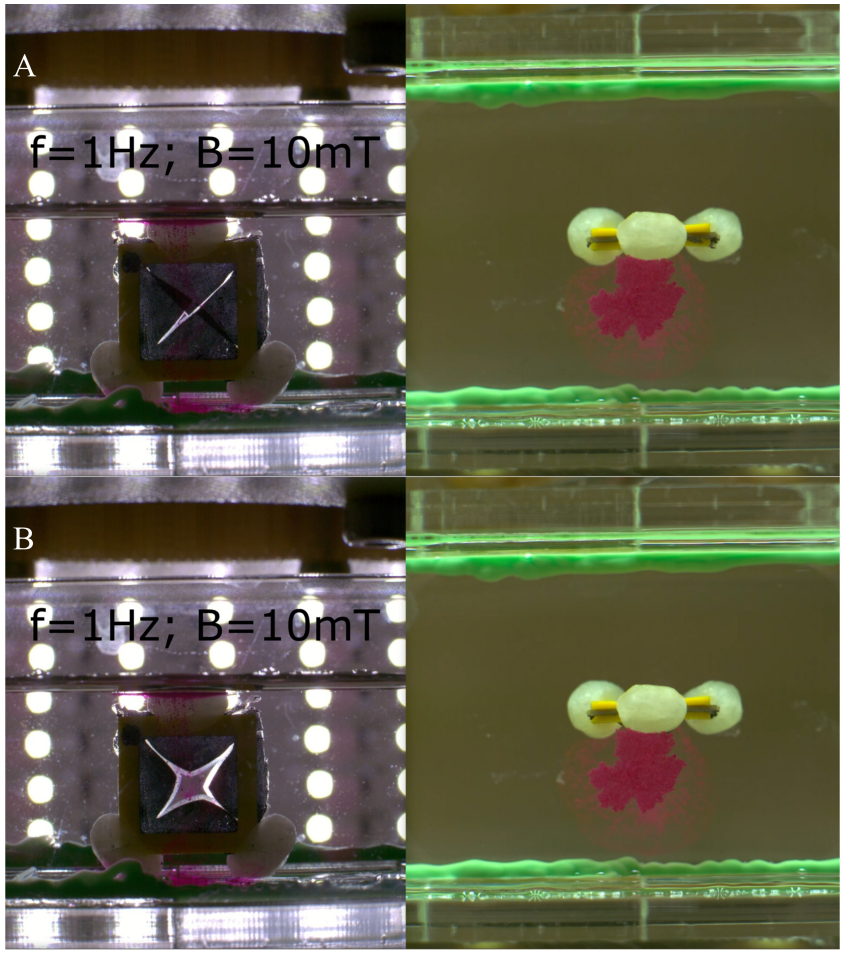

Figure 5.9: Open and closed states of the magnetic pump at 1 Hz. Side view of the system (left) and top view (right). The dye remained in the same position.

When a sinusoidal field was applied, different mixing patterns were observed depending on the frequency of the field. In addition, the pump movement was asymmetrical with respect to the ferrogel plane, which made possible the mixing of the surrounding environment. Two states were discerned: i) closed (Figure 5.9 A), the cross was completely closed, avoiding deformations due to gravity; ii) open (Figure 5.9 B), in which the ferrogel recovered the shape of its swollen state. Regarding the effect of the frequency, at 1 Hz, no significant mixing was observed (Figure 5.9), at 5 Hz there was a slight mixing in front of the ferrogel (Figure 5.10 A), at 10 Hz the whole solution was mixed (Figure 5.10 B), and at 15 Hz the pump could not follow the field frequency due to inertia, and no mixing was observed.

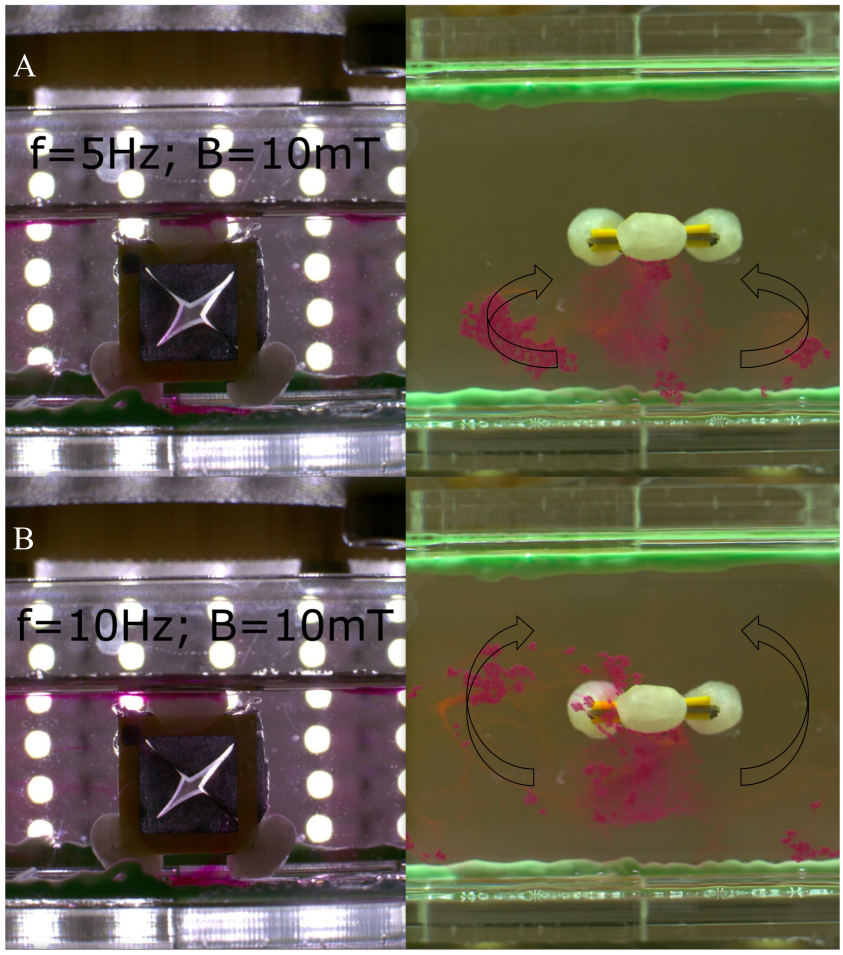

Figure 5.10: The magnetic pump was operated at 5 Hz A) and 10 Hz B). Side view of the system (left) and top view (right). The black arrows indicate the direction of the flow followed by the dye. The flow originates from pump actuation.

5.4 Conclusions

In this chapter different SIPN ferrogels have been evaluated as two soft actuators. The first one, a cylindrical torsional actuator with magnetically induced MPs chains contained in planes perpendicular to its axis. And the second one, a programmable multi-responsive magnetic pump.

In the first part of the chapter, we studied the response of the cylindrical ferrogels by fixing one end of the cylinder, while the other end was free to rotate in a uniform magnetic field. Experimentally, the free end tended to align with the external field generating a deformation along the cylinder length. In addition, we observed hysteresis when the fixed base was rotated during the experiment. These experimental

results were compared with a previously reported theoretical model [Vázquez Pérez, 2024] for this system. However, comparing the experimental and theoretical results, we observed noticeable differences in some samples, which can be attributed to discrepancies between the real values and the experimentally determined values of quantities involved in the actuation phenomena.

In the second part, we presented a magnetic pump. In this case, a cross-linking gradient was introduced into the SIPN and NdFeB particles were used as the magnetic phase. For the design of a magnetic pump, the pH and magnetic responsiveness of the ferrogels were used, one to achieve the desired deformation and the other to record the deformation in the material. The resulting pump demonstrated the capacity to mix its surrounding environment under certain frequencies of a sinusoidal alternating magnetic field, of interests in fluid and biological systems.

Part III

Chapter 6. Conclusions

The aim of this thesis was to prepare ferrogels by controlling their microstructure and magnetic behavior. To achieve that, different polymers, such as sodium alginate, cellulose, and polyacrylamide, were used to prepare hydrogels via supramolecular or covalent polymerization, with different types of MPs trapped within the material structure. These ferrogels were synthesized with suitable internal order owing to the nature of the polymers, their interaction with the MPs, and their spatial arrangement, which were controlled by magnetic fields or mechanical stresses. In addition, the ferrogels were characterized from a macroscopical point of view, including their mechanical properties under different stresses, swelling capacity, and bulk magnetic behavior, and from a microscopical point of view using different techniques such as SEM and FT-IR spectroscopy. As a result, the ferrogels exhibited a wide range of mechanical properties and microstructural arrangement, which met the requirements for their application as soft actuators, robots, and sensors. In the chapters that are part of this thesis, various ferrogels, MPs, synthesis protocols, characterization techniques, and applications were analyzed and discussed.

In Chapter 2 we studied the effects of a stress-controlled dehydration process (SCDP) on the mechanical properties and internal structure of alginate hydrogels. For this purpose, alginates with different molecular weights were used to prepare physical hydrogels. These materials were dehydrated under compressive or tensile stress to obtain different final alginate concentrations. After the SCDPs the hydrogel were mechanically and microscopically characterized to analyze the effects of the dehydration process, the stress applied, the degree of dehydration, and the type of alginate. From the analysis and discussion of these results we concluded that:

- After the SCDPs, the hydrogel robustness increased, but this effect was not only related to the increase in polymer fiber concentration that is predicted by classical gel theory; instead, the type of stress applied resulted in different effects. Differences between the compressive, tensile, and control samples with similar alginate concentrations were observed, with the compressive stress

being the one that most enhanced the gel stiffness.

- The SCDPs not only caused an increase in stiffness but also rearranged the polymeric fibers, which was corroborated by an anisotropic mechanical behavior and SEM images. Dehydration of the hydrogels under tensile stress resulted in the formation of anisotropic structures in the stress direction.
- The previous results can be explained by the above-described polymer rearrangement caused by SCDPs. Indeed, we corroborated that this rearrangement was irreversible because the complete rehydration of the alginate hydrogels was impossible due to the possible formation of hydrogen bonds between the -OH groups present in the alginate fibers.
- The compressive SCDP were applied to a cross-shaped magnetic actuator, which consisted of a central nonmagnetic hydrogel beam connected to two lateral magnetic hydrogel beams that bent in response to magnetic fields. We observed that the threshold value of the magnetic field required to obtain a significant bending of the magnetic hydrogel beams decreased for samples subjected to the SCDP compared to nondehydrated samples containing similar concentrations of MPs.

In Chapter 3, we reported the microscopic analysis of anisotropic sodium alginate ferrogels using FT-IR microspectroscopy. These ferrogels were prepared using MPs coated with amine groups that are able to electrostatically interact with alginate carboxyl groups. During the gelling process, the ferrogels were placed under a uniform magnetic field to arrange the MPs. After their preparation, the anisotropic ferrogels were analyzed using polarized synchrotron radiation-based FT-IR microspectroscopy at the facilities of ALBA synchrotron. The vibration modes of the carboxyl groups present in alginate were analyzed to shed light on the microscopic arrangement of alginate fibers, which exhibited a certain degree of alignment in the magnetic field direction. From the result we concluded that:

- In the 1600 cm^{-1} peak ratios of the FT-IR microspectra of the samples, the hydrogels without particles and with nonfunctionalized particles showed homogeneous values near unity over the analyzed area in agreement with the expected absence of alignment.
- The ferrogels with functionalized MPs showed changes in the ratios of their FT-IR peaks, which were related to the expected alignment of the alginate fibers due to the orientation of the COO^{-} group. Nevertheless, the only sample that showed a clear arrangement associated with the MPs alignment was the B1 anime group MPs aligned in a 8 kA/m field (MB1-MF8).
- These results provide new insights into the microscopic structure of anisotropic alginate ferrogels. However, a more detailed and extensive analysis is

required to undeniably confirm the polymeric arrangement due to the particles alignment.

In Chapter 4, semi-interpenetrating polymer networks (SIPNs) made of a chemically cross-linked network of acrylamide and entangled cellulose/alginate biopolymers were used to prepare magnetic SIPN (Mag-SIPN) hydrogels with excellent stretchability, high water content, and strong magnetic response. The magnetic properties were achieved by adding different concentrations of silica-coated iron microparticles to the polymer network, which did not substantially deteriorate the mechanical properties of the SIPNs. The mechanical properties, swelling capacity, and magnetic behavior of these materials were characterized with the aim of evaluating their performance, reliability, and stability in proof-of-concept applications requiring strong responsiveness to magnetic fields, specifically as a valve and oxygen sensor controlled by a magnetic field. From studying these materials we concluded that:

- The SIPNs could accommodate a high load of magnetic microparticles without substantially weakening the mechanical properties of the resulting Mag-SIPNs, although a minimum amount of accelerant was required to minimize particle settling during gelling.
- The Mag-SIPNs showed rather low elastic moduli (both under tensile and compressive stresses) and viscoelastic moduli, together with large compressibility and stretchability values, making them optimum for maximizing their magneto-mechanical response under a magnetic field.
- The Mag-SIPNs showed a high swelling capacity and strong magnetic response, which, in conjunction with their mechanical properties, make them ideal materials for smart actuators and sensors with remote control by magnetic fields.
- The Mag-SIPN hydrogels under a magnetic field gradient exhibited considerably large compression values, as well as perfect reversibility during many cycles of application/removal of a magnetic field. These excellent performance and reversibility make them promising materials as active parts with remote magnetic control in valve applications for microfluidic or gas devices.
- The sensor made of the Mag-SIPNs solves the problem of the lack of fixation in the measurement cell, which usually prevents reliable optical signal reading. In addition, it allowed a stable oxygen concentration signal, which is of interest for cellular and enzymatic bioprocesses.

In Chapter 5, the previously studied SIPN ferrogels were evaluated as a torsional actuator and as a multi-stimuli programmable actuator. In the torsional actuator case,

Fe-CC particles and permalloy flakes were fixed in a cylindrical hydrogel. During the gelling process, a uniform field aligned the particles in chain-like structures in parallel planes perpendicular to the cylinder axis. The experimental results were compared with a previously reported theoretical model. In the multi-stimuli programmable actuator, the same SIPN ferrogel containing NdFeB particles was used exploiting two stimuli: magnetic response and swelling capacity. In these ferrogels, the entangled polymer was partially cross-linked by diffusing Ca^{2+} ions. This asymmetric cross-linking density translated into the folding of the material when swollen, which was recorded by magnetizing the NdFeB particles under a uniform high-intensity magnetic field. After reducing the swelling of the ferrogel, which recovered its unfolded state, the folded state was obtained by applying a uniform low magnetic field to the material. From these two applications we concluded that:

- Cylindrical SIPN ferrogels with different MPs aligned into parallel chains can be used as torsional actuators. By fixing one end and applying a uniform field, the free end of the cylinder rotated, showing hysteresis if the fixed end is rotated during the experiment.
- There was a disagreement between the experimental and theoretical results, which was attributed to differences between the real and experimentally determined values of the shear modulus and the orthogonal effective susceptibilities of the cylindrical composite. The use of higher values of the shear modulus, improved the agreement between both.
- The presented magnetic pump was designed as a multi-stimuli programmable actuator, which demonstrated the capacity to mix its surrounding environment under certain frequencies of a sinusoidal alternating magnetic field.

To summarize, we studied alginate hydrogels with an anisotropic internal structure induced by mechanical stresses or alignment of functionalized MPs. Regarding these materials, we have demonstrated that the anisotropy is reflected macroscopically, in their mechanical properties, and microscopically, in the arrangement of the polymeric fibers. Subsequently, the analysis focused on SIPN ferrogels based on acrylamide and biopolymers, which showed promising properties for use in soft robots, actuators, and sensors. The applications presented in Chapter 4 and 5 demonstrated the potential and versatility of SIPN ferrogels, which can be prepared under different experimental conditions, such as shape, MPs, and polymerization processes, and sense and actuate to different environmental conditions.

Chapter 7.
Resumen

Introducción

En la última década se ha desarrollado una amplia gama de materiales funcionales capaces reaccionar a distintos estímulos, como luz, humedad, calor, pH, campo eléctrico, campo magnético, disolventes, etc. [Arif et al., 2024, Liu et al., 2022]. La funcionalidad de estos materiales sensibles a estímulos se debe a su capacidad de cambiar sus propiedades físicas o su forma bajo la aplicación de un estímulo externo [Lucarini et al., 2022]. Entre estos materiales destacan los sintetizados con polímeros, debido a su amplio espectro de propiedades mecánicas, adaptabilidad y fácil fabricación. Entre los materiales poliméricos se incluyen los hidrogeles, objeto de estudio en esta tesis.

En general, los hidrogeles tienen la capacidad de responder de forma natural a determinados estímulos, como la temperatura, el pH, diferentes compuestos químicos, etc. Sin embargo, estos no responden naturalmente a campos magnéticos. Por este motivo, partículas con propiedades magnéticas son incorporadas a la estructura del material, obteniendo lo que se conoce como hidrogeles magnéticos o ferrogeles. Estos materiales son capaces de cambiar sus propiedades físicas o su forma bajo un campo magnético externo, ser manipulados fácilmente sin contacto o incluso calentarse, lo que aumenta sus potenciales aplicaciones [Wu et al., 2020]. Además, se caracterizan por su consistencia blanda, peso ligero, gran capacidad para deformarse, propiedades mecánicas adaptables y biocompatibilidad.

Síntesis de hidrogeles magnéticos o ferrogeles

Partículas magnéticas

La naturaleza de las partículas magnéticas (PMs) es muy diversa, en la Tabla 7.1 hay es una recopilación de las PMs más usadas en ferrogeles que se pueden

encontrar en la literatura científica. Normalmente, la fracción de volumen máxima de partículas que la matriz del material puede contener es de alrededor de 0.4 [Dargahi et al., 2019]. Además, las PMs pueden disponerse dentro del material de dos formas distintas: 1) orientadas direccionalmente [Zhai et al., 2023, Shi et al., 2020]; 2) distribuidas aleatoriamente [Mañas-Torres et al., 2021b]. Para alinear las partículas sólo es necesario aplicar un campo magnético durante el proceso de síntesis. Además, las PMs pueden ser magnetizadas por un campo externo, clasificándolas en ferromagnéticas blandas o duras. El tamaño de partícula también es un parámetro fundamental en las propiedades magnéticas. Cuando estas son lo suficientemente pequeñas, aparece lo que se denomina superparamagnetismo, que se manifiesta en partículas sin remanencia y coercitividad pero que aún poseen una alta permeabilidad [Xuan et al., 2009]. Algunas ventajas de las partículas superparamagnéticas son la posibilidad de calentamiento inductivo bajo campos magnéticos alternos [Chen et al., 2023b,Ganguly and Margel, 2022], su distribución homogénea dentro del material sin sedimentarse debido a su tamaño, y su biocompatibilidad [Campos et al., 2021].

La aplicación de un campo magnético uniforme a ferrogeles isótropos con PMs blandas induce interacciones dipolo-dipolo entre partículas vecinas que se magnetizan por el campo. Las partículas magnetizadas tienden a alinearse con el campo y organizarse dentro de la matriz del material, lo que provoca cambios en las propiedades del mismo, causando lo que se denomina magnetoestricción [Vazquez-Perez et al., 2021]. Por otro lado, cuando se aplica un campo magnético a un ferrogel anisótropo, surgen fuerzas magnéticas que ayudan a mantener la orientación de las cadenas de partículas, oponiéndose a las deformaciones mecánicas (efecto magnetorreológico), o produciendo torques dentro del material.

En algunos casos, para aumentar la interacción entre las PMs y la matriz del material, la superficie de la partícula se trata químicamente recubriéndose con diferentes compuestos que cambian su naturaleza química. Esto abre la posibilidad de la formación de enlaces químicos entre las partículas y las cadenas poliméricas, lo que mejora la estabilidad estructural y química de los ferrogeles [Daya et al., 2022, Barczak et al., 2020]. Además, el recubrimiento también dificulta la agregación de las partículas debido a las fuerzas de Van der Waals y su sedimentación, lo que lleva a una distribución más homogénea de las mismas.

Matriz polimérica

Los hidrogeles se pueden definir como redes tridimensionales de polímeros hidrófilos entrecruzados en una fase acuosa continua. Se caracterizan por su consistencia blanda, alto contenido de agua, propiedades mecánicas, biocompatibilidad, respuesta natural a ciertos estímulos y semejanza con tejidos vivos. Para obtener un hidrogel, el punto de partida es una mezcla de agua y polímeros, la cual tiene que gelificarse mediante un proceso físico o químico. En cuanto a la naturaleza de las interacciones que mantienen

Tabla 7.1: Tipos de partículas magnéticas y sus principales características (comportamiento magnético y morfología) que se pueden encontrar en la literatura en relación a ferrogeles.

Material	Comportamiento	Morfología	Referencias
Óxidos de hierro	Blandas Superpara-magneticas	Esféricas, flores, varillas (10 nm - 30 µm)	[Wang et al., 2022b] [Goudu et al., 2020] [Gao et al., 2019]
Hierro carbonilo	Blandas	Esféricas (1 - 40 µm)	[Lawrence and Rao, 2023] [Selzer and Odenbach, 2020]
Ferritas	Duras	Esféricas (40 nm - 400 nm)	[Rincón-Iglesias et al., 2020] [Naderi and Azizian, 2018]
Neodimio (NdFeB)	Duras	Esféricas (5-25µm)	[Liu et al., 2021] [Kuang et al., 2021]
Níquel	Blandas	Esféricas, varillas ($<$ µm)	[Awasthi et al., 2020] [Safronov et al., 2019]

unidas las cadenas poliméricas, los hidrogeles se pueden clasificar en tres grupos [Estevam et al., 2023, Pal and Banerjee, 2018]: físicos, están entrecruzados mediante interacciones iónicas o intermoleculares; químicos, la red polimérica se forma mediante enlaces covalentes entre los componentes; entrelazados, se forman mediante interacciones topológicas de los polímeros sin enlaces químicos. Otra clasificación se puede realizar atendiendo a la estructura química de la red polimérica [Estevam et al., 2023, Pal and Banerjee, 2018]: homopoliméricas, el hidrogel está formado por un único monómero; copoliméricas, el hidrogel presenta diferentes tipos de monómeros, siendo al menos uno de ellos hidrófilo; redes poliméricas interpenetradas (IPNs), formadas por la combinación de dos o más redes entrecruzadas independientes y sin enlaces covalentes entre ellas. El interés en estas últimas redes poliméricas ha ido creciendo debido a sus propiedades mecánicas, lo que aumenta el número de potenciales aplicaciones. Su característica más destacada es su elevada tenacidad, manteniendo al mismo tiempo las propiedades de cada matriz polimérica que la constituyente, incluso en presencia de PMs [Zhang et al., 2023, Lee et al., 2019]. Un tipo concreto de redes IPNs son las semi-IPNs, que son redes simples o IPNs con al menos un polímero lineal o ramificado entrelazado en la matriz del hidrogel.

Hidrogeles magnéticos o ferrogeles

Como se mencionó anteriormente, los hidrogeles magnéticos o ferrogeles se obtienen mediante la adición de PMs a un hidrogel. Hay tres métodos para incluir las PMs en la matriz del hidrogel: mediante mezcla, por precipitación in situ o mediante injerto de PMs funcionalizadas [Lavrador et al., 2021]. Cuando se agregan partículas, es importante considerar las posibles interacciones que pueden surgir entre ellas y las cadenas de polímero [Ahmadian et al., 2023].

En cuanto a la naturaleza de las fibras, existen dos grupos de hidrogeles según su origen sea natural o sintético. Los polímeros de origen natural son muy utilizados debido a sus propiedades fisicoquímicas, compatibilidad con tejidos biológicos y degradabilidad natural. Entre ellos estas los carbohidratos como el alginato, el quitosano y la celulosa, productos de origen animal como la fibrina, el ácido hialurónico, el colágeno y la gelatina. Además de estos polímeros naturales, también se pueden utilizar polímeros sintéticos, como la gelatina metacrilada, la poli(N-isopropilacrilamida), la acrilamida, el ácido poliacrílico, el alcohol de polivinilo, el polietilenglicol, entre otros. Es importante señalar que en los hidrogeles magnéticos, la fase magnética está generalmente compuesta por óxidos de hierro debido a su biocompatibilidad intrínseca y alta resistencia a la corrosión en medios acuosos. Sin embargo, en algunos casos, se utilizan otros tipos de PMs dependiendo de la aplicación del ferrogel (Tabla 7.1).

Propiedades y caracterización de los ferrogeles

Propiedades generales

En el campo de los materiales poliméricos, las propiedades mecánicas de la matriz del material son fundamentales. Además, se debe considerar la inclusión de partículas, como las PMs, porque su presencia afecta las propiedades físicas finales del material [Song et al., 2020]. En el caso de los ferrogeles, cuando se aplica un campo magnético externo se generan fuerzas internas en la matriz compuesta que también alteran el campo aplicado [Garcia-Gonzalez et al., 2021, Moreno et al., 2021]. En cuanto a las propiedades mecánicas, las principales magnitudes estudiadas son los módulos mecánicos bajo esfuerzos de cizalla, compresión o tracción, cuyos valores pueden varían desde decenas hasta miles de Pascales (Pa). Además, la tenacidad y la resistencia a la rotura también son propiedades cruciales. Centrándonos en las propiedades magnéticas de los ferrogeles, estos heredan el comportamiento magnético de los partículas incluidas en la matriz polimérica, pero con una magnetización efectiva inferior a la de las partículas aisladas.

Técnicas de caracterización

Los dispositivos utilizados para caracterizar las propiedades mecánicas y magnetorreológicas de ferrogeles son los reómetros y las máquinas de pruebas universales. Los primeros permite realizar ensayos esfuerzo-deformación bajo esfuerzos de cizalla para muestras relativamente blandas, mientras que las segundas también se utilizan para la caracterización de muestras más rígidas bajo esfuerzos de tracción o compresión [Mondal et al., 2023, Moreno et al., 2021]. En ambos casos, se puede aplicar un campo magnético a la muestra mientras se mide, lo que permite observar el efecto magnetorreológico [Bastola and Hossain, 2020]. La

muestra puede ser sometida a esfuerzos de compresión, tracción o cizalla en régimen dinámico o cuasiestático, así como a experimentos de relajación [Moreno et al., 2021]. En cuanto a las propiedades magnéticas, las curvas de magnetización se miden mediante magnetómetros de muestra vibrante (VSM) o dispositivos superconductores de interferencia cuántica (SQUID). La composición y, en algunos casos, la estructura se pueden observar mediante espectroscopía infrarroja por transformada de Fourier (FT-IR) o por difracción de rayos X (DRX). Finalmente, la microestructura se observa comúnmente mediante métodos directos como la microscopía electrónica de barrido (SEM) [Zhou et al., 2020], que permite observar la distribución de PMs, analizar la composición química u obtener información sobre la red polimérica.

Aplicaciones de Ferrogeles

Las aplicaciones de los ferrogeles incluyen: ingeniería de tejidos [Almeida et al., 2023, Taghizadeh et al., 2023, Hao and Mao, 2023, Zhang et al., 2020b, Koons et al., 2020], bioelectrónica [Li et al., 2024, Li et al., 2021, Guo and Ma, 2018], administración de fármacos [Xia et al., 2023, Ganguly and Margel, 2021], apósitos para heridas [Nam and Mooney, 2021, Qu et al., 2018, Dimatteo et al., 2018], tratamiento del cáncer [Andrade et al., 2021], remediación ambiental [Gang et al., 2021, Weerasundara et al., 2020], robots blandos [Zhao et al., 2022, Goudu et al., 2020, Liu et al., 2020b] y actuadores blandos [He et al., 2023, Vazquez-Perez et al., 2021]. Su interés reside en su consistencia blanda, alto contenido en agua, porosidad, amplio espectro de propiedades mecánicas, degradabilidad, biocompatibilidad, bajo coste y capacidad de respuesta a campos magnéticos, lo que les otorga la posibilidad de ser calentados, transportados y deformados sin contacto directo.

Hipótesis y objetivos

La hipótesis de partida de esta tesis doctoral es la posibilidad de ejercer un control preciso sobre la microestructura y distribución espacial de PMs en hidrogeles mediante la aplicación de esfuerzos mecánicos o campos magnéticos. En esta tesis, se prepararon tanto hidrogeles como ferrogeles controlando su microestructura y comportamiento magnético. Estos materiales se caracterizaron desde un punto de vista macroscópico a través de sus propiedades mecánicas bajo diferentes esfuerzos y su comportamiento magnético, y desde un punto de vista microscópico utilizando diferentes técnicas como la microscopía electrónica de barrido (SEM) y la espectroscopía infrarroja por transformada de Fourier (FT-IR). Además, se diseñaron diferentes tipos de aplicaciones para estos hidrogeles en función de las propiedades observadas.

Para lograr lo anterior, se utilizaron diferentes tipos de polímeros, como el alginato de sodio, la celulosa o la poliacrilamida. Estos polímeros tienen la capacidad

de formar hidrogeles mediante polimerización supramolecular y covalente, lo que permite atrapar diferentes tipos de PMs dentro de la red polimérica. Se sintetizaron varios hidrogeles y ferrogeles con un orden interno adecuado. Como resultado, los ferrogeles exhibieron propiedades mecánicas adaptables a través de la concentración, la naturaleza, el tamaño y la disposición espacial de las PMs, así como de las fibras poliméricas. Estos ferrogeles fueron diseñados con las propiedades necesarias para su uso en el campo de los actuadores y robots blandos, así como en otros campos de interés. Para alcanzar estos objetivos generales se plantearon los siguientes objetivos específicos:

- **Funcionalización de su superficie:** (i) uso de PMs de diferentes tamaños y morfologías; (ii) funcionalización de la superficie de las PMs mediante adsorción de moléculas que les proporcionan biocompatibilidad y permiten la interacción física o química con las fibras del hidrogel.

- **Síntesis de ferrogeles:** fabricación de hidrogeles y/o ferrogeles con una microestructura controlada mediante esfuerzos mecánicos o la alineación de PMs bajo campos magnéticos. Como fase magnética se utilizarán MPs comerciales funcionalizadas, mientras que para la matriz del gel se usarán polímeros naturales o sintéticos.

- **Caracterización de las propiedades físicas macroscópicas de ferrogeles:** (i) comportamiento magnético y respuesta a campos magnéticos; (ii) propiedades mecánicas bajo diferentes esfuerzos en diferentes direcciones; (iii) integridad macroscópica y grado de hinchamiento.

- **Caracterización de propiedades microscópicas:** (i) naturaleza de las fibras, patrón interno y grado de entrecruzamiento. (ii) distribución de las PMs dentro del hidrogel, utilizando técnicas espectroscópicas y de microscopía electrónica, como FT-IR, SEM y EDX.

- **Modelado teórico y simulación:** modelado teórico de los ferrogeles para comprender su comportamiento macroscópico desde la perspectiva de los mecanismos físicos que lo gobiernan, considerando su microestructura. Simulaciones computacionales para conocer las distribuciones de campos magnéticos usadas.

- **Aplicaciones de los ferrogeles:** diseño de aplicaciones de los hidrogeles en los campos de actuadores, sensores, y robots blandos.

Hidrogeles de alginato estructurados mecánicamente

Introducción

El objetivo principal de esta sección es analizar de forma exhaustiva los efectos de la deshidratación parcial bajo esfuerzos mecánicos sobre las propiedades mecánicas de hidrogeles de alginato. Además, se analizará si estos cambios mejoran la respuesta de un actuador magnético blando. Para ello, estudiamos hidrogeles de alginato sintetizados usando dos alginatos de sodio con diferentes pesos moleculares, y deshidratándolos mediante dos métodos diferentes: bajo esfuerzo de tracción y bajo esfuerzo de compresión. Tras ellos, analizamos el efecto de la deshidratación sobre las propiedades de estos hidrogeles en términos de pérdida de agua, peso molecular de los alginatos, propiedades mecánicas y estructura microscópica. Además, estudiamos el efecto que tuvo la deshidratación bajo compresión sobre la respuesta de una pinza de hidrogel magnético capaz de doblarse bajo un campo magnético. Estos resultados demuestran que la deshidratación bajo un esfuerzo controlado afecta positivamente a la rigidez de los hidrogeles de alginato y mejora la respuesta de una pinza de ferrogel. La razón detrás de estos cambios se debe a la creación de nuevos enlaces entre las fibras de polímero durante los procesos de deshidratación, a lo que se suma el aumento de la concentración de polímero.

Materiales y métodos

Materiales

Alginato de sodio de baja viscosidad (LVSA) de peso molecular 120000-160000 g/mol, carbonato de calcio ($CaCO_3$), D-glucono-δ-lactona (GDL), cloruro de calcio ($CaCl_2$), hidróxido de sodio (NaOH) de Sigma Aldrich (EE. UU.). Alginato de sodio de viscosidad media (MVSA) de peso molecular 10000-600000 g/mol de PanReac AppliChem ITW Reagents (España). Micropartículas de hierro recubiertas de sílice (Fe-CC) de BASF, Alemania. Las partículas Fe-CC son esféricas, de tamaño micrométrico, con un diámetro de 1.4 $\pm$ 0.6 µm, una densidad de 7.71 $\pm$ 0.19 g/cm^3 y un comportamiento ferromagnético blando típico con magnetización de saturación M_S = 1587 $\pm$ 2 kA/m. Todas las disoluciones se prepararon en agua milli-Q.

Síntesis de hidrogeles e hidrogeles magnéticos

Para preparar hidrogeles isótropos, necesarios para este trabajo, se utilizó un protocolo descrito en un trabajo anterior [Gila-Vilchez et al., 2018] con ligeras modificaciones. Resumidamente, para sintetizar los hidrogeles no magnéticos, preparamos 12 ml de disoluciones de alginato de sodio en agua destilada a distintas concentraciones (4.0,

4.5, 5.0 y 5.5 % p/p), a las que añadimos 36 mg de $CaCO_3$. Posteriormente, agregamos 128.2 mg de GDL y vertimos esta mezcla homogeneizada en un recipiente cuadrado. Las mezclas pre-gel se dejaron en reposo a temperatura ambiente durante 2 horas. Pasado este tiempo, agregamos 12 mL de una disolución de $CaCl_2$ 0.5 M y dejamos la muestra gelificar hasta el día siguiente a temperatura ambiente. Preparamos dos tipos de estos hidrogeles, uno que contenía solo LVSA (AH100-0) y el otro que contenía una mezcla al 50-50 % de LVSA y MVSA (AH50-50).

En el caso de los hidrogeles utilizados para el actuador, se prepararon dos partes: una activa (magnética) y una pasiva (no magnética). Para la parte magnética, se modificó ligeramente el protocolo anterior para incorporar las PMs al actuador. A 10 ml de una disolución de MVSA a una concentración de 1 % p/p, se agregaron 15 mg de $CaCO_3$. Posteriormente, se agregaron 53.4 mg de GDL y partículas Fe-CC, se homogeneizó mecánicamente la mezcla y se dejó durante 10 minutos en un baño de ultrasonidos. A continuación, se vertió la mezcla en un molde en forma de cruz y se dejó gelificar durante dos horas a temperatura ambiente. Tras esto, se agregaron 10 mL de una disolución 45 mM de $CaCl_2$ para aumentar la densidad de entrecruzamiento, dejando el hidrogel en reposos hasta el día siguiente a temperatura ambiente. La parte no magnética de los actuadores se preparó de la misma forma pero sin introducir PMs en la formulación. En el actuador, solo utilizamos MVSA en una concentración de 1 % p/p para obtener la rigidez adecuada del material con el fin de maximizar la respuesta de los hidrogeles. Con el alginato y la concentración usadas, obtuvimos un actuador flexible que tuvo una consistencia adecuada para su manipulación y respuesta.

Procesos de deshidratación controlada bajo esfuerzo (SCDPs)

Se utilizaron dos procesos diferentes de deshidratación controlada bajo esfuerzo, basados en los métodos descritos en trabajos anteriores [Mredha et al., 2018, Scionti et al., 2013]. Estos SCDPs se diferencian por el tipo de esfuerzo aplicado: tracción o compresión. Como base para este proceso se utilizaron muestras con una concentración total de alginato antes de la deshidratación del 4 % p/p, denominados C4.0AH100-0 y C4.0AH50-50. Para deshidratar estos hidrogeles bajo un esfuerzo de tracción, se utilizó un dispositivo casero que permitía fijar los extremos de la muestra y estirarla. En primer lugar, dos hidrogeles rectangulares se fijaban simultáneamente en el dispositivo y se estiraban ligeramente. Después, se colocaba el sistema en un desecador a temperatura ambiente en el que se creaba un vacío parcial. Las muestras se dejaban secar durante 8, 14 y 24 h para obtener diferentes pérdidas de agua. Durante el proceso, la humedad relativa se controlaba utilizando una disolución de NaOH al 25 % p/p, que mantenía una humedad relativa del 60 % a 25 °C [Madge, 1961]. El aumento del esfuerzo de tracción durante la deshidratación se cree que es el responsable de los cambios que experimentaron las muestras.

Para la deshidratación de los hidrogeles no magnéticos bajo esfuerzo de compresión, muestras cuadradas se colocaban entre dos placas de vidrio rodeadas de papel secante, sobre las que se ponía un peso de 6.5 kg para producir la compresión. Las muestras se dejaban secar en estas condiciones durante 10, 20 y 30 minutos, obteniéndose diferentes grados de deshidratación. En el caso de los hidrogeles para el actuador magnético, debido a su consistencia más blanda, los hidrogeles se colocaban entre dos trozos de papel secante, comprimidos con un peso mucho menor (96 g) y durante un tiempo más corto (90 s). El proceso se repetía hasta dos veces para algunas muestras.

Caracterización mecánica de los hidrogeles de alginato

Para caracterizar las propiedades mecánicas de los hidrogeles, se sometieron a esfuerzos de tracción y cizalla. Las medidas de tracción se llevaron a cabo utilizando un reómetro Discovery HR-1 (TA Instruments, EE. UU.) a temperatura ambiente. Para ello, las muestras se cortaron en forma de mancuerna y se fijaron entre las dos abrazaderas de la geometría de tracción. En todos los casos, aplicamos una precarga de 0.3 N para establecer la misma condición inicial. Los hidrogeles se estiraron a una velocidad constante de 50 µm/s hasta su rotura. Luego, a partir de las curvas de esfuerzo frente a la deformación se obtuvo el módulo de Young (E), que se calculó como la pendiente de la regresión lineal del esfuerzo de tracción (σ) frente a la amplitud de deformación (ϵ) [Draghi, 2017]. La deformación y el esfuerzo de rotura se obtuvieron del último punto de las curvas antes de la rotura del material.

La caracterización del comportamiento viscoelástico de los hidrogeles de alginato bajo cizalla oscilatoria se realizó utilizando un reómetro rotacional Physica MCR 300 (Anton Paar, Austria) con una geometría plato-plato de 20 mm de diámetro a una temperatura constante de 25.0 $\pm$ 0.1 °C. Para garantizar reproducibilidad, los hidrogeles se sometieron a una fuerza normal constante de 0.1 N durante 100 s antes de medir y esta fuerza se mantuvo durante toda la medida para garantizar un contacto adecuado entre el hidrogel y la geometría. El comportamiento reológico de las muestras se analizó mediante barridos de amplitud y frecuencia. En los barridos de amplitud, se aplicó una amplitud de deformación creciente (rampa logarítmica desde γ_i = 0.01 % hasta γ_f = 10 %) y frecuencia constante ν_0 = 1 Hz. En los barridos de frecuencia, se aplicó una amplitud de deformación constante (γ_0 = 0.1 %) y frecuencia creciente (rampa logarítmica desde ν_i = 0.1 Hz hasta ν_f = 20 Hz). Cada barrido constaba de 23 puntos que se mantenían durante 10 s.

Análisis de la respuesta del actuador

Para analizar la respuesta de los ferrogeles, se diseñó un actuador plano con forma de cruz que constaba de dos partes: dos brazos de hidrogel magnético (parte activa)

conectados a un hidrogel no magnético (parte pasiva). Para sintetizar el actuador se utilizó un molde en forma de cruz. Una vez completado el proceso de gelificación, el actuador se colocó sobre un soporte de aluminio a media altura dentro de una bobina que generaba el campo magnético.

El estudio de la flexión de los brazos de ferrogel se realizó aumentando gradualmente el campo magnético aplicado hasta una intensidad máxima de 60 kA/m. Después, el campo se redujo a cero para estudiar la histéresis de la actuación. Para cada valor del campo, esperamos 30 s antes de medir el ángulo de flexión con respecto a la horizontal. Hay que tener en cuenta que debido a la falta de continuidad de las fuerzas de adhesión entre el actuador y el soporte, y al interés en el equilibrio entre las fuerzas magnéticas, elásticas y gravitacionales, para valores bajos del campo magnético, los brazos magnéticos del actuador se separaron manualmente de la superficie de soporte, aumentando el campo hasta que se alcanzaba el equilibrio para un ángulo mayor que cero. Tras esto, se procedía como se ha indicado anteriormente. Los ángulos de flexión se calcularon a partir de los valores de la altura del extremo libre de los brazos magnéticos con respecto a la horizontal.

Resultados y discusión

Grado de deshidratación

El grado de deshidratación se cuantificó utilizando la concentración de alginato y la pérdida de agua después de los SCDPs. Para ello, se midieron las masas de los hidrogeles recién preparados y sus masas finales después de cada SCDP, para calcular la concentración final de polímero y de agua perdida (Tabla 7.2).

Tabla 7.2: Medidas de la concentración de alginato (c) y la pérdida de agua (wl) medias después de los SCDPs. La concentración de alginato antes del SCDP era del 4 % p/p en todos los casos. Los datos de las muestras AH100-0 fueron previamente presentados en [Gila Vilchez, 2022].

Esfuerzo aplicado	Tiempo	AH100-0		AH50- 50	
		c (% p/p)	wl (% p/p)	c (% p/p)	wl (% p/p)
Compresión	10 min	4.72 ± 0.21	16 ± 4	4.41 ± 0.04	9.8 ± 0.9
	20 min	5.00 ± 0.16	21 ± 3	4.61 ± 0.07	13.8 ± 1.4
	30 min	5.3 ± 0.3	26 ± 5	4.79 ± 0.07	17.1 ± 1.3
Tracción	8 h	4.67 ± 0.07	15.0 ± 1.4	4.87 ± 0.11	19 ± 2
	14 h	4.86 ± 0.12	18 ± 2	5.34 ± 0.10	26.1 ± 1.6
	24 h	5.48 ± 0.21	28 ± 3	6.2 ± 0.3	37 ± 3

Los hidrogeles recién preparados también se deshidrataron sin aplicar ningún esfuerzo durante 24 h. Después, los hidrogeles se rehidrataron sumergiéndolos en agua milli-Q durante 24 h adicionales para recuperar el agua perdida. Sin embargo, el estado inicial de hidratación no se recuperó en ningún caso.

Caracterización mecánica bajo esfuerzo de tracción

En las muestras de control bajo tracción uniaxial (Figura 7.1 A y B), para un valor dado de la amplitud de la deformación, el esfuerzo de tracción aumentó con la concentración de alginato para AH100-0 y AH50-50. Por tanto, el módulo de Young también aumentó con la concentración de alginato para las muestras de control. Sin embargo, otros factores también influyeron en los cambios de las propiedades mecánicas, por ejemplo, el esfuerzo máximo y la deformación de rotura fueron mucho mayores para las muestras AH50-50 que para los AH100-0. En las Figura 7.1 C y D, se observa que en los SCDPs bajo compresión se obtuvieron valores considerablemente más altos del esfuerzo de tracción para un valor dado de la amplitud de la deformación tanto para AH100-0 como para AH50-50, en comparación con las muestras de control. En el caso de los SCDPs bajo tracción, hubo un claro aumento en el esfuerzo con respecto a las muestras de control para una amplitud de deformación dada para AH50-50, pero no para AH100-0. En resumen, el módulo de Young obtenido (Figura 7.1 E y F) fue mayor para las muestras sometidas a SCDPs que para las muestras de control, lo que confirma el efecto positivo de la deshidratación y la consiguiente formación de nuevos enlaces entre las cadenas alginato durante la deshidratación, aunque parece que este efecto fue mayor para AH50-50.

Caracterización mecánica bajo esfuerzo de cizalla oscilatorio

La caracterización reológica de las muestras bajo esfuerzo de cizalla oscilatorio reveló un comportamiento típico de sólido viscoelástico (Figuras 7.2). De manera similar al módulo de Young, tanto G' como G'' aumentaron con la concentración de polímero para las muestras de control (Figura 7.2 columna A), aunque las diferencias no son significativas. El efecto de la compresión durante la deshidratación en las muestras AH100-0 y AH50-50 dio como resultado valores considerablemente mayores de G' y G'' en comparación con las muestras de control con concentraciones de alginato similares (Figura 7.2 columna B). Se obtuvo un aumento similar para las muestras AH100-0 sometidas a esfuerzo de tracción durante los SCDPs, mientras que no se observaron diferencias significativas para las muestras AH50-50 (Figura 7.2 columna C).

Análisis de la anisotropía mecánica de los hidrogeles

De los resultados de las subsecciones anteriores, queda claro que los cambios en las propiedades mecánicas de las muestras sometidas a SCDPs no fueron solo una consecuencia del aumento en la concentración del polímero. La creación de nuevos enlaces entre cadenas de polímeros también parece jugar un papel crucial en las propiedades finales de los hidrogeles deshidratados. Para investigar más a fondo los

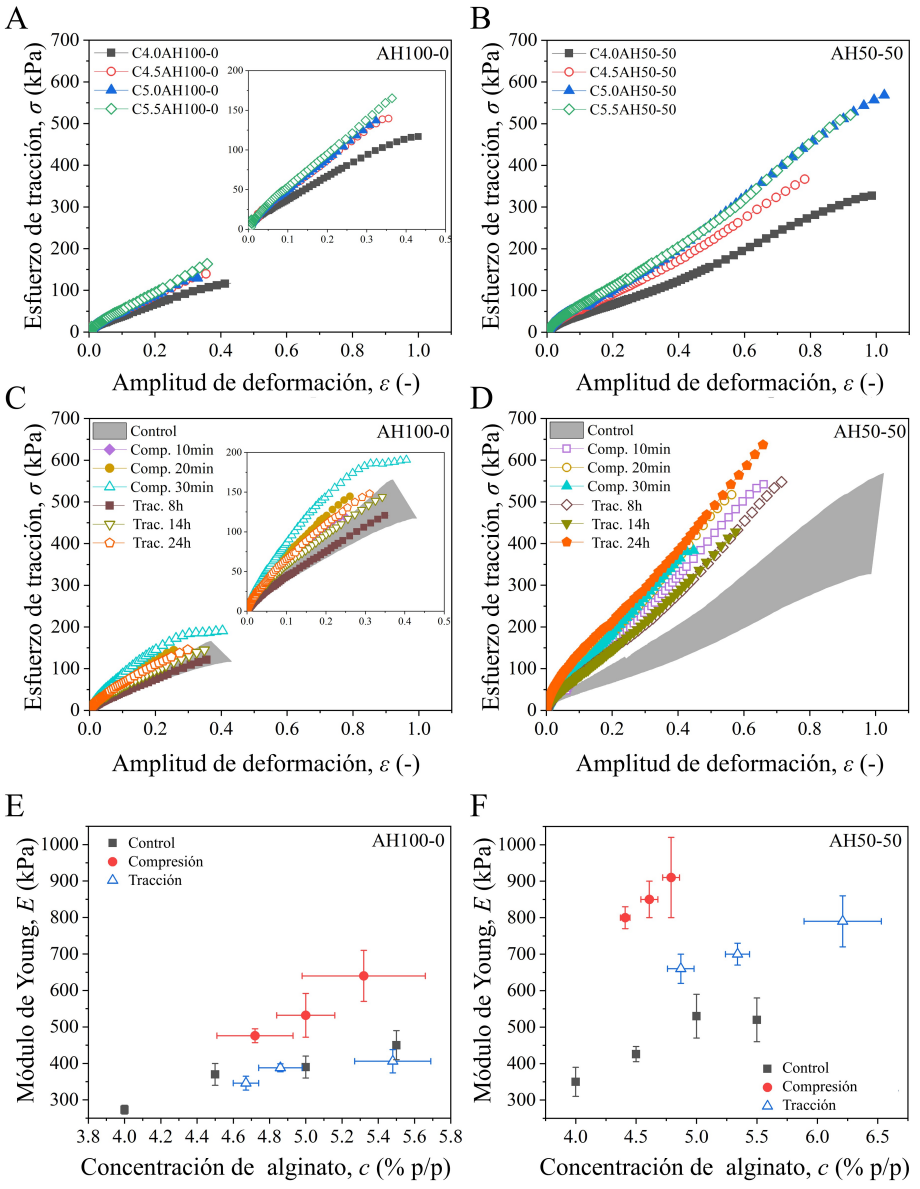

Figura 7.1: Resultados de la caracterización bajo tracción uniaxial. De A) a D) curvas de ejemplo del esfuerzo frente a la deformación para las distintas muestras estudiadas. A) y B) muestras de control de los dos tipos de hidrogeles de alginato (CYAH100-0 y CYAH100-0 donde Y es la concentración de alginato). Los recuadros muestran los mismos datos en diferentes escalas. C) y E) curvas del esfuerzo frente a la deformación para cada SCDP. Las bandas sombreadas representan los valores de las muestras de control. En E) y F), se muestran los valores del módulo de Young para cada SCDP y las concentraciones de alginato obtenidas después de la deshidratación, junto con los valores de las muestras de control. En todos los casos comparables se utilizan las mismas escalas en ambos ejes.

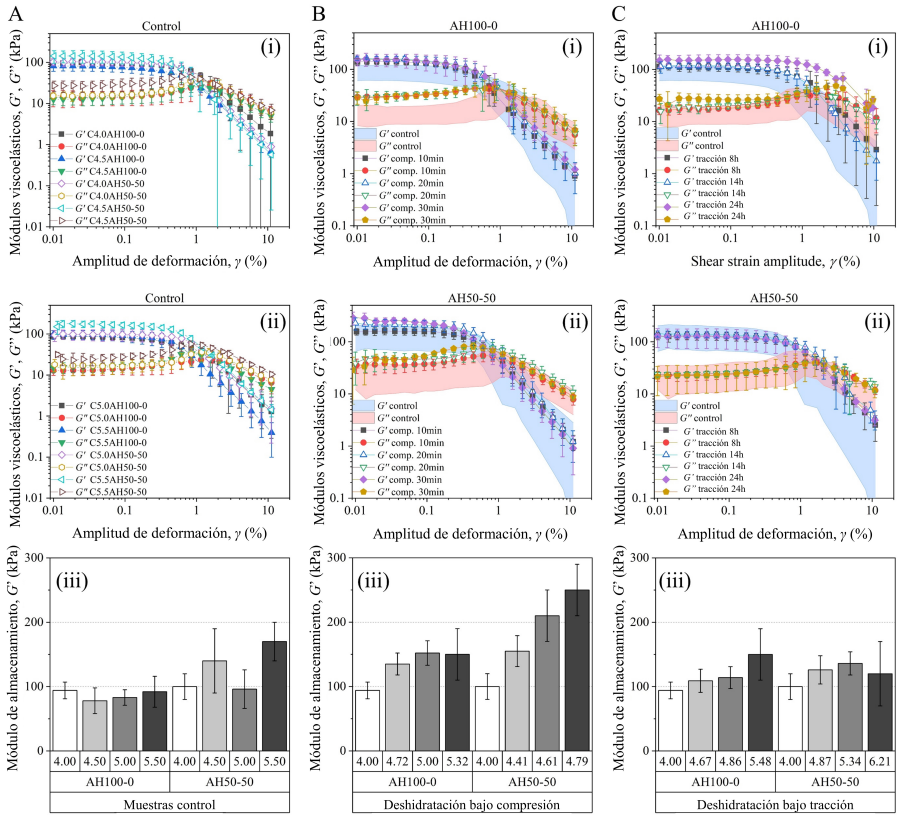

Figura 7.2: Resultados de la caracterización reológica bajo cizalla oscilatoria. Los datos en cada columna están relacionados con el esfuerzo aplicado durante la deshidratación: A) muestras de control (CYAH100-0 y CYAH100-0 donde Y es la concentración de alginato), B) muestras deshidratadas bajo esfuerzo de compresión y C) muestras deshidratadas bajo esfuerzo de tracción (los datos de las muestras AH100-0 fueron previamente presentados en [Gila Vilchez, 2022]). Los datos de las dos primeras filas presentan una comparación entre las curvas obtenidas para (i) AH100-0 y (ii) AH50-50, y en la tercera fila (iii), los valores del módulo de almacenamiento G' en función de la concentración de alginato. Las áreas en (B, (i)), (B, (ii)), (C, (i)) y (C, (ii)) representan los valores para las muestras de control. En todos los casos se utilizan las mismas escalas en ambos ejes.

efectos de la SCDP sobre los hidrogeles, se estudió su anisotropía desde un punto de vista mecánico, aunque sólo los hidrogeles deshidratados bajo esfuerzo de tracción pudieron caracterizarse en dos direcciones: paralela y perpendicular a la dirección del esfuerzo aplicado durante el SCDP.

Como se puede observar para ambos tipos de muestras (AH100-0 y AH50-50), el módulo de Young (Figura 7.3 A) en la dirección paralela a la tracción durante el SCDP es mayor que en la dirección perpendicular. La tensión de rotura (Figura 7.3 B) también demostró valores más grandes (aunque las diferencias sólo son significativas para las muestra AH50-50) en la dirección paralela con respecto a la dirección perpendicular. En cuanto a la deformación de rotura (Figura 7.3 C), se observó el

comportamiento inverso, con valores menores en la dirección paralela, aunque las diferencias observadas en este caso sólo son significativas para las muestras AH50-50.

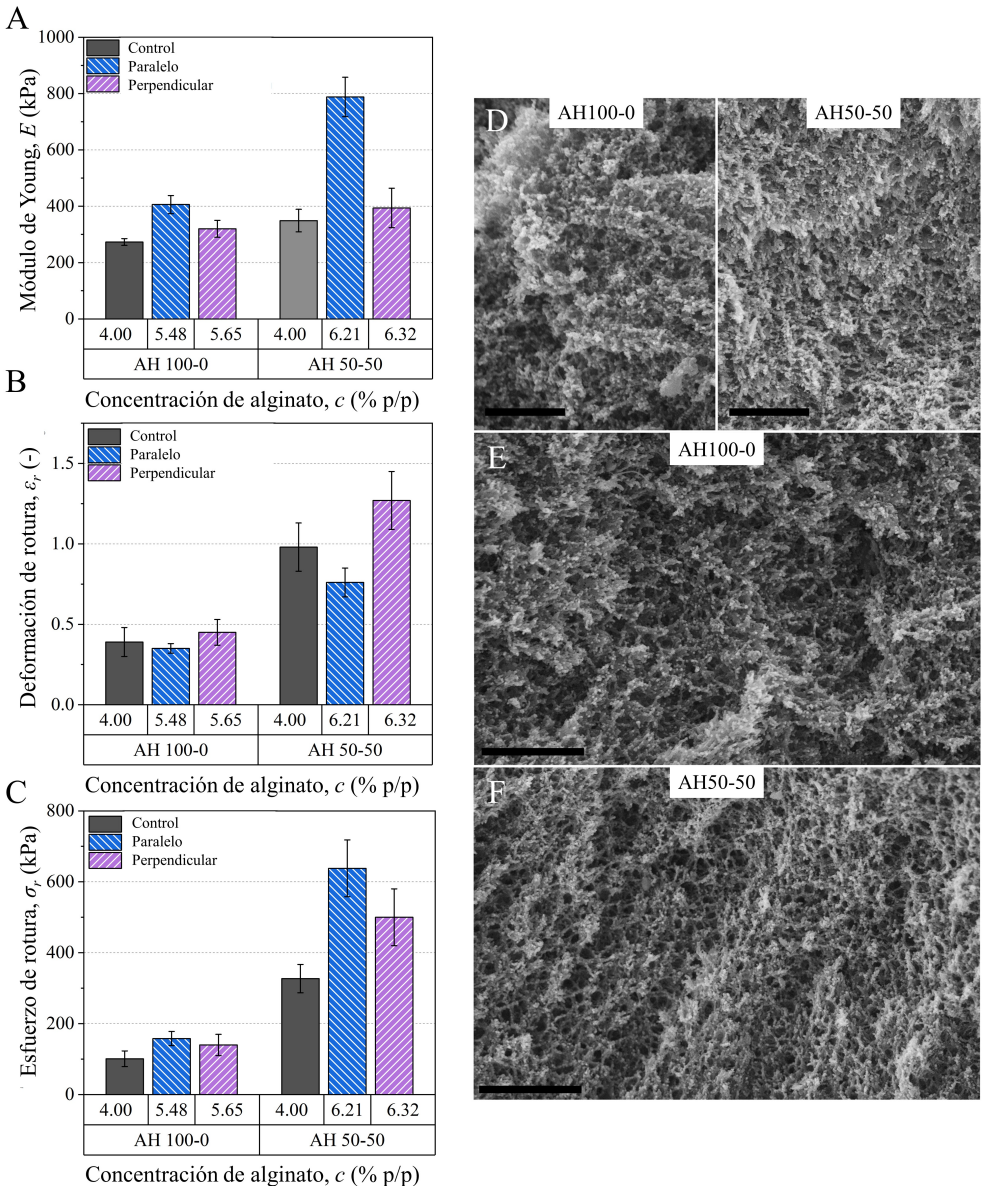

Figura 7.3: Módulo de Young (E), tensión de rotura (σ_r), deformación máxima en rotura (ϵ_r) y estructura microscópica de hidrogeles de alginato deshidratados bajo esfuerzo de tracción. En cada gráfico (A–C), de izquierda a derecha se muestra, el valor de las muestras de control, el valor en la dirección del esfuerzo durante el SCDP, y el valor en la dirección perpendicular. D) Imágenes SEM de AH100-0 y AH50-50 después de su preparación (vista cenital). E) y F) Imágenes SEM de las redes poliméricas de AH100-0 y AH50-50 (vista cenital), respectivamente, después de un proceso de deshidratación controlado bajo tracción durante 24 h. Las barras de escala representan 1 µm.

Con el fin de esclarecer esta anisotropía macroscópica, investigamos la estructura microscópica de las muestras utilizando microscopía SEM (Figura 7.3 D-F).Para las muestras de control, se obtuvieron estructuras porosas homogéneas e isótropas (Figura 7.3 D). Para las muestras sometidas a SCDP bajo esfuerzo de tracción, se observaron estructuras isótropas similares a las muestras de control en el caso de AH100-0 (Figura 7.3 E), mientras que se observaron bandas paralelas de polímeros en el caso de AH50-50 (Figura 7.3 F), lo que explicaría la anisotropía mecánica.

Efecto del SCDP bajo compresión en la respuesta de un actuador magnético

En esta subsección, investigamos si los SCDPs también pueden afectar positivamente la actuación magnética de los hidrogeles. En este caso nos centraremos únicamente en la deshidratación bajo esfuerzo de compresión. En la Tabla 7.3, se muestran las concentraciones de PMs y alginato después de la deshidratación de los hidrogeles magnéticos. La deshidratación bajo compresión provocó un aumento general en el módulo de Young (Figura 7.4 A). Bajo un campo magnético aplicado perpendicular al plano del actuador, los brazos del ferrogel se doblaron debido al momento de la fuerza magnética, que resultó en un movimiento en forma de pinza (Figura 7.4 B). Los brazos alcanza un equilibrio debido al balance entre los momentos de las fuerzas magnética, gravitatoria y elástica.

Tabla 7.3: Concentración de partículas magnéticas (Fe-CC) y concentración de alginato (c) de los diferentes hidrogeles tras una primera y segunda deshidratación (P.D. y S.D., respectivamente). En los nombres de las muestras MXAH, X indica la concentración de Fe-CC en % v/v.

	Fe-CC (% v/v)		c (% p/p)	
	P.D.	S.D.	P.D.	S.D.
M5AH	7.3 ± 1.4	8.0 ± 1.2	1.5 ± 0.3	1.7 ± 0.3
M7.5AH	9.7 ± 1.6	12.2 ± 2.5	1.33 ± 0.23	1.7 ± 0.4
M10AH	14.7 ± 1.2	18.4 ± 1.8	1.56 ± 0.15	2.03 ± 0.23
M20AH	26 ± 5	36 ± 6	1.4 ± 0.4	1.9 ± 0.6

Los experimentos demostraron la existencia de un valor umbral de la intensidad del campo magnético para obtener una respuesta del hidrogel (Figura 7.4 C). La existencia de este umbral de campo concuerda con el hecho de que el momento de la fuerza gravitatoria era máximo en la posición horizontal. En equilibrio, el momento de la fuerza gravitatoria debe estar compensado por el momento de la fuerza magnética tan pronto como el brazo del hidrogel magnético se separa del soporte. Cuando la intensidad del campo magnético superaba el valor umbral, se producía un aumento progresivo del ángulo de actuación (Figuras 7.4 C). Posteriormente, el ángulo de actuación se redujo progresivamente hasta cero al disminuir el campo magnético aplicado. En todos los casos, el ángulo obtenido al aumentar el campo magnético fue menor que el obtenido al disminuir el campo magnético, lo que indica la existencia de

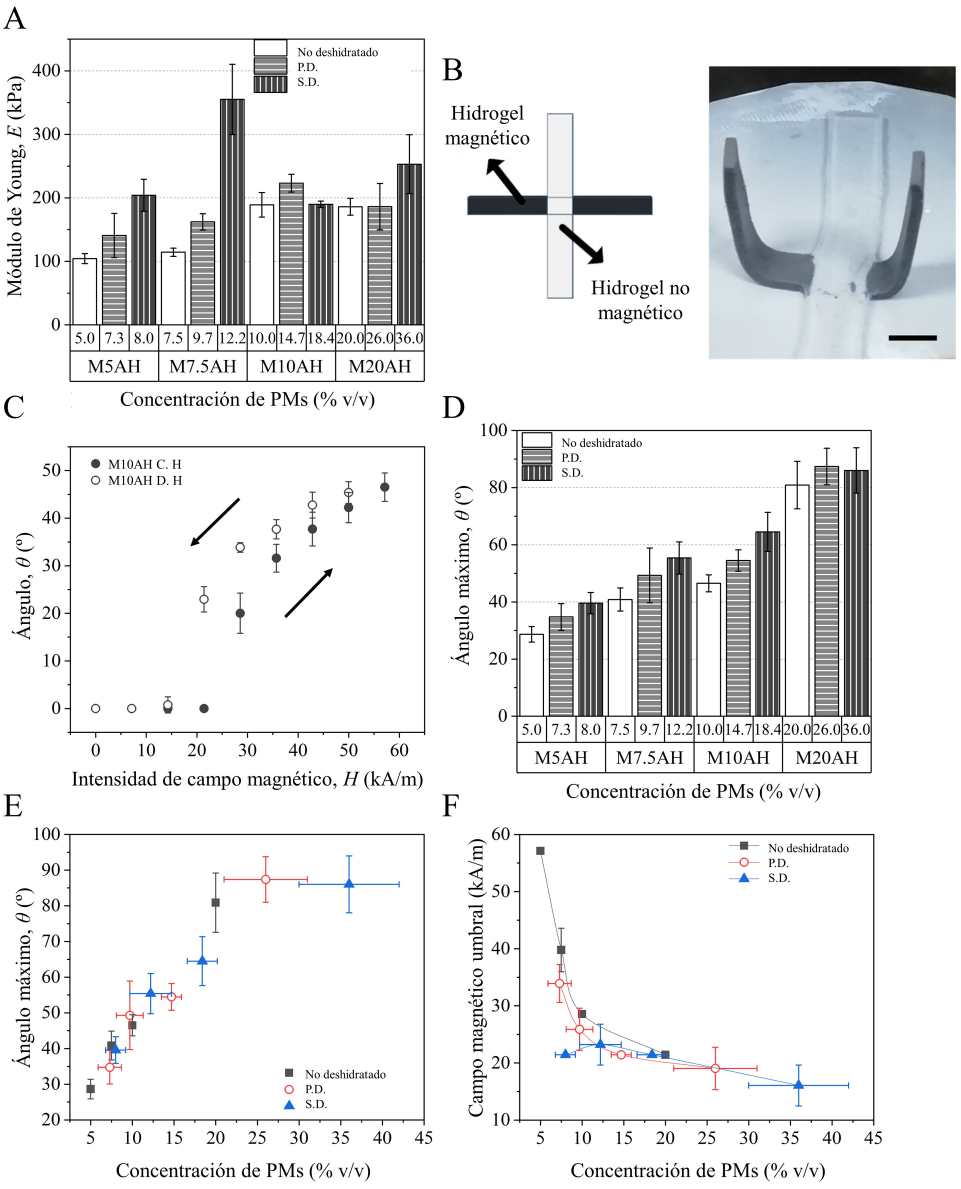

Figura 7.4: Propiedades mecánicas y respuesta magnética del actuador. A) Módulo de Young de la parte activa del actuador antes y después de los dos pasos de deshidratación bajo tensión de compresión. B) Croquis e imagen del actuador. La barra de escala es de 10 mm. C) Ángulo en función de la intensidad del campo magnético para un actuador no deshidratado con una concentración de partículas del 10% v/v. C.: Creciente; D.: Decreciente. D) Ángulo máximo alcanzado por el actuador para una intensidad de campo magnético de 57 kA/m. E) Ángulo máximo alcanzado por el actuador bajo un campo de 57 kA/m en función de la concentración de PMs. F) Campo magnético umbral en función de la concentración de PMs del actuador.

histéresis. Además, el valor umbral de la intensidad del campo magnético fue menor cuando la intensidad del campo se disminuyó que cuando se aumentó (Figura 7.4 C).

Para analizar el papel de la concentración de PMs y los procesos de deshidratación en el comportamiento de los actuadores en forma de cruz, es importante centrarse en dos magnitudes: el ángulo de equilibrio para el campo máximo aplicado (57 kA/m) y el valor umbral del campo magnético. En nuestro caso, el ángulo para el campo máximo aplicado aumentó con el contenido de partículas para todas las muestras (Figura 7.4 D). Los datos experimentales de todas las muestras se ajustaron a una única curva maestra (Figura 7.4 E). Con respecto a la intensidad umbral del campo magnético, esta disminuyó con la concentración de PMs (Figura 7.4 F). Además, los datos muestran una tendencia a disminuir en las muestras deshidratadas con respecto a las no deshidratadas. Este resultado indica que el SCDP tuvo una influencia positiva en la respuesta de los actuadores en forma de cruz.

Hidrogeles de alginato estructurados magnéticamente

Introducción

La hipótesis de partida de esta sección es la posibilidad de generar hidrogeles anisótropos mediante la aplicación de un campo magnético uniforme, para posteriormente analizar su estructura mediante microespectroscopia FT-IR. La validez de esta hipótesis se basa en resultados de dos trabajos previos [Kreuzer et al., 2022, Lopez-Lopez et al., 2015]. Para ello, se prepararon ferrogeles de alginato de sodio que incluían PMs recubiertas con grupos amino, que previamente han demostrado interacción atractiva con los polímeros de alginato [Barczak et al., 2020]. Los hidrogeles se colocaron bajo campos magnéticos uniformes durante las etapas iniciales del proceso de gelificación, con el fin de alinear las partículas y con ello las fibras poliméricas. Después de su preparación, los hidrogeles fueron analizados mediante microespectroscopia FT-IR en las instalaciones del sincrotrón ALBA. En los espectros, se analizaron los picos asociados con los modos de vibración del grupo carboxilo presente en las macromoléculas de alginato, teniendo en cuenta la polarización de la luz infrarroja y el tipo de recubrimiento en las PMs. Los resultados arrojaron luz sobre la disposición microscópica de las fibras de alginato, que presentaban un cierto grado de alineación tras aplicar el campo magnético.

Materiales y métodos

Materiales

Alginato MVSA. Carbonato de calcio, ($CaCO_3$), D-glucono-δ-lactona (GDL) y cloruro de calcio ($CaCl_2$) de Sigma Aldrich, EE. UU. Micropartículas de hierro recubiertas de sílice Fe-CC (B0). Ventanas de fluoruro de bario (BaF_2) de Crystran Limited, Reino Unido.

Funcionalización de partículas magnéticas

Las micropartículas Fe-CC funcionalizadas fueron proporcionadas por el doctor Mariusz Barczak, quien siguió el protocolo descrito en [Barczak et al., 2020]. Se usaron dos alcoxisilanos organofuncionales: aminopropiltrietoxisilano (APTES, I° amina, B1) y (3-trimetoxisilil propil) dietilentriamina (TPMMT, I° y II° amina, B2).

Síntesis de ferrogeles de alginato

Para sintetizar los ferrogeles de alginato, se partió de una disolución de alginato al 1 % p/p. Se preparó una mezcla de 99.32 p/p % de la disolución de alginato, 0.15 % p/p de $CaCO_3$ y 0.53 % p/p de GDL. En primer lugar, el $CaCO_3$ se dispersó en la disolución de alginato. Luego, el GDL se disolvió en la mezcla anterior usando un vórtex y un baño de ultrasonidos. Finalmente, se agregaron 0.4 % v/v de partículas de Fe-CC funcionalizadas a la mezcla previa, que se dispersaron y sonicaron para reducir la agregación.

Para realizar las medidas de microespectroscopia polarizada FT-IR, es necesario preparar muestras delgadas. Para ello, se utilizó un reómetro con una geometría plato-plato para controlar el espesor de las muestras y unos carretes de Helmholtz para aplicar un campo magnético uniforme durante el proceso de gelificación. Primero, se colocó una gota de la mezcla de pre-gel en la placa inferior del reómetro. Luego, se bajó el plato superior presionando la gota hasta alcanzar un espesor de 90 µm. Después de colocar la mezcla, se aplicó el campo magnético durante 15 min, después de los cuales, los hidrogeles continuaron gelificandose durante 45 min adicionales sin campo. Pasado este tiempo, se añadió una disolución de $CaCl_2$ 45 mM alrededor del plato superior para aumentar la densidad de entrecruzamiento del hidrogel, y después de un par de minutos se levantó el plato lentamente para anadir más $CaCl_2$ que se dejó otros 10 min en contacto con el gel. En la Tabla 7.4 se muestran todas las muestras preparadas y las condiciones experimentales.

Tabla 7.4: Ferrogeles de alginato preparados: grupo funcional de las PMs, campo magnético y concentración de PMs.

Nombre de la muestra	Funcionalización de PMs	Concentración de las PMs (v/v %)	Intensidad campo magnético (kA/m)
Ctrl-MF0	-	0	0
MB0-MF16	control B0	0.4	16
MB1-MF0	B1-APTES	0.4	0
MB1-MF8	B1-APTES	0.4	8
MB1-MF16	B1-APTES	0.4	16
MB2-MF16	B2-TMPET	0.4	16

Microespectroscopia FT-IR con radiación de sincrotrón

Las medidas de microespectroscopia FT-IR se llevaron a cabo en la línea de luz MIRAS del sincrotrón ALBA (Barcelona, España). La línea está equipada con un microscopio Hyperion 3000 acoplado a un espectrómetro Vertex 70 (Bruker, Alemania), donde la luz infrarroja del sincrotrón se enfocó en la muestra utilizando un objetivo Schwarzschild de 36$\times$ y un condensador. Los espectros se registraron con un detector MCT enfriado con nitrógeno líquido.

Ciertas áreas de las muestras se midieron utilizando dos polarizaciones diferentes: paralela a la alineación de las partículas (0°) y perpendicular a la alineación de las partículas (90°). Cada muestra se secó antes de las medidas para evitar bandas de absorción de agua. Para colocar las muestras en el microscopio se utilizaron dos métodos diferentes: 1) entre dos ventanas BaF_2; 2) dentro de una cámara de control ambiental y de temperatura (Linkam, Reino Unido). Además, se utilizaron diferentes aperturas, A, número de escaneos y número de puntos mapeados (Tabla 7.5).

Análisis de los espectros

El preprocesamiento y los análisis de los espectros obtenidos en el sincrotrón ALBA se realizaron utilizando el software Quasar. A los espectros se les aplicó una corrección de línea base y se normalizó al vector unitario en la región de números de onda de interés entre 900 cm^{-1} y 1800 cm^{-1}.

Resultados y discusión

Para observar cambios en la orientación de las cadenas de alginato, se analizaron las bandas de vibración del grupo carboxilo (COO^-) presentes en el alginato. En nuestro caso, el espectro promedio de un hidrogel de alginato no magnético seco se muestra en la Figura 7.5 A, en el que se han marcado dos picos: (a) alrededor de 1600

Tabla 7.5: Condiciones experimentales durante la microespectroscopia FT-IR usando radiación de sincrotrón en el sincrotrón ALBA. A es la apertura y Pol. la polarización.

Nombre muestra	Método	A (µm^2)	Pol. (°)	Escaneos	Puntos
Ctrl-MF0	Linkam	20×20	0	256	4
	Linkam	20×20	90		
MB0-MF16	Linkam	20×20	0	256	6
	Linkam	20×20	90		
MB1-MF0	BaF_2	8×8	0	128	25
	BaF_2	8×8	90		
MB1-MF8	BaF_2	8×8	0	128	96
	BaF_2	8×8	90		
MB1-MF16	Linkam	20×20	0	512	256
	Linkam	20×20	90		
MB2-MF16	BaF_2	10×10	0	128	400
	BaF_2	10×10	90		

cm^{-1}, y (b) alrededor de 1423 cm^{-1}. Estos dos picos corresponden a los modos de estiramiento asimétrico y simétrico del grupo carboxilo (Figura 7.5 B). La razón para elegir este grupo químico es que la interacción entre las PMs funcionalizadas y las fibras de alginato, se debe a que la carga positiva en la superficie de las partículas interacciona con la carga negativa en los grupos carboxilo de los polímeros. Como resultado, la alineación de las partículas se reflejará en la orientación de este grupo y, por tanto, de las cadenas de alginato. Para analizar estos resultados, se calcularon las razones de las áreas bajo cada pico de ambas polarizaciones ($Area_0/Area_{90}$). Estas proporciones indican si hay un cambio en la orientación del grupo químico si son mayores o menores que uno.

En primer lugar, el análisis de los resultados se centra en el efecto de la presencia de PMs funcionalizadas en los espectros. Para ello, se realizó una comparación entre un hidrogel no magnético (Ctrl-MF0) y uno con PMs B1 (MB1-MF0) (Figura 7.6). Según la Figura 7.6 A y B, las razones de las áreas de los picos de 1600 cm^{-1} y 1423 cm^{-1} son cercas a uno y el valor es bastante homogéneo a lo largo del área de análisis como es de esperar en este caso. Sin embargo, cuando se incluyeron PMs B1 en los hidrogeles, la homogeneidad de los valores de las razones cambió del orden del 10 %. En este caso, estas diferencias reflejan que los grupos carboxilo no están distribuidos aleatoriamente como en Ctrl-MF0, sino que están unidos a las partículas y, en algunos casos, orientados en cierta medida.

Después de discutir el efecto de la presencia de PMs funcionalizadas, el análisis se centra en el efecto de la intensidad del campo magnético. En la Figura 7.7 se muestran las razones para los picos de diferentes áreas de ferrogeles anisótropos con PMs B1 alineadas bajo 8 kA/m y 16 kA/m. En las imágenes visibles de las áreas medidas (Figura 7.7 C y D), se observan estructuras en forma de cadena de PMs, pero

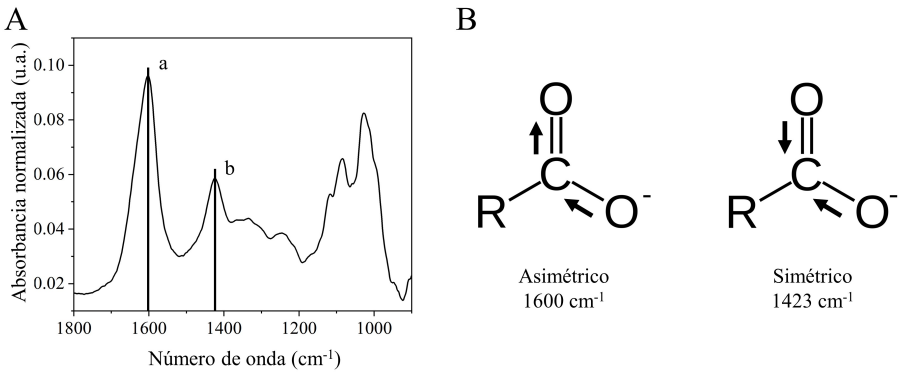

Figura 7.5: A) Espectro FT-IR promedio de un hidrogel de alginato no magnético seco, en el que se marcan dos picos de interés: (a) alrededor de 1600 cm^{-1}, y (b) alrededor de 1423 cm^{-1}. Estos picos están relacionados, respectivamente, con los modos de estiramiento asimétrico y simétrico de los grupos carboxilo (COO-) presentes en las macromoléculas de alginato B). Dependiendo de la muestra, estos picos pueden estar ligeramente desplazados.

no hay diferencias apreciables entre las dos muestras. Sin embargo, las regiones entre cadenas en MB1-MF16 están altamente pobladas con agregados aislados de PMs. En el caso de la muestra MB1-MF8, se observa un comportamiento interesante para el pico de 1600 cm^{-1}. En la región medida que se encuentra entre dos cadenas de partículas, si se espera observar una orientación del grupo COO^{-}, se debe observar un cambio anisótropo en la razón del pico. En este caso esto es evidente, ya que se observa una disminución en la razón en la mitad superior, mientras que se produce un aumento en la mitad inferior. Por otra parte, en el mapeo del pico 1423 cm^{-1}, no hay cambios significativos asociados con las cadenas de partículas.

Cuando el campo aumenta de 8 kA/m a 16 kA/m en el área medida, los cambios no son tan notables salvo para el pico de 1600 cm^{-1}. Sin embargo, cerca de las cadenas a 1600 cm^{-1}, generalmente se observa una disminución en la razón, pero esto no es lo suficientemente claro debido a la apertura usada. La falta de claridad en estos resultados puede atribuirse a dos hechos. Primero, el área bajo análisis para cada punto es lo suficientemente grande como para perder los detalles observados para MB1-MF8 (*cf.* Tabla 7.5). En segundo lugar, la presencia de agregados aislados de PMs en toda la muestra puede ocultar la orientación del grupo carboxilo debido al tamaño del área promediada.

Finalmente, se compararon dos ferrogeles anisótropos con PMs no funcionalizadas (B0) y funcionalizadas (B2) preparadas bajo un campo magnético de 16 kA/m. En la muestra MB0-MF16, se obtuvieron resultados similares a los de Ctrl-MF0. Ello indicaría que las partículas sin funcionalizar no interaccionan con las fibras de alginato, por lo tanto, no se observó orientación del grupo COO^{-}. En el caso de MB2-MF16, existen problemas similares a los que se encontraron en MB1-MF16.

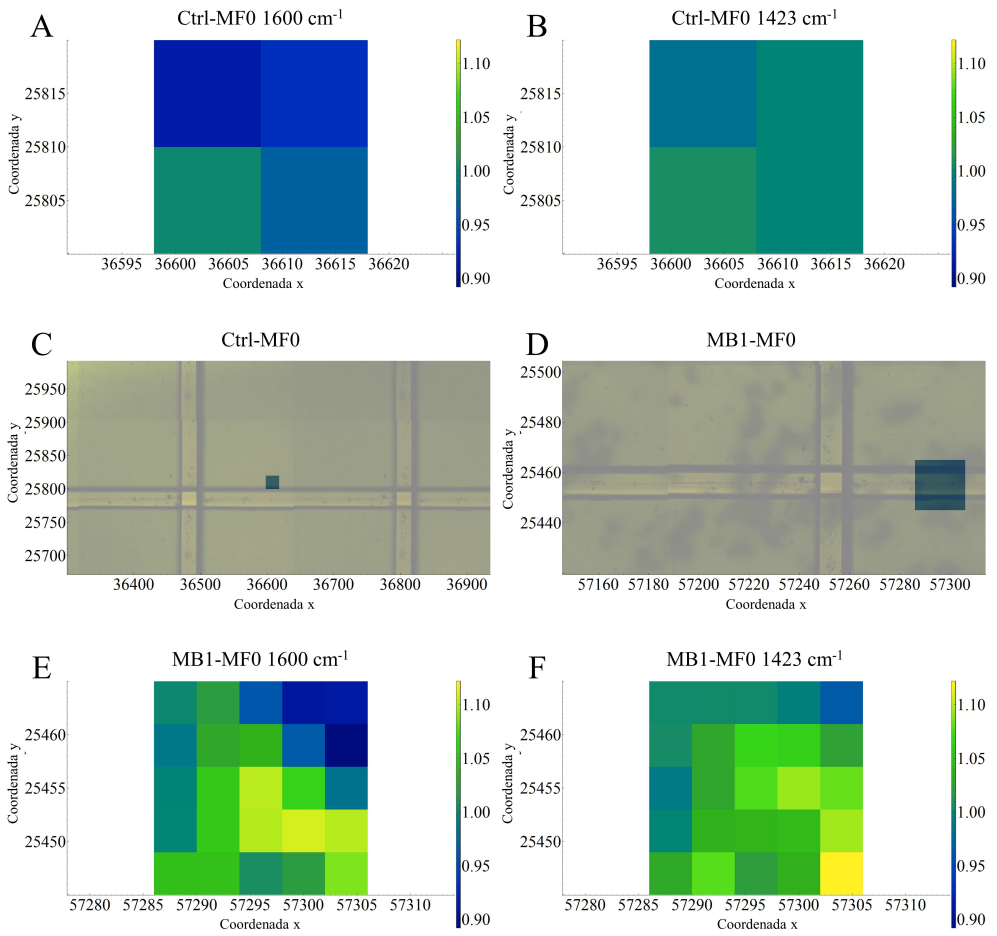

Figura 7.6: A) y B) Razones de los picos 1600 cm^{-1} y 1423 cm^{-1} de un hidrogel de alginato no magnético. C) Imagen visible de la región analizada en el hidrogel de alginato no magnético. D) Imagen visible de la región analizada en un ferrogel de alginato isótropo con PMs B1. E) y F) Relaciones de picos de 1600 cm^{-1} y 1423 cm^{-1} del ferrogel de alginato isótropo con PMs B1. Las coordenadas están dadas en µm. En las imágenes visibles, el rectángulo azul delimita el área medida. El color amarillo se debe al polarizador y las franjas horizontales y verticales son la apertura del microscopio, que no se retiraron cuando se tomaron las imágenes.

Redes poliméricas semi-interpenetradas de acrilamida y biopolímeros

Introducción

En esta sección, estudiaremos redes poliméricas semi-interpenetradas (SIPNs) formadas por una red entrecruzada de acrilamida y N,N'-metilenbisacrilamida, junto

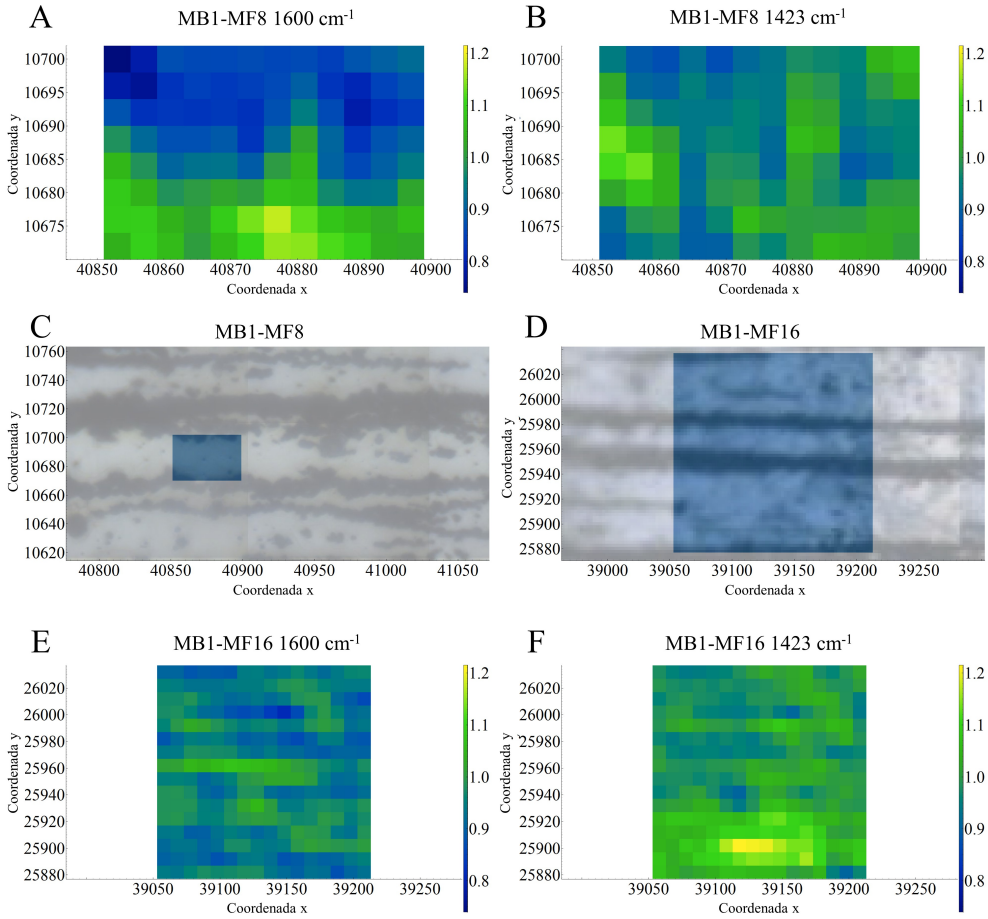

Figura 7.7: A) y B) Razones de los picos de 1600 cm^{-1} y 1423 cm^{-1} de un ferrogel anisótropo con PMs B1 alineadas bajo un campo magnético de 8 kA/m. C) Imagen visible de la región analizada en el ferrogel con PMs B1 alineadas bajo 8 kA/m. D) Imagen visible de la región analizada en un ferrogel de alginato anisótropos con PMs B1 alineadas bajo un campo magnético de 16 kA/m. E) y F) Razones de los picos de 1600 cm^{-1} y 1423 cm^{-1} del ferrogel de alginato isótropo con PMs B1 alineadas a 16 kA/m. Las coordenadas están dadas en µm. En las imágenes visibles, el rectángulo azul delimita el área medida.

con un biopolímero natural. Estos hidrogeles se utilizaron para preparar SIPNs magnéticas (Mag-SIPN) con excelente capacidad de deformación, alto contenido de agua, y una buena respuesta a campos magnéticos. Esta capacidad de respuesta magnética se consiguió incorporando micropartículas de hierro, sin que esto supusiera un debilitamiento sustancial de las propiedades mecánicas de estos materiales.

Por otro lado, se evaluó el rendimiento y la estabilidad de estas Mag-SIPNs como sensor de oxígeno luminiscente controlable por un campo magnético externo. Para ello, diseñamos un hidrogel en forma de disco formado por un círculo interior no

magnético que contenía nanopartículas luminiscentes sensibles al O_2 y un anillo magnético exterior. Gracias a la capacidad de respuesta magnética de la Mag-SIPN, el sensor pudo fijarse firmemente dentro de la celda de medida desde el exterior mediante un sistema de imanes coaxiales. Esto permitió una lectura sencilla y correcta de la señal luminiscente. Con esto conseguimos solucionar uno de los principales problemas de las medidas ópticas de O_2 en sistemas líquidos, la falta de fijación del sensor en la celda de medida.

Materiales y métodos

Materiales

Acrilamida (AAm), N,N'-metilenbisacrilamida (Bis-AAm), 2-hidroxietilcelulosa $M_v \sim 720000$ (HC720), 2-hidroxietilcelulosa $M_v \sim 1300000$ (HC1300), carboximetilcelulosa de sodio de alta viscosidad (CChigh), carboximetilcelulosa de sodio de viscosidad media (CCmedium,), N,N,N',N",N"-pentametildietilentriamina (PMDTA) y octaetilporfirina de platino (PtOEP; sonda luminiscente O_2; λ_{exc} = 380 nm, λ_{em} = 650 nm) de Sigma Aldrich (EE.UU.). Alginato MVSA. Lauril sulfato de sodio (SDS), cloroformo ($CHCl_3$) e hidróxido de sodio (NaOH) de Scharlau (España). Poli(anhídrido estireno-co-maleico; 7 % de anhídrido maleico, M_w=80000 Da) de ARKEMA Sartomer (Francia). Micropartículas de hierro micrométrico recubiertas de sílice (Fe-CC). Todas las disoluciones se prepararon en agua milli-Q.

Síntesis de las Mag-SIPNs

En primer lugar, se prepararon por separado disoluciones acuosas al 1.67 % p/p de alginato de sodio, 2-hidroxietilcelulosa y carboximetilcelulosa de sodio. Posteriormente, se añadieron micropartículas de Fe-CC a las disoluciones poliméricas. Las mezclas resultantes se sonicaron durante 15 minutos, seguido de agitación mecánica hasta que se formaron suspensiones homogéneas (1 h). Posteriormente, se disolvieron Bis-AAm y AAm en agua, que se mezcló con las suspensiones de Fe-CC bajo agitación mecánica durante 1h. Finalmente, se añadió una disolución del iniciador térmico (KPS, 10 mg/mL) y del acelerante (PMDTA) a las mezclas de Bis-AAm/Aam/Fe-CC/biopolímero. Tras homogeneizarlas, se gelificaron en un horno a 50 °C hasta el día siguiente. Las concentraciones de los compuestos utilizados fueron: 87.89 % p/p de agua milli-Q, 0.89 % p/p de biopolímero, 0.13 % p/p de Bis-AAm, 11.02 % p/p de AAm, 0.07 % p/p de KPS, y 0.11 µmol/g de PMDTA (todas estas concentraciones se dan con respecto a la mezcla total sin partículas). Las concentraciones de Fe-CC fueron 6.4, 12.0, 17.2, 21.9 y 26.2 % p/p (con respecto a la masa total de hidrogel).

Tabla 7.6: Biopolímeros naturales utilizados para sintetizar las diferentes Mag-SIPNs junto con el nombre utilizado a lo largo de la sección y las diferentes concentraciones de PMs empleadas en cada caso.

Biopolímero	Nombre Mag-SIPN	Concentración PMs (% p/p)
Alginato de sodio (viscosidad media)	Alginate	6.4, 12.0, 17.2, 21.9, 26.2
Carboximetilcelulosa de sodio (viscosidad media)	CCmedium	6.4
Carboximetilcelulosa de sodio (alta viscosidad)	CChigh	6.4
2-Hidroxietilcelulosa ($M_v \sim 720000$)	HC720	6.4
2-Hidroxietilcelulosa ($M_v \sim 1300000$)	HC1300	6.4

Caracterización de las propiedades mecánicas

Las propiedades reológicas bajo cizalla oscilatoria se determinaron a una temperatura constante de 25 $\pm$ 1 °C utilizando un reómetro MCR300 Physica, equipado con una geometría plato-plato de 20 mm de diámetro. La zona viscoelástica lineal (ZVL) se determinó sometiendo los hidrogeles a barridos de amplitud de deformación a una frecuencia constante de 1 Hz y aumentando gradualmente la amplitud de deformación (γ). A partir de estas curvas, se calcularon los valores medios de G' y G'' correspondientes a la ZVL. Posteriormente, se midieron G' y G'' frente a la frecuencia realizando barridos de frecuencia a una amplitud de deformación constante (γ_0 = 0.3 %) dentro del ZVL y aumentando la frecuencia de 0.1 a 10 Hz. El comportamiento mecánico de los hidrogeles bajo esfuerzos de tracción y compresión se determinó a temperatura ambiente utilizando un reómetro Discovery HR-1 y una máquina de pruebas universal Instron 3345, respectivamente. Para la caracterización bajo esfuerzo de tracción, las muestras se prepararon con forma de mancuerna. Una vez que los hidrogeles se fijaron en la geometría, se aplicó una ligera fuerza axial de 0.01 N para alcanzar una condición inicial uniforme para todas las muestras y asegurar una transmisión de la fuerza homogénea al comienzo de la medida. Durante la medida, los hidrogeles se deformaron a una velocidad constante de 50 µm/s hasta su rotura. Luego, a partir de las curvas de esfuerzo frente a la deformación, se obtuvieron el módulo elástico bajo tracción y la deformación de rotura. El módulo elástico bajo tracción se calculó como la pendiente de la regresión lineal del esfuerzo frente a la deformación desde una deformación del 10 % hasta su rotura. La deformación en rotura se obtuvo como el valor del último punto de las curvas antes de la rotura de la muestra. Para las medidas bajo compresión, los materiales se caracterizaron utilizando una geometría plato-plato. En este caso, los hidrogeles se prepararon con

forma cilíndrica y el proceso de medida se realizó en las mismas condiciones que la caracterización bajo tracción pero cambiando la dirección de la fuerza. El análisis de los resultados fue similar al del caso de tracción, con la única diferencia de que el módulo elástico bajo compresión se determinó sólo para deformaciones inferiores al 20 %.

Sensor magnético luminiscente de O_2 (ML-OSen)

Los hidrogeles para el sensor de oxígeno fueron preparados siguiendo los pasos descritos anteriormente, utilizando HC720 como biopolímero. En este caso, fue necesario un cambio en el protocolo para evitar el excesivo hinchamiento de los hidrogeles. Para ello, se aumentó la concentración del agente entrecruzante (Bis-AAm) en un factor cuatro para el hidrogel no magnético y en un factor ocho para el hidrogel magnético. El sensor estaba formado por dos partes diferenciadas: una magnética y otra sensora no magnética. Primero, el hidrogel magnético, con forma cilíndrica, se preparó con una concentración de Fe-CC del 26.2 % p/p. A continuación, se perforó en el ferrogel un orificio cilíndrico de un diámetro de 8 mm. Posteriormente, se preparó una mezcla de pre-gel sustituyendo partículas magnéticas por nanopartículas luminiscentes sensibles al O_2 (Lu-NP) en una concentración del 2.0 % p/p con respecto a la masa total del polímero. Esta mezcla se vertió en el orificio previamente perforado en el ferrogel y el sistema se gelificó a 50 °C durante toda la noche. Después de la gelificación, la muestra cilíndrica se cortó en discos con un espesor de 2 mm.

Las Lu-NP antes mencionadas (99 $\pm$ 7 nm de diámetro) se prepararon encapsulando PtOEP en poli(estireno-co-anhídrido maleico; 7 % anhídrido maleico) mediante evaporación de disolvente en una miniemulsión siguiendo el protocolo descrito en [Mistlberger et al., 2010]. La superficie de las Lu-NPs fue hidrolizada con NaOH (potencial Z de 60.0 $\pm$ 0.6 mV).

Resultados y discusión

Caracterización mecánica de las Mag-SIPNs de alginato

Se llevó a cabo una caracterización exhaustiva de las propiedades mecánicas de las Mag-SIPNs de alginato bajo diferentes esfuerzos (cizalla oscilatoria, compresión y tracción). Los barridos de amplitud de deformación demostraron el comportamiento típico de un material viscoelástico tipo gel.

En primer lugar, se investigó el efecto de la incorporación de PMs en las SIPNs de alginato. En la Figura 7.8 A y B se encuentran los valores promedio de los módulos viscoelásticos dentro de la ZVL para concentraciones de micropartículas de hierro que van desde 6.4 a 26.2 % p/p. Como se observa, existe una disminución de G'

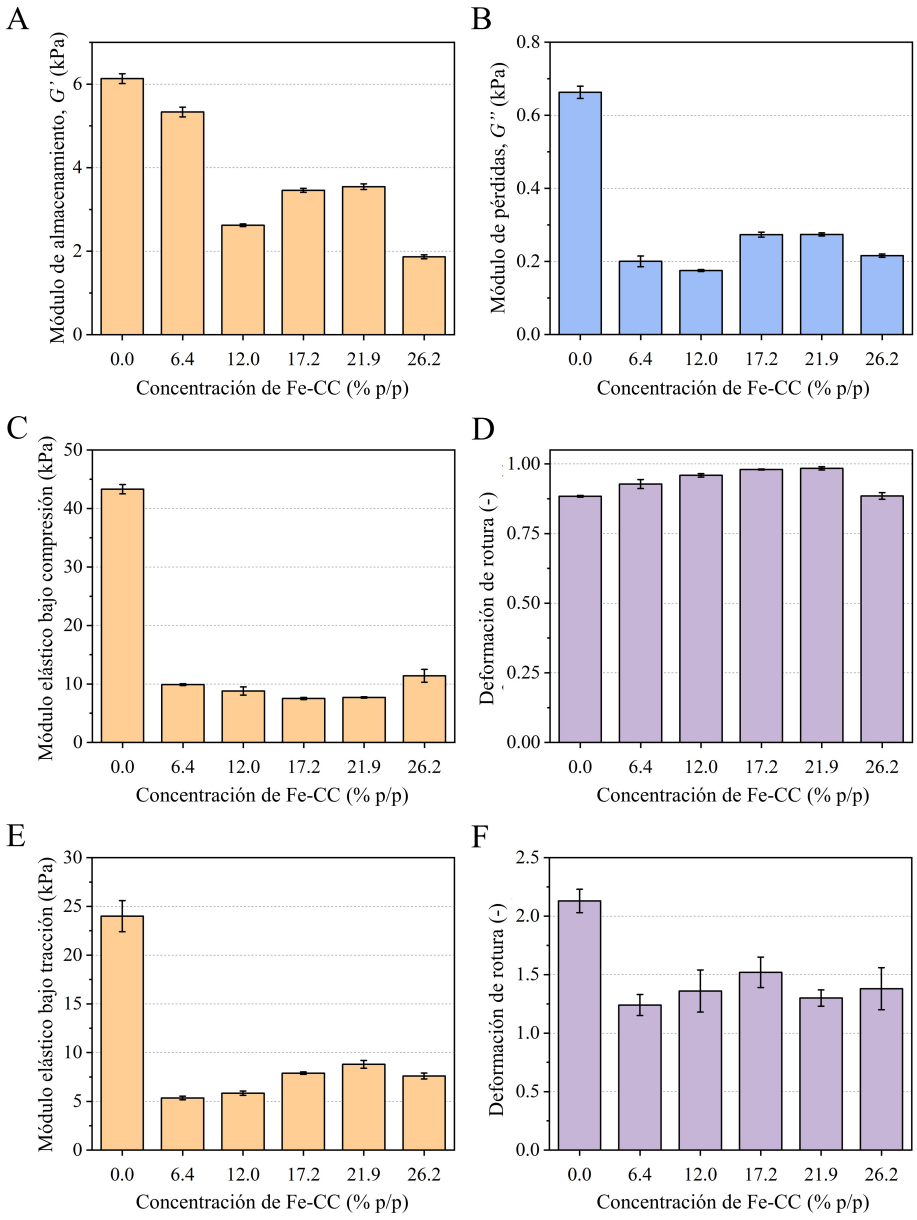

Figura 7.8: Propiedades mecánicas de las Mag-SIPNs de alginato con una cantidad fija de acelerante PDMTA (0.11 µmol/g) y concentraciones PMs de 0.0 % a 26.2 % p/p. Módulo de almacenamiento G' A) y módulo de pérdidas G'' B) correspondientes a la ZVL. Módulo elástico C) y deformación de rotura D) obtenidos bajo esfuerzo de compresión. Módulo elástico E) y deformación de rotura F) obtenidos bajo esfuerzo de tracción.

para los hidrogeles que contienen entre 12.0 y 26.2 % p/p de PMs. Esto indica que la presencia de partículas parece afectar al proceso de polimerización, y por tanto, a las propiedades mecánicas finales del hidrogel. Por otra parte, las Mag-SIPN de alginato

también se caracterizaron bajo esfuerzos de compresión y tracción. Como se observa, cuando se agregan micropartículas de hierro al hidrogel, se produce una disminución considerable en los módulos elásticos bajo ambos esfuerzos (Figura 7.8 C y E), lo que indica una disminución en la rigidez de los materiales.

Otro parámetro mecánico relevante es la deformación de rotura. Para los hidrogeles de alginato (Figura 7.8 D y F), se observaron dos comportamientos diferentes según el tipo de esfuerzo aplicado. Para las medidas bajo esfuerzo de compresión (Figura 7.8 D), hubo principalmente un ligero aumento en la deformación de rotura con el contenido de PMs, con un máximo para 17.2 y 21.9 % p/p –remarcar la enorme compresibilidad de las Mag-SIPNs que pueden comprimirse hasta un máximo de aprox. 98 % de su altura inicial. Para las medidas bajo esfuerzo de tracción, se observó el comportamiento inverso, con una disminución sustancial en la deformación de rotura (aproximadamente de 210 % a 140 %) cuando se incluyeron PMs. Esta diferencia de comportamiento cuando las muestras fueron sometidas estos esfuerzos probablemente estuvo relacionada con el efecto en la red polimérica de las PMs, que provocan defectos en ella. Las medidas bajo esfuerzo de tracción son más sensibles a estos defectos en la red, mientras que las ligeras mejoras bajo esfuerzo de compresión pueden deberse a la oposición de las PMs a ser comprimidas.

Propiedades mecánicas de las Mag-SIPNs con diferentes biopolímeros

Para modular las propiedades mecánicas de las Mag-SIPNs, el alginato fue reemplazado por otros biopolímeros con diferentes propiedades fisicoquímicas (consultar la Tabla 7.6). En el caso de los hidrogeles no magnéticos, se observó un aumento en el módulo de almacenamiento con el peso molecular del polímero para los hidrogeles con hidroxietilcelulosa (HC720 o HC1300), aunque no se obtuvieron diferencias con respecto a los hidrogeles con alginato (Figura 7.9 A y B). Para los hidrogeles con celulosa con grupos carboxilo (CCmedium o CChigh), se observó una notable disminución en G' con respecto a los otros hidrogeles no magnéticos. En todos los casos, G' disminuyó con la adición de PMs, observándose el valor más alto para el alginato y obteniéndose valores similares para todas las celulosas.

También se realizó una caracterizaron bajo esfuerzos de compresión y tracción (Figura 7.9). Para los hidrogeles no magnéticos, el valor más alto del módulo elástico bajo compresión se obtuvo para los sistemas con HC1300 o alginato, mientras que se observó una disminución sustancial para los materiales con los otros biopolímeros (Figura 7.9 C). Se observó algo distinto para las medidas bajo esfuerzo de tracción, siendo los hidrogeles con alginato, CCmedium y CChigh los que exhibieron el módulo elástico bajo tracción más alto (Figura 7.9 E). Además, la introducción de PMs resultó en una reducción sustancial de los módulos elásticos en todos los casos. Para la deformación de rotura (Figura 7.9 D y F), no se observaron diferencias significativas para los diferentes hidrogeles no magnéticos, aunque se obtuvieron

valores ligeramente superiores para los hidrogeles con celulosa bajo esfuerzo de tracción. La adición de PMs no causó cambios sustanciales en esta magnitud bajo esfuerzo de compresión, mientras que resultó en una disminución bajo esfuerzo de tracción.

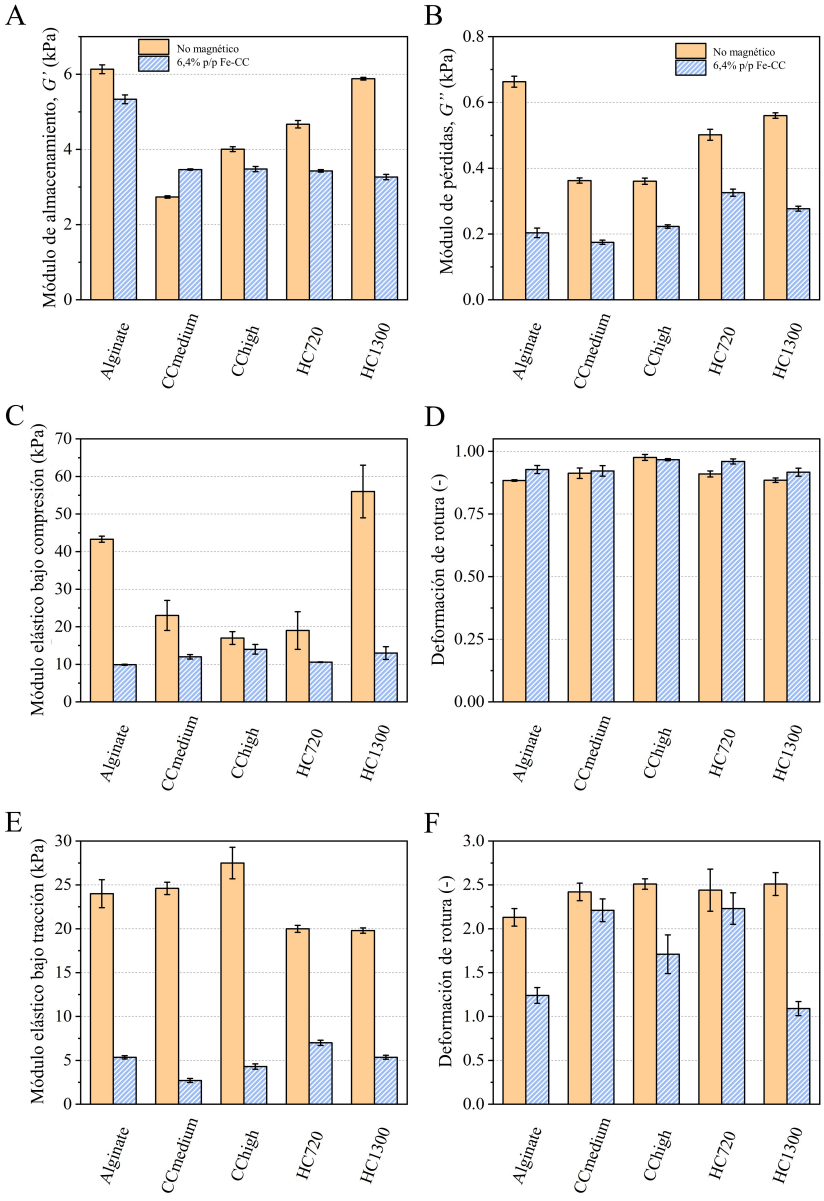

Figura 7.9: Propiedades mecánicas de las SIPNs (no magnéticas y magnéticas) con diferentes biopolímeros y con una cantidad fija de acelerante PDMTA (0.11 µmol/g). Módulo de almacenamiento G' A) y módulo de pérdidas G'' B) correspondientes a la ZVL. Módulo elástico C) y deformación de rotura D) obtenidos bajo esfuerzo de compresión. Módulo elástico E) y deformación a la rotura F) obtenidos bajo esfuerzo de tracción.

En resumen, el rendimiento mecánico de las SIPNs (magnéticos y no magnéticos) depende no sólo del tipo de biopolímero sino también de su peso molecular medio. Las Mag-SIPNs mostraron valores más pequeños de módulo de almacenamiento y módulos elásticos, manteniendo una alta deformabilidad. Esta combinación de módulos elásticos bajos con alta capacidad de deformación los convierte en materiales ideales para aplicaciones que requieren maximizar la deformación bajo estímulos externos [Liu et al., 2020b].

Caracterización morfológica y magnética de las Mag-SIPNs

Algunas Mag-SIPNs presentaban un gradiente macroscópico en la concentración de partículas (Figura 7.10 A). Es interesante observar que las Mag-SIPN con celulosa de alto peso molecular (CChigh y HC1300) no mostraron ningún gradiente apreciable en la concentración de PMs, mientras que aquellas con polímeros de bajo peso molecular (HC720 o Alginate) mostraron un gradiente visible. Las imágenes de microscopía electrónica de barrido (SEM) de las Mag-SIPNs (Figura 7.10 B) revelaron la presencia de agregados de PMs rodeadas por polímeros. La inclusión de estas partículas en la matriz del hidrogel produjo un ligero aumento en la porosidad de la red, posiblemente debido a la interferencia de estas partículas con el proceso de polimerización y porque parte del polímero se encuentra recubriendo las partículas y no formando parte de la red tridimensional. Este efecto no se observó en los hidrogeles que no contenían PMs (Figura 7.10 C).

La capacidad de hinchamiento de los hidrogeles (magnéticos y no magnéticos) se estudió midiendo su masa ($M_H(t)$)) a lo largo del tiempo después de estar sumergidos en agua mili-Q (Figura 7.10). El grado de hinchamiento se cuantificó mediante la siguiente ecuación:

$$Q(t) = \frac{M_H(t) - M_H(t=0)}{M_H(t=0)} \tag{7.1}$$

Se observaron diferencias en el grado de hinchamiento cuando se utilizaron diferentes biopolímeros. Los hidrogeles con alginato o carboximetilcelulosa mostraron una mayor capacidad de absorción de agua que los hidrogeles con hidroxietilcelulosa, independientemente del peso molecular. Cabe destacar el mayor hinchamiento de las Mag-SIPNs (valores máximos de Q de aproximadamente 28) en comparación con las SIPNs no magnéticas (valores máximos Q de aproximadamente 2)(Figura 7.10 D y E). Además, mientras que la absorción de agua de las SPINs no magnéticos llegaron a la saturación dentro de las primeras 24 h, las Mag-SIPNs mantuvieron su capacidad de absorber agua durante más tiempo (48-72 h).

Las curvas de magnetización de las Mag-SIPN demostraron un comportamiento ferromagnético blando típico con valores de remanencia y coercitividad pequeños, de forma similar al caso de las partículas Fe-CC.

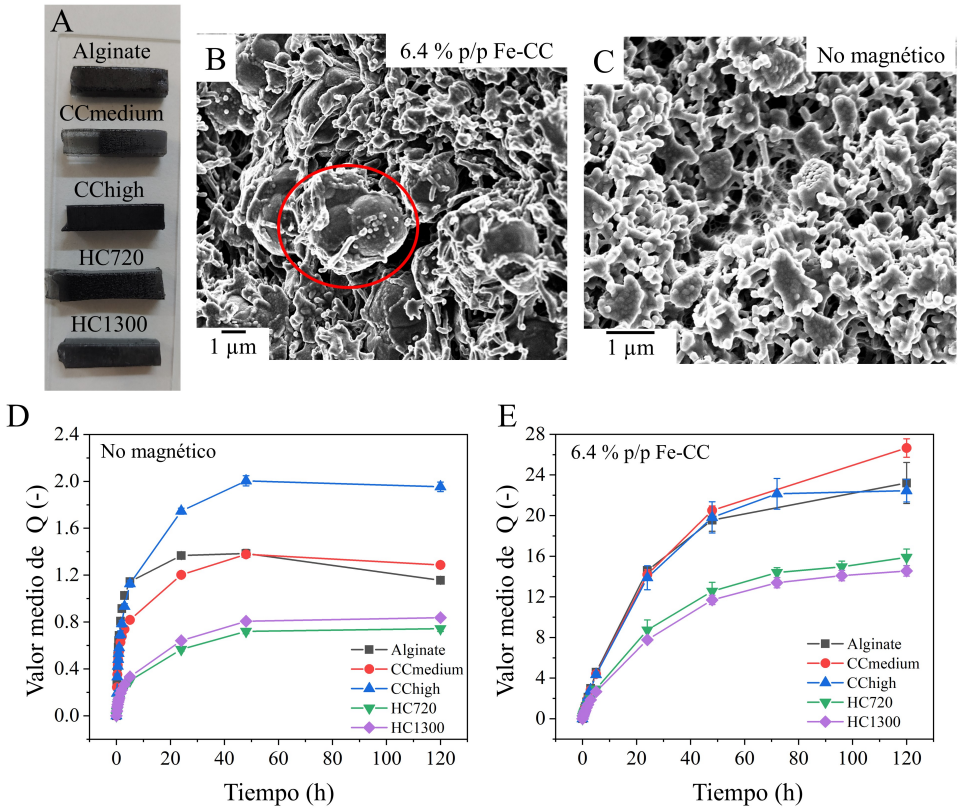

Figura 7.10: A) Mag-SIPNs que contienen 26.4 % p/p de micropartículas de hierro. En algunos casos se puede observar un gradiente de partículas. B) y C) Imágenes SEM de la estructura interna de una SIPN de HC720, con una concentración de Fe-CC de 6.4 % p/p y sin micropartículas magnéticas, respectivamente. Una PM están marcadas con un círculo rojo. D) y E) Grado de hinchamiento en función del tiempo, D) para las SIPNs no magnéticas y E) para las Mag-SIPNs con una concentración de PMs del 6.4 % p/p.

Sensor magnético luminiscente de O_2 (ML-Osen)

En esta subsección estudiamos un sensor de oxígeno luminiscente (ML-Osen) fabricado usando Mag-SIPNs. Dicho sensor puede controlarse gracias a la fuerte respuesta magnética de un anillo de ferrogel externo, que rodea la región interna sensible al O_2 (Figura 7.11 A).

Para fabricar el ML-OSen, se seleccionó el biopolímero neutro HC720 para evitar la agregación debido a la repulsión entre las Lu-NP cargadas negativamente y las cargas negativas del alginato y de la carboximetilcelulosa, además de por sus propiedades mecánicas y su bajo grado de hinchamiento. Para facilitar la medida de la concentración de oxígeno en medios acuosos desde el exterior del recipiente que contiene el líquido, el ML-OSen fabricado se fijó mediante un campo magnético generado por una serie de imanes (colector magnético) colocados alrededor de una

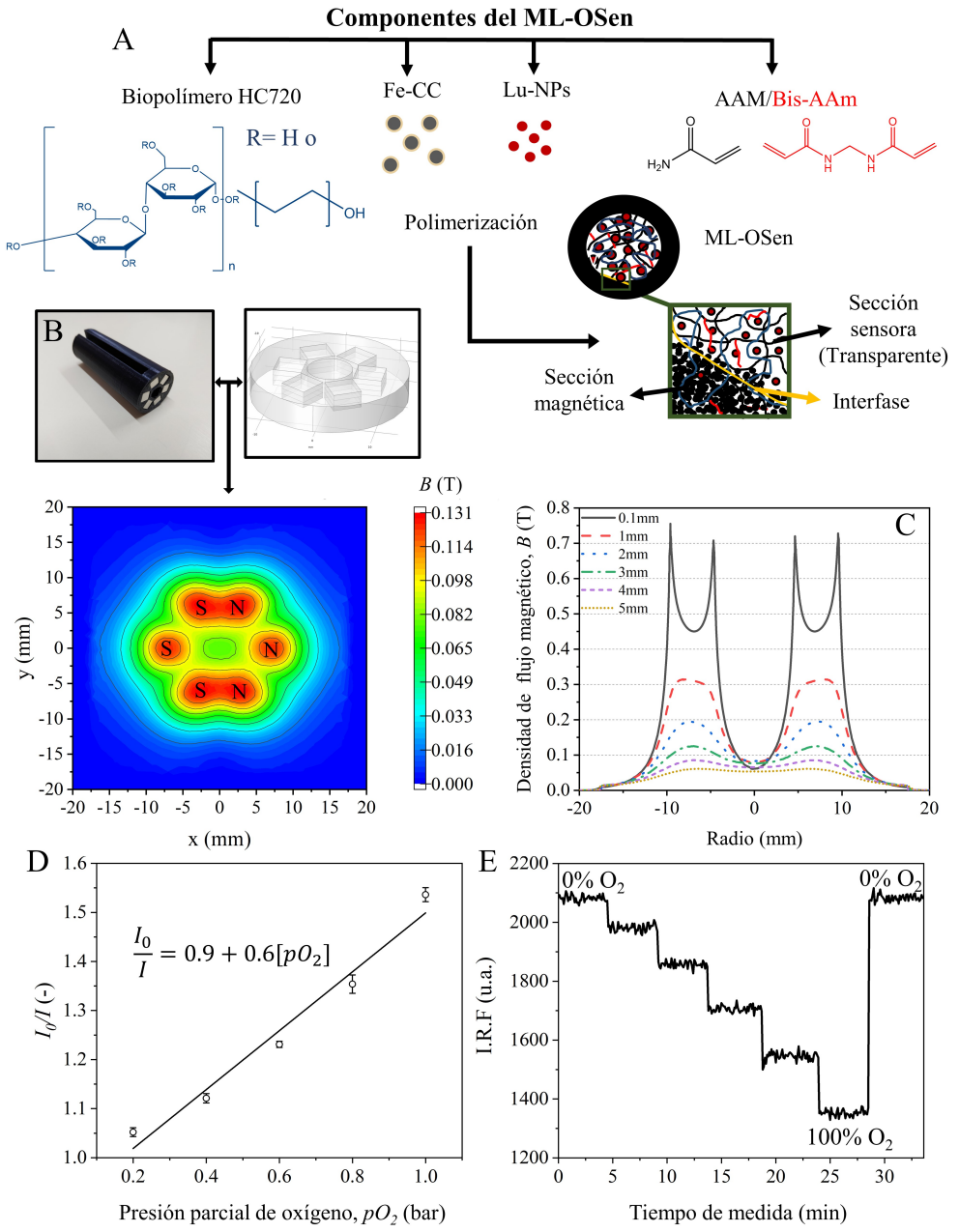

Figura 7.11: A) Composición y estructura del sensor magnético luminiscente O_2 (ML-Osen). B) Estructura del colector magnético y simulación COMSOL del campo magnético resultante en un plano a 3 mm por encima de la superficie del colector. C) Simulación en COMSOL del campo magnético resultante a lo largo de una línea a diferentes alturas sobre la superficie del colector. D) Calibración de Stern-Volmer y E) intensidad relativa de fluorescencia (I.R.F.) frente al tiempo de medida.

fibra óptica con un diámetro de 0.5 mm que se utilizó para la calibración del sensor O_2 (Figura 7.11 B y C). Para determinar la sensibilidad y reversibilidad de la detección de oxígeno del ML-OSen, se registró la variación en la intensidad de fluorescencia de la SIPN interna frente a la concentración de oxígeno [Medina-Castillo et al., 2011]. La sonda de fibra óptica se acopló al colector magnético y se conectó a un espectrómetro multi-led de alta resolución. Para realizar las medidas con esta configuración, se introdujo el ML-OSen en una cubeta de cuarzo que contenía 100 ml de agua. Luego, el campo magnético generado por la matriz de imanes atrajo y fijó el ML-OSen en la pared de la cubeta, y se registró la intensidad de luminiscencia para cada concentración de O_2. Las diferentes concentraciones de O_2 se establecieron burbujeando en el agua un flujo de gas con cuatro porcentajes diferentes de O_2 equilibrados con N_2. Los resultados de las mediciones demostraron una correlación casi lineal entre la intensidad de luminiscencia relativa (I_0/I, con I_0 en ausencia de O_2 e I en presencia de O_2) frente a la presión parcial de oxígeno (pO_2), con una sensibilidad a O_2 de K_{sv}= 0.6 bar^{-1} (Figura 7.11 D). La reversibilidad (Figura 7.11 E), la correlación lineal entre I_0/I y pO_2 y la estabilidad de la medida hacen que este sensor pueda ser adecuado para aplicaciones donde se requiera la medida de la concentración de O_2.

Evaluación de SIPNs magnéticas como actuadores blandos

Introducción

Como se ha mencionado en secciones anteriores, las aplicaciones interesantes y de vanguardia de los ferrogeles están relacionadas con el campo de los robots y actuadores blandos [He et al., 2023, Vazquez-Perez et al., 2021, Goudu et al., 2020, Liu et al., 2020b]. Las ventajas de estos materiales sobre los materiales convencionales incluyen su consistencia blanda, manipulación sin contacto directo, ausencia de circuitos eléctricos, biocompatibilidad y versatilidad. Sin embargo, tienen algunos inconvenientes importantes como difícil programación, aunque esto no disminuye su potencial. En esta sección nos centraremos en evaluar SIPNs magnéticas aplicadas como dos actuadores blandos diferentes.

La primera parte de la sección se centra en la evaluación de estos materiales como un actuador de torsión, el cual se ha estudiado previamente en ferrogeles de alginato [Vázquez Pérez, 2024]. En este caso, se utilizaron partículas Fe-CC y copos de una aleación para preparar ferrogeles cilíndricos. Durante el proceso de gelificación, se aplicó un campo magnético uniforme para alinear las partículas en cadenas paralelas contenidas en planos perpendiculares al eje del cilindro. Este sistema se comparó con los resultados de un modelo teórico desarrollado en [Vázquez Pérez, 2024], que predice la actuación de este ferrogel, cuando un extremo del cilindro se fija mientras el otro queda libre.

En la segunda parte, las SIPNs con partículas de NdFeB, se diseñaron como un actuador programable capaz de responder a varios estímulos: a campos magnéticos y cambios en el pH. Primero, estos ferrogeles se prepararon entrecruzando parcialmente el polímero lineal mediante la difusión de iones Ca^{2+}. Esto dio como resultado un gradiente de entrecruzamiento, que se tradujo en la flexión del material cuando este se hinchaba. Esta flexión del hidrogel se puede grabar mediante la magnetización de las partículas de NdFeB. Tras reducir la cantidad del agua en el ferrogel, este es capaz de recupera su estado original. Posteriormente, el estado flexionado se puede recuperar aplicando un campo magnético uniforme al material, que experimenta momentos flexores debido a los momentos magnéticos de las partículas de NdFeB magnetizadas.

Actuador de torsión

Modelo teórico

Considérese un ferrogel en forma de cilindro con una alta relación de aspecto cuyas PMs han sido estructuradas por un campo magnético uniaxial aplicado perpendicularmente al eje del cilindro durante la gelificación. Si se aplica un campo magnético uniaxial a este material perpendicularmente a su eje, las cadenas de partículas formadas durante el proceso de gelificación tenderán a alinearse con el campo aplicado, girando con ello el material. Si un extremo del ferrogel está fijo, el material no puede girar en su conjunto, por lo que el campo inducirá una deformación de cizalla del cilindro, cuya amplitud en el extremo libre dependerá del ángulo θ que forman las cadenas en el extremo fijo con respecto al campo aplicado.

En un trabajo anterior [Vázquez Pérez, 2024] se describió un modelo teórico para este actuador. Este modelo, está basado en el equilibrio entre energía elástica y magnética, y la deformación del cilindro de ferrogel viene dada por:

$$\frac{d\theta(z)}{dz} = \frac{2}{R^2 G}\mu_0 H_0^2 (A_{\parallel} - A_{\perp}) \int_z^L sin(2\theta(z'))dz' \tag{7.2}$$

, donde G es el módulo de rigidez del ferrogel, μ_0 es la permeabilidad magnética del vacío, H_0 es la fuerza del campo magnético aplicado y $A_{\parallel}$ y $A_{\perp}$ son las susceptibilidades efectivas paralela y perpendicular a las cadenas, dadas por $\chi_{\parallel}/(1 + n\chi_{\parallel})$ y $\chi_{\perp}/(1 + n\chi_{\perp})$, respectivamente, donde n es el factor de desmagnetización (alrededor de 0.5 para muestras cilíndricas). Esta ecuación integrodiferencial no es trivial de resolver, por lo que se usó un programa para resolverla.

Materiales y métodos

Materiales

Acrilamida (AAm), N,N'-metilenbisacrilamida (Bis-AAm), 2-hidroxietilcelulosa (HC720), peroxodisulfato de potasio (KPS) y N,N,N',N'',N''-pentametildietilentriamina (PMDTA) de Sigma Aldrich (EE.UU.). Micropartículas de hierro recubiertas de sílice (Fe-CC). Copos de aleación permalloy de hierro (Fe), níquel (Ni) y molibdeno (Mo) de Novamet Specialty Products Corporation (EE.UU.).

Síntesis del actuador

El protocolo utilizado para la síntesis de las SIPNs magnéticas se ha descrito previamente en la cuarta sección. En este caso se utilizó únicamente 2-hidroxietilcelulosa de $M_v \sim 720000$, y las concentraciones de partículas fueron 2 y 15 % v/v para las Fe-CC, y 2 % v/v para los copos de permalloy, un nuevo tipo de PMs blandas utilizadas en esta aplicación. Para preparar las muestras con la forma y organización interna requerida para la aplicación, la mezcla de disolución pre-gel y PMs se vertió en un molde cilíndrico transparente. Luego, el molde se colocó durante 40 minutos en un campo uniforme de 16.5 mT generado por unos carretes de Helmholtz. Durante este tiempo, el hidrogel se expuso a luz ultravioleta (UV) (λ = 370 nm) para iniciar la gelificación. Finalmente, el hidrogel se colocó en un horno a 50 °C para terminar su gelificación.

Caracterización mecánica

La caracterización mecánica de los hidrogeles se realizó utilizando un reómetro Discovery HR-1 equipado con una geometría plato-plato de 40 mm de diámetro. Las medidas de cizalla cuasiestáticas se realizaron a 25 °C, y en ellas el esfuerzo de cizalla se midió en función de la deformación a una velocidad de cizalla constante de 10^{-4} s^{-1}. Para asegurar el contacto entre la muestra y la geometría durante la medida, se aplicó una fuerza normal de 0.1 N. A partir de estas medidas, el módulo de rigidez (G) se obtuvo como la pendiente de la curva.

Caracterización de la susceptibilidad de las PMs

Para calcular la susceptibilidad de los materiales con copos de permalloy al 2 % v/v, se siguió la metodología descrita en [Martin et al., 2000]. Las susceptibilidades magnéticas para las partículas esféricas de Fe-CC se obtuvieron del mismo trabajo [Martin et al., 2000]. Los datos obtenidos se encuentran en la Tabla 7.7.

Tabla 7.7: Susceptibilidades medidas (χ_m) y corregidas (χ) para matrices con copos de aleación permalloy al 2 % v/v.

Orientación	Relación de aspecto	χ_m (-)	χ (-)	Media χ (-)
Aleatorio	1.55	0.6826	0.8097	0.89 ± 0.05
	1.55	0.723	0.8667	
	1.45	0.8027	0.9939	
Paralelo al eje mayor	1.6	1.2567	1.7244	1.74 ± 0.04
	1.6	1.3053	1.8153	
	1.6	1.2321	1.6794	
Perpendicular al eje mayor	1.6	0.6955	0.8237	0.94 ± 0.06
	1.5	0.7988	0.9823	
	1.55	0.8223	1.0118	

Análisis de la actuación

La respuesta del actuador se caracterizó mediante dos experimentos independientes, siguiendo el protocolo previamente descrito para ferrogeles de alginato [Vázquez Pérez, 2024]:

- Base fija: durante el experimento la base del actuador se fijó de modo que las cadenas de partículas en la base formaban un cierto ángulo (θ) con la dirección perpendicular al campo aplicado (θ = 30 °, 45° y 60°). La intensidad del campo magnético se aumentó en pasos de 6.51 kA/m y se midió el ángulo de las cadenas de partículas en el extremo libre (θ') (Figura 7.12 A).
- Rotación de la base: mientras se aplicaba una intensidad de campo magnético constante de 32.7 kA/m, la base del actuador se giró en pasos de 10° en el sentido de las agujas del reloj. El experimento se realizó de θ = 90° a θ = -90°, midiéndose el ángulo de las cadenas de partículas en el extremo libre (θ') (Figura 7.12 B).

Análisis experimental y validación del modelo teórico

La respuesta del actuador se estudió considerando el tipo y concentración de PMs. En primer lugar, es importante señalar que independientemente del ferrogel, la respuesta del actuador en la ecuación 7.2 se refleja en el parámetro $c = \frac{2}{R^2 G}\mu_0 H_0^2 (A_{\parallel} - A_{\perp})$, que recoge toda la información física del material. Por tanto, las diferencias que puedan surgir en los resultados deberían, en principio, deberse a diferencias en este parámetro (Tabla 7.8)

Al observar los resultados experimentales en la Figura 7.13, se puede ver que el comportamiento de los tres ferrogeles fue similar cuando la base del cilindro estaba

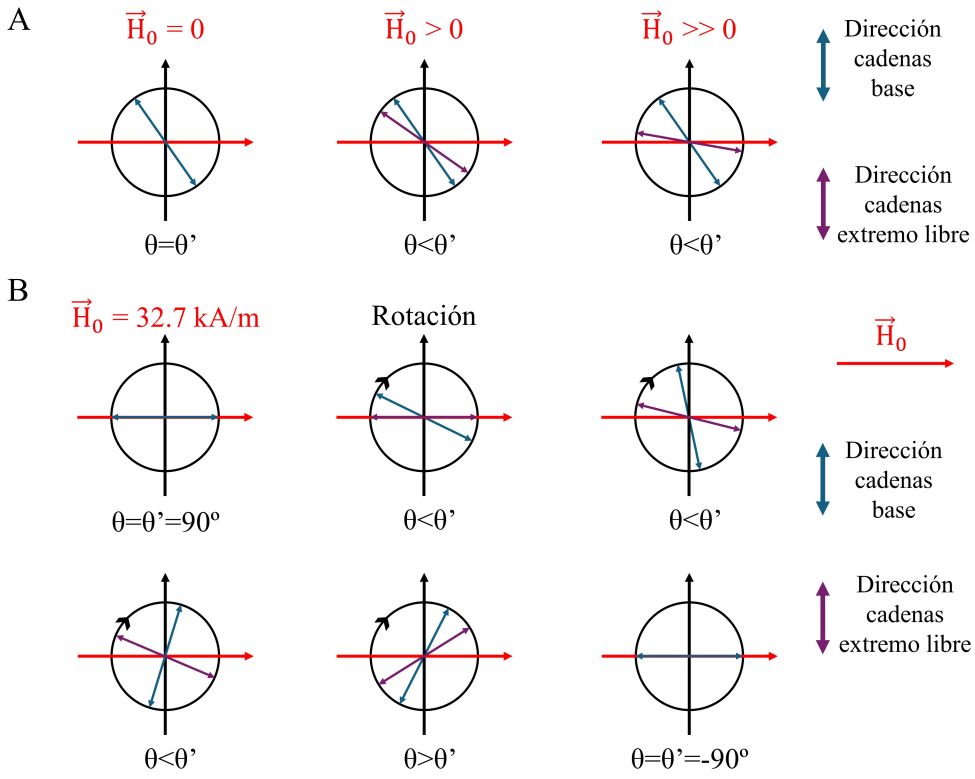

Figura 7.12: Esquema de la vista cenital del cilindro durante los experimentos. A) Experimento con la base fija. Nótese que cuando se aplica un campo magnético, las cadenas en el extremo libre del cilindro tienden a alinearse con el campo. B) Experimento girando la base. Primero, las cadenas se alinean con el campo aplicado en la dirección inicial. A un cierto ángulo en la base $\theta < 0$, las cadenas en el extremo libre giran abruptamente para formar un ángulo menor con el campo magnético.

Tabla 7.8: Magnitudes físicas involucradas en el cálculo del parámetro c para cada ferrogel.

Concentración	L/R (-)	G (Pa)	$A_{\parallel}$ (-)	$A_{\perp}$ (-)	$A_{\parallel} - A_{\perp}$ (-)	c/H_0^2 (m^2/A^2)
Fe-CC 2 % v/v	4	1400	0.26	0.11	0.15	$4.3{\cdot}10^{-9}$
Fe-CC 15 % v/v	4.5	2400	1.03	0.63	0.39	$8.2{\cdot}10^{-9}$
Escamas 2 % v/v	4	5200	0.93	0.64	0.29	$2.2{\cdot}10^{-9}$

fija. A 0 kA/m, θ' era igual a θ y se corresponden con el valor establecido en el experimento, como se esperaba. Cuando se incrementó la intensidad del campo, θ' aumentó ligeramente con una tendencia lineal después de una pequeña transición del estado inicial para valores más altos del campo magnético. A un campo magnético

de aproximadamente 45 kA/m, la pendiente de la curva disminuyó, indicando que el material estaba alcanzando el ángulo máximo posible. En teoría, este ángulo máximo debería ser 90°, pero al parecer se deben aplicar campo magnético más intensos para alcanzar ese punto. Las diferencias al cambiar el ángulo de la base afectaron tanto al ángulo máximo θ' que alcanzó el material, debido a que el punto de equilibrio entre la energía elástica y magnética cambió con el valor de θ, como a la forma de la curva para θ = 60° (Figura 7.13 C). Centrándonos en los valores de c, se deben observar diferencias entre las tres muestras. Sorprendentemente, 2 % v/v y 15 % v/v de Fe-CC mostraron una respuesta bastante similar a pesar de tener un c/H_0^2 de $4.3{\cdot}10^{-9}$ m^2/A^2 y $8.2{\cdot}10^{-9}$ m^2/A^2, respectivamente, mientras que 2 % v/v de copos de permalloy mostró la respuesta más alta con un c/H_0^2 de $2.2{\cdot}10^{-9}$. Las razones detrás de este comportamiento se discutirán más adelante.

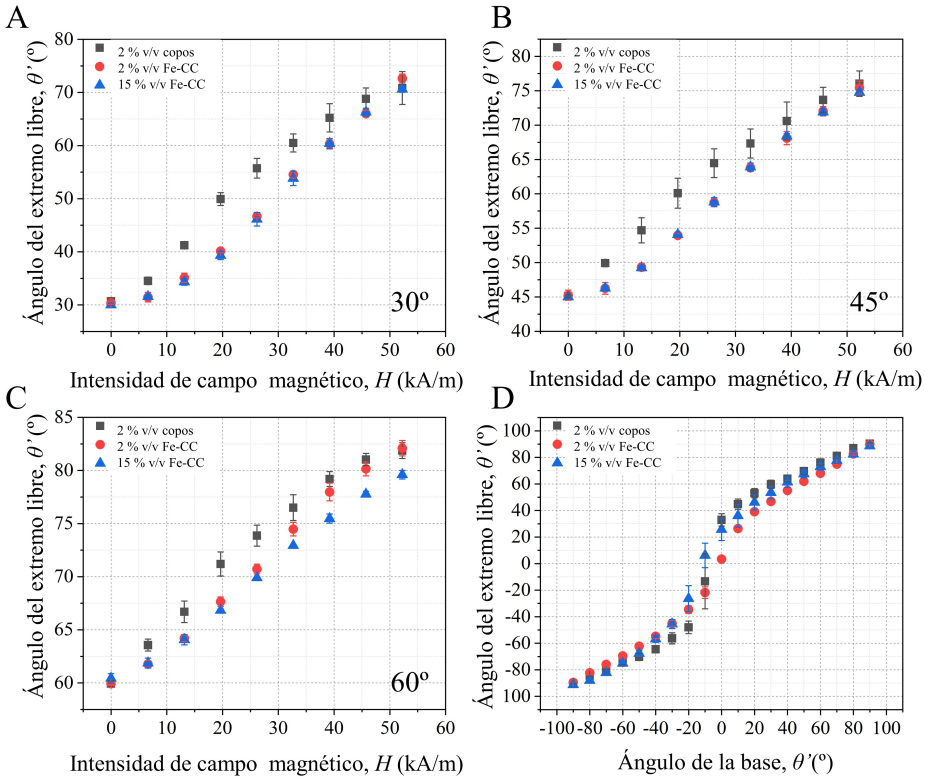

Figura 7.13: Resultados experimentales para la respuesta del actuador fabricado con cada tipo de ferrogel. A), B) y C) Los experimentos se realizaron con la base del cilindro fijada en un cierto ángulo θ = 30°, 45° y 60°, respectivamente. D) Los experimentos se realizaron girando la base del cilindro de θ = 90° a θ = -90° bajo una intensidad de campo constante de 32.7 kA/m.

Para el experimento girando la base bajo un campo constante (Figura 7.13 D), el extremo libre del cilindro tendía a alinearse con el campo magnético como consecuencia del equilibrio entre las energías elástica y magnética, mientras cambiaba

el ángulo de la base. En cierto momento, el ángulo de la base alcanzó valores negativos y el extremo libre todavía estaba orientado próximo a la dirección inicial con un ángulo inferior a 90°. Sin embargo, cuando la base se giró a -10°, el extremo libre giró abruptamente, orientándose hacia ángulos negativos. La posterior reducción del ángulo de la base también redujo el ángulo del extremo libre hasta alcanzar ambos -90°.

Finalmente, es importante comparar estos resultados experimentales con el modelo teórico. Para hacerlo, se utilizaron las magnitudes de la Tabla 7.8 para calcular el desplazamiento angular. Los resultados experimentales y teóricos están representados en la Figura 7.14. Lo primero que llama la atención es la discrepancia entre los resultados experimentales y la teoría. Para 2 % v/v y 15 % v/v de partículas Fe-CC (ver Figura 7.14 A y C), en el primer experimento, la teoría predice una torsión importante del cilindro para una menor intensidad del campo magnético, y el extremo libre es capaz de alinearse perfectamente con el campo dentro del rango estudiado. Sin embargo, los resultados experimentales mostraron una torsión suave y el ángulo máximo del extremo libre fue de alrededor de 70° para 52.08 kA/m. En el caso de girar la base, la transición teórica del extremo libre ocurre para un ángulo menor y es más pronunciada que la transición experimental, que exhibe una torsión suave para ángulos superiores a -20°. Además, teóricamente, el extremo libre tiende a estar casi alineado ($\theta' \sim 90°$) con el campo, mientras que, experimentalmente, el ángulo del extremo libre se reduce lentamente con el cambio del ángulo de la base. Por otra parte, para las copos de permalloy, hubo una mejor concordancia entre la teoría y los experimentos.

Los resultados experimentales descritos por Váquez Pérez [Vázquez Pérez, 2024] para ferrogeles de alginato tuvieron una buena concordancia con el modelo teórico. Por tanto, la discrepancia en este caso puede atribuirse a las particularidades de los materiales estudiados. Como se discutió anteriormente, las propiedades físicas de las muestras se recogen en el parámetro c, que está relacionado con el módulo de rigidez y la anisotropía magnética del ferrogel. En el caso de las partículas Fe-CC, donde las diferencias son más notorias, para obtener un mejor ajuste a los datos experimentales, el parámetro c debe ser menor que el valor calculado. Considerando las dos cantidades mencionadas anteriormente, una hipótesis es que, experimentalmente, el material es más rígido y las partículas no están perfectamente alineadas en una dirección privilegiada. Estas dos suposiciones son posibles debido a las dificultades experimentales asociadas con la reacción de radicalaria involucrada en la polimerización de acrilamida. Esta reacción ocurre a temperaturas por encima de los 50 °C o bajo exposición a la luz ultravioleta. El montaje experimental no permitía iniciar la reacción usando temperatura, por lo que se utilizó luz ultravioleta. Tras los 40 minutos de exposición a la luz ultravioleta en un campo magnético uniforme, los ferrogeles cilíndricos se colocaron en un horno a 50 °C para finalizar la gelificación. Por un lado, el módulo de rigidez de la muestra cilíndrica puede diferir del medido en muestras en forma de disco completamente gelificadas en el horno. Por otro lado, las

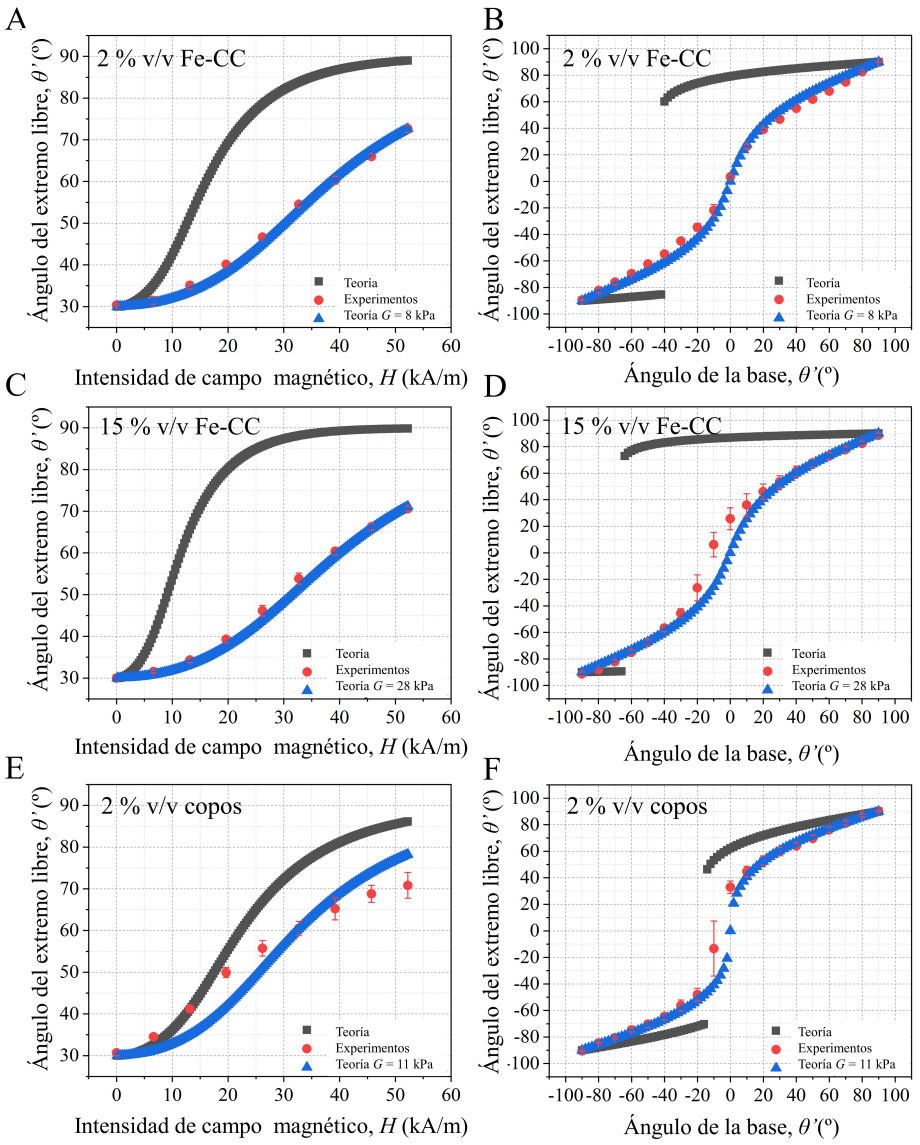

Figura 7.14: Comparación entre datos experimentales y resultados teóricos. A la izquierda, experimento con la base fijada en 30°. A la derecha, experimento girando la base. A) y B) resultados para hidrogeles con 2 % v/v de partículas de Fe-CC. C) y D) resultados para hidrogeles con 15 % v/v de partículas de Fe-CC. E) y F) resultados para hidrogeles con 2 % v/v de copos de permalloy. Nótese que los datos teóricos donde se especifica G (en azul) son los valores que ajustan aproximadamente los datos experimentales.

PMs pueden estar parcialmente alineados debido a la precipitación y al protocolo de preparación en dos pasos. Para ilustrar cómo la rigidez del material afecta la respuesta de los ferrogeles, en la Figura 7.14, además de los datos experimentales y teóricos de

nuestras muestras, se representan las predicciones del modelo teórico para los valores del módulo de rigidez que mejor se ajusta los datos experimentales. Como puede verse, el aumento de la rigidez del material mejoró la capacidad del modelo teórico para reproducir los datos experimentales, lo que apoya en parte nuestra hipótesis sobre la discrepancias entre el modelo y los experimentos.

Actuador programable con respuesta a múltiples estímulos

Hipótesis y objetivo

El segundo actuador presentado en esta sección es un actuador programable con respuesta a múltiples estímulos. De los materiales estudiados en esta tesis, los ferrogeles SIPN magnéticos de acrilamida y biopolímero son capaces responder a múltiples estímulos. Hasta ahora, sólo se ha explorado la respuesta magnética, mientras que se ha pasado por alto su capacidad de hinchamiento. Por este motivo, en este apartado se aprovechan ambos estímulos para diseñar una bomba magnética programable. El concepto detrás del proceso de programación se ilustra en la Figura 7.15. Brevemente, el ferrogel de acrilamida y biopolímero se sintetiza con un gradiente de entrecruzamiento a lo largo de su espesor. Cuando el ferrogel se coloca en una disolución acuosa a un pH determinado, el ferrogel se hincha de manera no homogénea. De hecho, el ferrogel se curva debido al hinchamiento diferencial de la doble red. Si se aplica un campo magnético de alta intensidad en este momento, las partículas de NdFeB se magnetizarán en la dirección del campo. Posteriormente, podemos retirar el campo y reducir el hinchamiento del gel cambiando el pH del medio, obteniendo un ferrogel de características similares al sintetizado. Finalmente, si aplicamos un campo magnético de baja intensidad al ferrogel anterior, las PMs generarán momentos flectores dentro de la red polimérica para alinear su momento magnético, $\vec{m}$, con el campo externo. Esto provoca que el material se doble, recuperando la forma de su estado hinchado.

Materiales y métodos

Materiales

Acrilamida (AAm), N,N'-metilenbisacrilamida (Bis-AAm), alginato de sodio LVSA, sulfato de calcio ($CaSO_4$), fenil-2,4,6-trimetilbenzoilfosfinato de litio (TPO-Li), bicarbonato de sodio ($NaHCO_3$), dihidrógenofosfato de sodio 1-hidratado ($NaH_2PO_4.H_2O$), hidróxido de sodio (NaOH) y 37 % de ácido clorhídrico (HCl) de Sigma-Aldrich (EE. UU.). Partículas de neodimio-hierro-boro (NdFeB) con un diámetro de 5 µm y una densidad de ρ = 7.61 g/cm^3 de Magnequench (Alemania). Todas las disoluciones se prepararon en agua milli-Q.

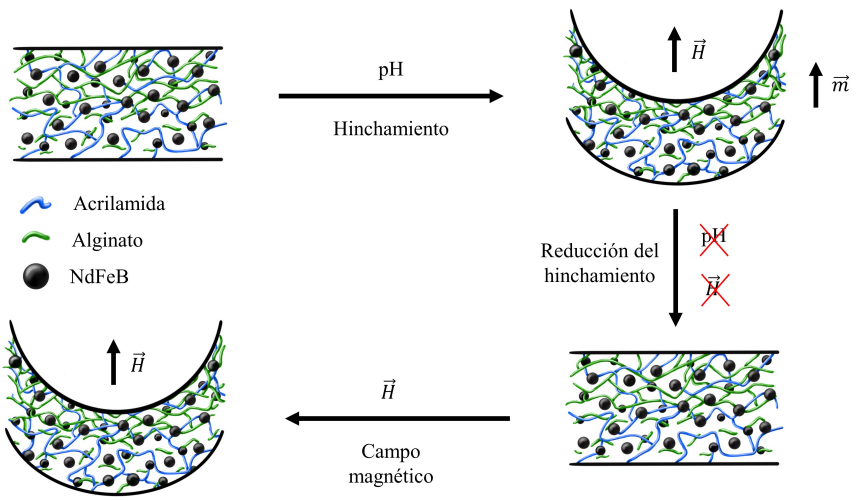

Figura 7.15: Proceso de programación y actuación de un SIPNs magnético con gradiente de entrecruzamiento a lo largo de su espesor y partículas ferromagnéticas duras.

Síntesis de películas delgadas de ferrogel

El protocolo se basa en el descrito en la cuarta sección. En primer lugar, se preparó una disolución acuosa de LVSA al 4.8 % p/p. Posteriormente, a la disolución polimérica se le agregaron micropartículas de NdFeB, las cuales se agitaron y sonicaron durante 10 min hasta obtener una suspensión homogénea. Posteriormente, se disolvieron Bis-AAm y AAm en agua y se mezclaron con la suspensión de polímero/NdFeB. Finalmente, se añadió una disolución acuosa del fotoiniciador TPO-Li (10 mg/ml) a la mezcla de Bis-AAm/Aam/NdFeB/alginato. La disolución pre-gel se inyectó entre dos vidrios separados 500 µm. Este sistema se colocó bajo luz ultravioleta (λ = 365 nm) durante 15 min. Las concentraciones de los compuestos utilizados fueron las siguientes: 83.93 % v/v de agua milli-Q, 1.82 % v/v de LVSA, 0.1 % v/v de Bis-AAm, 9.05 % v/v de AAm, 0.1 % v/v de TPO-Li y 5.0 % v/v de partículas de NdFeB.

Programación del hidrogel multiestímulo

La programación de una bomba magnética reconfigurable constó de dos fases: i) deformación del material utilizando su capacidad de hinchamiento y gradiente de entrecruzamiento; y ii) magnetización de las partículas de NdFeB con el material hinchado. Para ello, la película delgada sintetizada se secó a temperatura ambiente, y se entrecruzó a lo largo de su espesor poniendo en contacto una de las superficies del hidrogel con una disolución de $CaSO_4$ 19 mM durante 10 s. Luego, la película se cortó

en la forma deseada usando un láser. Posteriormente, el ferrogel se colocó en agua milli-Q hasta su hinchamiento. Una vez hinchado se colocó entre las bobinas de un VSM que generaron un campo magnético de 1.8 T que magnetizó las PMs de NdFeB. Finalmente, el ferrogel se colocó en un medio básico para reducir el hinchamiento y recuperar la forma plana de la película delgada.

Actuación del hidrogel multiestímulo

Para estudiar la respuesta de la bomba magnética diseñada siguiendo el proceso descrito, la película delgada se fijó en un marco impreso en 3D dentro de una disolución acuosa, donde mantuvo su estado no hinchado. Este montaje se colocó en un sistema de bobinas que generaba un campo magnético uniaxial sinusoidal de intensidad 10 mT y frecuencia variable de 1, 5, 10 y 15 Hz.

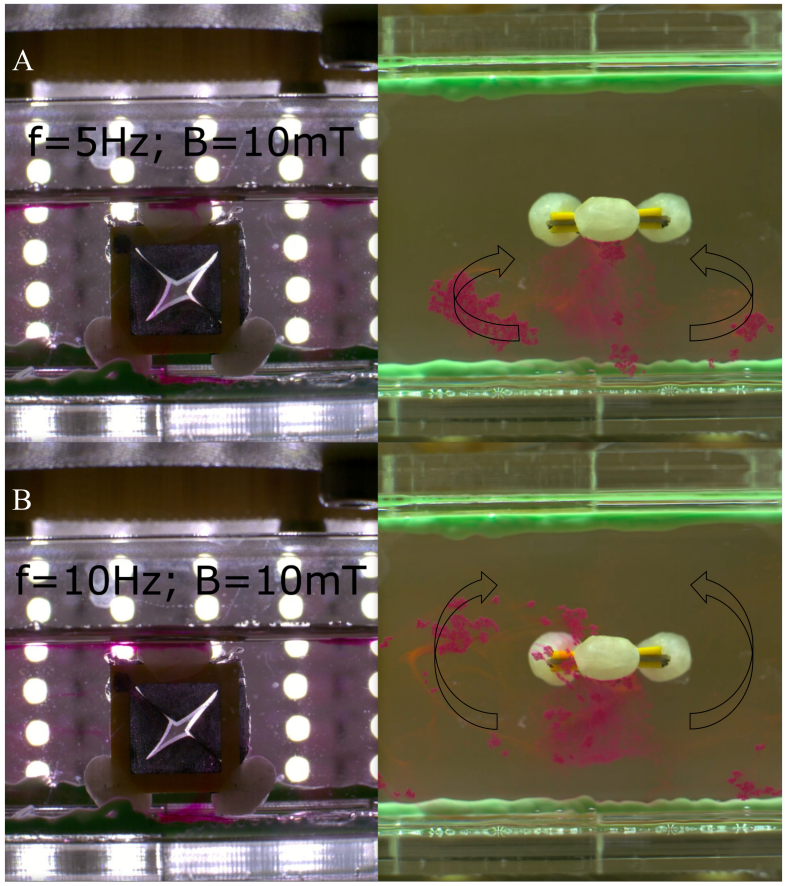

Figura 7.16: Funcionamiento de la bomba magnética a 5 Hz A) y 10 Hz B). Vista lateral del sistema (izquierda) y vista superior (derecha). Las flechas negras indican la dirección del flujo que sigue el tinte. El flujo se origina por el movimiento de la bomba.

Cuando se aplicó un campo sinusoidal, se observaron diferentes patrones de mezcla dependiendo de la frecuencia del campo. Además, el movimiento del corte en forma de cruz en el ferrogel no era simétrico con respecto al plano del ferrogel, lo que hacía posible la mezcla del entorno circundante. En cuanto al efecto de la frecuencia, a 1 Hz no se observó una mezcla significativa, a 5 Hz hubo una ligera mezcla delante del ferrogel (ver Figura 7.16 A), a 10 Hz se mezcló toda la disolución (ver Figura 7.16 B), y a 15 Hz la bomba no pudo seguir la frecuencia del campo debido a la inercia y no se observó proceso de mezcla.

Conclusiones

El objetivo de esta tesis era preparar ferrogeles con control de su microestructura y comportamiento magnético. Para ello, se utilizaron diferentes polímeros, como alginato de sodio, celulosa y acrilamida, para preparar hidrogeles entrecruzados física o químicamente, a los que se incorporaron diferentes tipos de PMs. Además, los ferrogeles se caracterizaron desde un punto de vista macroscópico, atendiendo a sus propiedades mecánicas bajo diferentes esfuerzos, a su capacidad de hinchamiento y a su comportamiento magnético, y desde un punto de vista microscópico, utilizando diferentes técnicas como microscopía electrónica de barrido y espectroscopía infrarroja. Estos ferrogeles exhibieron un amplio espectro de propiedades mecánicas y estructura interna, que cumplen con los requisitos necesarios para su aplicación como actuadores blandos, robots blandos o sensores. A lo largo de la tesis se analizaron y discutieron distintos hidrogeles, PMs, protocolos de síntesis, técnicas de caracterización y aplicaciones.

En la segunda sección estudiamos los efectos de la deshidratación controlada bajo un esfuerzo (SCDP) sobre las propiedades mecánicas y la estructura interna de hidrogeles de alginato. Del análisis y discusión de estos resultados concluimos que:

- Después de los SCDP, la rigidez del hidrogel aumentó, pero este efecto no se debió solo al aumento de la concentración de polímero como predice la teoría clásica para geles, sino que el tipo de esfuerzo aplicado también afectó a los resultados. Se observaron diferencias entre los controles y los distintos esfuerzos, siendo la compresión la que mejoró en mayor medida la rigidez de los hidrogeles.

- Los SCDPs no solo causaron un aumento en la rigidez sino que también reorganizaron las fibras poliméricas, que se corroboró mediante la anisotropía mecánica de los geles así como mediante imágenes de SEM.

- Los resultados anteriores pueden explicarse por la reorganización de las fibras poliméricas debido a los SCDPs. De hecho, esta reorganización es irreversible, ya que la rehidratación completa de los hidrogeles de alginato era imposible

debido probablemente a la formación de enlaces de hidrógeno entre los grupos -OH presentes en las fibras de alginato.

- Los SCDPs bajo compresión se utilizaron sobre un actuador magnético en forma de cruz capaz de responder a un campo magnético flexionando dos de sus brazos. Observamos que el valor umbral del campo magnético requerido para obtener una respuesta significativa disminuyó para las muestras sometidas al SCDP, demostrando el efecto positivo de este proceso en las propiedades y respuesta del actuador.

En la tercera sección, se estudió la estructura microscópica de ferrogeles de alginato de sodio anisótropos mediante microespectroscopia FT-IR usando radiación de sincrotrón polarizada. De los resultados concluimos que:

- En las razones del pico a 1600 cm^{-1} (perteneciente al grupo carboxilo (COO^{-}) del alginato) bajo dos polarizaciones perpendiculares en los espectros FT-IR, los hidrogeles sin partículas y con partículas no funcionalizadas mostraron valores homogéneos cercanos a la unidad sobre el área analizada, lo que reflejó una distribución aleatoria del grupo como cabría esperar.
- Los ferrogeles con PMs funcionalizadas mostraron cambios en las razones de sus picos, relacionados con la alineación de las fibras de alginato debido a la orientación del grupo COO^{-}. Sin embargo, la única muestra que mostró una disposición clara asociada con la alineación de las PMs fue la amina primaria.
- Los resultados arrojan luz sobre la estructura microscópica de los ferrogeles de alginato anisótropos. Sin embargo, se requiere un análisis más detallado y extenso para confirmar si existe una reorganización de las fibras de alginato debido a la alineación de las PMs.

En la cuarta sección, se estudiaron redes semi-interpenetradas de polímeros (SIPNs) compuestas por una red entrecruzada químicamente de acrilamida y biopolímeros de celulosa/alginato entrelazados en la primera red con el fin de preparar hidrogeles magnéticos (Mag-SIPN). También se diseño un sensor de oxígeno usando estos materiales, que podía ser controlado por un campo magnético. De este estudio llegamos a las siguientes conclusiones:

- Las SIPNs pueden acomodar una gran cantidad de micropartículas magnéticas sin un debilitamiento sustancialmente de sus propiedades mecánicas. Sin embargo, fue necesaria una cantidad mínima de acelerante para minimizar la sedimentación de las PMs durante la gelificación.
- Las Mag-SIPNs mostraron módulos elásticos (tanto bajo esfuerzos de tracción como de compresión) y módulos viscoelásticos bastante bajos, junto con

valores de deformabilidad considerablemente grandes, lo que los convierte en material de interés para maximizar la respuesta magneto-mecánica bajo un campo magnético.

- Las Mag-SIPNs mostraron una alta capacidad de hinchamiento y una fuerte respuesta magnética, que junto con sus propiedades mecánicas los convierten en materiales ideales para actuadores y sensores inteligentes capaces de ser controlados remotamente.

- El sensor fabricado usando Mag-SIPNs resuelve el problema de la falta de fijación en la celda de medida que suelen presentar métodos convencionales, que generalmente impide una lectura confiable de la señal óptica. Además, permitió una lectura estable de la concentración de oxígeno, de interés para distintos bioprocesos celulares y enzimáticos.

En la quinta sección, los SIPNs magnéticos previamente estudiados se evaluaron como un actuador capaz de torsionarse y como un actuador programable capaz de responder a varios estímulos. De esta evaluación concluimos que:

- Los ferrogeles SIPNs cilíndricos con diferentes PMs alineados en cadenas paralelas se pueden utilizar como actuadores de torsión. Al fijar un extremo y aplicar un campo uniforme, el extremo libre del cilindro es capaz de girar, y mostrar histéresis si el extremo fijo se gira durante el experimento.

- El modelo teórico no fue capaz de reproducir los datos experimentales con los valores de rigidez y anisotropía magnética medidos, lo que se atribuyó a diferencias entre los valores reales y los determinados experimentalmente. El uso de valores más altos del módulo de rigidez mejoró la concordancia entre ambos.

- La bomba magnética presentada como un actuador programable capaz de responder a múltiples estímulos demostró la capacidad de mezclar el entorno acuoso circundante bajo ciertas frecuencias de un campo magnético alterno sinusoidal.

En resumen, durante esta tesis hemos estudiamos hidrogeles de alginato con una estructura interna anisótropa inducida por esfuerzos mecánicos o por la alineación de PMs funcionalizadas. Respecto a estos materiales, hemos demostrado que la anisotropía se refleja macroscópicamente, en sus propiedades mecánicas, y microscópicamente, así como en la disposición de las fibras poliméricas. Posteriormente, estudiamos ferrogeles SIPN compuestos de acrilamida y biopolímeros, que mostraron propiedades prometedoras para su uso en robots blandos, actuadores blandos y sensores. Las aplicaciones presentadas en la cuarta y quinta sección demostraron el potencial y la versatilidad de estos materiales, que pueden

prepararse bajo diferentes condiciones experimentales, así como detectar y actuar bajo diferentes estímulos externos.

Bibliography

[Ahmadian et al., 2023] Ahmadian, Z., Kazeminava, F., Afrouz, M., Abbaszadeh, M., Mehr, N. T., Shiran, J. A., Gouda, C., Adeli, M., and Kafil, H. S. (2023). A review on the impacts of metal/metal nanoparticles on characteristics of hydrogels: Special focus on carbohydrate polymers. *International Journal of Biological Macromolecules*, 253:126535.

[Ahmed, 2015] Ahmed, E. M. (2015). Hydrogel: Preparation, characterization, and applications: A review. *Journal of Advanced Research*, 6(2):105–121.

[Almeida et al., 2023] Almeida, D., Sanjuan-Alberte, P., C. Silva, J., and Castelo Ferreira, F. (2023). 3D (bio)printing of magnetic hydrogels: Formulation and applications in tissue engineering. *International Journal of Bioprinting*, 10(1):0965.

[An et al., 2023] An, C., Wang, T., Wu, S., Gao, L., Deng, Q., Zhao, L., and Hu, N. (2023). Progress and prospective of the soft robots with the magnetic response. *Composite Structures*, 324:117568.

[Andrade et al., 2021] Andrade, F., Roca-Melendres, M. M., Durán-Lara, E. F., Rafael, D., and Schwartz, S. (2021). Stimuli-Responsive Hydrogels for Cancer Treatment: The Role of pH, Light, Ionic Strength and Magnetic Field. *Cancers*, 13(5):1164.

[Arif et al., 2024] Arif, Z. U., Khalid, M. Y., Tariq, A., Hossain, M., and Umer, R. (2024). 3D printing of stimuli-responsive hydrogel materials: Literature review and emerging applications. *Giant*, 17:100209.

[Arvand et al., 2024] Arvand, M. P., Moghimi, A., and Salehi, N. (2024). A novel removal of Ni^{2+} ions from water solutions using dispersive solid-phase extraction method with nano Fe_3O_4/chitosan-acrylamide hydrogel. *Environmental Monitoring and Assessment*, 196(2):136.

[Awasthi et al., 2020] Awasthi, S., Gaur, J. K., and Bobji, M. (2020). Advanced ferrogels with high magnetic response and wear resistance using carbon nanotubes. *Journal of Alloys and Compounds*, 848:156259.

[Barczak et al., 2020] Barczak, M., Borowski, P., Gila-Vilchez, C., Alaminos, M., González-Caballero, F., and López-López, M. T. (2020). Revealing importance of particles' surface functionalization on the properties of magnetic alginate hydrogels. *Carbohydrate Polymers*, 247:116747.

[Bardajee et al., 2020] Bardajee, G. R., Khamooshi, N., Nasri, S., and Vancaeyzeele, C. (2020). Multi-stimuli responsive nanogel/hydrogel nanocomposites based on κ-carrageenan for prolonged release of levodopa as model drug. *International Journal of Biological Macromolecules*, 153:180–189.

[Barrera et al., 2019] Barrera, G., Tiberto, P., Allia, P., Bonelli, B., Esposito, S., Marocco, A., Pansini, M., and Leterrier, Y. (2019). Magnetic Properties of Nanocomposites. *Applied Sciences*, 9:212.

[Bastola and Hossain, 2020] Bastola, A. K. and Hossain, M. (2020). A review on magneto-mechanical characterizations of magnetorheological elastomers. *Composites Part B: Engineering*, 200:108348.

[Betsch et al., 2018] Betsch, M., Cristian, C., Lin, Y., Blaeser, A., Schöneberg, J., Vogt, M., Buhl, E. M., Fischer, H., and Campos, D. F. D. (2018). Incorporating 4D into Bioprinting: Real-Time Magnetically Directed Collagen Fiber Alignment for Generating Complex Multilayered Tissues. *Advanced Healthcare Materials*, 7:1800894.

[Bigdeli et al., 2017] Bigdeli, A., Ghasemi, F., Golmohammadi, H., Abbasi-Moayed, S., Nejad, M. A. F., Fahimi-Kashani, N., Jafarinejad, S., Shahrajabian, M., and Hormozi-Nezhad, M. R. (2017). Nanoparticle-based optical sensor arrays. *Nanoscale*, 9:16546–16563.

[Bonhome-Espinosa et al., 2017] Bonhome-Espinosa, A. B., Campos, F., Rodriguez, I. A., Carriel, V., Marins, J. A., Zubarev, A., Duran, J. D. G., and Lopez-Lopez, M. T. (2017). Effect of particle concentration on the microstructural and macromechanical properties of biocompatible magnetic hydrogels. *Soft Matter*, 13:2928–2941.

[Borisov and Wolfbeis, 2008] Borisov, S. M. and Wolfbeis, O. S. (2008). Optical Biosensors. *Chemical Reviews*, 108:423–461.

[Calascione et al., 2021] Calascione, T. M., Fischer, N. A., Lee, T. J., Thatcher, H. G., and Nelson-Cheeseman, B. B. (2021). Controlling magnetic properties of 3D-printed magnetic elastomer structures via fused deposition modeling. *AIP Advances*, 11:025223.

[Campos et al., 2021] Campos, F., Bonhome-Espinosa, A. B., Carmona, R., Durán, J. D. G., Kuzhir, P., Alaminos, M., López-López, M. T., Rodriguez, I. A., and Carriel, V. (2021). In vivo time-course biocompatibility assessment of biomagnetic

nanoparticles-based biomaterials for tissue engineering applications. *Materials Science and Engineering: C*, 118:111476.

[Chambon and Winter, 1987] Chambon, F. and Winter, H. H. (1987). Linear Viscoelasticity at the Gel Point of a Crosslinking PDMS with Imbalanced Stoichiometry. *Journal of Rheology*, 31:683–697.

[Chaudhuri et al., 2020] Chaudhuri, O., Cooper-White, J., Janmey, P. A., Mooney, D. J., and Shenoy, V. B. (2020). Effects of extracellular matrix viscoelasticity on cellular behaviour. *Nature*, 584(7822):535–546.

[Chen et al., 2022a] Chen, W., Sun, B., Biehl, P., and Zhang, K. (2022a). Cellulose-Based Soft Actuators. *Macromolecular Materials and Engineering*, 307:2200072.

[Chen et al., 2023a] Chen, X., Tian, C., Zhang, H., and Xie, H. (2023a). Biodegradable Magnetic Hydrogel Robot with Multimodal Locomotion for Targeted Cargo Delivery. *ACS Applied Materials & Interfaces*, 15:28922–28932.

[Chen et al., 2023b] Chen, X., Wang, H., Shi, J., Chen, Z., Wang, Y., Gu, S., Fu, Y., Huang, J., Ding, J., and Yu, L. (2023b). An injectable and active hydrogel induces mutually enhanced mild magnetic hyperthermia and ferroptosis. *Biomaterials*, 298:122139.

[Chen et al., 2023c] Chen, Y., Chen, L., Geng, B., Chen, F., Yuan, Y., Li, D., Wang, Y.-X., Jia, W., and Hu, W. (2023c). Triple-network-based conductive polymer hydrogel for soft and elastic bioelectronic interfaces. *SmartMat*, 5:e1229.

[Chen et al., 2021] Chen, Y., Zhao, X., Li, Y., Jin, Z.-Y., Yang, Y., Yang, M.-B., and Yin, B. (2021). Light- and magnetic-responsive synergy controlled reconfiguration of polymer nanocomposites with shape memory assisted self-healing performance for soft robotics. *Journal of Materials Chemistry C*, 9(16):5515–5527.

[Chen et al., 2022b] Chen, Z., Song, S., Ma, J., Ling, S. D., Wang, Y. D., Kong, T. T., and Xu, J. H. (2022b). Fabrication of magnetic core/shell hydrogels via microfluidics for controlled drug delivery. *Chemical Engineering Science*, 248:117216.

[Chen et al., 2019] Chen, Z., Zhao, D., Liu, B., Nian, G., Li, X., Yin, J., Qu, S., and Yang, W. (2019). 3D Printing of Multifunctional Hydrogels. *Advanced Functional Materials*, 29:1900971.

[Chin et al., 2018] Chin, S. Y., Poh, Y. C., Kohler, A.-C., and Sia, S. K. (2018). An Additive Manufacturing Technique for the Facile and Rapid Fabrication of Hydrogel-based Micromachines with Magnetically Responsive Components. *Journal of Visualized Experiments*, (137):e56727.

[Choi et al., 2016] Choi, J.-r., Shin, D.-M., Song, H., Lee, D., and Kim, K. (2016). Current achievements of nanoparticle applications in developing optical sensing and imaging techniques. *Nano Convergence*, 3:30.

[Chojnacki et al., 2007] Chojnacki, P., Mistlberger, G., and Klimant, I. (2007). Separable Magnetic Sensors for the Optical Determination of Oxygen. *Angewandte Chemie*, 119:9006–9009.

[Chung et al., 2021] Chung, H., Parsons, A. M., and Zheng, L. (2021). Magnetically Controlled Soft Robotics Utilizing Elastomers and Gels in Actuation: A Review. *Advanced Intelligent Systems*, 3:2000186.

[Contreras-Montoya et al., 2018] Contreras-Montoya, R., Bonhome-Espinosa, A. B., Orte, A., Miguel, D., Delgado-López, J. M., Duran, J. D. G., Cuerva, J. M., Lopez-Lopez, M. T., and Álvarez de Cienfuegos, L. (2018). Iron nanoparticles-based supramolecular hydrogels to originate anisotropic hybrid materials with enhanced mechanical strength. *Materials Chemistry Frontiers*, 2:686–699.

[Dargahi et al., 2019] Dargahi, A., Sedaghati, R., and Rakheja, S. (2019). On the properties of magnetorheological elastomers in shear mode: Design, fabrication and characterization. *Composites Part B: Engineering*, 159:269–283.

[Daya et al., 2022] Daya, R., Xu, C., Nguyen, N.-Y. T., and Liu, H. H. (2022). Angiogenic Hyaluronic Acid Hydrogels with Curcumin-Coated Magnetic Nanoparticles for Tissue Repair. *ACS Applied Materials & Interfaces*, 14(9):11051–11067.

[Dimatteo et al., 2018] Dimatteo, R., Darling, N. J., and Segura, T. (2018). In situ forming injectable hydrogels for drug delivery and wound repair. *Advanced Drug Delivery Reviews*, 127:167–184.

[Donati et al., 2003] Donati, I., Gamini, A., Skjåk-Bræk, G., Vetere, A., Campa, C., Coslovi, A., and Paoletti, S. (2003). Determination of the diadic composition of alginate by means of circular dichroism: a fast and accurate improved method. *Carbohydrate Research*, 338:1139–1142.

[Dong et al., 2020] Dong, M., Wang, X., Chen, X., Mushtaq, F., Deng, S., Zhu, C., Torlakcik, H., Terzopoulou, A., Qin, X., Xiao, X., Puigmartí-Luis, J., Choi, H., Pêgo, A. P., Shen, Q., Nelson, B. J., and Pané, S. (2020). 3D-Printed Soft Magnetoelectric Microswimmers for Delivery and Differentiation of Neuron-Like Cells. *Advanced Functional Materials*, 30:1910323.

[Draghi, 2017] Draghi, L. (2017). *Characterization of Polymeric Biomaterials*, chapter Static and uniaxial characterizationof polymer biomaterials, pages 177–202. Elsevier.

[Edward and Golecki, 2023] Edward, S. and Golecki, H. M. (2023). Gelatin Soft Actuators: Benefits and Opportunities. *Actuators*, 12:63.

[Emi et al., 2018] Emi, T. T., Barnes, T., Orton, E., Reisch, A., Tolouei, A. E., Madani, S. Z. M., and Kennedy, S. M. (2018). Pulsatile Chemotherapeutic Delivery Profiles Using Magnetically Responsive Hydrogels. *ACS Biomaterials Science & Engineering*, 4:2412–2423.

[Estevam et al., 2023] Estevam, B. R., Perez, I. D., Moraes, A. M., and Fregolente, L. V. (2023). A review of the strategies used to produce different networks in cellulose-based hydrogels. *Materials Today Chemistry*, 34:101803.

[Evans et al., 2012] Evans, B. A., Fiser, B. L., Prins, W. J., Rapp, D. J., Shields, A. R., Glass, D. R., and Superfine, R. (2012). A highly tunable silicone-based magnetic elastomer with nanoscale homogeneity. *Journal of Magnetism and Magnetic Materials*, 324:501–507.

[Filippi et al., 2019] Filippi, M., Dasen, B., Guerrero, J., Garello, F., Isu, G., Born, G., Ehrbar, M., Martin, I., and Scherberich, A. (2019). Magnetic nanocomposite hydrogels and static magnetic field stimulate the osteoblastic and vasculogenic profile of adipose-derived cells. *Biomaterials*, 223:119468.

[Fox et al., 2009] Fox, A. J. S., Bedi, A., and Rodeo, S. A. (2009). The Basic Science of Articular Cartilage: Structure, Composition, and Function. *Sports Health: A Multidisciplinary Approach*, 1(6):461–468.

[Gambin et al., 2024] Gambin, B., Kruglenko, E., Tymkiewicz, R., and Litniewski, J. (2024). Heating efficiency of agarose samples doped with magnetic nanoparticles subjected to ultrasonic and magnetic field. *International Journal of Heat and Mass Transfer*, 226:125467.

[Gan et al., 2021] Gan, W., Wang, Y., Xiao, S., Gao, R., Shang, Y., Xie, Y., Liu, J., and Li, J. (2021). Magnetically Driven 3D Cellulose Film for Improved Energy Efficiency in Solar Evaporation. *ACS Applied Materials & Interfaces*, 13:7756–7765.

[Gang et al., 2021] Gang, F., Jiang, L., Xiao, Y., Zhang, J., and Sun, X. (2021). Multifunctional magnetic hydrogel: Design strategies and applications. *Nano Select*, 2(12):2291–2307.

[Gang et al., 2019] Gang, F., Yan, H., Ma, C., Jiang, L., Gu, Y., Liu, Z., Zhao, L., Wang, X., Zhang, J., and Sun, X. (2019). Robust magnetic double-network hydrogels with self-healing, MR imaging, cytocompatibility and 3D printability. *Chemical Communications*, 55:9801–9804.

[Ganguly et al., 2022] Ganguly, K., Jin, H., Dutta, S. D., Patel, D. K., Patil, T. V., and Lim, K.-T. (2022). Magnetic field-assisted aligned patterning in an alginate-silk fibroin/nanocellulose composite for guided wound healing. *Carbohydrate Polymers*, 287:119321.

[Ganguly and Margel, 2021] Ganguly, S. and Margel, S. (2021). Design of Magnetic Hydrogels for Hyperthermia and Drug Delivery. *Polymers*, 13(23):4259.

[Ganguly and Margel, 2022] Ganguly, S. and Margel, S. (2022). 3D printed magnetic polymer composite hydrogels for hyperthermia and magnetic field driven structural manipulation. *Progress in Polymer Science*, 131:101574.

[Gao et al., 2019] Gao, F., Xie, W., Miao, Y., Wang, D., Guo, Z., Ghosal, A., Li, Y., Wei, Y., Feng, S., Zhao, L., and Fan, H. M. (2019). Magnetic Hydrogel with Optimally Adaptive Functions for Breast Cancer Recurrence Prevention. *Advanced Healthcare Materials*, 8:1900203.

[Garcia-Gonzalez et al., 2021] Garcia-Gonzalez, D., Moreno, M. A., Valencia, L., Arias, A., and Velasco, D. (2021). Influence of elastomeric matrix and particle volume fraction on the mechanical response of magneto-active polymers. *Composites Part B: Engineering*, 215:108796.

[Gila Vilchez, 2022] Gila Vilchez, C. (2022). *Hidrogeles magnéticos para medicina regenerativa y aplicaciones tecnológicas.* PhD thesis, University of Granada.

[Gila-Vilchez et al., 2018] Gila-Vilchez, C., Bonhome-Espinosa, A. B., Kuzhir, P., Zubarev, A., Duran, J. D. G., and Lopez-Lopez, M. T. (2018). Rheology of magnetic alginate hydrogels. *Journal of Rheology*, 62:1083–1096.

[Gila-Vilchez et al., 2019a] Gila-Vilchez, C., Duran, J. D. G., Gonzalez-Caballero, F., Zubarev, A., and Lopez-Lopez, M. T. (2019a). Magnetorheology of alginate ferrogels. *Smart Materials and Structures*, 28:35018.

[Gila-Vilchez et al., 2019b] Gila-Vilchez, C., Manas-Torres, M. C., Contreras-Montoya, R., Alaminos, M., Duran, J. D. G., Cienfuegos, L. A. D., and Lopez-Lopez, M. T. (2019b). Anisotropic magnetic hydrogels: Design, structure and mechanical properties. *Philosophical Transactions of the Royal Society A: Mathematical, Physical and Engineering Sciences*, 377(2143):20180217.

[Gold, 2019] Gold, V., editor (2019). *The IUPAC Compendium of Chemical Terminology*. International Union of Pure and Applied Chemistry (IUPAC).

[Gong et al., 2022] Gong, C., Zhai, Y., Zhou, J., Wang, Y., and Chang, C. (2022). Magnetic field assisted fabrication of asymmetric hydrogels for complex shape deformable actuators. *Journal of Materials Chemistry C*, 10:549–556.

[Goudu et al., 2020] Goudu, S. R., Yasa, I. C., Hu, X., Ceylan, H., Hu, W., and Sitti, M. (2020). Biodegradable Untethered Magnetic Hydrogel Milli-Grippers. *Advanced Functional Materials*, 30(50):2004975.

[Grosberg and Chochlov, 1994] Grosberg, A. and Chochlov, A. R. (1994). *Statistical physics of macromolecules*. AIP series in polymers and complex materials. American Institute of Physics, New York.

[Guo and Ma, 2018] Guo, B. and Ma, P. X. (2018). Conducting Polymers for Tissue Engineering. *Biomacromolecules*, 19(6):1764–1782.

[Haefner et al., 2018] Haefner, S., Koerbitz, R., Frank, P., Elstner, M., and Richter, A. (2018). High Integration of Microfluidic Circuits Based on Hydrogel Valves for MEMS Control. *Advanced Materials Technologies*, 3:1700108.

[Haider et al., 2015] Haider, H., Yang, C. H., Zheng, W. J., Yang, J. H., Wang, M. X., Yang, S., Zrínyi, M., Osada, Y., Suo, Z., Zhang, Q., Zhou, J., and Chen, Y. M. (2015). Exceptionally tough and notch-insensitive magnetic hydrogels. *Soft Matter*, 11:8253–8261.

[Hao and Mao, 2023] Hao, L. and Mao, H. (2023). Magnetically anisotropic hydrogels for tissue engineering. *Biomaterials Science*, 11(19):6384–6402.

[He et al., 2021] He, Y., Li, Y., Sun, Y., Zhao, S., Feng, M., Xu, G., Zhu, H., Ji, P., Mao, H., He, Y., and Gu, Z. (2021). A double-network polysaccharide-based composite hydrogel for skin wound healing. *Carbohydrate Polymers*, 261:117870.

[He et al., 2023] He, Y., Tang, J., Hu, Y., Yang, S., Xu, F., Zrínyi, M., and Chen, Y. M. (2023). Magnetic hydrogel-based flexible actuators: A comprehensive review on design, properties, and applications. *Chemical Engineering Journal*, 462:142193.

[Hu et al., 2019] Hu, X., Nian, G., Liang, X., Wu, L., Yin, T., Lu, H., Qu, S., and Yang, W. (2019). Adhesive Tough Magnetic Hydrogels with High Fe_3O_4 Content. *ACS Applied Materials & Interfaces*, 11:10292–10300.

[Huang et al., 2023a] Huang, H., Dong, Z., Ren, X., Jia, B., Li, G., Zhou, S., Zhao, X., and Wang, W. (2023a). High-strength hydrogels: Fabrication, reinforcement mechanisms, and applications. *Nano Research*, 16:3475–3515.

[Huang et al., 2019] Huang, H.-W., Uslu, F. E., Katsamba, P., Lauga, E., Sakar, M. S., and Nelson, B. J. (2019). Adaptive locomotion of artificial microswimmers. *Science Advances*, 5:eaau1532.

[Huang et al., 2023b] Huang, Y., Qian, S., Zhou, J., Chen, W., Liu, T., Yang, S., Long, S., and Li, X. (2023b). Achieving Swollen yet Strengthened Hydrogels by Reorganizing Multiphase Network Structure. *Advanced Functional Materials*, 33:2213549.

[Huxley, 1988] Huxley, A. (1988). Muscular Contraction. *Annual Review of Physiology*, 50(1):1–17.

[Huxley, 1974] Huxley, A. F. (1974). Muscular contraction. *The Journal of Physiology*, 243(1):1–43.

[Khalid et al., 2024] Khalid, M. Y., Arif, Z. U., Tariq, A., Hossain, M., Khan, K. A., and Umer, R. (2024). 3D printing of magneto-active smart materials for advanced actuators and soft robotics applications. *European Polymer Journal*, 205:112718.

[Kim and Zhao, 2022] Kim, Y. and Zhao, X. (2022). Magnetic Soft Materials and Robots. *Chemical Reviews*, 122:5317–5364.

[Kong et al., 2018] Kong, W., Wang, C., Jia, C., Kuang, Y., Pastel, G., Chen, C., Chen, G., He, S., Huang, H., Zhang, J., Wang, S., and Hu, L. (2018). Muscle-Inspired Highly Anisotropic, Strong, Ion-Conductive Hydrogels. *Advanced Materials*, 30(29):1801934.

[Koo et al., 2004] Koo, Y.-E. L., Cao, Y., Kopelman, R., Koo, S. M., Brasuel, M., and Philbert, M. A. (2004). Real-Time Measurements of Dissolved Oxygen Inside Live Cells by Organically Modified Silicate Fluorescent Nanosensors. *Analytical Chemistry*, 76:2498–2505.

[Koons et al., 2020] Koons, G. L., Diba, M., and Mikos, A. G. (2020). Materials design for bone-tissue engineering. *Nature Reviews Materials*, 5(8):584–603.

[Kovacs, 1998] Kovacs, G. T. A. (1998). *Micromachined transducers sourcebook*. McGraw-Hill.

[Kreuzer et al., 2022] Kreuzer, M., Mor, L. R., Castillo, D. A., Mañas, G. V. J., Torres, C. M. F., Domínguez, I. G., and Yousef, I. (2022). A tensile stage for high resolution synchrotron-based infrared microspectroscopy at MIRAS. *Journal of Physics: Conference Series*, 2380:012111.

[Kuang et al., 2023] Kuang, X., Arıcan, M. O., Zhou, T., Zhao, X., and Zhang, Y. S. (2023). Functional Tough Hydrogels: Design, Processing, and Biomedical Applications. *Accounts of Materials Research*, 4:101–114.

[Kuang et al., 2021] Kuang, X., Wu, S., Ze, Q., Yue, L., Jin, Y., Montgomery, S. M., Yang, F., Qi, H. J., and Zhao, R. (2021). Magnetic Dynamic Polymers for Modular Assembling and Reconfigurable Morphing Architectures. *Advanced Materials*, 33:2102113.

[Larson, 1999] Larson, R. G. (1999). *The structure and rheology of complex fluids*. Topics in chemical engineering. Oxford University Press, New York.

[Lavrador et al., 2021] Lavrador, P., Esteves, M. R., Gaspar, V. M., and Mano, J. F. (2021). Stimuli-Responsive Nanocomposite Hydrogels for Biomedical Applications. *Advanced Functional Materials*, 31:2005941.

[Lawrence and Rao, 2023] Lawrence, M. B. and Rao, R. (2023). Structure of water in poly(vinyl alcohol)-based ferrogels: effect of carbonyl iron concentration. *Journal of Polymer Research*, 30(2):94.

[Lee et al., 2019] Lee, J. H., Han, W. J., Jang, H. S., and Choi, H. J. (2019). Highly Tough, Biocompatible, and Magneto-Responsive Fe_3O_4/Laponite/PDMAAm Nanocomposite Hydrogels. *Scientific Reports*, 9:15024.

[Lee et al., 2020] Lee, M., Park, T., Kim, C., and Park, S.-M. (2020). Characterization of a magneto-active membrane actuator comprising hard magnetic particles with varying crosslinking degrees. *Materials & Design*, 195:108921.

[Leon-Cecilla et al., 2024] Leon-Cecilla, A., Gila-Vilchez, C., Vazquez-Perez, F. J., Capitan-Vallvey, L. F., Martos, V., Fernandez-Ramos, M. D., Álvarez de Cienfuegos, L., Medina-Castillo, A. L., and Lopez-Lopez, M. T. (2024). Highly deformable and strongly magnetic semi-interpenetrating hydrogels based on alginate or cellulose. *International Journal of Biological Macromolecules*, 260:129368.

[Leon-Cecilla et al., 2023] Leon-Cecilla, A., Vazquez-Perez, F. J., Gila-Vilchez, C., Álvarez de Cienfuegos, L., and Lopez-Lopez, M. T. (2023). Alginate Hydrogels Reinforced by Dehydration under Stress–Application to a Soft Magnetic Actuator. *Gels*, 9:39.

[Li et al., 2023] Li, F., Cai, X., Liu, G., Xu, H., and Chen, W. (2023). Piezoionic SnSe Nanosheets-Double Network Hydrogel for Self-Powered Strain Sensing and Energy Harvesting. *Advanced Functional Materials*, 33(32):2300701.

[Li et al., 2022] Li, L., Wu, P., Yu, F., and Ma, J. (2022). Double network hydrogels for energy/environmental applications: challenges and opportunities. *Journal of Materials Chemistry A*, 10:9215–9247.

[Li et al., 2021] Li, S., Cong, Y., and Fu, J. (2021). Tissue adhesive hydrogel bioelectronics. *Journal of Materials Chemistry B*, 9(22):4423–4443.

[Li and Su, 2018] Li, X. and Su, X. (2018). Multifunctional smart hydrogels: potential in tissue engineering and cancer therapy. *Journal of Materials Chemistry B*, 6:4714–4730.

[Li et al., 2015] Li, Y., Poon, C. T., Li, M., Lu, T. J., Pingguan-Murphy, B., and Xu, F. (2015). Chinese-Noodle-Inspired Muscle Myofiber Fabrication. *Advanced Functional Materials*, 25:5999–6008.

[Li et al., 2024] Li, Z., Lu, J., Ji, T., Xue, Y., Zhao, L., Zhao, K., Jia, B., Wang, B., Wang, J., Zhang, S., and Jiang, Z. (2024). Self-Healing Hydrogel Bioelectronics. *Advanced Materials*, 36(21):2306350.

[Lima-Tenório et al., 2015] Lima-Tenório, M. K., Tenório-Neto, E. T., Guilherme, M. R., Garcia, F. P., Nakamura, C. V., Pineda, E. A. G., and Rubira, A. F. (2015). Water transport properties through starch-based hydrogel nanocomposites responding to both pH and a remote magnetic field. *Chemical Engineering Journal*, 259:620–629.

[Lin et al., 2020] Lin, H., Tan, J., Zhu, J., Lin, S., Zhao, Y., Yu, W., Hojaiji, H., Wang, B., Yang, S., Cheng, X., Wang, Z., Tang, E., Yeung, C., and Emaminejad, S. (2020). A programmable epidermal microfluidic valving system for wearable biofluid management and contextual biomarker analysis. *Nature Communications*, 11:4405.

[Liu et al., 2020a] Liu, J., Miller, K., Ma, X., Dewan, S., Lawrence, N., Whang, G., Chung, P., McCulloch, A. D., and Chen, S. (2020a). Direct 3D bioprinting of cardiac micro-tissues mimicking native myocardium. *Biomaterials*, 256:120204.

[Liu et al., 2023] Liu, T., Chen, W., Li, K., Long, S., Li, X., and Huang, Y. (2023). Toughening Weak Polyampholyte Hydrogels with Weak Chain Entanglements via a Secondary Equilibrium Approach. *Polymers*, 15:2644.

[Liu et al., 2022] Liu, X., Gao, M., Chen, J., Guo, S., Zhu, W., Bai, L., Zhai, W., Du, H., Wu, H., Yan, C., Shi, Y., Gu, J., Qi, H. J., and Zhou, K. (2022). Recent Advances in Stimuli-Responsive Shape-Morphing Hydrogels. *Advanced Functional Materials*, 32(39):1.

[Liu et al., 2020b] Liu, X., Liu, J., Lin, S., and Zhao, X. (2020b). Hydrogel machines. *Materials Today*, 36:102–124.

[Liu et al., 2021] Liu, X., Yang, Y., Inda, M. E., Lin, S., Wu, J., Kim, Y., Chen, X., Ma, D., Lu, T. K., and Zhao, X. (2021). Magnetic Living Hydrogels for Intestinal Localization, Retention, and Diagnosis. *Advanced Functional Materials*, 31:2010918.

[Lopez-Lopez et al., 2015] Lopez-Lopez, M. T., Scionti, G., Oliveira, A. C., Duran, J. D. G., Campos, A., Alaminos, M., and Rodriguez, I. A. (2015). Generation and Characterization of Novel Magnetic Field-Responsive Biomaterials. *PLOS ONE*, 10(7):e0133878.

[Lu et al., 2006] Lu, C., Xie, Y., Yang, Y., Cheng, M. M.-C., Koh, C.-G., Bai, Y., Lee, L. J., and Juang, Y.-J. (2006). New Valve and Bonding Designs for Microfluidic Biochips Containing Proteins. *Analytical Chemistry*, 79:994–1001.

[Lucarini et al., 2022] Lucarini, S., Hossain, M., and Garcia-Gonzalez, D. (2022). Recent advances in hard-magnetic soft composites: Synthesis, characterisation, computational modelling, and applications. *Composite Structures*, 279:114800.

[López-Valdeolivas et al., 2017] López-Valdeolivas, M., Liu, D., Broer, D. J., and Sánchez-Somolinos, C. (2017). 4D Printed Actuators with Soft-Robotic Functions. *Macromolecular Rapid Communications*, 39(5):1700710.

[Madge, 1961] Madge, D. S. (1961). The control of relative humidity with aqueous solutions of sodium hydroxide. *Entomologia Experimentalis et Applicata*, 4(2):143–147.

[Madison, 2003] Madison, K. C. (2003). Barrier Function of the Skin: "La Raison d'être" of the Epidermis. *Journal of Investigative Dermatology*, 121(2):231–241.

[Mandal et al., 2021] Mandal, S., Kumari, S., Kumar, M., and Ojha, U. (2021). Supplementary Networking of Interpenetrating Polymer System (SNIPSy) Strategy to Develop Strong & High Water Content Ionic Hydrogels for Solid Electrolyte Applications. *Advanced Functional Materials*, 31:2100251.

[Marelli et al., 2015] Marelli, B., Ghezzi, C. E., James-Bhasin, M., and Nazhat, S. N. (2015). Fabrication of injectable, cellular, anisotropic collagen tissue equivalents with modular fibrillar densities. *Biomaterials*, 37:183–193.

[Martin et al., 2000] Martin, J., Venturini, E., Odinek, J., and Anderson, R. (2000). Anisotropic magnetism in field-structured composites. *Physical Review E*, 61:2818–2830.

[Matsuda et al., 2019] Matsuda, T., Kawakami, R., Namba, R., Nakajima, T., and Gong, J. P. (2019). Mechanoresponsive self-growing hydrogels inspired by muscle training. *Science*, 363:504–508.

[Mazaheri et al., 2018] Mazaheri, H., Namdar, A. H., and Amiri, A. (2018). Behavior of a smart one-way micro-valve considering fluid–structure interaction. *Journal of Intelligent Material Systems and Structures*, 29:3960–3971.

[Mañas-Torres et al., 2021a] Mañas-Torres, M. C., Gila-Vilchez, C., Durán, J. D. G., Lopez-Lopez, M. T., and Álvarez de Cienfuegos, L. (2021a). *Biomedical applications of magnetic hydrogels*, pages 253–271. Elsevier.

[Mañas-Torres et al., 2021b] Mañas-Torres, M. C., Gila-Vilchez, C., Vazquez-Perez, F. J., Kuzhir, P., Momier, D., Scimeca, J.-C., Borderie, A., Goracci, M., Burel-Vandenbos, F., Blanco-Elices, C., Rodriguez, I. A., Alaminos, M., Álvarez de Cienfuegos, L., and Lopez-Lopez, M. T. (2021b). Injectable Magnetic-Responsive Short-Peptide Supramolecular Hydrogels: Ex Vivo and In Vivo Evaluation. *ACS Applied Materials & Interfaces*, 13:49692–49704.

[Małecki et al., 2016] Małecki, P., Królewicz, M., Hiptmair, F., Krzak, J., Kaleta, J., Major, Z., and Pigłowski, J. (2016). Influence of carbonyl iron particle coating with silica on the properties of magnetorheological elastomers. *Smart Materials and Structures*, 25:105030.

[McClendon and Stupp, 2012] McClendon, M. T. and Stupp, S. I. (2012). Tubular hydrogels of circumferentially aligned nanofibers to encapsulate and orient vascular cells. *Biomaterials*, 33:5713–5722.

[McDonagh et al., 2008] McDonagh, C., Burke, C. S., and MacCraith, B. D. (2008). Optical Chemical Sensors. *Chemical Reviews*, 108:400–422.

[Medina-Castillo et al., 2011] Medina-Castillo, A. L., Fernández-Sánchez, J. F., and Fernández-Gutiérrez, A. (2011). One-Step Fabrication of Multifunctional Core-Shell Fibres by Co-Electrospinning. *Advanced Functional Materials*, 21:3488–3495.

[Medina-Castillo et al., 2009] Medina-Castillo, A. L., Mistlberger, G., Fernandez-Sanchez, J. F., Segura-Carretero, A., Klimant, I., and Fernandez-Gutierrez, A. (2009). Novel Strategy to Design Magnetic, Molecular Imprinted Polymers with Well-Controlled Structure for the Application in Optical Sensors. *Macromolecules*, 43:55–61.

[Megdich et al., 2023] Megdich, A., Habibi, M., and Laperrière, L. (2023). A review on 4D printing: Material structures, stimuli and additive manufacturing techniques. *Materials Letters*, 337:133977.

[Mei et al., 2023] Mei, L., Cong, J., Li, S., Ren, T., Bai, Y., Liu, Q., Miao, C., Ding, W., and Luo, T. (2023). Polyacrylamide-Chitosan based magnetic hydrogels with high stiffness and ultra-toughness. *Composites Part A: Applied Science and Manufacturing*, 168:107478.

[Merazzo et al., 2021] Merazzo, K. J., Lima, A. C., Rincón-Iglesias, M., Fernandes, L. C., Pereira, N., Lanceros-Mendez, S., and Martins, P. (2021). Magnetic materials: a journey from finding north to an exciting printed future. *Materials Horizons*, 8:2654–2684.

[Mistlberger et al., 2009] Mistlberger, G., Borisov, S. M., and Klimant, I. (2009). Enhancing performance in optical sensing with magnetic nanoparticles. *Sensors and Actuators B: Chemical*, 139:174–180.

[Mistlberger et al., 2008] Mistlberger, G., Chojnacki, P., and Klimant, I. (2008). Magnetic sensor particles: an optimized magnetic separator with an optical window. *Journal of Physics D: Applied Physics*, 41:85003.

[Mistlberger et al., 2010] Mistlberger, G., Medina-Castillo, A. L., Borisov, S. M., Mayr, T., Fernández-Gutiérrez, A., Fernandez-Sanchez, J. F., and Klimant, I. (2010). Mini-emulsion solvent evaporation: a simple and versatile way to magnetic nanosensors. *Microchimica Acta*, 172:299–308.

[Moghimi et al., 2017] Moghimi, E., Jacob, A. R., Koumakis, N., and Petekidis, G. (2017). Colloidal gels tuned by oscillatory shear. *Soft Matter*, 13(12):2371–2383.

[Mohan et al., 2011] Mohan, R., Schudel, B. R., Desai, A. V., Yearsley, J. D., Apblett, C. A., and Kenis, P. J. A. (2011). Design considerations for elastomeric normally closed microfluidic valves. *Sensors and Actuators B: Chemical*, 160:1216–1223.

[Mondal et al., 2023] Mondal, S., Katzschmann, R., and Clemens, F. (2023). Magnetorheological behavior of thermoplastic elastomeric honeycomb structures fabricated by additive manufacturing. *Composites Part B: Engineering*, 252:110498.

[Moreno et al., 2021] Moreno, M. A., Gonzalez-Rico, J., Lopez-Donaire, M. L., Arias, A., and Garcia-Gonzalez, D. (2021). New experimental insights into magneto-mechanical rate dependences of magnetorheological elastomers. *Composites Part B: Engineering*, 224:109148.

[Moreno-Mateos et al., 2022] Moreno-Mateos, M. A., Hossain, M., Steinmann, P., and Garcia-Gonzalez, D. (2022). Hybrid magnetorheological elastomers enable versatile soft actuators. *npj Computational Materials*, 8:162.

[Morris et al., 1980] Morris, E. R., Rees, D. A., and Thom, D. (1980). Characterisation of alginate composition and block-structure by circular dichroism. *Carbohydrate Research*, 81:305–314.

[Mredha et al., 2018] Mredha, M. T. I., Guo, Y. Z., Nonoyama, T., Nakajima, T., Kurokawa, T., and Gong, J. P. (2018). A Facile Method to Fabricate Anisotropic Hydrogels with Perfectly Aligned Hierarchical Fibrous Structures. *Advanced Materials*, 30(9):1704937.

[Mredha and Jeon, 2022] Mredha, M. T. I. and Jeon, I. (2022). Biomimetic anisotropic hydrogels: Advanced fabrication strategies, extraordinary functionalities, and broad applications. *Progress in Materials Science*, 124:100870.

[Naderi and Azizian, 2018] Naderi, Z. and Azizian, J. (2018). Synthesis and characterization of carboxymethyl chitosan/Fe_3O_4 and $MnFe_2O_4$ nanocomposites hydrogels for loading and release of curcumin. *Journal of Photochemistry and Photobiology B: Biology*, 185:206–214.

[Nam and Mooney, 2021] Nam, S. and Mooney, D. (2021). Polymeric Tissue Adhesives. *Chemical Reviews*, 121(18):11336–11384.

[Narayanaswamy and Wolfbeis, 2004] Narayanaswamy, R. and Wolfbeis, O. S. (2004). *Optical Sensors*. Springer Berlin Heidelberg.

[Oh and Ahn, 2006] Oh, K. W. and Ahn, C. H. (2006). A review of microvalves. *Journal of Micromechanics and Microengineering*, 16:R13–R39.

[Omidinia-Anarkoli et al., 2017] Omidinia-Anarkoli, A., Boesveld, S., Tuvshindorj, U., Rose, J. C., Haraszti, T., and De Laporte, L. (2017). An Injectable Hybrid Hydrogel with Oriented Short Fibers Induces Unidirectional Growth of Functional Nerve Cells. *Small*, 13(36):1702207.

[Orellana and Moreno-Bondi, 2005] Orellana, G. and Moreno-Bondi, M. C., editors (2005). *Frontiers in Chemical Sensors*. Springer-Verlag.

[Pal and Banerjee, 2018] Pal, K. and Banerjee, I., editors (2018). *Polymeric gels*. Woodhead Publishing series in biomaterials. Woodhead Publishing, Cambridge.

[Park et al., 2023] Park, S., Bang, J., and So, H. (2023). 3D printing-assisted and magnetically-actuated superhydrophobic surfaces for droplet control. *Surfaces and Interfaces*, 37:102678.

[Poole et al., 2001] Poole, A. R., Kojima, T., Yasuda, T., Mwale, F., Kobayashi, M., and Laverty, S. (2001). Composition and Structure of Articular Cartilage. *Clinical Orthopaedics and Related Research*, 391:S26–S33.

[Pourmadadi et al., 2023] Pourmadadi, M., Darvishan, S., Abdouss, M., Yazdian, F., Rahdar, A., and Díez-Pascual, A. M. (2023). pH-responsive polyacrylic acid (PAA)-carboxymethyl cellulose (CMC) hydrogel incorporating halloysite nanotubes (HNT) for controlled curcumin delivery. *Industrial Crops and Products*, 197:116654.

[Proksch et al., 2008] Proksch, E., Brandner, J. M., and Jensen, J.-M. (2008). The skin: an indispensable barrier. *Experimental Dermatology*, 17(12):1063–1072.

[Qi et al., 2019] Qi, S., Fu, J., Xie, Y., Li, Y., Gan, R., and Yu, M. (2019). Versatile magnetorheological plastomer with 3D printability, switchable mechanics, shape memory, and self-healing capacity. *Composites Science and Technology*, 183:107817.

[Qin et al., 2019] Qin, H., Zhang, T., Li, N., Cong, H.-P., and Yu, S.-H. (2019). Anisotropic and self-healing hydrogels with multi-responsive actuating capability. *Nature Communications*, 10:2202.

[Qiu and Zhang, 2023] Qiu, X. and Zhang, X. (2023). Self-healing polymers for soft actuators and robots. *Journal of Polymer Science*, 62(14):3137.

[Qu et al., 2018] Qu, J., Zhao, X., Liang, Y., Zhang, T., Ma, P. X., and Guo, B. (2018). Antibacterial adhesive injectable hydrogels with rapid self-healing, extensibility and compressibility as wound dressing for joints skin wound healing. *Biomaterials*, 183:185–199.

[Rincón-Iglesias et al., 2020] Rincón-Iglesias, M., Delgado, A., Peřinka, N., Lizundia, E., and Lanceros-Méndez, S. (2020). Water-based 2D printing of magnetically active cellulose derivative nanocomposites. *Carbohydrate Polymers*, 233:115855.

[Roy et al., 2023] Roy, A., Zhang, Z., Eiken, M. K., Shi, A., Pena-Francesch, A., and Loebel, C. (2023). Programmable Tissue Folding Patterns in Structured Hydrogels. *Advanced Materials*, page 2300017.

[Rubinstein and Colby, 2014] Rubinstein, M. and Colby, R. H. (2014). *Polymer physics*. Oxford University Press.

[Rutkowski et al., 2019] Rutkowski, S., Si, T., Gai, M., Sun, M., Frueh, J., and He, Q. (2019). Magnetically-guided hydrogel capsule motors produced via ultrasound assisted hydrodynamic electrospray ionization jetting. *Journal of Colloid and Interface Science*, 541:407–417.

[Ryabchun and Bobrovsky, 2018] Ryabchun, A. and Bobrovsky, A. (2018). Cholesteric Liquid Crystal Materials for Tunable Diffractive Optics. *Advanced Optical Materials*, 6:1800335.

[Saadi et al., 2022] Saadi, M. A. S. R., Maguire, A., Pottackal, N. T., Thakur, M. S. H., Ikram, M. M., Hart, A. J., Ajayan, P. M., and Rahman, M. M. (2022). Direct Ink Writing: A 3D Printing Technology for Diverse Materials. *Advanced Materials*, 34:2108855.

[Safronov et al., 2019] Safronov, A. P., Stadler, B. J. H., Um, J., Zamani Kouhpanji, M. R., Alonso Masa, J., Galyas, A. G., and Kurlyandskaya, G. V. (2019). Polyacrylamide Ferrogels with Ni Nanowires. *Materials*, 12(16):2582.

[Sano et al., 2018] Sano, K., Ishida, Y., and Aida, T. (2018). Synthesis of Anisotropic Hydrogels and Their Applications. *Angewandte Chemie - International Edition*, 57:2532–2543.

[Scionti et al., 2013] Scionti, G., Moral, M., Toledano, M., Osorio, R., Durán, J. D. G., Alaminos, M., Campos, A., and López-López, M. T. (2013). Effect of the hydration on the biomechanical properties in a fibrin-agarose tissue-like model. *Journal of Biomedical Materials Research Part A*, 102(8):2573–2582.

[Selzer and Odenbach, 2020] Selzer, L. and Odenbach, S. (2020). Effects of carbonyl iron particles on the rheological behavior of nanocomposite hydrogels. *Journal of Magnetism and Magnetic Materials*, 501:166394.

[Shi et al., 2019] Shi, L., Zeng, Y., Zhao, Y., Yang, B., Ossipov, D., Tai, C.-W., Dai, J., and Xu, C. (2019). Biocompatible Injectable Magnetic Hydrogel Formed by Dynamic Coordination Network. *ACS Applied Materials & Interfaces*, 11:46233–46240.

[Shi et al., 2020] Shi, W., Huang, J., Fang, R., and Liu, M. (2020). Imparting Functionality to the Hydrogel by Magnetic-Field-Induced Nano-assembly and Macro-response. *ACS Applied Materials & Interfaces*, 12:5177–5194.

[Shi et al., 2021] Shi, X., Deng, Z., Zhang, P., Wang, Y., Zhou, G., and Haan, L. T. (2021). Wearable Optical Sensing of Strain and Humidity: A Patterned Dual-Responsive Semi-Interpenetrating Network of a Cholesteric Main-Chain Polymer and a Poly(ampholyte). *Advanced Functional Materials*, 31:2104641.

[Singh and Datta, 2023] Singh, R. and Datta, B. (2023). Advances in Biomedical and Environmental Applications of Magnetic Hydrogels. *ACS Applied Polymer Materials*, 5:5474–5494.

[Song et al., 2020] Song, X., Wang, W., Yang, F., Wang, G., and Rui, X. (2020). The study of enhancement of magnetorheological effect based on natural rubber/thermoplastic elastomer SEBS hybrid matrix. *Journal of Intelligent Material Systems and Structures*, 31:339–348.

[Spangenberg et al., 2021] Spangenberg, J., Kilian, D., Czichy, C., Ahlfeld, T., Lode, A., Günther, S., Odenbach, S., and Gelinsky, M. (2021). Bioprinting of Magnetically Deformable Scaffolds. *ACS Biomaterials Science & Engineering*, 7:648–662.

[Taghizadeh et al., 2023] Taghizadeh, S., Tayebi, L., Akbarzadeh, M., Lohrasbi, P., and Savardashtaki, A. (2023). Magnetic hydrogel applications in articular cartilage tissue engineering. *Journal of Biomedical Materials Research Part A*, 112(2):260–275.

[Tang et al., 2021a] Tang, J., Sun, B., Yin, Q., Yang, M., Hu, J., and Wang, T. (2021a). 3D printable, tough, magnetic hydrogels with programmed magnetization for fast actuation. *Journal of Materials Chemistry B*, 9(44):9183–9190.

[Tang et al., 2019] Tang, J., Yin, Q., Qiao, Y., and Wang, T. (2019). Shape Morphing of Hydrogels in Alternating Magnetic Field. *ACS Applied Materials & Interfaces*, 11:21194–21200.

[Tang et al., 2021b] Tang, L., Wang, L., Yang, X., Feng, Y., Li, Y., and Feng, W. (2021b). Poly(N-isopropylacrylamide)-based smart hydrogels: Design, properties and applications. *Progress in Materials Science*, 115:100702.

[Tay et al., 2018a] Tay, A., Sohrabi, A., Poole, K., Seidlits, S., and Carlo, D. D. (2018a). A 3D Magnetic Hyaluronic Acid Hydrogel for Magnetomechanical Neuromodulation of Primary Dorsal Root Ganglion Neurons. *Advanced Materials*, 30:1800927.

[Tay et al., 2018b] Tay, Z. W., Chandrasekharan, P., Chiu-Lam, A., Hensley, D. W., Dhavalikar, R., Zhou, X. Y., Yu, E. Y., Goodwill, P. W., Zheng, B., Rinaldi, C., and Conolly, S. M. (2018b). Magnetic Particle Imaging-Guided Heating in Vivo Using Gradient Fields for Arbitrary Localization of Magnetic Hyperthermia Therapy. *ACS Nano*, 12:3699–3713.

[Vazquez-Perez et al., 2021] Vazquez-Perez, F. J., Gila-Vilchez, C., Duran, J. D. G., Zubarev, A., de Cienfuegos, L. A., Rodriguez-Arco, L., and Lopez-Lopez, M. T. (2021). Composite polymer hydrogels with high and reversible elongation under magnetic stimuli. *Polymer*, 230:124093.

[Vázquez Pérez, 2024] Vázquez Pérez, F. J. (2024). *Desarrollo y Caracterización de Actuadores Blandos Basados en Hidrogeles Magnéticos*. PhD thesis, Universidad de Granada.

[Wan et al., 2023] Wan, T., Wang, J., He, S., Wang, T., Zheng, Y., Xie, F., and Tang, Q. (2023). Synthesis and lead ion absorption of magnetic hydrogel nanocomposite absorbents with semi-IPNs structure. *Polymer Bulletin*, 80:3633–3647.

[Wang et al., 2022a] Wang, H., Zhu, Z., Jin, H., Wei, R., Bi, L., and Zhang, W. (2022a). Magnetic soft robots: Design, actuation, and function. *Journal of Alloys and Compounds*, 922:166219.

[Wang et al., 2018] Wang, Y., Li, B., Xu, F., Han, Z., Wei, D., Jia, D., and Zhou, Y. (2018). Tough Magnetic Chitosan Hydrogel Nanocomposites for Remotely Stimulated Drug Release. *Biomacromolecules*, 19:3351–3360.

[Wang et al., 2020] Wang, Y., Toyoda, K., Uesugi, K., and Morishima, K. (2020). A simple micro check valve using a photo-patterned hydrogel valve core. *Sensors and Actuators A: Physical*, 304:111878.

[Wang et al., 2019] Wang, Y.-h., Zhong, M., Wang, L., Liu, Y.-l., Wang, B., and Li, Y. (2019). Chelerythrine loaded composite magnetic thermosensitive hydrogels as a novel anticancer drug-delivery system. *Journal of Drug Delivery Science and Technology*, 54:101293.

[Wang et al., 2022b] Wang, Z., Valenzuela, C., Xue, P., Zhang, X., Zhang, X., Chen, Y., Yang, Y., Wang, L., and Xu, X. (2022b). Magnetic Structural Color Hydrogels for Patterned Photonic Crystals and Dynamic Camouflage. *ACS Applied Polymer Materials*, 4(5):3618–3626.

[Weber and Murray, 1973] Weber, A. and Murray, J. M. (1973). Molecular control mechanisms in muscle contraction. *Physiological Reviews*, 53(3):612–673.

[Weerasundara et al., 2020] Weerasundara, L., Gabriele, B., Figoli, A., Ok, Y.-S., and Bundschuh, J. (2020). Hydrogels: Novel materials for contaminant removal in water–A review. *Critical Reviews in Environmental Science and Technology*, 51(17):1970–2014.

[Winter, 1987] Winter, H. H. (1987). Can the gel point of a cross-linking polymer be detected by the G'-G" crossover? *Polymer Engineering and Science*, 27:1698–1702.

[Wolfbeis, 1991] Wolfbeis, O. S. (1991). *Fibre Optic Chemical Sensors and Biosensors*. CRC Press: Boca Raton.

[Wright et al., 2022] Wright, A. L., Righelli, L., Broomhall, T. J., Lamont, H. C., and El Haj, A. J. (2022). Magnetic Nanoparticle-Mediated Orientation of Collagen Hydrogels for Engineering of Tendon-Mimetic Constructs. *Frontiers in Bioengineering and Biotechnology*, 10:797437.

[Wu et al., 2020] Wu, S., Hu, W., Ze, Q., Sitti, M., and Zhao, R. (2020). Multifunctional magnetic soft composites: a review. *Multifunctional Materials*, 3:042003.

[Wu et al., 2022] Wu, Y., Dong, X., kang Kim, J., Wang, C., and Sitti, M. (2022). Wireless soft millirobots for climbing three-dimensional surfaces in confined spaces. *Science Advances*, 8(21):eabn3431.

[Xia et al., 2023] Xia, Y., Ma, Z., Wu, X., Wei, H., Zhang, H., Li, G., Qian, Y., Shahriari-Khalaji, M., Hou, K., Cao, R., and Zhu, M. (2023). Advances in Stimuli-Responsive Chitosan Hydrogels for Drug Delivery Systems. *Macromolecular Bioscience*, 24:2300399.

[Xiong et al., 2018] Xiong, Z., Zheng, C., Jin, F., Wei, R., Zhao, Y., Gao, X., Xia, Y., Dong, X., Zheng, M., and Duan, X. (2018). Magnetic-field-driven ultra-small 3D hydrogel microstructures: Preparation of gel photoresist and two-photon polymerization microfabrication. *Sensors and Actuators B: Chemical*, 274:541–550.

[Xu et al., 2001] Xu, H., Aylott, J. W., Kopelman, R., Miller, T. J., and Philbert, M. A. (2001). A Real-Time Ratiometric Method for the Determination of Molecular Oxygen Inside Living Cells Using Sol-Gel-Based Spherical Optical Nanosensors with Applications to Rat C6 Glioma. *Analytical Chemistry*, 73:4124–4133.

[Xuan et al., 2009] Xuan, S., Wang, Y.-X. J., Yu, J. C., and Leung, K. C.-F. (2009). Tuning the Grain Size and Particle Size of Superparamagnetic Fe_3O_4 Microparticles. *Chemistry of Materials*, 21:5079–5087.

[Yan et al., 2022] Yan, G., He, S., Chen, G., Tang, X., Sun, Y., Xu, F., Zeng, X., and Lin, L. (2022). Anisotropic, strong, self-adhesive and strain-sensitive hydrogels enabled by magnetically-oriented cellulose/polydopamine nanocomposites. *Carbohydrate Polymers*, 276:118783.

[Yang et al., 2022] Yang, L., Miao, J., Li, G., Ren, H., Zhang, T., Guo, D., Tang, Y., Shang, W., and Shen, Y. (2022). Soft Tunable Gelatin Robot with Insect-like Claw for Grasping, Transportation, and Delivery. *ACS Applied Polymer Materials*, 4:5431–5440.

[Yao et al., 2018] Yao, J., Sun, Y., Wang, Y., Fu, Q., Xiong, Z., and Liu, Y. (2018). Magnet-induced aligning magnetorheological elastomer based on ultra-soft matrix. *Composites Science and Technology*, 162:170–179.

[Yarali et al., 2022] Yarali, E., Baniasadi, M., Zolfagharian, A., Chavoshi, M., Arefi, F., Hossain, M., Bastola, A., Ansari, M., Foyouzat, A., Dabbagh, A., Ebrahimi, M., Mirzaali, M. J., and Bodaghi, M. (2022). Magneto-/ electro-responsive polymers toward manufacturing, characterization, and biomedical/ soft robotic applications. *Applied Materials Today*, 26:101306.

[Yu et al., 2020] Yu, Y., Guo, J., Wang, Y., Shao, C., Wang, Y., and Zhao, Y. (2020). Bioinspired Helical Micromotors as Dynamic Cell Microcarriers. *ACS Applied Materials & Interfaces*, 12(14):16097–16103.

[Zeng et al., 2022] Zeng, Y., Zhang, C., Du, D., Li, Y., Sun, L., Han, Y., He, X., Dai, J., and Shi, L. (2022). Metal-organic framework-based hydrogel with structurally dynamic properties as a stimuli-responsive localized drug delivery system for cancer therapy. *Acta Biomaterialia*, 145:43–51.

[Zhai et al., 2023] Zhai, Y., Gong, C., Chen, J., and Chang, C. (2023). Magnetic-field induced asymmetric hydrogel fibers for tough actuators with programmable deformation. *Chemical Engineering Journal*, 477:147088.

[Zhalmuratova and Chung, 2020] Zhalmuratova, D. and Chung, H.-J. (2020). Reinforced Gels and Elastomers for Biomedical and Soft Robotics Applications. *ACS Applied Polymer Materials*, 2:1073–1091.

[Zhang et al., 2020a] Zhang, C., Dai, Y., Wu, Y., Lu, G., Cao, Z., Cheng, J., Wang, K., Yang, H., Xia, Y., Wen, X., Ma, W., Liu, C., and Wang, Z. (2020a). Facile preparation of polyacrylamide/chitosan/Fe_3O_4 composite hydrogels for effective removal of methylene blue from aqueous solution. *Carbohydrate Polymers*, 234:115882.

[Zhang et al., 2020b] Zhang, C., Wu, B., Zhou, Y., Zhou, F., Liu, W., and Wang, Z. (2020b). Mussel-inspired hydrogels: from design principles to promising applications. *Chemical Society Reviews*, 49(11):3605–3637.

[Zhang et al., 2020c] Zhang, J., Pang, H., Wang, Y., and Gong, X. (2020c). The magneto-mechanical properties of off-axis anisotropic magnetorheological elastomers. *Composites Science and Technology*, 191:108079.

[Zhang et al., 2023] Zhang, L., Du, H., Sun, X., Cheng, F., Lee, W., Li, J., Dai, G., Fang, N. X., and Liu, Y. (2023). 3D Printing of Interpenetrating Network Flexible Hydrogels with Enhancement of Adhesiveness. *ACS Applied Materials & Interfaces*, 15:41892–41905.

[Zhang et al., 2022] Zhang, M.-K., Ling, X.-H., Zhang, X.-H., and Han, G.-Z. (2022). A novel alginate/PVA hydrogel-supported Fe_3O_4 particles for efficient heterogeneous Fenton degradation of organic dyes. *Colloids and Surfaces A: Physicochemical and Engineering Aspects*, 652:129830.

[Zhang et al., 2021] Zhang, M.-K., Zhang, X.-H., and Han, G.-Z. (2021). Magnetic alginate/PVA hydrogel microspheres with selective adsorption performance for aromatic compounds. *Separation and Purification Technology*, 278:119547.

[Zhang et al., 2015] Zhang, Y., Fu, Q., and Ge, J. (2015). Photonic sensing of organic solvents through geometric study of dynamic reflection spectrum. *Nature Communications*, 6:7510.

[Zhao et al., 2011] Zhao, X., Kim, J., Cezar, C. A., Huebsch, N., Lee, K., Bouhadir, K., and Mooney, D. J. (2011). Active scaffolds for on-demand drug and cell delivery. *Proceedings of the National Academy of Sciences*, 108:67–72.

[Zhao et al., 2022] Zhao, Y., Hua, M., Yan, Y., Wu, S., Alsaid, Y., and He, X. (2022). Stimuli-Responsive Polymers for Soft Robotics. *Annual Review of Control, Robotics, and Autonomous Systems*, 5(1):515–545.

[Zhou et al., 2020] Zhou, Y., Li, L., Li, W., Wen, S., Jiang, L., Jerrams, S., Ma, J., and Chen, S. (2020). The fabrication and properties of magnetorheological elastomers employing bio-inspired dopamine modified carbonyl iron particles. *Smart Materials and Structures*, 29:055005.

[Zhu et al., 2020] Zhu, Q. L., Dai, C. F., Wagner, D., Daab, M., Hong, W., Breu, J., Zheng, Q., and Wu, Z. L. (2020). Distributed Electric Field Induces Orientations of Nanosheets to Prepare Hydrogels with Elaborate Ordered Structures and Programmed Deformations. *Advanced Materials*, 32(47):2005567.

Appendix A.

Table A.1: Two samples t-test with a significance level of 0.05 and null hypothesis mean1-mean2 = 0 for the magnitudes from the uniaxial tensile tests measured parallel to the direction of the tensile stress applied during the SCDPs. Column a: equal variance is assumed. Column b: equal variance is not assumed.

Magnitude	Samples	a	b
Young's modulus	AH100-0 control 4.5 % w/w & AH100-0 control 5.5 % w/w	✓	✓
	AH100-0 control 5.0 % w/w & AH100-0 control 5.5 % w/w	✓	✓
	AH100-0 traction 8h & AH100-0 traction 14h	✓	✓
	AH100-0 compression 20 min & AH100-0 compression 20 min	X	X
	AH50-50 traction 14h & AH50-50 traction 24h	X	X
	AH50-50 compression 30 min & AH50-50 traction 24h	X	X
Maximum deformation at break	AH100-0 control 4.0 % w/w & AH100-0 compression 20 min	X	X
	AH100-0 compression 10 min & AH100-0 compression 20 min	✓	X
	AH100-0 compression 10 min & AH100-0 compression 30 min	X	X
	AH50-50 control 4.0 % w/w & AH50-50 traction 8h	✓	✓
	AH50-50 control 4.0 % w/w & AH50-50 traction 24h	✓	✓
Tensile stress at break	AH100-0 control 4.5 % w/w & AH100-0 control 5.5 % w/w	✓	✓
	AH100-0 compression 20 min & AH100-0 compression 30 min	✓	✓
	AH100-0 traction 8h & AH100-0 traction 14h	X	X
	AH100-0 compression 30 min & AH100-0 traction 24h	✓	✓
	AH50-50 control 4.0 % w/w & AH50-50 traction 14h	✓	✓
	AH50-50 traction 8h & AH50-50 traction 24h	✓	X
	AH50-50 compression 30 min & AH50-50 traction 24h	✓	✓

Table A.2: Two samples t-test with a significance level of 0.05 and null hypothesis mean1-mean2 = 0 for the magnitudes from the oscillatory shear tests. Column a: equal variance is assumed. Column b: equal variance is not assumed.

Magnitude	Samples	a	b
Storage modulus	AH100-0 control 4 wt.% & AH100-0 compression 30 min	X	X
	AH100-0 control 5.5 % w/w & AH100-0 compression 30 min	X	X
	AH100-0 control 4 % w/w & AH100-0 traction 14h	X	X
	AH100-0 control 5 % w/w & AH100-0 traction 14h	✓	X
	AH100-0 compression 10 min & AH100-0 traction 8h	X	X
	AH100-0 compression 20 min & AH100-0 traction 14h	X	X
Loss modulus	AH100-0 control 4 % w/w & AH100-0 traction 24h	X	X
	AH100-0 control 5 % w/w & AH100-0 traction 14h	X	X
	AH100-0 control 5.5 % w/w & AH100-0 traction 24h	X	X
	AH100-0 traction 8h & AH50-50 traction 24h	X	X
	AH50-50 compression 10 min & AH50-50 traction 8h	X	X

Table A.3: Two samples t-test with a significance level of 0.05 and null hypothesis mean1-mean2 = 0 for the magnitudes from the uniaxial tensile tests measured perpendicularly to the direction of the tensile stress applied during the SCDPs. Column a: equal variance is assumed. Column b: equal variance is not assumed.

Magnitude	Samples	a	b
Young's modulus	AH100-0 control 4 % w/w & & AH100-0 traction 24h perpendicular	✓	✓
	AH100-0 control 4.0 % w/w & & AH50-50 control 4.0 % w/w	✓	✓
	AH100-0 traction 24h perpendicular & & AH50-50 traction 24h perpendicular	X	✓
Tensile stress at break	AH100-0 control 4.0 % w/w & & AH100-0 traction 24h perpendicular	X	X
	AH50-50 traction 24h & & AH50-50 traction 24h perpendicular	✓	✓
Deformation at break	AH100-0 traction 24h & & AH100-0 traction 24h perpendicular	X	X
	AH50-50 control 4.0 % w/w & & AH50-50 traction 24h	✓	✓

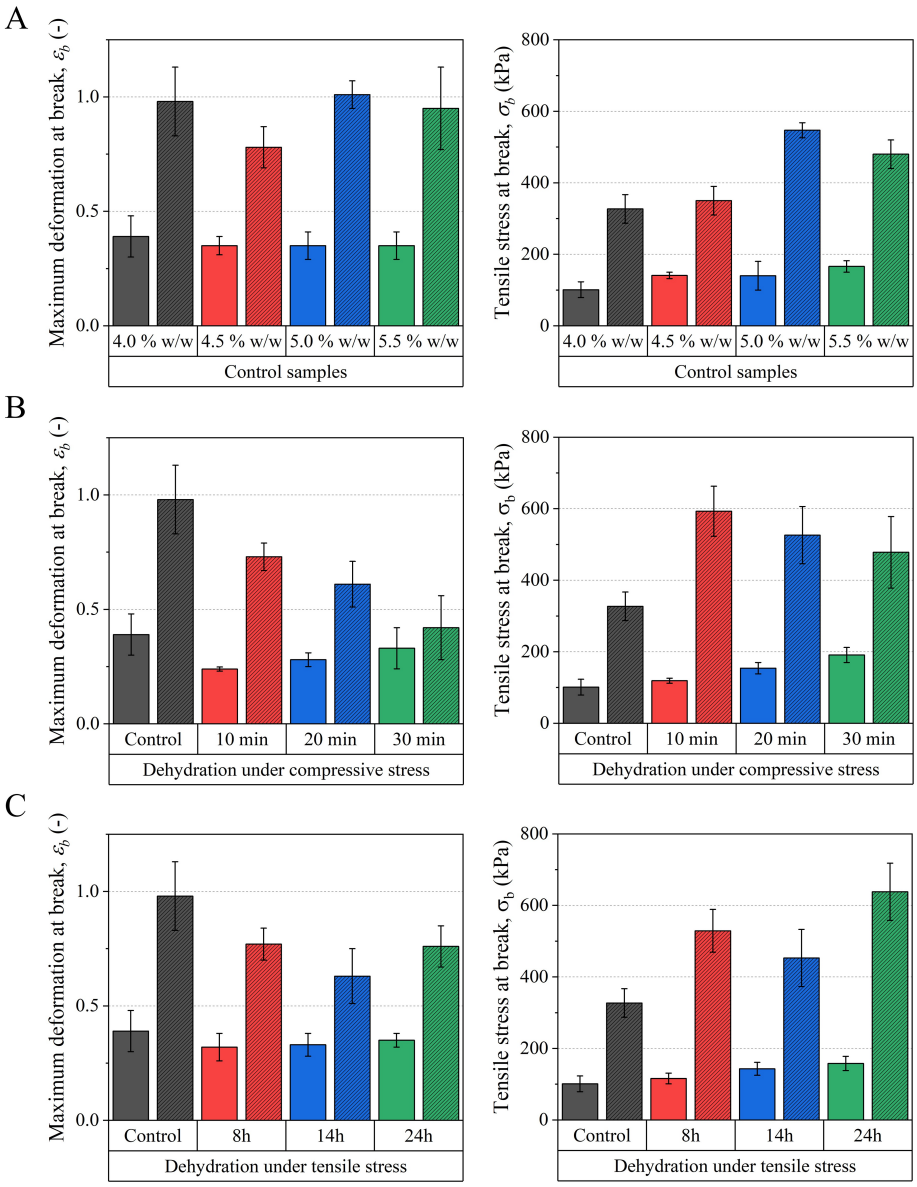

Figure A.1: Deformation at break (on the left) and and tensile stress at break (on the right) of the hydrogels measured under tensile stress. This figure presents the data of the control samples, and the data of the samples dehydrated under compressive and tensile stress. The bar with solid colors are the values for AH100-0 samples and the striped ones for AH50-50 samples. A) Control samples. B) Samples dehydrated under compressive stresses. C) Samples dehydrated under tensile stress. Note that the same scale is used in the axis.

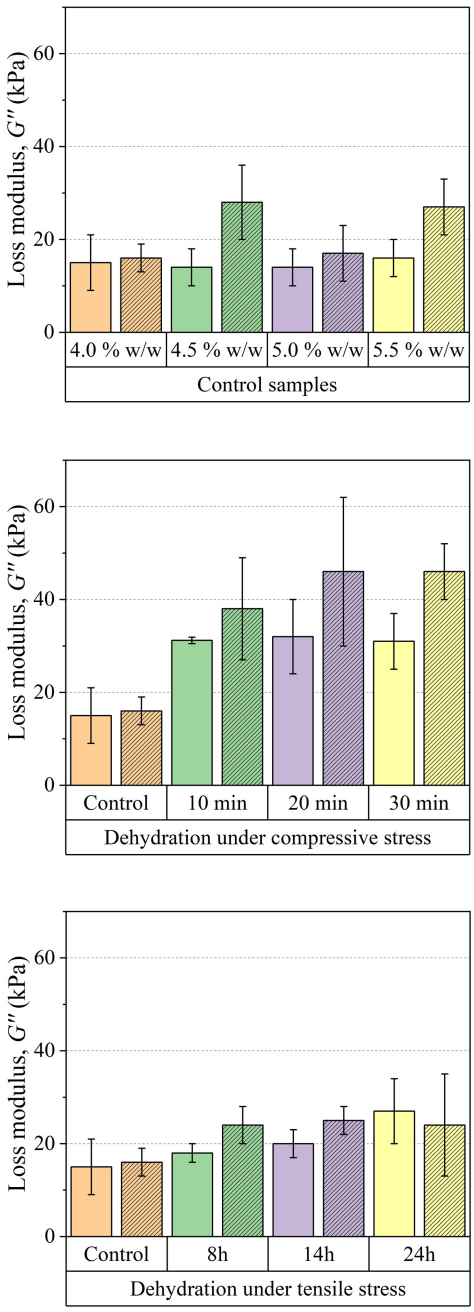

Figure A.2: Loss modulus of the hydrogels measured under oscillatory shear stress. This figure presents the data for the control samples and the samples dehydrated under compressive and tensile stress. The solid bars represent the values for AH100-0 samples and the striped ones for AH50-50 samples. Note that the same scale is used for the axes.

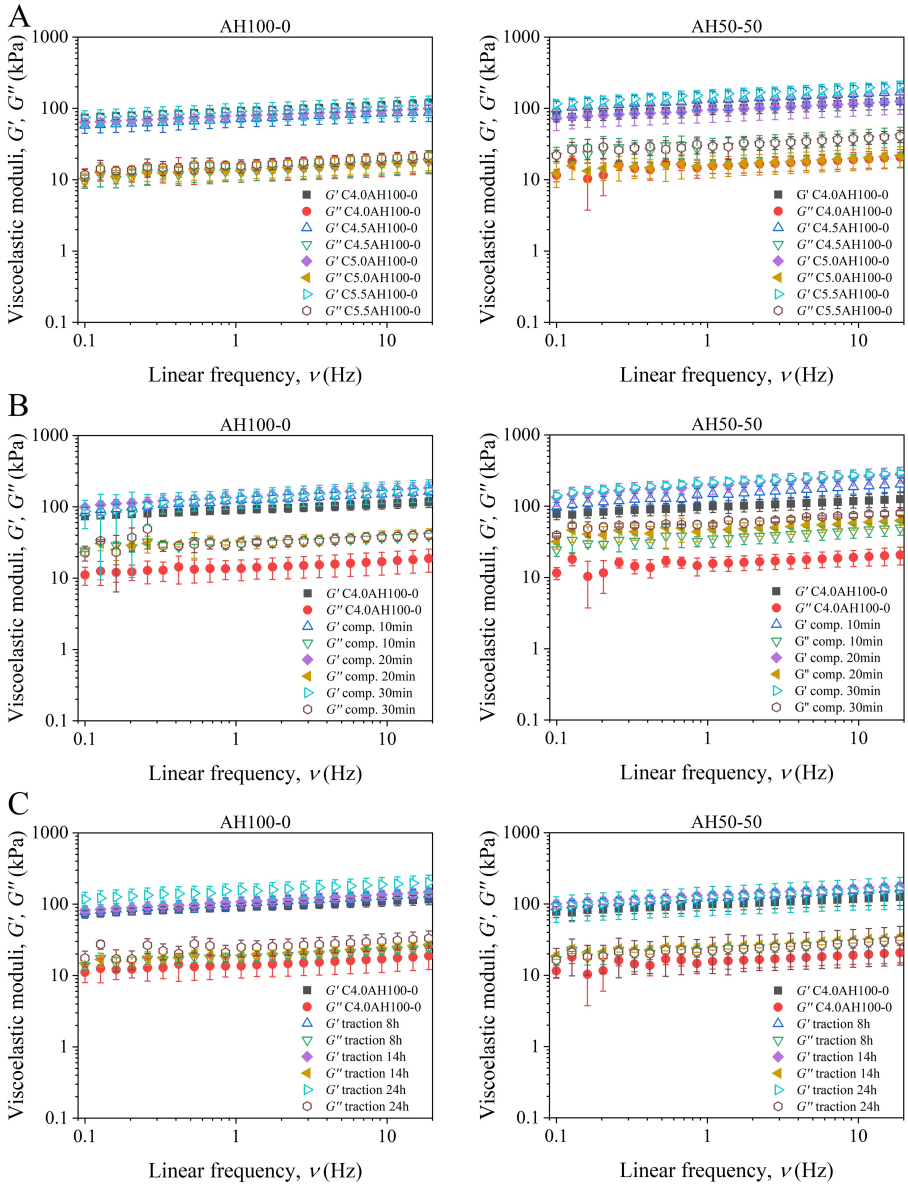

Figure A.3: Oscillatory frequency sweeps of the dehydrated alginate hydrogels. On the left, AH100-0 samples and on the right, AH50-50 samples A) Control samples. B) Samples dehydrated under compressive stress. C) Samples dehydrated under tensile stress. Note that different graphs use the same scale.

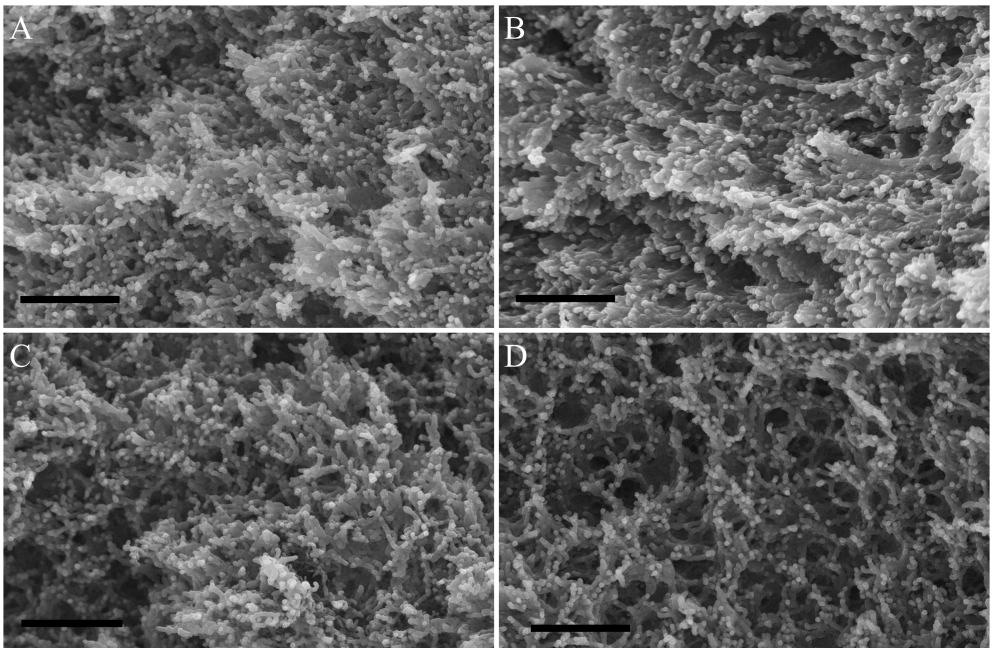

Figure A.4: SEM images of the alginate hydrogels studied. A) and B) polymeric structure of AH100-0 and AH50-50 samples after the SCDP under compressive stress (side view), respectively. C) and D) polymeric structure of AH100-0 and AH50-50 samples after the SCDP under compressive stress (top view), respectively. The compressive stress in all cases was applied during 30 minutes. Scale bars correspond to 1 μm.

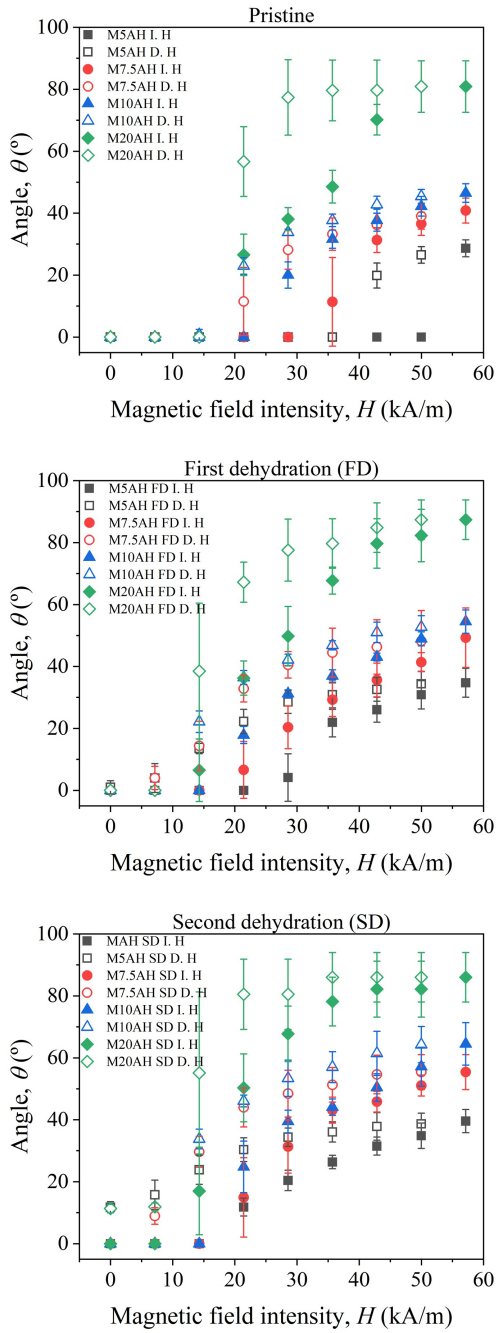

Figure A.5: Angle vs. magnetic field intensity for the different concentrations of MPs and dehydration of the actuator. F.D.: First dehydration; S.D.: Second Dehydration; I.: Increasing; D.: Decreasing. Note that same scales are used in both axes.

Appendix B.

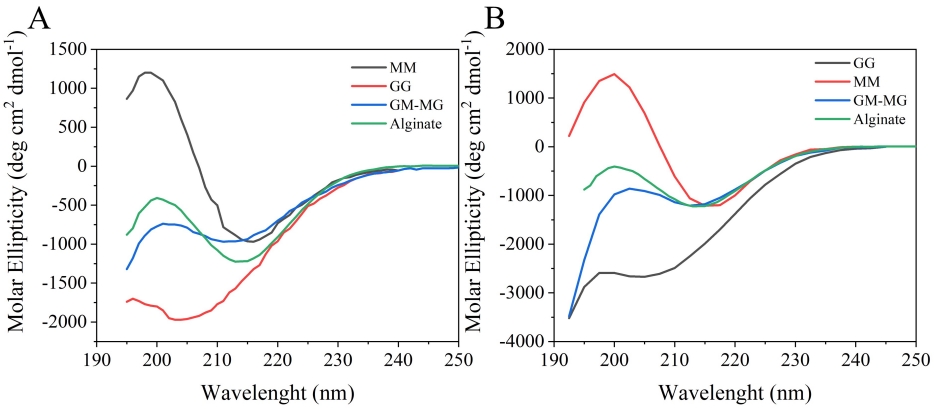

Figure B.1: A) and B) determination of M/G composition by ellipsometry (Donati et al. [Donati et al., 2003]; Morris, Rees, & Thom [Morris et al., 1980]).

Table B.1: Results from the two-way Anova test with Tukey's post hoc with a significance level of 0.05 in both cases. A) The upper-right part of the table shows the comparisons between the loss modulus (G'') for the different concentrations of Fe-CC (% w/w) in Alginate Mag-SINPs, whereas the lower-left shows the comparisons for the storage modulus (G'). B) The upper-right part of the table shows the comparisons between the compressive modulus (E_c) for the different concentrations of Fe-CC (% w/w) in Alginate Mag-SINPs, whereas the lower-left shows the comparisons for the compressive strain at break (ϵ_c). C) Same as B) but under tensile stress. S = significant difference; NS = no significant difference.

A)

$G' \backslash G''$	**0.0**	**6.4**	**12.0**	**17.2**	**21.9**	**26.2**
0.0		S	S	S	S	S
6.4	S		NS	S	S	NS
12.0	S	S		S	S	S
17.2	S	S	S		NS	S
21.9	S	S	S	NS		S
26.2	S	S	S	S	S	

B)

$\epsilon_C \backslash E_C$	**0.0**	**6.4**	**12.0**	**17.2**	**21.9**	**26.2**
0.0		S	S	S	S	S
6.4	S		NS	NS	NS	NS
12.0	S	NS		NS	NS	NS
17.2	S	S	NS		NS	S
21.9	S	S	NS	NS		S
26.2	NS	S	S	S	S	

C)

$\epsilon_T \backslash E_T$	**0.0**	**6.4**	**12.0**	**17.2**	**21.9**	**26.2**
0.0		S	S	S	S	S
6.4	S		NS	NS	S	NS
12.0	S	NS		NS	NS	NS
17.2	NS	NS	NS		NS	NS
21.9	S	NS	NS	NS		NS
26.2	S	NS	NS	NS	NS	

Table B.2: Results from the two-way Anova test with Tukey's post hoc with a significance level of 0.05 in both cases. The upper-right part of the tables shows the comparisons between one of the quantities for the control samples of each nonmagnetic SINP, whereas the lower-left shows the comparisons for the same quantity but for the Mag-SIPNs with a particle concentration of 6.4 % w/w. The diagonal shows the comparisons between nonmagnetic and magnetic SIPNs. A) Storage modulus. B) Loss modulus. C) Compressive modulus. D) Strain at break under compressive stress. E) Tensile modulus. F) Strain at break under tensile stress. S = significant difference; NS = no significant difference.

A) Storage modulus

Fe-CC\nonmagnetic	**Alginate**	**CCmedium**	**CChigh**	**HC720**	**HC1300**
Alginate	S	S	S	S	NS
CCmedium	S	S	S	S	S
CChigh	S	NS	S	S	S
HC720	S	NS	NS	S	S
HC1300	S	NS	NS	NS	S

B) Loss modulus

Fe-CC\nonmagnetic	**Alginate**	**CCmedium**	**CChigh**	**HC720**	**HC1300**
Alginate	S	S	S	S	S
CCmedium	NS	S	NS	S	S
CChigh	NS	NS	S	S	S
HC720	S	S	S	S	S
HC1300	S	S	S	NS	S

C) Compressive modulus

Fe-CC\nonmagnetic	**Alginate**	**CCmedium**	**CChigh**	**HC720**	**HC1300**
Alginate	S	S	S	S	NS
CCmedium	NS	NS	NS	NS	S
CChigh	NS	NS	NS	NS	S
HC720	NS	NS	NS	NS	S
HC1300	NS	NS	NS	NS	S

D) Strain at break under compressive stress

Fe-CC\nonmagnetic	Alginate	CCmedium	CChigh	HC720	HC1300
Alginate	NS	NS	S	NS	NS
CCmedium	NS	NS	NS	NS	NS
CChigh	NS	NS	NS	NS	S
HC720	NS	NS	NS	NS	NS
HC1300	NS	NS	NS	NS	NS

E) Tensile modulus

Fe-CC\nonmagnetic	Alginate	CCmedium	CChigh	HC720	HC1300
Alginate	S	NS	NS	NS	S
CCmedium	NS	S	NS	S	S
CChigh	NS	NS	S	S	S
HC720	NS	NS	NS	S	NS
HC1300	NS	NS	NS	NS	S

F) Strain at break under tensile stress

Fe-CC\nonmagnetic	Alginate	CCmedium	CChigh	HC720	HC1300
Alginate	NS	NS	S	S	S
CCmedium	S	NS	NS	NS	NS
CChigh	NS	NS	S	NS	NS
HC720	S	NS	NS	NS	NS
HC1300	NS	S	NS	S	S

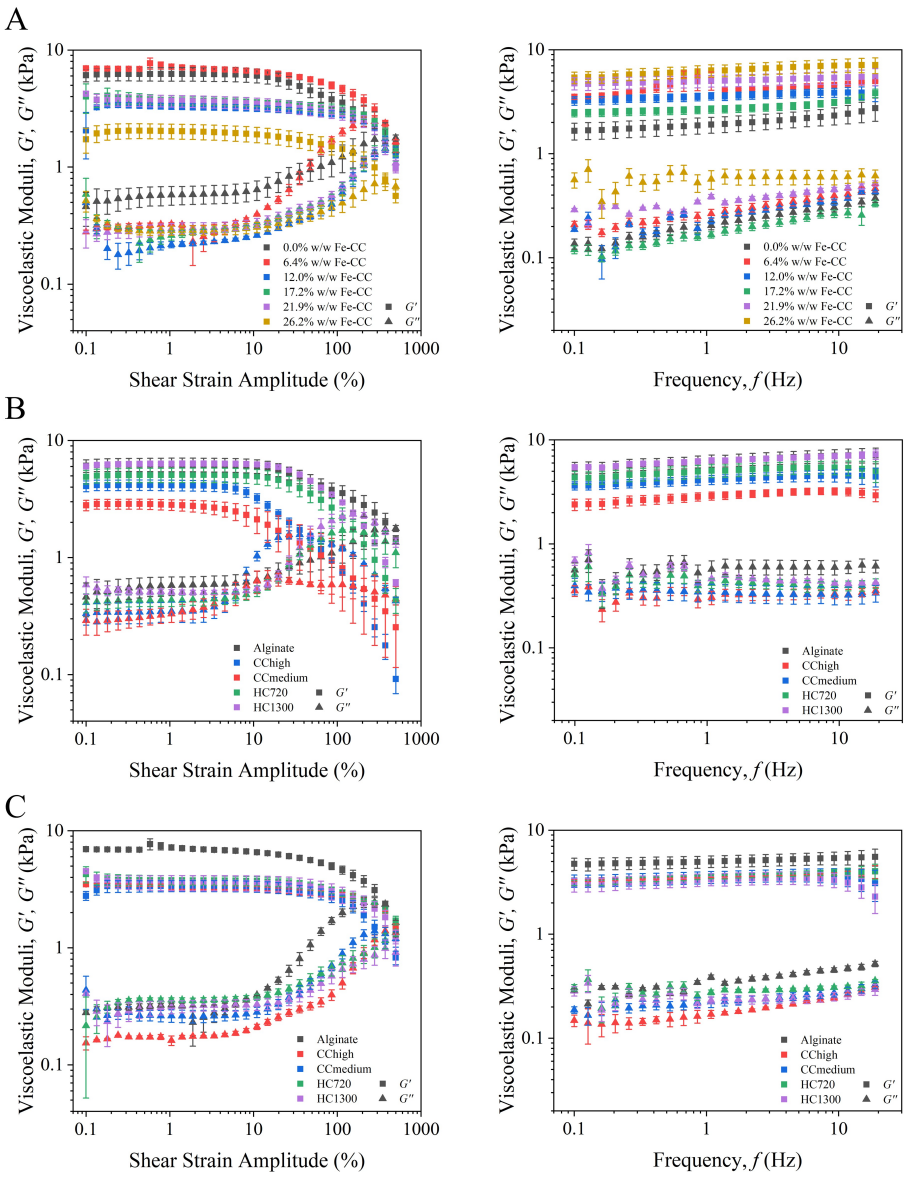

Figure B.2: Shear strain amplitude sweeps (on the left) and frequency sweeps (on the right). A) Alginate Mag-SIPNs with different concentrations of MPs. B) Mag-SIPNs with different biopolymers without particles. C) Mag-SIPNs with a particle concentration of 6.4 % w/w of MPs.

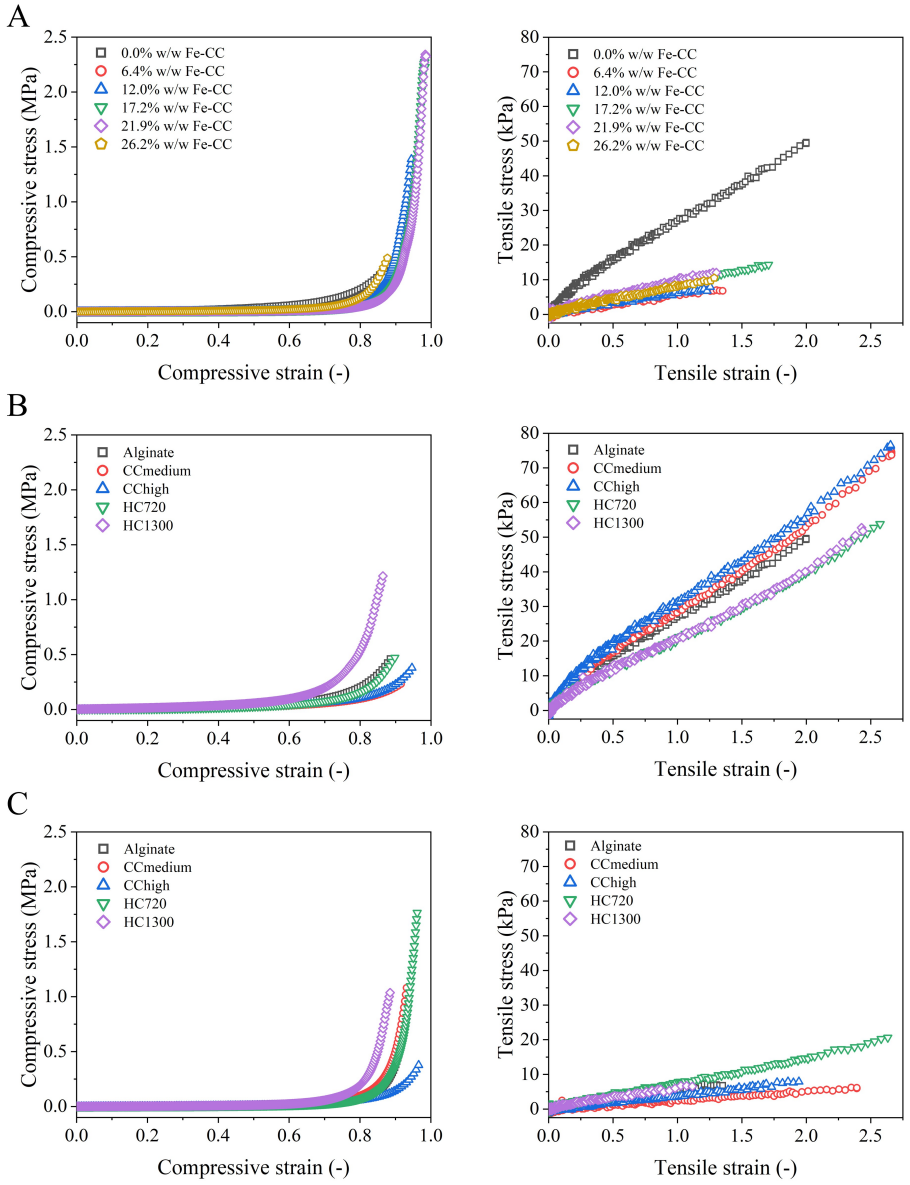

Figure B.3: Strain vs. stress curves under compressive stress (on the left) and strain vs. stress curves under tensile stress (on the right). A) Alginate Mag-SIPNs with different concentrations of MPs. B) Mag-SIPNs with different biopolymers without particles. C) Mag-SIPNs with a particle concentration of 6.4 % w/w of MPs.

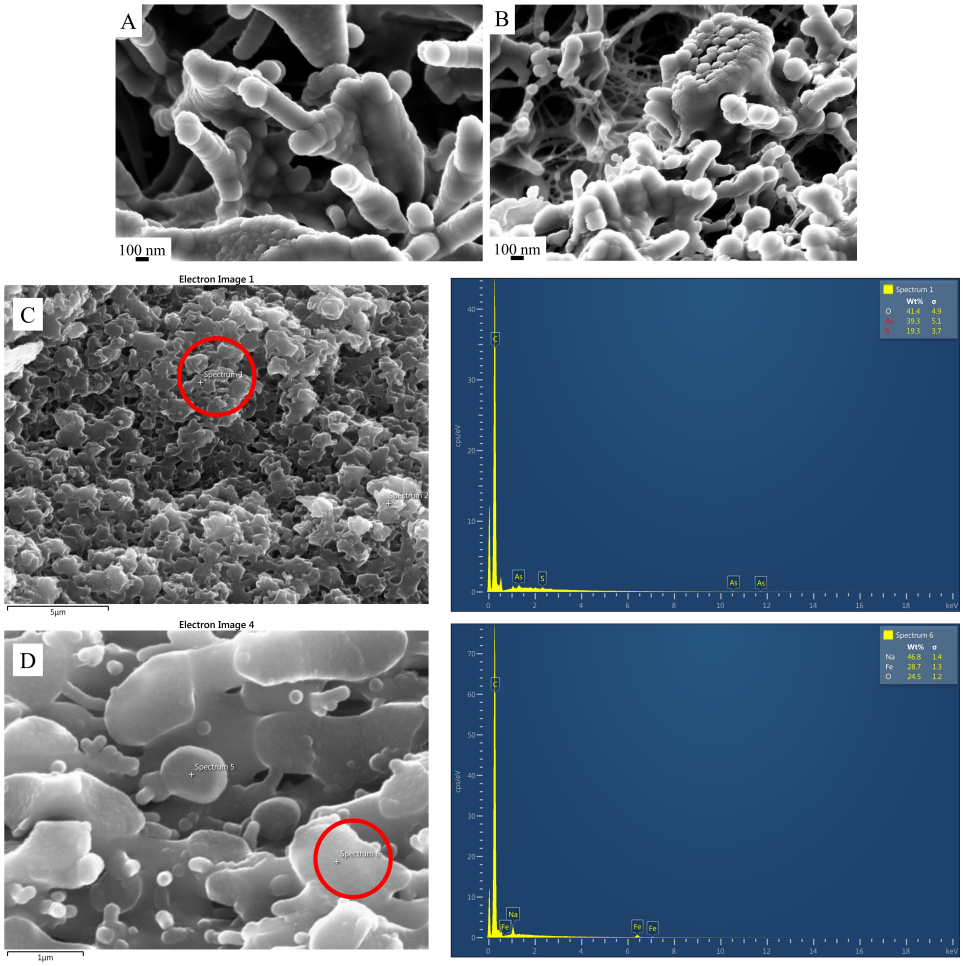

Figure B.4: Scanning Electron Microscopy (SEM) images and Energy-Dispersive X-ray spectroscopy (EDX) analysis for nonmagnetic and magnetic SIPNs. A) SEM image of the internal structure of nonmagnetic HC720 SIPN. B) SEM image of the internal structure of HC720 Mag-SIPN, with a concentration of magnetic microparticles of 6.4 % w/w. C) EDX analysis of nonmagnetic HC720 SIPN, in which iron is not observed. D) EDX analysis of HC720 Mag-SIPN, in which typical signal of iron are observed.

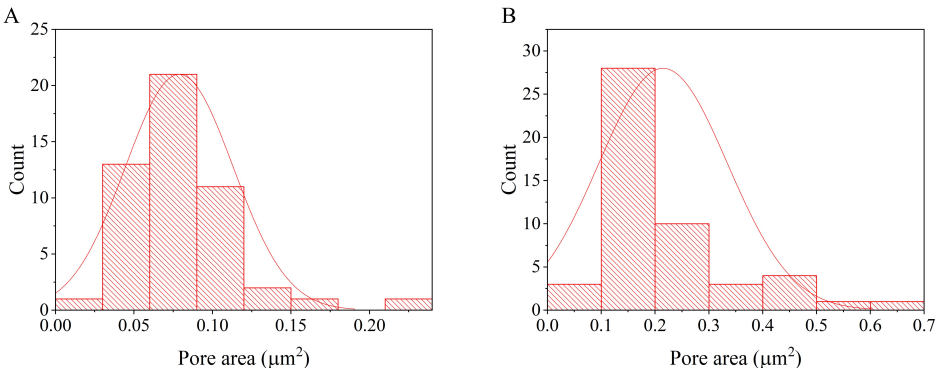

Figure B.5: Distribution of the area of the pore for HC720 SIPNs without magnetic microparticles A) and for the same hydrogel with a concentration of Fe-CC of 6.4 % w/w B). A total of 50 pores were measured in each case.

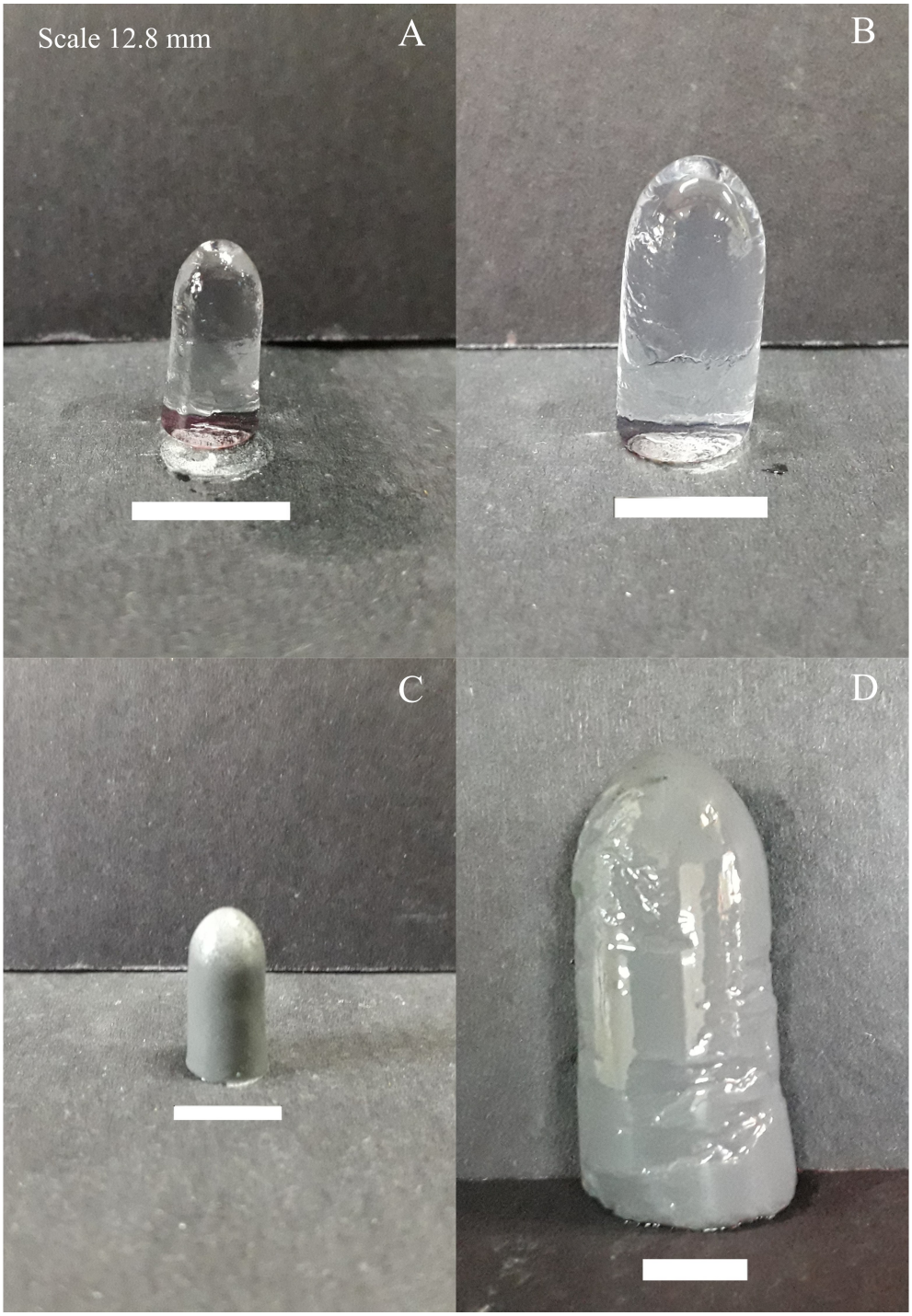

Figure B.6: A) Nonmagnetic Alginate SIPN hydrogel before swelling. B) Nonmagnetic Alginate SIPN hydrogel after 5 days in mili-Q water. C) Alginate Mag-SIPN hydrogel before swelling. C) Alginate Mag-SIPN hydrogel after 5 days in mili-Q water. Note that the Mag-SIPNs grew considerably larger than the nonmagnetic SIPNs after swelling for 5 days.

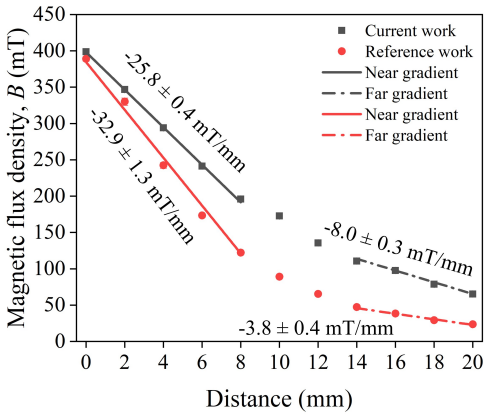

Figure B.7: Magnetic flux density (B) as a function of the distance for the two NdFeB permanent magnets in this study. As can be seen, the two magnets exhibit different field gradients depending on the distance from their surface. These differences are reflected in the response of Mag-SINPs under the actuation of each magnet. The dimensions of each magnet are as follows: current work 25 $\times$ 25 $\times$ 13 mm; reference work 15 $\times$ 15 $\times$ 8 mm.

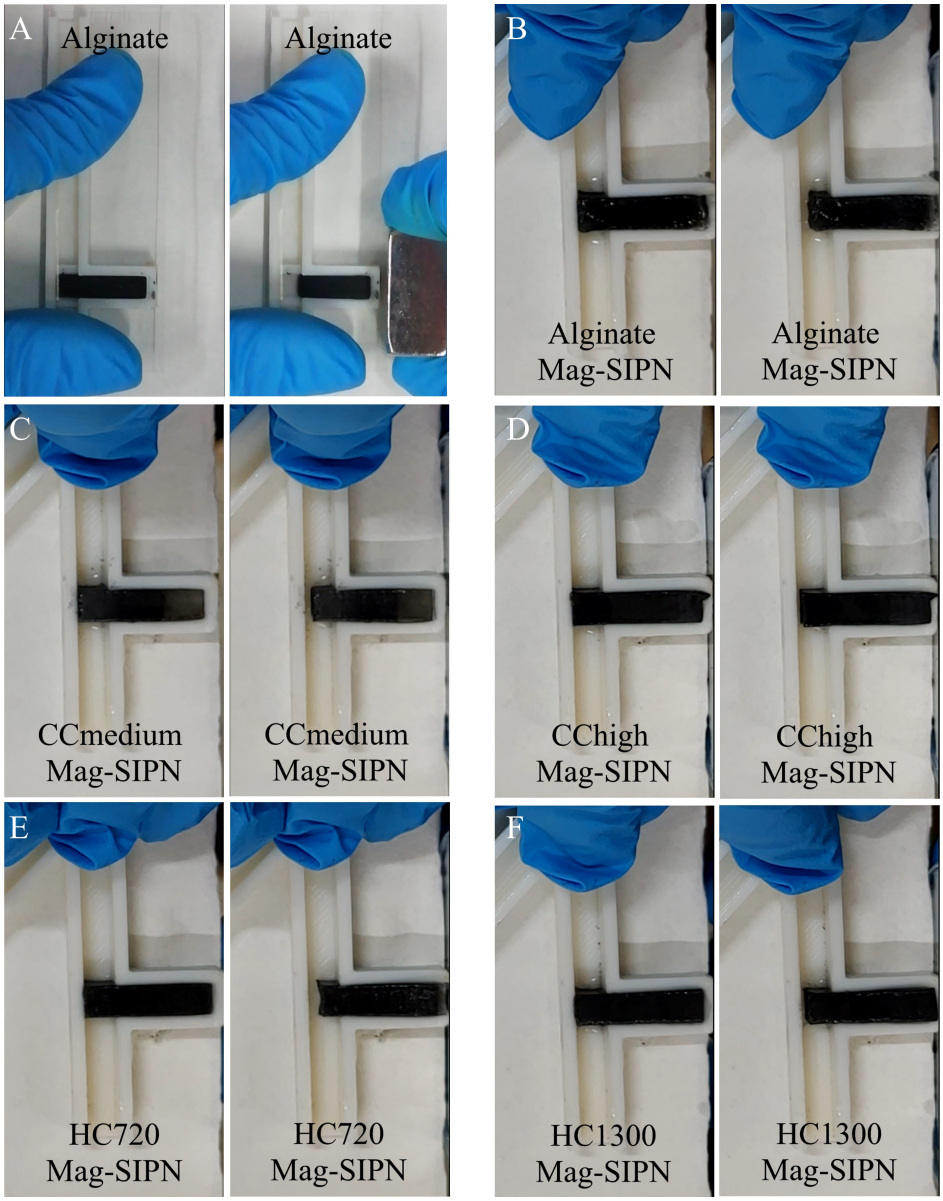

Figure B.8: Snapshot of the ferrogel actuation under a permanent magnet. The snapshots on the left shows the off-state and the ones on the right when the magnet approached one end of the ferrogel. A) Alginate hydrogels cross-linked with calcium ions. From B) to F) Mag-SIPN hydrogels studied in this chapter.

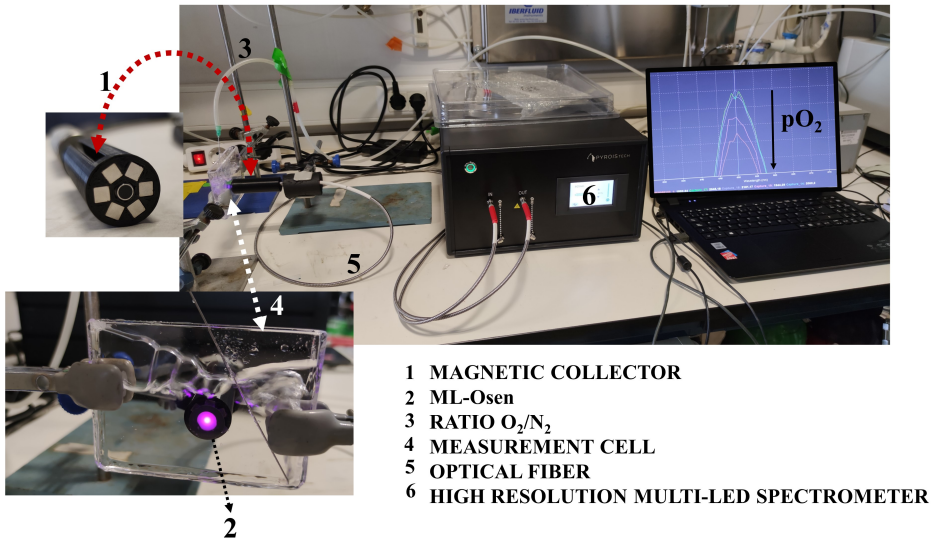

Figure B.9: Experimental setup for the application of the ML-OSen.